

**PHASE CHANGE THERMAL ENERGY STORAGE
FOR THE THERMAL CONTROL OF LARGE
THERMALLY LIGHTWEIGHT INDOOR SPACES**

A thesis submitted for the degree of
Doctor of Philosophy (PhD)

By

GOWREESUNKER, Baboo Lesh S. (BEng)

School of Engineering and Design
Brunel University

June 2013

ABSTRACT

Energy storage using Phase Change Materials (PCMs) offers the advantage of higher heat capacity at specific temperature ranges, compared to single phase storage. Incorporating PCMs in lightweight buildings can therefore improve the thermal mass, and reduce indoor temperature fluctuations and energy demand. Large atrium buildings, such as Airport terminal spaces, are typically thermally lightweight structures, with large open indoor spaces, large glazed envelopes, high ceilings and non-uniform internal heat gains. The Heating, Ventilation and Air-Conditioning (HVAC) systems constitute a major portion of the overall energy demand of such buildings.

This study presented a case study of the energy saving potential of three different PCM systems (PCM floor tiles, PCM glazed envelope and a retrofitted PCM-HX system) in an airport terminal space. A quasi-dynamic coupled TRNSYS®-FLUENT® simulation approach was used to evaluate the energy performance of each PCM system in the space. FLUENT® simulated the indoor air-flow and PCM, whilst TRNSYS® simulated the HVAC system. Two novel PCM models were developed in FLUENT® as part of this study. The first model improved the phase change conduction model by accounting for hysteresis and non-linear enthalpy-temperature relationships, and was developed using data from Differential Scanning Calorimetry tests. This model was validated with data obtained in a custom-built test cell with different ambient and internal conditions. The second model analysed the impact of radiation on the phase change behaviour. It was developed using data from spectrophotometry tests, and was validated with data from a custom-built PCM-glazed unit. These developed phase change models were found to improve the prediction errors with respect to conventional models, and together with the enthalpy-porosity model, they were used to simulate the performance of the PCM systems in the airport terminal for different operating conditions.

This study generally portrayed the benefits and flexibility of using the coupled simulation approach in evaluating the building performance with PCMs, and showed that employing PCMs in large, open and thermally lightweight spaces can be beneficial, depending on the configuration and mode of operation of the PCM system. The simulation results showed that the relative energy performance of the PCM systems relies mainly on the type and control of the system, the night recharge strategy, the latent heat capacity of the system, and the internal heat gain schedules. Semi-active systems provide more control flexibility and better energy performance than passive systems, and for the case of the airport terminal, the annual energy demands can be reduced when night ventilation of the PCM systems is not employed. The semi-active PCM-HX-8mm configuration without night ventilation, produced the highest annual energy and CO₂ emissions savings of 38% and 23%, respectively, relative to a displacement conditioning (DC) system without PCM systems.

PUBLICATIONS

Published Journal Papers

- Gowreesunker BL, Tassou SA, Kolokotroni M (2012), Improved simulation of phase change processes in applications where conduction is the dominant heat transfer mode, *Energy and Buildings* 47: 353-359
- Gowreesunker BL, Tassou SA (2013), Effectiveness of CFD simulation for the performance prediction of phase change building boards in the thermal environment control of indoor spaces, *Building and Environment* 59: 612-625
- Gowreesunker BL, Stankovic SB, Tassou SA, Kyriacou PA (2013), Experimental and numerical investigations of the optical and thermal aspects of a PCM-Glazed unit, *Energy and Buildings* 61: 239-249
- Gowreesunker BL, Tassou SA, Kolokotroni M (2013), Coupled TRNSYS-CFD simulations evaluating the performance of PCM plate heat exchangers in an Airport Terminal building displacement conditioning system, *Building and Environment* 65: 132-145

Published Conference Papers

- Gowreesunker BL, Tassou SA (2012), The energy storage capabilities of clay boards with phase change materials in building applications, In Proceedings of the 12th International Conference on Energy Storage, Innostock 2012, Lleida, Spain, 16-18 May 2012, Paper no. INNO-SP-117 (ISBN: 9788493879334).
- Gowreesunker BL, Tassou SA (2013), Evaluation of the energy impact of PCM tiles in an Airport Terminal Departure Hall, In Proceedings of the CIBSE Technical Symposium 2013, Liverpool John Moore's University, Liverpool, UK, 11-12 April 2013, www.cibse.org.
- Gowreesunker BL, Tassou SA (2013-Accepted), A TRNSYS-FLUENT coupled simulation of the thermal environment of an airport terminal space with a mixing and displacement air conditioning system, 13th International Conference of the International Building Performance Simulation Association, Chambéry, France, 25-28 August 2013.

ACKNOWLEDGEMENTS

I would like to express my appreciation and gratitude to Prof. Savvas Tassou for allowing me to work on this project, and for extending and guiding my potential; both intellectually and tactfully. I am also very grateful to Prof. Maria Kolokotroni for constantly supporting my professional development since my undergraduate years. Although both being very busy with administrative matters, their organisation, hard-work and dedication to research are inspiring.

I would like to thank the UK Engineering and Physical Sciences Research Council (EPSRC Grant no: EP/H004181/1), through Prof. Tassou, for financially supporting this research study. I am also thankful for the discussions with the other collaborating universities (City, Reading, Loughborough and Kent) at our regular meetings at Brunel, which facilitated the collaborative research paper with City University.

I am thankful to my colleagues in the Brunel Refrigeration Laboratory: IDewa, Emily, INyoman, Giovanna, Kostas and Amir, amongst others; and the technicians, Mr. C. Xanthos and K. Withers; for their help and enlivening conversations, not always related to Thermodynamics.

Finally, I would like to express my very special gratitude to my Father, Mother, Sister, Prabhupada, Radha and Krsna for their constant moral and emotional support. I dedicate this thesis to them.

TABLE OF CONTENTS

ABSTRACT.....	i
PUBLICATIONS.....	ii
ACKNOWLEDGEMENTS.....	iii
TABLE OF CONTENTS.....	iv
LIST OF FIGURES.....	viii
LIST OF TABLES.....	xiv
NOMENCLATURES.....	xv
ABBREVIATIONS.....	xix
CHAPTER 1 – INTRODUCTION.....	1
1.1 Problem Definition.....	1
1.2 The Airport Terminal Environment.....	5
1.3 Research Aims and Objectives.....	8
1.4 Structure of Thesis.....	9
CHAPTER 2 – BACKGROUND TO STUDY.....	10
2.1 Phase Change Materials (PCMs).....	10
2.1.1 Introduction to Latent Heat Storage.....	10
2.1.2 Classification of PCM.....	15
2.1.3 Thermal Analysis Techniques.....	20
2.1.4 Introduction to PCM related systems.....	25
2.1.5 Micro-encapsulated PCM systems.....	26
2.1.6 PCM panels and boards.....	30
2.1.7 PCM-Air heat exchanger type systems.....	34
2.1.8 PCM Glazing units.....	38
2.1.9 PCM in Heat/Cold Storage Units.....	40
2.2 Thermal Comfort.....	43
2.2.1 Thermal Comfort conditions.....	45
2.3 Summary of Chapter 2.....	48
CHAPTER 3 – THERMAL MODELLING OF PHASE CHANGE.....	51
3.1 Importance of Numerical Modelling.....	51
3.2 Common Phase Change Models.....	53
3.2.1 The Enthalpy-Porosity Method.....	54

3.2.2 The Effective Heat Capacity Method	57
3.3 Enhancements to Phase Change Models	59
3.3.1 Enhanced Phase Change Conduction Model	60
3.3.2 Validity of Model	61
3.4 Summary of Chapter 3	65
CHAPTER 4 – MODELLING OF INDOOR THERMAL ENVIRONMENT AND PCM	66
4.1 Introduction to Computational Fluid Dynamics (CFD)	66
4.1.1 Governing Equations	68
4.1.2 Turbulence Modelling	71
4.1.3 Renormalisation Group (RNG) k- ϵ Turbulence Model	76
4.1.4 Near-Wall Treatment	78
4.2 Modelling of Indoor Environment and PCM boards	79
4.3 Validity of CFD	83
4.4 Effectiveness of CFD	87
4.4.1 Impact of PCM boards	87
4.4.2 Ventilation heat transfer rates	89
4.4.3 Effective use of PCM boards	91
4.5 Summary of Chapter 4	93
CHAPTER 5 – OPTICAL MODELLING OF PCM	95
5.1 Development of Optical Model	96
5.2 Validity of Optical Model	100
5.3 Design Implications	104
5.4 Summary of Chapter 5	107
CHAPTER 6 – NUMERICAL CONSIDERATIONS FOR AIRPORT TERMINAL	109
6.1 Overview of Modelling Strategy	109
6.2 Introduction to TRNSYS	110
6.3 Coupling of CFD & TRNSYS	112
6.4 CFD Numerical Considerations	114
6.4.1 Radiation Modelling	117
6.5 TRNSYS HVAC System	119
6.6 L ₂ Norm – CFD Temporal and Spatial Convergence Study	121
6.7 Coupled Model	127
6.8 Summary of Chapter 6	129

CHAPTER 7 – AIRPORT PCM SYSTEMS	130
7.1 PCM Floor Tiles	131
7.2 PCM Glazing Envelope	134
7.2.1 PCM Glazing Model	134
7.2.2 TRNSYS-FLUENT Coupling for PCM Glazing	136
7.3 PCM Heat-Exchanger (PCM-HX)	138
7.3.1 PCM-HX Model	139
7.3.2 TRNSYS-FLUENT Coupling for PCM-HX	142
7.3.3 PCM-HX Control Strategies	143
7.4 Pressure Drop Calculations	144
7.5 Total Annual Energy Demand	145
7.6 Summary of Chapter 7	148
CHAPTER 8 – PERFORMANCE OF PCM SYSTEMS IN AIRPORT TERMINAL SPACE	149
8.1 Seasonal Performance of stand-alone DC system	150
8.2 Seasonal Performance of DC system and PCM Tiles	155
8.2.1 ‘Ebb’ Tiles	155
8.2.2 ‘Energain’ Tiles	158
8.3 Seasonal Performance of DC system and PCM Glazing	161
8.4 Seasonal Performance of DC system with retrofitted PCM-HX	164
8.4.1 DC-PCM-HX-16mm	164
8.4.2 DC-PCM-HX-8mm	168
8.5 Annual Energy Performance	172
8.5.1 Relative Energy Performance	174
8.5.2 Assessment of the Control Method	176
8.5.3 Cost and CO ₂ Emissions Analysis	178
8.6 Summary of Chapter 8	180
CHAPTER 9 – CONCLUSIONS AND RECOMMENDATIONS FOR FUTURE WORK	181
9.1 Concluding Remarks	183
9.2 Recommendations for Future Work	190
REFERENCES	192
Appendix A: Development of phase change conduction model	207
Appendix B: Validity and effectiveness of CFD	212

Appendix C: Development of optical phase change model.....	223
Appendix D: Numerical conditions	230
Appendix E: Pressure drop calculations for the Airport Terminal space.....	244
Appendix F: Annual Energy calculation procedure.....	248
Appendix G: Assumptions for costs and CO ₂ emissions analysis.....	250

LIST OF FIGURES

Fig. 2.1	Solid-Liquid phase change	11
Fig. 2.2	Classification of Phase Change Materials	15
Fig. 2.3	Typical curve of a DSC plot	21
Fig. 2.4	Heat Flow DSC	22
Fig. 2.5	Heat Flux DSC	22
Fig. 2.6	PCM Microcapsules	27
Fig. 2.7	Powdered PCM	28
Fig. 2.8	Rubitherm CSM® Panel	30
Fig. 2.9	TROX system	37
Fig. 2.10	PCM nodule by Cristopia	41
Fig. 3.1	Solid-liquid interface	53
Fig. 3.2	Enthalpy-temperature relation	55
Fig. 3.3	The Enthalpy method of representing phase change	56
Fig. 3.4	Effective heat capacity curve ($c_{p\ liq} = c_{p\ sol}$)	57
Fig. 3.5	DSC graph of investigated PCM composite	62
Fig. 3.6(a)	Experimental, UDF and Enthalpy-porosity temperatures of a representative point during the melting process	63
Fig. 3.6(b)	Experimental, UDF and Enthalpy-porosity temperatures of a representative point during the freezing process	63
Fig. 4.1	Schematic of CFD solution process	66
Fig. 4.2	Grid discretisation schematic	69
Fig. 4.3	Velocity fluctuations	71
Fig. 4.4(a)	Experimental Test cell and Wall construction	80
Fig. 4.4(b)	Locations of temperature sensors in experimental test cell	81
Fig. 4.5	Environmental chamber/ External air temperature	81
Fig. 4.6(a)	Mesh in main air-domain	83
Fig. 4.6(b)	Mesh distribution in walls and air boundary layer	83
Fig. 4.7	Local error analysis for non-ventilated scenario	84
Fig. 4.8	Local error analysis for ventilated scenario	85

Fig. 4.9	Comparison of Temperature evolutions at 3 points in the test cell, and Temperature contours (K) at the end of the heating period with PCM-Clay board and Plasterboard on the walls	88
Fig. 4.10	Area-weighted wall heat flux with PCM and plaster boards, and with different night ventilation rates for PCM boards only	89
Fig. 4.11	Liquid fraction change for different ventilation rates	91
Fig. 4.12	Velocity streams for ventilation rates of 12 ACH and 46 ACH	92
Fig. 5.1	Spectral transmittance of RT27 in solid, liquid and mushy phases ...	97
Fig. 5.2(a)	Schematic of Experimental setup	98
Fig. 5.2(b)	Actual setup in Environmental chamber	98
Fig. 5.3	Enthalpy-temperature curve of RT27	98
Fig. 5.4	Absorption (σ_a), scattering (σ_s) and extinction (σ_e) coefficients during phase change	99
Fig. 5.5	PCM finite volume model in PCM-glazed unit	102
Fig. 5.6(a)	Transmittance (with experimental error curves) of the PCM filled glazing under 950 W/m ² irradiation and 13°C	102
Fig. 5.6(b)	Numerical progression of PCM Temperature	103
Fig. 5.7	Model Temperature and transmittance progression for a PCM-glazed and a standard double glazed unit under 950 W/m ² irradiation and 13°C air/initial glazing temperature	105
Fig. 5.8	Visual aspect of phase change	106
Fig. 6.1	London Heathrow Terminal 5 Departure Hall	114
Fig. 6.2	CFD representation of investigated airport departure hall	115
Fig. 6.3	Internal heat gains schedule	116
Fig. 6.4	Schematic of HVAC system	119
Fig. 6.5(a)	External temperatures schedule input for L ₂ norm study	122
Fig. 6.5(b)	Heat gains schedule input for L ₂ norm study	122
Fig. 6.5(c)	Ventilation input schedule input for L ₂ norm study	122
Fig. 6.6	Scaled residuals for the benchmark model only, over the course of the simulation	123
Fig. 6.7(a)	L ₂ norm for Temperature	124
Fig. 6.7(b)	L ₂ norm for x-velocity	124
Fig. 6.7(c)	L ₂ norm for y-velocity	125

Fig. 6.8	Airport Terminal Space Model Grid	126
Fig. 6.9	Generic flow of information in TRNSYS-FLUENT coupling for normal HVAC system	128
Fig. 7.1	PCM tiles grid	131
Fig. 7.2	Flow of information in TRNSYS-FLUENT coupling for the PCM-glazed model	136
Fig. 7.3	Temperature nodes used in calculating the radiation properties of RT27	137
Fig. 7.4	Rubitherm GmbH CSM® plate	138
Fig. 7.5	Actual Heathrow Terminal 5 diffuser	138
Fig. 7.6	Schematic of DV diffuser, CSM® plate arrangement, and supply and by-pass ducts inside diffuser	139
Fig. 7.7	Model description of CSM® Plate	140
Fig. 7.8	Heat transfer rates of PCM-HX unit for different air-gaps between plates at a total mass flow rate of 6 kg/s. ΔT is the temperature difference between the incoming air and the PCM plate	141
Fig. 7.9	Modified information flow for DC with PCM-HX	142
Fig. 7.10	HVAC ducting for airport terminal space	144
Fig. 7.11	Generic Ambient temperatures for different seasons	146
Fig. 8.1(a)	Ambient and zone temperature (T_f) profiles for the three distinct seasons in ‘DC-only’ Case	150
Fig. 8.1(b)	Heating (+) and Cooling (-) Energy Load Profile for ‘DC-only’ case for 2D geometry	150
Fig. 8.2(a)	Temperature contour (°C) still-frame during the DC unit cooling mode	151
Fig. 8.2(b)	Temperature contour (°C) still-frame during the DC unit heating mode	151
Fig. 8.3(a)	Velocity vectors (m/s) in airport domain during DC cooling mode ..	152
Fig. 8.3(b)	Velocity vectors (m/s) in airport domain during DC heating mode ..	153
Fig. 8.4	Seasonal heating (+) and cooling (-) demands of Airport space for stand-alone DC case	153
Fig. 8.5(a)	Ambient and zone temperature (T_f) profiles with and without night ventilation for the Ebb-Tiles’ case	155

Fig. 8.5(b)	Heating (+) and cooling (-) load profiles for the Ebb-Tiles' case, with and without night ventilation, for 2D geometry	156
Fig. 8.6	Heating (+) and cooling (-) demands with and without night ventilation, with Ebb floor tiles	157
Fig. 8.7(a)	Ambient and zone temperature (T_f) profiles with and without night ventilation for the Energain-Tiles' case	158
Fig. 8.7(b)	Heating (+) and cooling (-) load profiles for the Energain-Tiles' case, with and without night ventilation, for 2D geometry	159
Fig. 8.8	Heating (+) and cooling (-) demands with/without night ventilation, with Energain floor tiles	160
Fig. 8.9(a)	Ambient and zone temperature (T_f) profiles with and without night ventilation for the PCM-glazing's case	161
Fig. 8.9(b)	Heating (+) and cooling (-) load profiles for the PCM glazing's case, with and without night ventilation, for 2D geometry	161
Fig. 8.10	Heating (+) and cooling (-) demands with and without night ventilation, with the PCM-glazing envelope	162
Fig. 8.11(a)	Ambient and zone temperature (T_f) profiles, with different night ventilation charging strategies for the PCM-HX-16mm case	164
Fig. 8.11(b)	Heating (+) and cooling (-) load profiles for the PCM-HX-16mm case, with different night ventilation charging strategies, for 2D geometry	165
Fig. 8.12	Heating (+) and cooling (-) demands with different night ventilation strategies, with PCM-HX-16mm	166
Fig. 8.13(a)	Zone temperatures (T_f) and PCM temperatures during one day in the intermediate season	167
Fig. 8.13(b)	Heating (+) and cooling (-) load trends for one day in the intermediate season	167
Fig. 8.14(a)	Ambient and zone temperature (T_f) profiles, with different night ventilation charging strategies for the PCM-HX-8mm case	168
Fig. 8.14(b)	Heating (+) and cooling (-) load profiles for the PCM-HX-8mm case, with different night ventilation charging strategies, for 2D geometry	169

Fig. 8.15	Heating (+) and cooling (-) demands with different night ventilation strategies, with PCM-HX-16mm	170
Fig. 8.16	Load comparison of PCM-HX-8mm and PCM-HX-16mm for a day in the intermediate season, under the limiting night control ventilation charging strategy	171
Fig. 8.17	Annual energy demand of the entire Airport Terminal Space for the different PCM system configurations	172
Fig. 8.18	Total annual energy demands of PCM System configurations relative to the 'DC-only' case	174
Fig. 8.19	Indoor temperature (T_i) for a typical summer day for the 'DC-only' case	176

In Appendices

Fig. A1.1	Environmental Chamber Air temperature surrounding the PCM composite sample	207
Fig. A1.2(a)	DSC, UDF and Enthalpy-Porosity curves used in the simulations for the melting process	208
Fig. A1.2(b)	DSC, UDF and Enthalpy-Porosity curves used in the simulations for the freezing process	209
Fig. A1.3	CFD model grid and monitored points' locations	210
Fig. B1.1	Test Cell Wall Configuration	212
Fig. B1.2	Location, description and uncertainty of air and surface thermocouples	214
Fig. B1.3	Melting and freezing curves of sample S-3 and the enthalpy-porosity model	216
Fig. B1.4	L2-planes and L2-norm for temperature and velocities	218
Fig. B1.5	TA-4 Non-ventilated experimental and simulated temperatures	220
Fig. B1.6	TS-5 Non-ventilated experimental and simulated temperatures	221
Fig. B1.7	TS-6 Non-ventilated experimental and simulated temperatures	221
Fig. B1.8	TA-4 Ventilated experimental and simulated temperatures	221
Fig. B1.9	TS-5 Ventilated experimental and simulated temperatures	222
Fig. B1.10	TS-6 Ventilated experimental and simulated temperatures	222

Fig. C1.1	Experimental setup for optical tests	223
Fig. C1.2(a)	Heat released-stored in given temperature intervals for RT27; HR – Heat released; HS – Heat stored	225
Fig. C1.2(b)	Mean experimental extinction coefficients and extinction coefficients using the relationship Eq. (C1.6) and Eq. (C1.12)	227
Fig. E1.1	Main Supply Duct dP	244
Fig. E1.2	Branch Supply Duct dP	245
Fig. E1.3	Main Return Duct dP	245
Fig. E1.4	DC Diffuser Return Path	246

LIST OF TABLES

Table 2.1	List of some Organic Paraffin PCMs	16
Table 2.2	List of some non paraffin organic PCMs	17
Table 2.3	List of Salt hydrates PCMs	18
Table 2.4	List of common commercial PCMs	19
Table 2.5	Differences between heat flow and heat flux DSC	23
Table 2.6	Comfort criteria for Airport Terminals	46
Table 3.1	User defined source terms required to fully defining the conduction phase change process	61
Table 4.1	PCM DSC enthalpy, onset and end temperatures for different PCM-Clay board samples and heating/cooling rates	82
Table 5.1	Viscosity and density variation of RT27 during phase change	100
Table 6.1	Building envelope physical and thermal properties	117
Table 6.2	Information exchanged in coupled simulation	128
Table 7.1	Floor tiles physical and thermal characteristics	132
Table 7.2	Discrete Simulation times	146
Table 7.3	Simulated and yearly Degree days for 15°C and 18°C base temperatures	146
Table 8.1	Payback period and CO ₂ emissions of PCM systems for the entire airport	178

In Appendices

Table A1.1	Additional CFD inputs	210
Table B1.1	Dynamic thermal properties of Walls	213
Table B1.2	Material properties from manufacturer	213
Table B1.3	Regression coefficient, enthalpy uncertainty in h-T curve fits and total uncertainty in enthalpy at heating/cooling rate of 0.5 K/min ...	215
Table C1.1	Sensor uncertainties and sensitivities	228

NOMENCLATURES

A	Area (m ²)
C	Heat capacity (J/K)
$C_{1\epsilon}, C_{2\epsilon}, C_{3\epsilon}, C_{\mu}, \beta_0$ and η_0	Empirical constants (-)
clo	Clothing factor (-)
c_p	Specific heat capacity (J/kgK)
d	Optical depth (-)
f	Friction factor (-)
G	Irradiation (W/m ²)
g or $g_{i,j}$	Gravity (m/s ²)
G_b and G_k	Turbulence generation rate (1/s ²)
h	Specific enthalpy (J/kg)
H	Enthalpy (J)
h_c	Convection heat transfer coefficient (W/m ² K)
L	Length (m)
L_f	Latent enthalpy (J/kg)
m	Mass (kg)
met	Metabolic rate (W)
n	Refractive index (-)
P	Pressure (Pa)
Pr	Prandtl number (-)
\bar{q}	Area-weighted wall heat flux (W/m ²)
Q	Heat flow / Power (W)
q	Heat flux (W/m ²)
R	Molecular gas constant (-)
R_ϵ	Additional term in turbulence equation
Re	Reynolds number (-)
s	Physical depth (m)
S_E	Energy source term (W/m ³)
S_M	Mass source term (kg/m ³)

T	Temperature (°C or K)
t	Time (s)
T_{amb}	Ambient air temperature (°C or K)
T_c	Comfort temperature (°C or K)
T_{exh}	Exhaust air temperature (°C or K)
T_{ext}	External surface temperature (°C or K)
T_f	Feedback temperature (°C or K)
T_m	Mixed air temperature (°C or K)
T_{pcm}	Mean PCM temperature (°C or K)
T_r	Return air temperature (°C or K)
T_s	Supply air temperature (°C or K)
T_{sky}	Sky temperature (°C or K)
U	Uncertainty (-)
$u_{i,j}$	Velocity vectors – u, v, w (m/s)
U -value	Overall heat transfer coefficient (W/m ² K)
u_τ	Friction velocity (m/s)
V_i	Volume of cell (m ³)
$x_{i,j}$	Direction vectors – x, y (m)
y^+	Dimensionless wall thickness (-)
∇	Vector differential (-)
α	Gray radiation absorptance (-)
β	Liquid fraction (-)
δ	Ratio of radiation absorption and scattering (-)
Δh	Change in specific enthalpy (J/kg)
ΔT	Change in temperature (K)
ε	Radiation emissivity (-)
λ	Thermal conductivity (W/mK)
μ	Dynamic viscosity (kg/m.s)
μ_t	Turbulent viscosity (kg/m.s)
ξ	Specific friction loss coefficient (-)
ρ	Density (kg/m ³)
σ	Stefan-Boltzmann constant (W/m ² K ⁴)
σ_a	Gray radiation absorption coefficient (m ⁻¹)

σ_s	Gray radiation scattering coefficient (m^{-1})
σ_e	Gray radiation extinction coefficient (m^{-1})
τ	Gray radiation transmittance (-)
τ_w	Wall shear stress (Pa)
φ	Cell Parameter (-)
\dot{V}	Volume flow rate (m^3/s)

Subscripts:

<i>amb</i>	Ambient air
<i>d</i>	Dynamic friction losses
<i>discrete</i>	Discrete solution of Navier-Stokes Equation
<i>eff</i>	Effective
<i>exact</i>	Exact solution of Navier-Stokes Equation
<i>ext</i>	External surface
<i>f</i>	Freezing
<i>fl</i>	Airport floor
<i>gl</i>	Airport glazing / glass
<i>gl-pcm</i>	PCM-glazed unit
<i>i</i>	Cell
<i>int</i>	Internal surface
<i>l</i>	Lower limit
<i>L</i>	Friction head loss
<i>liq</i>	Liquid PCM phase
<i>m</i>	Melting
<i>pcm</i>	Phase Change Material
<i>rad</i>	Radiation
<i>ref</i>	Reference
<i>ro</i>	Airport roof
<i>sam</i>	Sample
<i>sol</i>	Solid PCM phase
<i>sp</i>	Specific friction losses
<i>t</i>	Current time step
<i>t+1</i>	Next time step

$t-1$	Previous time step
u	Upper limit
$unit$	Overall glazing unit
τ	Transmitted radiation

Superscripts:

-	Average
'	Instantaneous fluctuations
th	Reference of time-steps

ABBREVIATIONS

ACH	Air Change per Hour
ACI	Airports Council International
ASHRAE	American Society of Heating, Refrigeration and Air-conditioning Engineers
BATA	British Air Transport Association
CAA	Civil Aviation Authority
CDD	Cooling Degree Days
CFD	Computational Fluid Dynamics
CIBSE	Chartered Institute of Building Services Engineering
DC	Displacement Conditioning
DC - Only	Stand-alone/ Conventional displacement diffuser
DC + Ebb tiles	Displacement diffuser and Ebb tiles in airport, without night ventilation recharge
DC + Ebb tiles Vent	Displacement diffuser and Ebb tiles in airport, with full night ventilation recharge
DC + Energain tiles	Displacement diffuser and Energain tiles in airport, without night ventilation recharge
DC + Energain tiles Vent	Displacement diffuser and Energain tiles in airport, with full night ventilation recharge
DC-PCM-HX-16mm	Displacement diffuser retrofitted with PCM-HX of 16 mm air gaps in between plates
DC-PCM-HX-8mm	Displacement diffuser retrofitted with PCM-HX of 8 mm air gaps in between plates
DD	Degree Days
DEC	Display Energy Performance Certificate
DECC	UK Department of Energy and Climate Change
DLL	Dynamic Link Library
DO	Discrete Ordinates radiation model
DSC	Differential Scanning Calorimetry
DTRM	Direct Transfer Radiation Model
DV	Displacement Ventilation

Ebb	Eco-Building boards Co. Ltd: produces the Ebb boards
Energain	Energain boards produced by DuPont Co. Ltd.
EPC	UK Energy Performance Certificate
ES	Energy Simulation tool
FLUENT	CFD software
Full-Ventilation / 'Full'	The scenario where the PCM systems are ventilated throughout the entire night period when the airport is closed.
GHG	Greenhouse Gas
HDD	Heating Degree Days
HDPE	High Density Polythene
HVAC	Heating Ventilation and Air-Conditioning
IEA	International Energy Agency
LES	Large Eddy Simulations
Limiting control / control	The scenario where limiting night ventilation control strategy is employed for the PCM-HX systems when the airport is closed.
NoVent	No night ventilation recharge when the airport is closed.
SSPCM	Shaped Stabilised Phase Change Materials
PCM	Phase Change Materials
PCS	Phase Change Slurries
PCM-HX	Phase Change Material Heat Exchanger
PID	Proportional, Integral and Differential controller
PMV	Predictive Mean Vote
PPD	Percentage of People Dissatisfied
PV	Photovoltaic
RANS	Reynolds-Average Navier Stokes
RHI	UK Renewable Heat Incentive
RMS	Root Mean Square
RNG	The Re-Normalisation Group Theory
RSM	Reynolds Stress turbulence Model
SST	Shear-Stress Transport turbulence model
TRNSYS	TRaNsient SYstem Simulation software
UDF	User Defined Functions

CHAPTER 1 – INTRODUCTION

1.1 Problem Definition

Following the Copenhagen Summit on Climate Change in 2009 and the Climate Change Act 2008, the UK Department of Energy and Climate Change (DECC) has set a 34% greenhouse gas emission reduction target for 2020 and 80% for 2050, relative to the 1990 levels (DECC, 2009). Greenhouse Gases (GHG) consist of mainly nitrogen oxides, carbon dioxide, methane and sulphur oxides, which are primarily a result of combustion of fossil fuels and the release of the combustion gases into the atmosphere. The impact of increasing concentrations of GHG in the atmosphere results in global warming, i.e. the effect of solar radiation being trapped in the earth's atmosphere causing an increase in global temperature.

The concept of global warming does not impact only the environment (rise in sea levels, more hurricanes or more intense droughts), but also affects countries from an economic point of view. Due to the rapid depletion of crude oil and its increased usage, the price of crude oil has been increasing at fast rates; \$15 per barrel in 1990 to \$80 per barrel in 2010 (Roper, 2010). Energy companies and governments have thus been shifting attention from oil-produced energy to more renewable sources of energy such as solar, wind or tidal. For instance, the UK renewable energy industry has received investments of up to £ 10.4 billion, intended towards the development, implementation and research of renewable energy technologies (HM Government, 2009).

In the UK, domestic, commercial and industrial buildings account for almost 50% of the total energy consumption and carbon emissions (DFPNI, 2010). Public and commercial buildings (e.g. retail, commercial office, hotel, education spaces) account for ~36% of the total building energy demand and emissions; industrial buildings account for ~12% and domestic buildings account for the rest (Delay *et al*, 2009). Heating, lighting and space cooling account for 46%, 23% and 11% of the public and commercial emissions, respectively, although cooling emissions may be more significant in air-conditioned buildings (Delay *et al*, 2009). In order to reduce carbon emissions, the UK government has implemented various measures to monitor and reduce the energy demand of

buildings and their dependencies on fossil fuels. The ‘display energy performance certificate’ (DEC) for large non-domestic buildings; the use of Energy Performance Certificate (EPC); the Low Carbon Homes Scheme; and the Renewable Heat Incentive (RHI) are some of the policies introduced. The Carbon Trust further recommends the use of passive features (daylighting, shading and natural ventilation); improvements in building fabric and equipments; and the use of on-site low energy technologies for both energy generation and storage, in order to meet the emissions reduction target for 2050 (Ashcroft *et al*, 2013; Strbac *et al*, 2012).

Recently, the trends in building design have been shifting towards the design of large glazed buildings such as atria (Bostick, 2009). Hotels, office buildings, shopping malls and other multi-purpose mega-structures have extensively exploited the atrium concept (Hung and Chow, 2001). The main benefits of the atrium concept are that they allow architects to incorporate the outdoor environment into the building design in such a way that the occupants do not feel confined to a closed space, and they provide day-lighting, which were found to create a more pleasing and productive environment (Ander, 2003). As a result, atrium buildings have become very popular with building designers and owners, and have found an increasing frequency of application (Hung, 2003; Bostick, 2009). However, a major drawback of using such structures relates to the reduction in the thermal mass of the building. For the case of the UK weather, it is accepted that thermal mass is beneficial to buildings with respect to increasing thermal comfort and reducing energy consumption (Pochee *et al*, 2012). Hence, although atrium buildings can provide some advantages, these come with an increased energy demand with respect to the HVAC system.

This study aims at reducing the energy demand and associated carbon emissions of large and thermally lightweight buildings. It focuses on the case of airport terminal buildings, which is assumed to serve as a template for atrium buildings with large open spaces, glazed envelope and high ceilings. These features were found to be common for most major modern airports around the world, including London Heathrow, Bangkok Suvarnabhumi International Airport, Chengdu Shuangliu International Airport, Dubai International Airport, amongst others.

The UK aviation industry comprises of 25 top airports and allows the traffic of approximately 200 million passengers per year (CAA, 2011). The total UK emissions

from the aviation industry in 2008 was 36.2 million tonnes of CO₂e representing 6.3% of UK's total emissions, while emissions from domestic aviation amounted to 2.3 million tonnes of CO₂e (BATA, 2008). Emissions from energy consumption of airport buildings contribute to 0.1-0.3% of global GHG emissions (ACI, 2009), amounting to an approximate annual 0.6-1.7 million tonnes of CO₂e for UK airports. The energy consumption is mainly gas for heating, and electricity for lighting, cooling, ventilation and other electrical equipment. On a global level, the recognition of the need for reduction of energy demand and carbon emissions by the aviation industry (ACI, 2009) has led to the development of various state-of-the-art systems.

For instance; Malaysian Airports have implemented intelligent natural lighting systems to control lighting but also internal gains (www.malaysiaairports.com, 2013); Italy's Fiumicino Airport uses tri-generation and LED lamps (Gregori, 2010); Australia's Alice Springs Airport uses PV concentrator systems to reduce emissions (ACI, 2010); Melbourne International Airport incorporated cool roofs with albedo of 0.95 to reduce cooling loads (SkyCool Pty, 2011); London Stansted Airport uses biomass boilers to reduce emissions (Stansted Energy Strategy, 2011); and London Heathrow Terminal 5 uses displacement conditioning system and solar shading by canopies and low eaves, to reduce HVAC energy consumption (UKTI, 2010).

This study aims at reducing the energy consumption and associated carbon emissions, with regards to heating, ventilation and air-conditioning (HVAC) systems, by implementing latent heat storage systems into airport terminal buildings. The concept of phase change materials (PCMs) for thermal storage in buildings has received considerable attention over recent years. Their ability to store large quantity of heat at narrow temperature ranges have made them popular with energy storage systems and for the passive control of thermal comfort in buildings. PCMs have allowed the effect of high thermal mass to be integrated into lightweight buildings, resulting in improved thermal comfort in free-floating buildings and reduced energy consumption in air-conditioned buildings. Extensive research is currently being undertaken on PCM systems for relatively small office buildings. The concept has not yet been applied to larger open spaces, with large glazing areas and highly variable occupancy, such as airport terminal buildings.

It is emphasised that although the emissions from airport terminal buildings are relatively small compared to global GHG emissions, many improvements can still be made with regards to a more efficient use of energy (ACI, 2009). Furthermore, the findings and methods used in this study are not limited to only airports, but can also be applied to other similar large buildings with low thermal mass. The typical airport environment is described in the next section.

1.2 The Airport Terminal Environment

Airport terminals can be separated into 5 main parts: baggage reclaim areas; check-in areas; concourses; customs area; and departure lounges (CIBSE A, 2006). Envelope heat transfers, occupancy heat gains, solar gains, lighting gains, electrical and mechanical appliance gains constitute the major heat gains in the space, often unwanted during the summer, while useful during the winter. Referring to CIBSE guide A (2006), it can be observed that the thermal comfort criteria may vary quite significantly within an airport terminal: from 12-19 °C for baggage reclaim areas to 21-23 °C for check-in areas. This is anticipated due to the large size and variety of activities encountered in airport terminal buildings.

One of the more noticeable features of modern airport terminals is the glass curtain walls. These glass walls are used for aesthetic and daylight reasons, and to improve the overall 'experience' of passengers. However, glass behaves in a similar way to greenhouse gases in the atmosphere, i.e. they transmit shorter wave radiation, but are opaque to long wave radiation. The radiation energy is therefore effectively trapped into the space, increasing the cooling load in the summer. Most common glass types used in airports are double or triple insulated glass units (IGU), with U-values usually in the range of 1.5 - 2.5 W/m²K (Piechowski *et al*, 2007; Meng *et al*, 2007). The drawback of such glazing units relates to their relatively low thermal mass compared to conventional brick or timber frame walls (CIBSE A, 2006), resulting in a low thermal mass in the building envelope which is detrimental for UK weather conditions (Pochee *et al*, 2012). Accordingly, the UK Building Regulations (2010) have limited the proportion of windows in the extension of existing or new large places of assembly to a maximum of 40% on exposed walls and 20% for roof-lights, with maximum solar transmittance of 0.46 and maximum U-values of 1.8 - 2.2 W/m²K.

Additionally, airport terminals generally possess high ceilings, usually for aesthetic reasons, with large volumes of empty space. Adopting an air-conditioning system that only conditions occupied spaces has therefore been of importance for energy efficiency (ACI, 2009). In the case of Heathrow Terminal 5, the airport design adopts an energy-efficient strategy using a displacement air conditioning system and shading by means of canopies and low eaves to reduce solar gain (UK Trade and Investment, 2010). Radiant floor/ ceiling systems (such as in the New Bangkok International Airport) have also

been used for airports, depicting the shift from the use of conventional mixed conditioning systems (such as in Barcelona International Airport).

Conventional mixing systems employ long-throw nozzles which supply air at relatively high levels and velocities, generating mixing in the space. On the other hand, displacement diffusers supply cold air at low velocities and levels, whereby upon reaching a heat source, the warm plume rises, displacing the air to higher regions where it is removed. The latter method enables for a more localised ventilation approach, where the supply air is specifically targeted to the conditioned zone. For heating purposes, both systems behave in the mixing conditioning mode (Gowreesunker and Tassou, 2013d). Furthermore, both lateral and vertical stratification has been optimised in various innovative designs such that the indoor temperatures near the building envelope is adjusted to match the external temperatures, reducing heat transfer with the external environment.

In general, modern airport spaces are complex indoor environments to control. The heat loads do not follow a uniform schedule (Parker *et al*, 2011), the terminal buildings usually have large open spaces and high ceilings (Simmonds and Gaw, 1996), different comfort conditions are required for different areas of the airport (CIBSE A, 2006), and the thermal mass of the terminal buildings is relatively low due to the large glazed areas. As a result, the indoor thermal control system (HVAC and control systems) employed in airports plays a significant role in both the distribution of comfort and the overall energy demand of the building. Furthermore, although the number of passengers passing through UK airports continues to increase, existing airports will continue to be in operations due to land space constraints (CAA, 2011). It is expected that UK airports for the next 40 years have already been built (Parker *et al*, 2012). Refurbishments of these existing airports will therefore be of considerable importance, and it is imperative that energy efficient solutions can be easily retrofitted to such buildings.

This research study will focus on the thermal conditioning of an airport terminal departure hall, with a large, glazed and open space, with high ceiling. The airport terminal geometry considered in this study is similar to London Heathrow Terminal 5 departure hall, which consists of a constant cross-sectional geometry (Designbuild-network, 2012). This terminal hall consists of a large glazed envelope which produces a relatively low thermal mass compared to conventional buildings, and the indoor space is

conditioned via a displacement conditioning (DC) system. The DC system provides both cooling and heating. This scenario therefore assumes a suitable template for the performance evaluation of energy storage systems using PCM for airports with large, open and glazed spaces.

Three types of PCM systems are investigated in this study: two passive systems and a semi-active system. The former systems consist of PCM floor tiles and PCM glazed units, while the latter system is a PCM heat exchanger system (PCM-HX) retrofitted in the airport DC diffuser. The passive systems have been chosen based on the simplicity of use, while the semi-active PCM-HX system was chosen on the basis of potential enhanced performance, control and retrofitting abilities, compared to the passive systems.

The aims and objectives for this research study are shown in the next section.

1.3 Research Aims and Objectives

The primary objective of this study is to obtain the relative energy impact of the different investigated PCM systems, which will require the use of valid numerical models to predict the relative energy performances of each system. Furthermore, because of the importance of the indoor air-movement on the energy demands of the airport terminal space, CFD must also be integrated in the simulations (Heiselberg *et al*, 1998), as opposed to only using simpler zonal models. Thus, the main aims and objectives of this study can be summarised as follows:

- Conduct an exhaustive literature review of the different PCMs and PCM systems employed in the thermal conditioning of buildings, including their modes of operation and associated performance.
- Analyse different phase change modelling approaches used in past studies, and assess their relevance for this study. Develop and validate new phase change models or enhance existing models, if necessary, in order to adequately simulate each PCM system.
- Integrate indoor air-movement aspects with the performance of HVAC systems, by coupling CFD with conventional energy simulation tools. It is known that such coupled approach usually requires the development of custom-built coupling codes between the CFD and Energy simulation tools. Therefore, the writing and debugging of such codes should also be investigated, and adequately interpreted for the simulation of each PCM system.
- Employ the coupled simulation approach to evaluate the relative energy performance of the PCM systems, and depict their energy saving potential.

1.4 Structure of Thesis

This thesis consists of nine chapters. **Chapter 1** provides an introduction and a general description of the work carried out in the project, including the main aims and objectives of the study. **Chapter 2** presents an overview of the concept of latent heat storage in buildings, and also evaluates different experimental and commercial PCMs and PCM systems used in buildings. The chapter additionally presents suitable thermal comfort conditions for airport terminal spaces.

Chapter 3 introduces the concept of numerical modelling when employed in energy performance evaluations. It also describes two conventional phase change models, and presents a new and validated enhanced phase change model suited specifically for thermal conduction dominant phase changes. **Chapter 4** describes the modelling approaches used in CFD, and presents the validity of CFD to simulate both the indoor environment and the phase change process. The chapter also portrays the benefits of using CFD in the building design process, especially when PCMs are involved. **Chapter 5** introduces a novel phase change model which considers the impact of radiation on the PCM. The chapter also presents the experimental validation of the model, and portrays its performance when used to investigate PCM-glazed units.

Chapter 6 provides a general introduction to the energy simulation tool TRNSYS, and the coupling between CFD and TRNSYS. This chapter describes: the considered airport terminal space; the boundary conditions used in the CFD model; the L_2 norm method used to evaluate the errors in the CFD model; and the general coupled strategy and exchanged parameters between the two simulation tools. **Chapter 7** extends on chapter 6 and provides a more detailed description of the coupling strategy and models used for each PCM system. Chapter 7 also presents the method of calculating the annual energy performance of the systems.

Chapter 8 presents the seasonal energy and temperature trends of the different PCM systems in an airport case study, and discusses the relative annual energy performance of the different systems and the associated payback period and CO₂ emissions. **Chapter 9** finally concludes the research work by describing the outcomes of the study, and provides recommendations for further work in this field.

CHAPTER 2 – BACKGROUND TO STUDY

This chapter provides a general understanding of the use of PCMs to provide thermal comfort in building spaces. It focuses on: the characterisation of PCMs; the description of some PCM-related systems; and the clarification of thermal comfort within buildings. It aims at providing background information for this study, and concentrates on solid-liquid PCMs.

2.1 Phase Change Materials (PCMs)

2.1.1 Introduction to Latent Heat Storage

In thermodynamics, a phase is defined as a state of matter which is homogeneous throughout, not only in chemical composition, but also in physical state (Wunderlich, 2005). The concept of solids and liquids is related primarily to the kinetics (or energy) of the molecules. Solids consist of molecular structures where the mobility is effectively zero and the molecules only vibrate, while liquids possess larger amplitude motion and a higher degree of disorder compared to solids (Wunderlich, 2005). Changing between a low energy phase and a higher energy phase therefore requires the addition or removal of energy. The addition of energy to a material leading to melting is known as an endothermic process, while the removal of energy leading to freezing is known as an exothermic process.

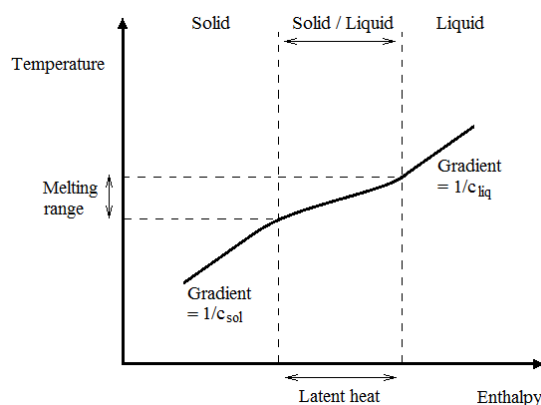
Melting/ crystallisation/ vapourisation/ condensation are 1st order transitions. These transitions are explained simply as involving a latent heat and a change in heat capacity of the material. 2nd order transitions, such as glass transitions involve only changes in heat capacity (Chung, 2010). The concept of latent heat storage is therefore limited to 1st order transitions, and in this study, ‘phase change’ will relate to 1st order transitions. These phase changes involve a re-arrangement of particles at a molecular level within a material, with heat storage/release taking place at a specific range of temperatures (the phase change temperature range). Intermolecular forces or potential forces dictate many chemical properties such as reactivity and stability of the material, but more importantly, they represent the high energy bonds between molecules, which when

broken or formed during phase change, involve a large amount of heat transfer known as latent heat. During phase change, the heat/energy transfer serves mainly to influence the potential forces between the molecules, i.e. the material absorbs energy for melting or releases energy for freezing.

As the molecular kinetics are slightly affected during phase changes, the result is large transfers of energy within a quasi-constant range of temperature (Evola *et al*, 2013), as shown in Fig. 2.1. Including the sensible heat capacity of a material, the total heat stored/released by a material during phase change can be expressed by:

$$Q = (m \cdot c_p \cdot \Delta T)_{PCM} + (m \cdot \Delta h_m)_{PCM} \quad \text{- Eq. (2.1)}$$

Q	Amount of heat stored/released [kJ]
ΔT	Temperature change of storage material [K]
m	Mass of storage material [kg]
Δh_m	Specific melting enthalpy of storage material [kJ/kg]
c_p	Storage material specific heat capacity [kJ/kgK]



The phase changes that can occur in a material are:

- Solid – Liquid Phase change (Fusion)
- Liquid – Vapour Phase change (Vapourisation)
- Solid – Vapour Phase change (Sublimation)
- Solid – Solid Phase change

Fig. 2.1 Solid-Liquid phase change

In building services engineering, emphasis has been placed on the solid-liquid phase change, and more recently on solid-solid phase change, as they both offer the smallest volume changes; in the order of 10% (Raoux and Wuttig, 2008) and are chemically and physically more stable. For the purpose of this study, only solid-liquid PCMs will be considered.

Two further important considerations in the behaviour of PCMs relate to the hysteresis and nucleation phenomena. It is conventional to assume that for instance, the enthalpy

changes for melting and freezing are equal; however in some PCMs, hysteresis occurs, whereby the two temperature ranges and enthalpy changes differ (Bony and Citherlet, 2007). Nucleation, on the other hand, is a more design dependent effect. During phase changes, the new crystals (solid) or droplets (liquid), jointly called nuclei, are formed by a physical reaction – known as the nucleation process. In most cases, the nucleation process will occur at the standard phase change temperature to form the new phase, however in some cases, the process does not start until the phase change temperature has passed, and nucleation begins at a new temperature known as the nucleation temperature (Gunther *et al*, 2007). This difference in temperature is known as the degree of subcooling or superheating. Nucleation is thus a design dependent issue because nuclei tend to grow at corners, imperfections or impurities, i.e. physical aspects of the design.

These two phenomena (hysteresis and nucleation) considerably increase the complexity in modelling phase change processes. Additionally, the heat transfer process during phase change is also complex and is dealt later, in relation to the Stefan problem.

For an optimum performance and use of a PCM, its properties have to be identified. The important properties for a PCM to be used in building environments can be separated into the following thermophysical, kinetic and chemical properties (Sharma *et al*, 2004):

Thermophysical Properties

- Melting temperature in desired range
- High Latent heat per unit volume
- High specific heat capacity
- High decomposition temperature
- High thermal conductivity
- Small volume change during phase change
- Congruent melting

Kinetic Properties

- High nucleation rate to avoid subcooling/superheating
- High rate of crystal growth to enhance phase change

Chemical Properties

- Chemical stability
- Maintains properties for long lifecycles
- No chemical decomposition over freeze/melt cycles
- Non-corrosiveness to the container
- Non-toxic, non-flammable and non-explosive

Moreover low cost, good recyclability and large scale availability are also important. For the purpose of passive thermal comfort, phase change temperatures in the range of 18°C to 25°C have been deemed satisfactory (Mehling *et al*, 2002), while the required melting enthalpy depends on the heat loads of the specific buildings. For active systems, the temperature ranges are more system and situation dependent.

Not all PCMs possess these desirable thermophysical properties, and the limitations of the PCMs may be compensated with adequate system design. The main problems relating to the thermal aspects of PCM are low conductivity, incongruent melting, phase segregation, superheating and subcooling, as described by the following:

Low thermal conductivity of PCMs is a very common disadvantage. Thermal conductivity varies between 0.1 - 0.2 W/mK for organic PCMs and between 0.4 – 0.6 W/mK for other PCMs (Lamberg, 2004b). During phase change, the solid-liquid interface moves away from the heat transfer surface, and the heat transfer resistance gradually increases due to the increased thickness of the molten/solidified medium. As a result, heat transfer enhancements are often required, and usually take the form of fins, carbon nanotubes, metal honeycombs, metal/graphite matrices, lessing rings (Lamberg, 2004b) or through the use of direct contact heat transfer methods, or appropriate types

of heat exchangers. Furthermore, the heat transfer area of the PCM can be increased by using slurries or granules in order to promote heat transfer.

Congruent melting refers to the melting of a compound without decomposition. Incongruent melting implies that the solid does not simply melt, but reacts and decomposes to form another substance of different composition (Weisstein, 2010). Semi-congruent melting implies that a salt hydrate compound breaks down into a low concentration solid salt hydrate and an aqueous solution of the salt. The original salt hydrate can however be re-formed upon freezing (Mehling and Cabeza, 2008). Incongruent melting affects the thermal properties of the material due to the new composition formed. This phenomenon can be suppressed by the use of suitable thicknesses (Sharma *et al*, 2004).

Phase segregation occurs in the solidification process. The molecules in the material must have time to diffuse in order to achieve a uniform composition. If cooling is done too fast, a non-uniform material composition will result in a process known as segregation (Ravikumar and Srinivasan, 2005). For instance, one phase may contain a higher proportion of water and another, a higher salt concentration (Raoux and Wuttig, 2008). This affects the thermal performance of the PCM by reducing the active volume used for heat storage, and prevents repetition of identical melt/freeze cycles required by the PCM. Phase segregation can be minimised through the use of nucleating, thickening agents (Farid *et al*, 2004) and artificial mixing, as well as by thickening the PCM with additional material to increase its viscosity (Raoux and Wuttig, 2008).

Some materials undergo phase changes at their standard melting/freezing temperatures only under very fast heating/cooling conditions, which is not always the case. For these materials, under 'normal' conditions, subcooling will occur as solidification takes place below the freezing temperature. Some salt hydrates can be cooled to 50°C below their freezing point without crystallisation (PCM Products Ltd, 2010). Similarly, superheating refers to the melting process taking place above the melting temperature. The degree of subcooling/superheating is obtained by the difference between the nucleation temperature and peak crystallisation/melting temperature, respectively. The heat transfer between these two temperatures is satisfied through sensible heat, and the actual latent heat capacity might be reduced with these phenomena (Sandnes and

Rekstad, 2006). Thus, the studies described in Callister (2006) are being conducted in relation to investigating different nucleating agents to minimise the risks of subcooling and superheating, through the promotion of heterogeneous nucleation. Stable subcooled PCMs can however also be employed in system designs (Sandnes and Rekstad, 2006).

2.1.2 Classification of PCM

With increasing research in the field of latent heat storage, developments in both experimental and commercial PCMs are expanding. PCMs are generally classified as organic, inorganic and eutectics. Each of these classifications contains sub-categories as portrayed in Fig. 2.2, with specific advantages and disadvantages, taken into consideration when choosing a specific type of PCM. The following Tables 2.1 - 2.4 present the melting enthalpy and the melting temperature of some common PCMs. Fig. 2.2 shows the general classification of PCMs.

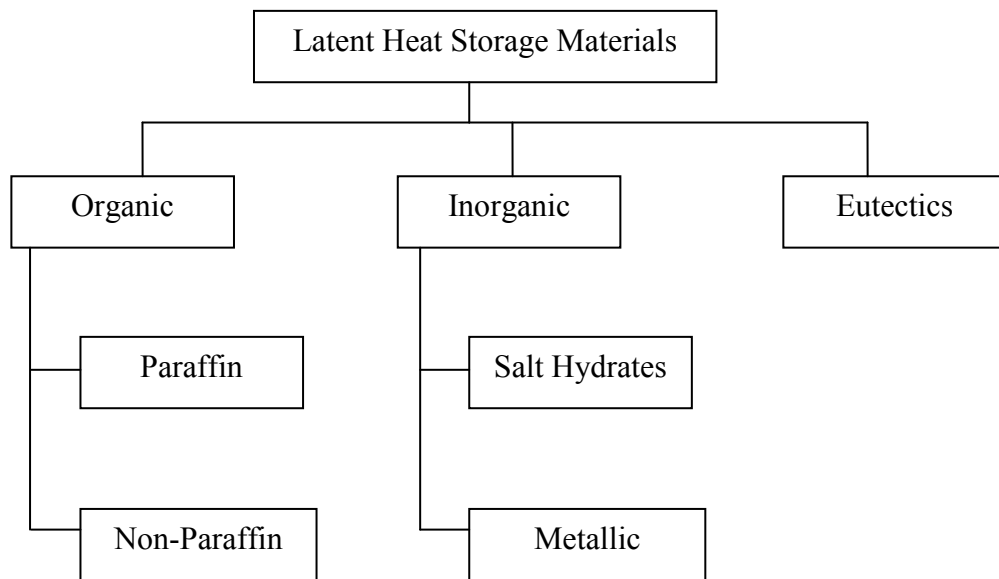


Fig. 2.2. Classification of Phase Change Materials (Sharma et al, 2004)

The main focus of this work will be on solid-liquid PCMs, which are largely available on the market. It should however be noted that melting happens in a range of temperature (either narrow or large), instead of the single value portrayed in the tables. These are only indicative values.

Eutectics refer to a composition of two or more components (organic or inorganic) which melt and freeze congruently, without segregation since the mixture crystals melt and freeze simultaneously. The properties of eutectics therefore depend on the specific constituents of the mixture (Sharma *et al*, 2004).

Organic - Paraffin

Paraffin consists of hydrocarbon chains of alkanes with the general monomer formula C_nH_{2n+2} . They exist mainly as liquids and waxy solids and are one of the most commonly used commercial organic PCMs (Sharma *et al*, 2004). Commercial grade paraffins are obtained from petroleum distillation and are not pure substances, but a mixture of different hydrocarbons. Some examples are given in Table 2.1.

Table 2.1. List of some organic pure paraffin PCMs (Sharma et al, 2004)

Material	Melting point (°C)	Latent heat (kJ/kg)
N-tetradecane	5.5	226
N-pentadecane	10	205
N-hexadecane	16.7	237
N-henicosane	40.5	161
N-pentacosane	53.7	164
N-hexacosane	56.3	255

The advantages of paraffins are that: they are more chemically stable than inorganic substances due to the strong chemical alkane bonds; they melt congruently and subcooling does not pose a problem, hence nucleating agents are not usually employed (Kelly, 2000); they show high heats of fusion and they are safe and non-reactive. Conversely, paraffins have low thermal conductivity; they have a relatively higher solid – liquid volume change compared to other PCM; they are flammable (Sharma *et al*, 2004); and because commercial grade paraffin contains various hydrocarbons, the melting temperature ranges are not clearly defined.

Organic – Non Paraffin

Organic non paraffin is the largest sub-category of PCM available. They consist of esters, fatty acids, alcohols and glycols suitable for latent heat storage (Sharma *et al*, 2004). Some examples are given in Table 2.2.

Table 2.2. List of some non paraffin organic PCMs (Sharma et al, 2004)

Material	Melting point (°C)	Latent heat (kJ/kg)
Formic acid	7.8	247
Acetic acid	16.7	187
Glycerin	17.9	198.7
Butyl stearate	19	140
Polyethylene Glycol-600	20-25	146
D-Lactic Acid	26	184
Myristic acid + Capric acid	24	147.7
1-3 Methyl pentacosane	29	197

These materials are flammable and should not be exposed to high temperatures. Fatty acids have similar physical and chemical characteristics as paraffins, but have sharper phase transformations. Furthermore, non paraffins are mildly corrosive and are about three times more expensive than paraffins (Sharma *et al*, 2004).

Inorganic PCM – Salt Hydrates

Salt hydrates are the most studied group of PCM. They consist of salts and water which combine in a crystalline matrix when the material solidifies. Salt hydrates behave in three different ways: congruent, incongruent and semi-congruent (Sharma *et al*, 2004), as explained section 2.1.1.

Some common salt hydrates can be found in Table 2.3.

Table 2.3. List of Salt hydrates PCMs (Sharma *et al*, 2004)

Material	Melting point (°C)	Latent heat (kJ/kg)
$K_2HO_4.6H_2O$	14	108
$KF.4H_2O$	18	330
$K_2HO_4.4H_2O$	18.5	231
$LiBO_2.8H_2O$	25.7	289
$FeBr_3.6H_2O$	27	105
$CaCl_2.6H_2O$	29-30	170-192
$Na_2SO_4.10H_2O$ (Glaubeur's salt)	32	251-254

Salt hydrates: are cheaper; tend to have relatively higher heat storage capacity per unit volume; and have higher thermal conductivity, than organic PCMs. They are the best options for low temperature ranging from 0°C to 99°C, based on their thermal properties. However, they have a tendency to subcool and not melt congruently (Ravikumar and Srinivasan, 2005). They also have sharp melting points and low volume change during phase transformation, but tend to corrode metal containers that are commonly used in thermal storage (Sharma *et al*, 2004).

Commercial PCMs

Some common commercial PCMs are presented in Table 2.4. These include organic paraffins, salt hydrates and blends of paraffins and salt hydrates.

Table 2.4. List of common commercial PCMs (Waqas and Din, 2013)

Name of PCM	Type of PCM	Melting point (°C)	Latent heat (kJ/kg)	Manufacturing Company
SP22 A4	Blends	24	165	Rubitherm GmbH
SP25 A8	Blends	25	180	Rubitherm GmbH
SP22 A17	Blends	22	180	Rubitherm GmbH
RT27	Paraffin	27	184	Rubitherm GmbH
RT21	Paraffin	22	134	Rubitherm GmbH
A26	Paraffin	26	150	PCM products Ltd
A24	Paraffin	24	145	PCM products Ltd
A22	Paraffin	22	145	PCM products Ltd
S21	Salt hydrate	22	170	PCM products Ltd
S23	Salt hydrate	23	175	PCM products Ltd
Micronal® PCM	Paraffin	21; 23; 26	90-110	BASF Ltd

Commercial PCMs are being increasingly used in the development of thermal storage systems because of the different variety of commercial PCMs available in the thermal comfort range of buildings. Paraffinic PCMs are preferred to salt hydrates or blends, as they do not react with the encapsulating material (Waqas and Din, 2013).

2.1.3 Thermal Analysis Techniques

In order to optimally implement PCMs into the design of energy efficient systems, the selection of a suitable material is important. This requires the measurement of the PCMs' thermophysical properties (Yinping *et al*, 1999). Other physical and chemical properties in regards to density, chemical stability, etc. are also important, but these can be obtained with reasonable accuracy from the manufacturers. 'Thermophysical properties' are defined as the material properties affecting the transfer and storage of heat which vary with the state variables temperature, pressure, composition and other relevant variables, without altering the material's chemical identity (NPL, 2010). Past literatures have reported that the phase change temperature, latent heat, heat capacity and thermal conductivity are the most important parameters in the experimental and numerical study of PCMs (Dolado *et al*, 2011; Yinping *et al*, 1999, 2006). The most commonly used thermal analysis techniques to evaluate these parameters are the DSC and the T-history methods.

Differential Scanning Calorimetry (DSC)

Differential Scanning Calorimetry (DSC) refers to a technique whereby the thermal properties of a material can be determined through the analysis of heat flows into and out of the sample material relative to a reference sample, under different heating/cooling temperature rates. The reference is usually an empty pan identical to the sample pan. The differential heat flows are plotted against temperature, and various micro-structural transitions and thermophysical properties can be deduced from the plot. The test is done in an inert atmosphere usually nitrogen gas, which is used to remove any corrosive gases from the sample (MRFN, 2010) and to minimise the risk of condensation inside the DSC instrument when the temperature gets below the air dew point.

The heating/cooling temperature rates are important features of the analysis. These are usually limited to 40°C/min, above which the effects of non-linearity becomes dominant and the calibration parameters become no longer applicable (Bershtein and Egorov, 1994). Faster temperature rates give more inherent sensitivity, but better resolution can be obtained at lower temperature rates. Resolution refers to the ability to separate close thermal events, while sensitivity refers to the ability to detect weak events. Increased resolution is always at the expense of sensitivity, and vice versa (Verdonck *et al*, 1999).

Furthermore, the mass of the sample, i.e. thermal inertia of the material should also be considered before choosing a rate. Small samples (< 10 - 30mg) can have faster rates, while heavier samples should have a slower rate (Bershtein and Egorov, 1994) in order to allow for uniformity in temperature distribution in the sample and improved resolution.

Because of the differential nature of the technique, the heat flow during phase transitions in the sample is composed of (Bershtein and Egorov, 1994) (Eq. 2.2):

$$\frac{dh}{dt} = -\frac{dq}{dt} + (C_{sam} - C_{ref}) \frac{dT}{dt} - RC_{sam} \frac{d^2q}{dt^2} \quad - \text{Eq. (2.2)}$$

As depicted in Fig. 2.3;

- I: is dq/dt , the recorded heat flux from zero line, i.e. the experimental DSC curve.
- II: is $(C_{sam} - C_{ref}) dT/dt$, the displacement of the baseline from the zero level; here C_{sam} and C_{ref} are the heat capacity of the sample and reference respectively, and dT/dt is the rate of change of temperature.
- III: is $RC_{sam} d^2q/dt^2$, which represents the slope of the experimental curve at any point, characterising the effect of thermal lag.

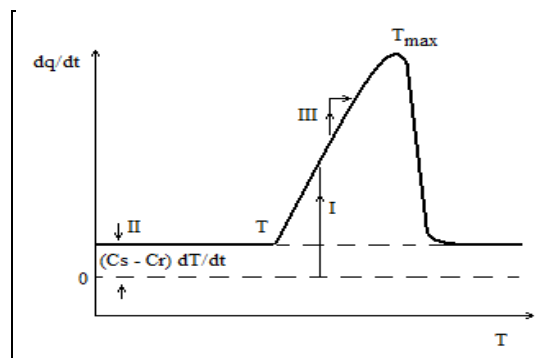


Fig. 2.3. Typical curve of a DSC plot (Bershtein and Egorov, 1994)

There exist two types of DSC: heat-flow DSC and heat-flux DSC as explained in the following sections.

The distinguishing aspect of a heat flow DSC is the double-furnace, where heating is done through the individual heaters mainly by conduction, and cooling is done through a refrigeration system.

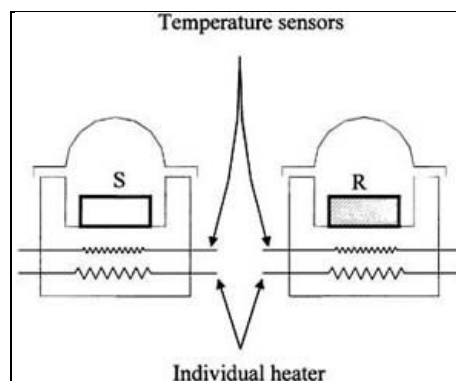


Fig. 2.4. Heat Flow DSC (source: www.pedia.educdz.com, 2010)

This type of DSC operates by maintaining the sample and reference at the same temperature by modulating the heat flow directly, hence the name ‘heat flow’ DSC. This allows for very precise control of temperature, very accurate enthalpy and heat capacity measurements, and true isothermal performance (Ye *et al*, 2010). Apparatus from PerkinElmer Ltd. claim an accuracy of $\leq \pm 0.2\%$ and a precision of $\leq \pm 0.03\%$ for calorific values of their heat flow DSC 8000/8500®, with temperatures ranging from -180°C to 750°C , and heating/cooling rates varying from $0.01^{\circ}\text{C}/\text{min}$ to $750^{\circ}\text{C}/\text{min}$ (Ye *et al*, 2010).

Heat flux DSCs also work on the principle of heat flows, however they operate by measuring temperature differences and changes between a sample and a reference (ΔT), and calculate heat flux from calibration data. Because of their single furnace design, heat flux DSCs are less sensitive to small transitions, heat and cool at slower rates than heat flow DSC, and give less accurate values for specific heat capacity and enthalpy (Ye *et al*, 2010).

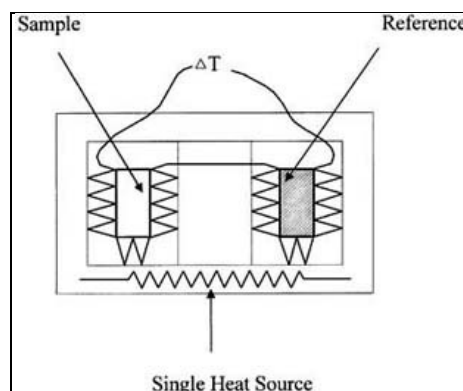


Fig. 2.5. Heat Flux DSC (source: www.pedia.educdz.com, 2010)

The DSC 6000® from PerkinElmer, employed in this study, is a heat flux DSC which provides a $\pm 2\%$ accuracy in enthalpy change and $\pm 0.1\text{K}$ accuracy, with a temperature range of -180°C to 450°C , and heating/cooling rate of $0.1^\circ\text{C}/\text{min}$ to $100^\circ\text{C}/\text{min}$. This provides an adequate range of parameters, suitable for the analysis of materials to be used in buildings.

In essence, both types of DSC give comparable and good data, and allow the sample to undergo lifecycle tests. Table 2.5 summarises the main differences between them:

*Table 2.5. Differences between heat flow and heat flux DSC
(Ye et al, 2010)*

	Heat Flow DSC	Heat Flux DSC
Fast heating ($> 250^\circ\text{C}/\text{min}$)	Yes	No
Modulated Techniques	Yes	Yes
Accuracy of c_p values	High	Moderate
Delta H values	High	Moderate
Isotherm performance	Excellent	Affected by sample

To an extent, only the validity of the results \pm an error margin from the DSC plot is of interest to the research engineer. As a result, calibration of the DSC instrument is of vital importance. In the case of DSCs, a successful calibration will result in good data agreement with the standards, a smooth baseline and a reasonable separation of sample peak from any noise in the baseline (Ye *et al*, 2010). The DSC used in this study is industry-calibrated for temperature and enthalpy using Indium, which has stable properties and can be manufactured to a high level of purity.

The limitations of DSC are that it is often difficult to interpret the heat flow from a DSC experiment if multiple processes overlap over the same temperature range (Verdonck *et al*, 1999), and as the samples are very small, the thermophysical properties may be different from those in bulk materials used in practical systems (Yinping *et al*, 1999). Furthermore, with conventional DSCs, the distinction between hysteresis and subcooling/superheating during phase change is usually unobservable, and thus the difference between the melting and freezing peaks is globally termed ‘subcooling’ for DSC experiments.

The T- History method

DSC has been a popular and efficient method of determining the thermal properties of materials. However, one limitation put forward by many researchers is the inability of DSC results to represent the actual bulk properties of the materials which may be different to the small samples used in DSCs (Yinping *et al*, 1999). As a result, Yinping *et al.* (1999) developed the T-history method of determining the melting point, degree of subcooling, heat of fusion, specific heat capacities and thermal conductivity of several PCMs simultaneously.

The principle consists of a rapid change of environment of liquid PCM in a test tube from a temperature above its melting point to a temperature below the melting point. The test tube is connected to a temperature sensor and a data logger which records the changes in temperature that occurs during the process, i.e. the Temperature (T) - history. The method uses the lumped capacity concept, whereby all temperatures in the test sample are assumed to be uniform. This is true for Biot number < 0.1 . The unknowns developed in the process, such as the heat convection coefficient outside the test tube, are calculated through a simultaneous test, under similar conditions, but with a test tube containing water. By a process of elimination, all unknowns, including thermal conductivity are obtained.

Compared with conventional DSC methods, the T-history method has the advantages of having a simple experimental setup; of analysing several PCMs at the same time; and of measuring various thermal properties simultaneously. Furthermore, the distinction between hysteresis and subcooling/superheating parameters is also possible. The results obtained from the T-history method agree well with the literature and the precision obtained from the measurements satisfies the requirements for engineering purposes. On the other hand, tests such as repeating charging and discharging cycles cannot be easily performed and the thermal conductivity of PCM can only be deduced for material that have a clear interface, which is not the case for some salt hydrates (Yinping *et al*, 1999). Nevertheless, this technique has received considerable attention in the engineering sector, partly because of its simplicity, adaptability and reasonable accuracy. As a result, it is constantly being improved, as shown by the works of Kravvaritis *et al.* (2010) and Stankovic *et al.* (2012).

In this study, it is not essential to obtain the detailed phenomena occurring within the PCM as it changes phase. A global perspective of the latent enthalpy, phase change temperature range and the variation of the enthalpy with temperature are more important. As a result, the Perkin Elmer DSC 6000® was employed for the thermal characterisations of all PCMs in this study, due to its availability and simplicity of use.

2.1.4 Introduction to PCM related systems

PCM systems developed in the market tend to focus on PCM as a medium: to recover waste or ‘free’ energy; to act as a means of heat transport (i.e. to move thermal energy from one place to another); and to store large quantities of heat at specific temperatures. These systems are designed to operate in a passive or active mode. Passive systems refer to systems in which the charging/discharging of the PCM is done without any mechanical equipment, such as thermosyphons or night cooling, whilst active systems refer to systems in which the operation of the PCM is directly influenced by mechanical means, such as auxiliary heaters/coolers (Zhu *et al*, 2009). In some cases, semi-active systems have also been introduced, referring to a combination of active and passive systems. These involve the minimal use of mechanical means in the system, where the mechanical components usually do not affect the PCM directly, but rather, influence the performance of the overall system design; such as the use of ‘active’ fans blowing air on a ‘passive’ PCM panel.

In order to allow repetitive operation of PCM systems, the energy potential of the PCM must be adequately recharged. Although earth to air heat exchangers and evaporative cooling have been used for PCM recharge, ventilation strategies have been the most popular (Raj and Velraj, 2010). Ventilation charging commonly takes the form of passing cold night ambient air to the PCM to restore its cooling potential which can be later used for cooling purposes during the day – ‘free-cooling’. A diurnal temperature fluctuation of 12-15°C is usually considered appropriate for an effective use of free-cooling systems (Waqas and Din, 2013). Recharging PCMs, with respect to heating, can be done by solar energy or low cost night-time electricity, although the specific systems/strategies employed can vary. For the purpose of passive or semi-active PCM systems in buildings, it has been argued that materials with peak melting temperature in

the range of 18°C – 25°C are most appropriate (Mehling *et al*, 2002; Dimaano and Watanabe, 2002; Raj and Velraj, 2010). For active systems, the PCM temperature ranges may differ depending on the application.

This study excludes phase change slurries (PCS); because the thermophysical and rheological properties of such heat transfer fluids are still not fully understood (Delgado *et al*, 2011). Thus, PCS have received little attention to date in terms of their implementation into actual building system designs. The following sub-sections describe some experimental and commercial PCM systems that have been employed in building scenarios.

2.1.5 Micro-encapsulated PCM systems

Microencapsulated PCM is a term that refers to two types of PCM containment; shape-stabilised (powder) and granular (microcapsule) forms. Their uses in buildings have been primarily oriented towards their integration into wall structures; such as wallboards or concrete, and in the development of phase change slurries (PCS). Microencapsulation is limited to organic materials, because although salt hydrates would be desirable, the mobility of the water crystals prevents their encapsulation (Mehling *et al*, 2002).

The methods of incorporating PCMs into building fabric include direct incorporation (adding PCM to the mix when creating the fabric), and immersion (placing the block or board in liquid PCM at specific temperatures and for specific time period). In the case of wallboards, direct incorporation is a more economical process, while both methods are satisfactory for concrete blocks (Kelly, 2000).

PCM microcapsules

Microcapsules commonly refer to impermeable solid-shelled containers ranging from 1-1000 µm in diameter with the PCM enclosed inside. The PCM microcapsules can be manufactured using physical processes such as spray-drying, or by chemical processes (Jahns, 2010).

Paraffins can be filled inside the capsules, while the outer shell may consist of various formaldehydes or polyacrylates (Mehling *et al*, 2002). The outer shell is designed to be highly resistant to thermal and mechanical stresses, which depends on the material and the micro-encapsulation technique (Boh and Sumiga, 2008), and to be chemically compatible with the PCM. Heat transfer in PCM microcapsules is improved due to the high surface area to volume ratio, relative to macro-encapsulated PCMs.

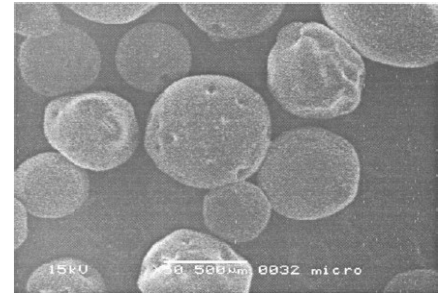


Fig. 2.6. PCM Microcapsules (Uddin et al, 2002)

Bentz and Turpin (2007) investigated the incorporation of granular PCMs into concrete. The high thermal mass of concrete is advantageous as it stores heat during the day and releases it at night. However in tropical climates, the nocturnal release of heat can be uncomfortable without forced cooling. The incorporation of PCM therefore adjusts the heat absorption and temperature of the wall to comfortable values. Butyl stearate and other paraffin microcapsules were impregnated in concrete and tested using computer simulations. The results showed a 30% annual reduction in freeze/thaw cycles with the addition of PCM to concrete, for several American regions. This shows promising enhancement in the thermal properties of concrete through the incorporation of PCM microcapsules.

Castellon *et al* (2007) studied the effects of Micronal[®] PCM in concrete for a small cubicle in Spain. The PCM had a melting point of 26°C and melting enthalpy of 110 kJ/kg. They observed that the passive cooling impact of the PCM was most prominent with the windows closed during the day and opened at night, to allow for better charging and discharging. A reduction of 4°C in temperatures and a peak temperature shift of 2 hours were observed with the use of PCM in the concrete. They also studied the heating potential of the PCM-wall through the use of a Trombe Wall. The Trombe wall consisted of an external glass panel separated from the PCM wall by 10cm; in order to allow solar radiation to penetrate through, but minimise heat losses by conduction and convection. As opposed to cooling, heating is more efficient by closing all windows for the whole day and night, in order to allow the appropriate charging of the PCM in winter. They therefore concluded that for continental weather conditions, it

is best to have a Trombe wall installed for the winter, which has to be de-activated / removed over the summer period.

Shape-Stabilised PCM

As opposed to granular PCM, shape stabilised PCM (SSPCM) refers to the PCM being embedded in a support matrix, which allows it to keep its shape during phase transitions. The leakage of PCM, the selection of suitable container material, the additional thermal resistance of the container and container cost are often problematic when using granular forms of PCM, but shape stabilised PCM eliminates these drawbacks (Yinping *et al*, 2006). In the case of building walls, it should be noted that the effect of surface tension in the host material prevents the PCM from leaking from the wall, even in the liquid phase (Kelly, 2000).



*Fig. 2.7. Powdered PCM
(Rubitherm GmbH, 2010)*

The common PCMs used in SSPCMs consist mainly of various types of paraffin with different melting temperature, due to their stable properties (Kelly, 2000). The supporting material matrix essentially provides a form of encapsulation to the PCM during phase change. Common supporting materials include high density polythene (HDPE), silica and carbon graphite (which also enhances the thermal conductivity), and these should have a melting temperature higher than the PCM.

Miao *et al* (2007) conducted experiments using different paraffins, with HDPE as the supporting structure, to determine the performance of PCMs suitable for building walls. The PCMs had a melting temperature range of 21°C - 27°C and melting enthalpy in the range of 95 kJ/kg - 140 kJ/kg. Experiments were conducted using DSC, and they concluded that: increasing the mass content of PCM increases the heat storage capacity of the wall; HDPE and paraffin form a homogeneous structure; the structure has good stability; a melting range of 21°C - 27°C is satisfactory for thermal comfort and, that SSPCMs provide large heat storage capability, good uniformity and stability when used in building walls.

Guobing *et al* (2007) performed a set of experiments to determine whether incorporating SSPCM plates in walls or using PCM-gypsum wallboards, with the same amount of PCM, is more effective. HDPE was used as the supporting structure and PCMs of various melting points were studied. They found that both methods help in reducing temperature swings in a passive environment, but using the SSPCM plates improves the thermal response and better utilises the latent heat capacity of the PCM. They also emphasised the importance of the location of the PCM plates/boards in the building.

Micro-encapsulation enhances the heat transfer abilities compared to macro-encapsulated PCMs. The larger heat transfer area to volume ratio improves heat transfer and compensates for the low thermal conductivity of the PCM (Castellon *et al*, 2007). Incorporating PCMs in building structures saves on space, and does not impact on the mechanical properties of the host material, which opens opportunities for structural applications (Kelly, 2000). The porosity of the host material plays an important role in the amount of PCM that can be incorporated. The higher the amount of PCM incorporated, the higher the heat storage capacity of the overall material. Wallboards can absorb a maximum of 50% of its mass in PCM, and depending on the type of concrete, a maximum of 20% by mass of PCM can be absorbed (Kelly, 2000). It is important to note that micro-encapsulated PCMs are not only used in structural components, but also as replacements in some applications for macro-encapsulated PCM and in heat/cold stores. However, uneven porosity distribution in a microencapsulated PCM system prevents the exact determination of the heat transfer properties of the entire composite, which increases the modelling complexity.

Rubitherm GmbH and BASF Co Ltd. manufacture a wide range of commercially available microencapsulated PCMs, as well as different passive systems that can be used in buildings (Rubitherm GmbH, 2010; BASF, 2010). The performance of micro-encapsulated PCM in wallboards is discussed in section 2.1.6.

2.1.6 PCM panels and boards

PCM panels consist of the PCM inside a thermally conductive container, while PCM boards generally imply the PCM being embedded in building wallboards. They can both be used in various similar ways depending on the design of the building, but are usually added or substituted in the building envelope.

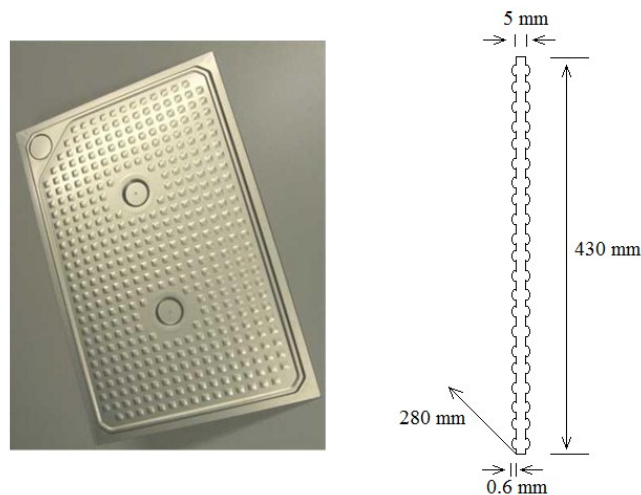


Fig. 2.8. Rubitherm CSM® Panel (Rubitherm GmbH, 2010)

A popular PCM panel employed in various studies is the Rubitherm CSM® panel as shown in Fig. 2.8. This plate consists of an aluminium casing and contains PCM developed by Rubitherm GmbH. Castell *et al* (2010) incorporated these CSM® panels (with RT-27® and SP-25 A8®) in the design of a Mediterranean style cubicle in Spain with conventional bricks and alveolar bricks. The results show that under free-floating conditions, the peak temperatures inside the closed cubicle reduced by 1°C and the temperature fluctuations were significantly reduced, relative to a cubicle without PCM. The importance of night ventilation during successively hot days is emphasised, in order to optimise the recharging process of the PCM. Furthermore, employing the PCM panels in an air-conditioned cubicle showed that a reduction of 15% in the energy consumption was possible, compared to cubicles without PCM. The popularity of the Rubitherm CSM® plates can be largely associated to their relative ease of use, wide variety of PCM available from Rubitherm GmbH and the enhanced heat transfer properties due to its surface design (Dolado *et al*, 2011). Although these can be

successfully employed in building envelopes, the CSM® plates have also been used as heat exchangers, as discussed in section 2.1.7.

Kuznik *et al* (2009a) tested the DuPont Energain® panel in a MICROBAT test-cell, where the panels are placed on the internal side of the walls. The results showed that the indoor air temperature of the test cell without the PCM closely follows the outdoor air temperature for both heating and cooling. Employing the PCM panel increases the time delay and reduces the peak air temperature in the test cell. Furthermore, the effects of temperature hysteresis in predicting the performance of the panels were also emphasised.

Kuznik *et al* (2009b) further extended their studies to the MINIBAT test-cell, investigating the performance of the DuPont Energain® panel and the effect of solar radiation over three seasons. The application of the PCM panels during summer caused the maximum air temperature to decrease by 3.9°C while the minimum air temperature increased by 0.8°C. During mid-season, the maximum air temperature decreased by 2.3°C, while the minimum air temperature increased by 0.4°C. And similarly during winter, the PCM effectively reduces the temperature swing within the space, by preventing overheating due to solar radiation. These results show that the main effect of the PCM panels was to maintain the indoor air temperature within comfortable levels. Furthermore, the study also showed the importance of free-cooling during summer, and the reduction in indoor air temperature stratification when employing the PCM panels.

PCM wallboards have clearly defined uses. They can substitute or complement the commonly employed gypsum plasterboard, improving the energy storage potential of a lightweight building envelope. Gowreesunker and Tassou (2013a) investigated the performance of a PCM-Clay composite board placed on the walls of a custom built test-cell, with wall properties similar to a timber frame wall. The board contained 21% Micronal® PCM, with a mean enthalpy of 16.5 kJ/kg over a temperature range of 12-22°C. The study consisted of the experimental validation of a CFD numerical model of the test-cell, later used to investigate different aspects of the PCM boards' performance. Firstly, applying the PCM boards resulted in 3°C reduction in peak air and surface temperatures, relative to gypsum plasterboards, preventing the overheating propensity of the building space. Secondly, the study portrayed the importance of night ventilation in the recharging process of the PCM boards. For the studied ventilation air inlet/outlet

configuration, a flow rate greater than 93 ACH would recharge the boards within 9hrs. The authors also showed that as the ventilation flow rate increases, the reduction in charging time decreases, due to the low conduction of the PCM board dominating the overall heat transfer process. Hence, in order to further reduce the charging times after a 'threshold' air-flow rate, the PCM board itself has to be modified.

Shilei *et al* (2007) experimentally investigated a PCM wallboard consisting of 82% Capric acid and 18% Lauric acid, impregnated to 26% by mass into gypsum plasterboard. The boards were tested in an experimental test room, with similar size to a common office. The experimental results agreed with DSC results, demonstrating the energy storage potential of the PCM boards. The authors concluded that the use of PCMs in the building envelope can shift heating and cooling loads to off-peak electrical hours.

Athienitis *et al* (1997) experimentally investigated the performance of PCM-gypsum boards used as wall linings in an outdoor full-scale test-room in Montreal, Canada. The PCM board consisted of butyl stearate, with a phase change range of 16-20.8 °C and a latent enthalpy of 30.7 kJ/kg. The boards were tested under typical Canadian winter conditions. The main conclusion was that the application of the PCM boards reduced the risk of overheating of the space by about 4°C, as it absorbed the excess solar heat during winter. Furthermore, the authors also developed a validated mathematical model that can be used to evaluate the performance of PCM boards.

As a variation to PCM boards, Cerón *et al* (2011) incorporated the ACUAL 20 PCM® into clay floor tiles and experimentally tested the tiles in a solar house in Madrid. Their results showed that during winter, under an incident solar radiation intensity of 1026 W/m², employing the PCM floor tiles limited the indoor temperature rise when the ambient temperature increased to above 17 °C because of the additional energy storage potential. Hence, the overall temperature swing within the space reduced compared to a non-PCM tiled floor. For summer purposes however, the authors suggest a PCM with higher phase change temperature. This PCM tile has been patented, patent no. P200501263.

Although PCM boards tend to be mostly used as passive systems, some researchers have explored the improved performance of these boards when used in semi-active

systems. Kondo *et al* (2002) designed and incorporated a rock wool PCM ceiling board in the false ceiling of an office building in Japan, to minimise the Air Handling Unit (AHU) running costs. During peak operating conditions, the room air is passed through the PCM board in order to pre-cool the air before it reaches the AHU, thus allowing for a smaller size AHU and reduction in running costs. After experiments in an environmental chamber, a reduction of 14.8% was obtained in the thermal load of the AHU when using the PCM board. Furthermore, using low cost night-time electricity in the recharging process resulted in an overall reduction of 91.6% in the running costs of the system, when employing the PCM ceiling board relative to a normal rock-wool board.

Koschenz and Lehmann (2004) developed a thermally activated PCM ceiling panel, employing capillary tubes to pass water for the recharging process of the PCM, and aluminium fins to improve the conductivity of the panel. The authors showed that employing such a system only required a 5 cm layer of microencapsulated PCM to maintain a comfortable room temperature in standard office spaces.

Lin *et al* (2007) studied an underfloor electric heating system fitted with shaped-stabilised PCM floor boards at Tsinghua University, China. The concept employed cheaper night time electricity to recharge the PCM floor boards in order to reduce the peak load during the day. For different Chinese regions, different phase change temperature ranges and different latent enthalpies were suggested. The results showed that: the PCM system is able to provide comfortable indoor environments at off peak hours and; the maximum electricity consumption was shifted from peak to off-peak hours.

The limitations associated with such concepts are due to the low conductivity of the PCM. Large surface areas must be available to passively control the thermal environment. Furthermore, incorporating PCM panels in the interior design of a space might affect aesthetics and compromise acoustics. PCMs incorporated in chilled cooling systems should have a temperature above the air dew point temperature to avoid condensation inside the conditioned space.

Although most studies tend to focus on PCM panels/boards for cooling, the use of PCM panels/boards in buildings can also be extended to reduce heating energy consumption.

This approach seeks to maximise the benefits of solar gain during winter, by allowing the PCM inside the conditioned space to absorb solar heat. The heat is then slowly released when the temperature drops, helping to keep the building warm and reduce the need for supplementary heating (De Saulles, 2009). This approach is effectively distributing the stored heat throughout the day to provide a lower temperature swing, improving thermal comfort in the building.

The benefits of adopting PCM panels and boards have been clearly portrayed in the literatures. However, they have all been applied to relatively small spaces, with rather uniform heat gains, as opposed to this study. This therefore reinforces the need for the study in this thesis, in reference to the performance of PCM systems when applied in larger and more open spaces. Commercial PCM panels/boards can be found from BASF Ltd, Eco Building Boards Ltd, Datum Phase change Ltd, Delta Membrane systems Ltd and Rubitherm GmbH.

2.1.7 PCM-Air heat exchanger type systems

PCMs used in heat exchangers are a relatively new concept, with few commercial products available on the market. Contrary to PCM panels and boards, the phase change properties of PCMs employed in AC units are more dependent on the AC system design. Nonetheless, as shown by the following literatures, because these systems mainly operate under the free-cooling principle, the PCM phase change temperatures are close to the comfort conditions. This aids in the maximisation of the energy saving potential of PCMs.

Dolado *et al.* (2009) numerically studied an energy storage device consisting of a PCM plate arrangement placed in an air duct system under free cooling. The candidate PCMs were E21® (from EPS Ltd), RT27® (from Rubitherm GmbH) and C32® (from Climator AB). The authors conveyed the importance of the encapsulation geometry and chemical compatibility of different PCMs with their encapsulation. Aluminium encapsulation was used in their study. The PCM was used to collect ‘cold’ from the ambient air during the night to be released during the day (free-cooling), in a semi-active way to minimise overheating of the conditioned space and maintain comfortable indoor thermal

conditions. The simulation results showed that the selected PCMs were not suitable for general rooms (comfort temperature of 20°C to 24°C) and 'biotech labs' (comfort temperature of 17°C to 27°C). They were however better suited to computer rooms requiring temperatures of 21°C to 40°C. This is because commercial PCMs tend to have large melting temperature ranges, and the associated latent capacity within the comfort temperature range is not always enough to maintain thermal comfort. This emphasises the fact that it is not the peak phase change temperature which is the crucial parameter, but rather, the melting range and enthalpy within the required comfort temperature limits.

Vakilaltojjar *et al* (2001) studied semi-analytically the heat transfer properties of an arrangement consisting of PCM plates placed in an air-conditioning system. The PCMs considered were calcium chloride hexahydrate and potassium fluoride tetrahydrate. The authors showed that for the same mass of PCM, increasing the plate thickness and air gap resulted in poorer heat transfer properties. Conversely, smaller air gaps and thinner PCM plates enhanced the heat transfer performance, at the expense of higher number of PCM containers, larger volume of the overall storage device and higher pressure drop. Furthermore, it was found that the air velocity profile at the inlet did not affect the heat transfer characteristics considerably.

Medved and Arkar (2008) numerically investigated the free-cooling performance of PCM RT20® spheres packed in a cylinder to be incorporated into air conditioning system ducts, for six European cities. They found that a PCM with broader temperature range is more favourable for such applications due to the large variations in ambient air temperature. For the cases studied, the authors showed that the PCM peak melting temperature should not differ by more than $\pm 2^\circ\text{C}$ from the optimum indoor temperature in order to allow an effective use of the PCM. They showed that the optimum size of the PCM unit for free-cooling should be between 1 and 1.5 kg of PCM per m^3/hr of fresh ventilation air, while the night ventilation rate should be approximately thrice the daytime flow rate.

Nagano *et al* (2006) experimentally studied the design of a floor supply AC system with granular PCM for the metropolitan area of Japan. The authors produced their own granules from a mixture of hexadecane and octadecane that were evenly distributed in the floor. The experiments were conducted in a test-cell mimicking an office building.

The results showed that employing a PCM packed bed in the floor AC system improved the time constant of the room temperature by a factor 1.5-2.1, and that the use of night-ventilation at a rate of 16.3 m³/hr allowed 89% of the daytime cooling energy to be provided by the PCM.

Gowreesunker and Tassou (2013b) numerically investigated a CSM[®] panel arrangement retrofitted inside an airport's displacement ventilation diffuser, using a TRNSYS-CFD quasi-dynamic simulation method. TRNSYS[®] was used to simulate the AC unit and control system, while the airflow and radiation within the airport terminal was simulated using CFD FLUENT[®]. The PCM system operated under the free-cooling principle during summer and mid-seasons, while the indoor air was re-circulated for winter recharge. The results showed that annual energy savings in the range of 22-34% are possible, and because of the operation schedule of the airport terminal, limiting the use of night ambient air for the PCM recharge is more beneficial.

Zalba *et al* (2004) experimentally studied an arrangement of PCM plates with RT-25[®] and C-22[®] inside air conditioning ducts. They found that the heat transfer rate was faster with thinner plates, higher air flow rates, and greater temperature difference between the PCM and the incoming air. They further employed the Design of Experiment (DoE) statistical method to formulate the relationship between these three variables and the melting/solidification times. Using these relations to size the PCM system, an economic analysis was conducted to depict the performance of the system. This showed that using the PCM plate system would require an additional 9% investment, but will have a payback period of 3-4 years and will consume 9.4 times less energy than a conventional AC system.

Dolado *et al* (2011) studied a real scale PCM-air heat exchanger in a laboratory experimental setup. They used the Ruitherm CSM[®] plates with an organic PCM of mean phase change temperature of 26.5°C. They quantified the surface of the plates in terms of rugosity, and convection heat transfer analyses in the PCM were simplified using an effective thermal conductivity. The authors showed that for a constant PCM mass, although increasing the PCM thickness increases the air convective heat transfer coefficient due to an increase in the air velocity, the solidification/melting process is delayed. Conversely, decreasing the PCM thickness improves the absorption/release of heat because of the larger heat transfer unit area, for a given volume.

A commercially available air-conditioning product with PCM is the TROX Type FSL-B-PCM[®] (see Fig. 2.9), which is a semi active system that can be placed in suspended ceilings or under-window sill.

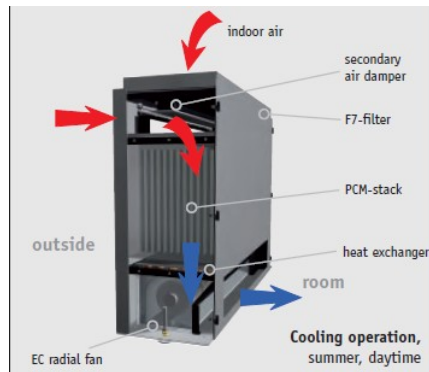


Fig. 2.9. TROX system
(www.troxuk.co.uk, 2013)

The charging process occurs at night with cold air passing through the PCM, and the discharging process happens during the day, with hot outside air passing through the unit (free-cooling) before entering the space. The product uses either paraffin or salt hydrates with melting points between 20°C to 25°C. The manufacturer claims a cooling capacity of 280W when used for 5 hours, and an auxiliary heating capacity of 2 kW, done by electric heating (TROX UK Ltd, 2013).

TROX Technik[®] produces other variations of AC units, comprising mainly of under-sill units and under floor units. During the UK-summer, the diurnal temperature fluctuation is around 10°C (De Saulles, 2009), which suggests that these systems may also provide semi-active heating at night, if a uniform temperature profile for both the day and night is required, without the need of electric heating. Nonetheless, auxiliary heating will be required for winter.

The Monodraught COOL-PHASE[®] unit is another commercially available AC unit, which incorporates PCM. The unit is placed on the ceiling and comprises of PCM plate heat exchangers. It operates by the free-cooling principle, using cold night air to recharge the PCM. For heating purposes, the unit recirculates indoor air to recharge the PCM accordingly. The manufacturer claims a reduction of 90% in the energy consumption relative to a conventional cooling system (MONODRAUGHT Ltd, 2013). The introduction of these commercial PCM units shows the market's interest in the concept of energy storage in reducing the energy consumption and CO₂ emissions in buildings, with regards to the 2020 UK emission reduction targets.

2.1.8 PCM Glazing units

It can be inferred from the literature that PCMs have received most attention in relation to their application to plasterboards, wallboards or concrete, as well as active systems such as PCM-heat exchangers (Gowreesunker *et al*, 2013c). These systems have already been shown to be effective for different building spaces, as described in sections 2.1.6 and 2.1.7, and resulted in various commercial products such as Dupont Energain®, Monodraught Cool-Phase® or Ebb PCM-Clay® boards. Most of the commercial and experimental systems are opaque, and therefore the understanding and consideration of the radiation aspect of PCM have been largely neglected in past research studies. However more recently, new commercially available types of glazing such as Delta®Cool-28 or GlassX®, which incorporate PCMs have been developed, showing the market interest for more thermally massive glazing.

Weinläder *et al* (2005) optically tested RT25® (paraffin), S27® and L30® (salt hydrates) placed in transparent plastic containers behind a double glazed window. The optical tests revealed that the PCMs have higher transmittance values in the liquid state relative to the solid states. In liquid phase, the PCMs are clear, transparent and non-scattering, while the solid phase is translucent and scattering. Nonetheless, the color of the transmitted light is constant for all phases, making PCMs viable options for day-lighting purposes. The authors further evaluated the thermal performance of such glazed systems in German weather conditions. During winter, the PCM improves the insulating effect of a double glazed window and shifts the heat gains to the evening, thus leveling the temperature of the space over an entire day/night period. During summer, a PCM façade can reduce the overall heat gains by 25 % and can provide a lower indoor temperature relative to conventional double glazed units. The authors concluded that facade panels with PCM can be very advantageous to office buildings, although the change in visual appearance in the PCM during phase change may be a drawback.

Gowreesunker *et al* (2013c) studied the optical and thermal aspects of a double glazed unit, where the cavity was filled with RT27®. The optical properties of the PCM-glazed unit were experimentally evaluated, and several relationships describing the variations of the absorption and scattering coefficients of the PCM during phase change were developed. Using a validated numerical model, they showed that employing the PCM

enhances the thermal mass of the window during phase change, relative to a standard double glazed unit. However, because of the higher radiation absorption coefficient of the PCM in the liquid phase, relative to air, overheating may be a limitation once the PCM has melted. The visual aspect of the PCM was found to be similar to observations by Weinläder *et al* (2004), where a PCM-glazed unit is suitable for day-lighting purposes, but depending on the application, the change in visual appearance during phase change may have to be concealed.

The Delta Cool-28® is a commercial PCM glazed unit, consisting of salt hydrates with a phase change temperature between 26 and 30 °C, and total heat capacity of 1.2 kWh/m² during phase change. The manufacturer claims an indoor temperature reduction of 4 °C to 6 °C during summer months, improving the thermal comfort of the occupants and reducing the building cooling loads. During winter, the PCM absorbs and stores solar gains, aiding in the reduction of heating loads (www.cosella-dorken.com, 2013).

Similarly, GlassX® is another commercial PCM glazed product incorporating calcium chloride hexahydrate within their glazing units. The manufacturer claims a reduction of 7 °C in indoor temperature with the application of GlassX® during summer. Up to 70% savings in cooling energy and 6% in heating load are anticipated through the use of GlassX® (www.glassx.ch, 2013). This product has already been fitted in various buildings in Switzerland and Germany, with very favourable outcomes. As a result, GlassX® Ltd has developed various other optimised products including: double and triple glazed units; a prismatic reflector pane at 35° to optimize reflection of solar radiation during winter and summer at high altitudes; and screen-printing options to mask the changing appearance of the PCM as it changes phase.

2.1.9 PCM in Heat/Cold Storage Units

Energy storage systems are crucial for the successful implementation of renewable energy technologies so as to ensure sufficient energy when the renewable energy is not available. Conventional storage of heat/cold is done in water tanks/towers, or electrically using PV cells, and has applications extending from building air-conditioning to nuclear reactors. Although water has been the main medium used in heat/cold stores, PCM can also be considered as a strong alternative due to its high energy density (Sharma *et al*, 2004).

Cold stores with PCMs work in a similar manner to PCM panels, i.e. they are charged by cool air/water or electricity at night, and discharged when needed. Ice has been commonly employed in cold stores, however, because of its fixed melting point at 0 °C, ice has limited applications. Other PCMs such as inorganic salt hydrates, organic paraffin waxes and eutectics have thus been investigated, and considered suitable for cold stores. For instance, RT5® (peak melting point 7 °C and latent heat of fusion 158 kJ/kg) was proposed to be a suitable candidate for cooling applications, because of its congruent melting, no subcooling, its stability after several heating and cooling cycles, and its self-nucleating properties (Sharma *et al*, 2004).

Additionally, Bo *et al* (1999) suggested the use of hexadecane and tetradecane, as well as mixtures of both for cold stores. The phase change temperatures of the different mixtures ranged from 1.7 °C to 17.9 °C, and latent heat from 146 kJ/kg to 227 kJ/kg. The thermal properties were measured using DSC. The paraffins showed stable chemical and thermal properties, and the volume change during phase changes was below 10%. They concluded that the studied materials qualify for cool storage.

Tay *et al* (2012) experimentally investigated a tube-in-tank design filled with a salt hydrate with phase change temperature of -27 °C. They based the performance of the PCM on the compact factor and heat exchanger effectiveness of the tank design, and proposed an equation for the average effectiveness of such tanks up to a tube spacing of 70 mm. They concluded that this tank design can deliver a high energy storage density with compactness factors above 90%.

Cristopia Ltd. developed an encapsulated nodule storage, or mini plastic PCM spheres, ranging from diameters of 77mm to 98mm, and phase change temperature of -33 °C to

0 °C. An example of such PCM nodule is shown in Fig. 2.10 (www.cristopia.com, 2010).

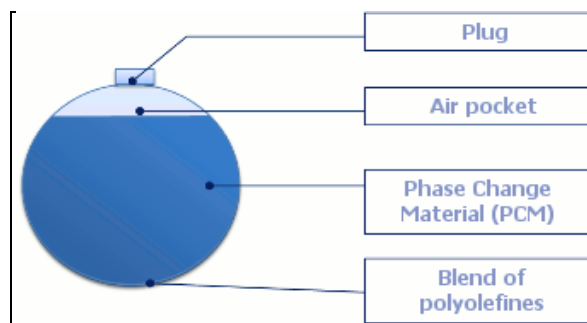


Fig. 2.10. PCM nodule by Cristopia
(Cristopia Co. Ltd, 2010)

These PCM nodules are put directly into the storage tank and the secondary heat transfer medium exchanges thermal energy by direct contact with the nodule. This nodular storage system has proven to be very effective, due to its low operating temperatures and high mechanical strength (Cristopia Co Ltd, 2010).

Heat stores are mainly used to capture solar energy for use in water and air heating systems, and sometimes in cooling applications (through absorption chillers) (Godarzi *et al*, 2013). The Solar Heating and Cooling (SHC) programme (Citherlet *et al*, 2007) investigated the use of PCM together with water as heat stores. One of the advantages of using water as the heat storage medium is that it can store heat at different temperatures due to stratification. Thus Citherlet *et al* (2007) designed a water tank with PCM at the top, operating at a relatively high melting temperature. When the water temperature at the top of the tank reaches the PCM melting point, the latter starts charging, therefore maintaining temperature stratification in the water as well as increasing the overall heat capacity of the tank. The PCM used was 90% sodium acetate and 10% graphite, with a melting point of 58°C, melting enthalpy of 180-200 kJ/kg and enhanced conductivity (due to graphite) of 2-5 W/m·K.

Other types of configurations may include entire heat stores filled with PCM, with the secondary fluid (water) passing through heat exchangers. Such studies include Mettawee and Assassa (2006) who experimentally investigated a paraffin wax with melting temperature of 54°C and melting enthalpy of 266 kJ/kg in a solar collector. Their study showed that the low thermal conductivity of the PCM is a limitation at the start of the melting process, which lowers the heat transfer coefficient. However, as the PCM melts and convection becomes more dominant, the heat transfer properties improve. During the discharging process, increasing the water flow rate improves heat transfer. Glauber's salt, calcium chloride hexahydrate, sodium thiosulfate penthydrate,

sodium carbonate decahydrate, fatty acids, and paraffin waxes were found to be important PCMs for solar heating applications (Koca *et al*, 2008).

Due to the popularity of PCM heat stores, their application has been extended from the air conditioning of buildings to district heating and cooling, waste heat recovery and heat transportation. The TransHeat® system combines the advantages of district heating with those of latent heat storage. This allows industrial waste heat to be used for other applications such as water heating or cooling (through absorption chillers) at other places. The PCM used in TransHeat® systems is sodium acetate trihydrate with melting point of 58°C but most PCMs in the melting temperature range of 58°C – 180°C have been deemed satisfactory (Mehling *et al*, 2002), with higher importance placed on the melting enthalpy.

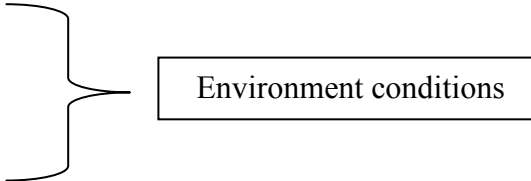
A common drawback for both heat and cold stores is the low conductivity of PCMs. Direct contact improves the heat transfer properties, but cannot be used for all PCMs. As a result, appropriate heat exchangers must be used. Furthermore, the use of heat transfer enhancements such as fins, high conductivity metal matrices, etc. were also found to be effective (Sharma *et al*, 2004). For heat exchangers, the heat transfer coefficient can also be enhanced by using a rough surface between air and the encapsulation (Dolado *et al*, 2011), promoting turbulence. Medrano *et al* (2009) experimentally investigated the thermal performance of five conventional heat exchangers working as latent energy storage devices, with RT35® and water as the heat transfer fluid. The authors concluded that a double pipe heat exchanger and a plate heat exchanger are not effective as heat stores. A compact heat exchanger, with PCM between the coils and fins provided the best performance, with 1kW heat transfer at a temperature difference of 25°C.

A report by the International Energy Agency (IEA) Task 32 (Steicher, 2008) showed that the performance of storage tanks is strongly dependent on the temperature variations in the tank. For temperature variations from 50 °C to 70 °C, a PCM tank with a heat exchanger can be sized to 1/3 of a conventional water tank. However, for macro-encapsulated PCM and a temperature variation of 25-85 °C or 20-70 °C, the PCM store will have the same size as water stores. Hence, hot water designs requiring large variations in temperature will have limited benefits with respect to store size when PCMs are employed.

2.2 Thermal Comfort

Thermal comfort is generally defined as the ‘*condition of mind which expresses satisfaction with the thermal environment*’ (Fanger, 1970). From this definition, thermal comfort is dependent on both the environment and the occupant, making it a subjective concept, whereby its evaluation can differ significantly between different studies. Two distinctive approaches to assessing thermal comfort are the heat balance model and the thermal adaptive model (Brager and de Dear, 1998), with a common index of thermal neutrality, referring to the conditions where the occupant would prefer neither a cooler or warmer surroundings (Fanger, 1970).

The heat balance model, also known as the static/ constancy model, is the basis of early works on thermal comfort (Gagge *et al*, 1967). The model consists of determining the energy balance between the occupant and its surrounding, such that the internal body temperature is constant, attaining thermal neutrality. The model has undergone extensive laboratory testing, identifying the main variables as (Fanger, 1970):

- Activity level (heat production in the body)
 - Thermal resistance of clothing (clo-value)
 - Air temperature
 - Mean radiant temperature
 - Relative air velocity
 - Air Humidity
- 
- Environment conditions

The activity level, consisting of the mean skin temperature and sweat secretion values, are used as basic parameters for thermal comfort, as only these two factors relate to the human physiological variables influencing the comfort equation (Fanger, 1970). These two variables combined with the heat transfer theory led to the formation of the general Fanger’s comfort equation. The activity level and clothing factor, obtainable from guides such as CIBSE or ASHRAE, together with the other parameters can thus be used in Fanger’s comfort equation to determine an optimal thermal condition for building occupants.

The thermal sensation of the occupants, i.e. ‘*the condition of mind*’ aspect from the definition of thermal comfort is quantified through the Predictive Mean Vote (PMV) or

Percentage of People Dissatisfied (PPD) indices under different conditions. These are statistical analyses showing the deviation in thermal neutrality for a large group of people for particular environmental conditions. An acceptable thermal environment would have a PMV of less than ± 0.5 , with PPD $< 10\%$ (Fanger, 1970). This mechanistic approach of the comfort equation has received numerous criticisms due to the simplicity in which the '*condition of mind*' of the occupant is evaluated.

The limitations of the heat balance model have therefore led to the development of the thermal adaptive model, aiming at enhancing the evaluation of comfort by considering the active customization of humans in different environment. Human interaction with the environment has been separated into 3 groups (Brager and de Dear, 1998):

- Behavioural response
- Physiological response
- Psychological response

Behavioural response consists of either conscious or unconscious modifications brought about by the occupant. This includes personal adjustments (e.g. adjusting clothes, postures, etc.), technological adjustments (e.g. opening/closing windows) and cultural adjustments (e.g. adapting dress codes), which modify the heat transfer with the surrounding environment, enhancing comfort (Brager and de Dear, 1998).

Physiological response refers to the acclimatization of the human body leading to a gradual reduction in the strain induced by the exposure to the environment. This is done through the thermoregulatory system of the human body (Brager and de Dear, 1998).

Psychological response relates to the habituation and expectation of a particular thermal environment. A person's reaction to a temperature which is less than perfect will depend very much on his/ her expectations (McIntyre, 1980). The psychological aspect is thought to be the most influencing aspect in the adaptivity of occupants to their environment (Brager and de Dear, 1998).

Although the thermal adaptive model's results are a better representation of the state of mind of the occupants, the complexity of the procedure makes its application to building design difficult (McCartney and Nicol, 2002). For this reason, international standards have been slow in implementing the adaptive theory in their guides, staying with Fanger's equation to evaluate thermal comfort.

From the previous discussion, the evaluation of design parameters for thermal comfort of a building, or even the assessment of thermal comfort is very complex. Brager and de Dear, (1998) suggested that both the heat balance and the adaptive models should be used complementarily, and showed that behavioural and psychological responses are more influential in determining thermal comfort. De Dear *et al.* (1997) suggested that the PMV model should be used for air-conditioned buildings, while the adaptive model should be employed for naturally ventilated buildings.

In the case of this study, the airport terminal occupancy is chaotic, and no specific parameters can be appropriately evaluated due to the diversity in occupants and sub-environments within the terminal. However, as suggested by Milne (1995), by providing occupants with greater control over their own indoor environment, and allowing temperatures to closely track patterns of the outdoor climate, significant energy savings can be obtained together with enhanced thermal comfort. The centrally air-conditioned terminal building provides passengers with an expectation (equivalent to values obtained from the CIBSE or ASHRAE guides, which are for a large group of people in the corresponding environment), and they therefore come prepared. Thus by allowing the indoor environment to vary in phase with the outdoor conditions, within the ‘expected’ norms described by the guides, and assuming that the passengers will adapt themselves toward thermal comfort, an acceptable indoor thermal environment can be produced.

Comfort also comprises of pollutant levels, noise, etc, in the building, but these non-thermal factors will not be considered in this study. As a result, the main parameters monitored for thermal comfort are the air temperature and velocity, while relative humidity is assumed constant at 50%.

2.2.1 Thermal Comfort conditions

The thermal comfort approach employed in this study is similar to the works of Piechowski and Rowe (2007), whereby thermal comfort was evaluated for a combined radiant floor and air ventilation system for an airport terminal in the tropical climate in Northern Australia, through CFD. The concept of adaptivity of occupants is incorporated into the determination of thermal comfort by allowing the indoor

conditions to vary in phase with the outdoor conditions, but maintaining a PPD < 10%. Piechowski and Rowe (2007) identified the appropriate parameters for comfort and obtained a summer design air temperature for the Australian Climate of 25-28 °C. These conditions are relaxed in areas where the occupancy is short and transient, in order to save energy, in relation to the adaptivity model. They also pointed out that many spaces in airport terminals are without occupants (e.g. high ceilings), and therefore thermally conditioning these unoccupied spaces results in waste of energy. In the works of Piechowski and Rowe (2007), a height of 2m from the ground is considered essential for conditioning.

The balance between thermal comfort and energy requirements is of prime importance in selecting an appropriate air-conditioning system, especially for large spaces. Energy demand relates primarily to the sensible and latent thermal loads of spaces, but also to the mechanical energy and efficiency of air-conditioning components. By maintaining the indoor conditions close to the outdoor conditions, significant energy savings can be achieved, provided thermal comfort limits are respected (Piechowski and Rowe, 2007). The airport thermal comfort criteria prescribed by the CIBSE standards are given in Table 2.6, for a clothing factor of 0.65-1.15 clo, metabolic rate of 1.3-1.8 met, relative humidity of 50% and air velocity of 0.15 m/s to provide a PMV of ±0.5.

Table 2.6. Comfort criteria for Airport Terminals (CIBSE A, 2006)

Airport Terminal Sectors	CIBSE Winter comfort operative temp (°C)	CIBSE Summer operative temp (°C)
Baggage Reclaim	12 - 19	21 - 25
Check-in areas	18 - 20	21 - 23
Concourse (no seats)	19 - 24	21 - 25
Customs area	17 - 21	20 - 24
Departure lounges	18 - 22	21 - 25

In airport terminals, there are transient passengers, but also staff members that are in the environment for longer periods of time. Depending on the rules and regulations of the airport, the latter occupants may be more flexible in their adaptation than the passengers. For the case of the ‘check-in areas’, considered in this study, the design comfort temperature range is 18-23°C, which is obtained from CIBSE Guide A (2006).

Furthermore, the movement of air is important in buildings as it provides fresh air, removes odours, and satisfies significant proportions of thermal loads (Piechowski and Rowe, 2007). Meng *et al* (2007) suggests that occupants do not feel air speeds lower than 0.5 m/s, whilst air speed over 5 m/s are very uncomfortable.

An interpretation of the adaptive comfort model would be a relaxation of the mechanistic comfort temperatures, described in Table 2.6. However the complexity lies in determining the extent to which the temperatures can be relaxed. Unfortunately, more research is required into the thermal comfort of airport terminals, considering the adaptation model and the requirements of different groups of people, in order to accurately quantify and relax the thermal comfort requirements. This is beyond the scope of this study.

2.3 Summary of Chapter 2

Chapter 2 introduced the concept of phase change materials, with a focus on solid-liquid PCMs. The important aspect of high heat content at narrow ranges of temperature supports the use of PCM in buildings, but various other thermo-physical, kinetic and chemical properties have also been identified as essential to the proper utilisation of PCMs. The lack of certain desired properties can be overcome through appropriate system design. The classification of PCMs into organic, inorganic and eutectics has been presented, with a description of some commonly employed experimental and commercial PCMs. Classical thermal analysis techniques consisting of the DSC and T-history methods have also been described.

The choice of PCMs is primarily related to the comfort temperatures required in the conditioned space. In passive systems, PCMs are generally chosen such that the peak phase change temperature lies within the comfort temperature range; although this does not imply that the PCM is most effectively used. The overall phase change temperature range should also ensure that most of the phase change occurs within the desired temperature range, in order to improve the effectiveness of the PCM and prevent energy 'wastage'. In semi-active or active systems, the phase change temperature and enthalpy ranges are more system dependent. The phase change enthalpies are determined based on the heat loads of the building, and are also system dependent. Thus, as the performance of PCM systems depends on the type of building, weather conditions, thermal comfort conditions, etc., the sizing of PCM systems is also case-dependent.

Solid-liquid PCMs are found to have poor heat transfer properties and hence are not used directly as a heat transfer medium. Micro-encapsulation, heat transfer enhancements and efficient system designs have been popular methods to improve the heat transfer properties. The application of PCMs to buildings has mainly been through their incorporation into the building envelope or their use in air-conditioned related systems. They are used to shift the thermal loads by providing additional thermal inertia. They have also been incorporated in gypsum wallboards, wooden structures and concrete, with very encouraging results.

The Rubitherm CSM® plates have been popular in the design of semi-active AC-related systems, where they have been used to provide free-conditioning or to reduce the size

and energy consumption of the AHU. Cold night ambient air is commonly used for recharging the PCMs in cooling applications, while for heating purposes, the relatively warmer room air can be re-circulated to restore the heating potential of the PCM. Other less popular PCM heat exchanger systems include the use of PCM spheres in the AC ducts, or the use of conventional heat exchangers with PCM incorporated in them. In passive systems, the PCM is allowed to operate on its own, based on the physics of the building, and therefore emphasising the importance of appropriately sizing the passive PCM system. Conversely, the employment of semi-active systems offers more flexibility in the performance of the PCM, as secondary parameters such as flow rates or temperatures can be further controlled during the operation of the PCM system. With regards to costs, the capital costs of implementing PCM systems in AC buildings may be high, but compared to conventional AC systems, the running costs are very favourable, with encouraging payback periods (Zalba *et al*, 2004).

Other uses of PCMs include heat/cold stores and PCM glazed units. Heat/cold stores can consist of macro- or micro- encapsulated PCM, possibly combined with water to allow for stratification. Direct contact methods were found to be more efficient than indirect methods. In general, the stores can be found to have enhanced thermal storage capacity, thus enabling smaller store sizes to be used. PCM glazed units can be mainly used to improve the thermal mass of lightweight and glazed structures by absorbing solar radiation and providing a thermally stable indoor climate. However, the optical properties of PCMs may affect the aesthetics of the space, and PCM-glazed units may therefore require concealment.

The majority of PCM systems encountered in the literature have been studied for relatively small indoor spaces such as offices, and for intermittently occupied buildings. The performance of PCM systems were found to be heavily dependent on the phase change temperatures, thermophysical properties, melting enthalpy, amount and type of PCM, orientation of the building, climatic conditions, type of systems (passive, active or semi-active), design of the system and building operation (ventilation schedules and heat loads) – i.e. a PCM system's performance is case dependent. Therefore, this emphasises the use of numerical models in the prediction and optimization of the performance of PCM systems.

Section 2.2 provides a general understanding of the thermal comfort criteria for airport terminal buildings – the two comfort models, i.e. Fanger’s equation and the adaptive model are described. As specified in section 2.2.1, the combined use of both models is a more accurate way of quantifying thermal comfort. The adaptive model basically specifies that occupants can adapt themselves to a specific environment, while Fanger’s equation of comfort provides a mechanistic approach to comfort. Using both methods simultaneously enables a relaxation of the thermal comfort requirements by closely tracking the external temperature patterns. This allows reduction in the AC running costs.

The following chapters describe the numerical methodologies employed in this study to evaluate the performance of PCM systems in the airport terminal space.

CHAPTER 3 – THERMAL MODELLING OF PHASE CHANGE

3.1 Importance of Numerical Modelling

Numerical modelling generally refers to the process of employing mathematical models or relations to describe the dynamic behaviour of a real system. Numerical models aid in the conceptualisation of a physical system into mathematical terms (Barbour and Krahn, 2004), and therefore, depending on the complexity of the actual problem, various assumptions may be present in the model. Numerical modelling has been popular in a wide variety of fields, ranging between quantum dynamics, thermodynamics, structural analysis, geotechnical engineering and climate modelling (ScienceDirect, 2013).

In the engineering field, numerical models are commonly employed for interpretative, design or predictive studies (Barbour and Krahn, 2004):

- **Interpretation:** refers to the use of numerical models to help in understanding field or laboratory data.
- **Design:** refers to the use of numerical models in comparative analyses. It helps in determining the relative performance of different systems, with less emphasis on the final absolute values.
- **Prediction:** refers to the use of numerical models to provide a final quantifiable performance of the investigated system.

In all cases, it is important to have a valid numerical model that reflects the physical reality. Validation refers to an iterative procedure where the model outputs are compared to experimental data, until the errors are justified within the limits of confidence (Thompson, 2005). Suitable validation metrics should be employed to quantify these errors and to provide a measure of the accuracy of the models (Oberkampf and Barone, 2006).

Once a model is validated, it can be used in parametric analyses, where specific model parameters are varied and their respective impacts on the main variables investigated. For instance, Li *et al.* (2012) validated a numerical model investigating the heat and moisture transfer in a test cell. The model was then used to study a further 12 cases with

different test cell configurations, monitoring the humidity and temperature levels as the main parameters. Gutiérrez-Montes *et al.* (2008) validated a numerical model in relation to the fire propagation in a test cell. Employing the validated model, they investigated the performance of different fans in order to extract the noxious fumes from the building. Gowreesunker and Tassou (2013a) validated a numerical model to investigate PCM building boards in a test cell. Using the model, they studied the effect of ventilation flow rates on the charging performance of the boards. Employing numerical models can therefore prevent the construction of expensive experimental setups for parametric studies, as well as save considerable amount of time and resources.

In this study, numerical models will be used to explore the phase change process of PCMs, and to model the indoor environment. Phase change simulations can be performed using finite volume methods (such as CFD) or lumped capacity methods. Both methods have been found to be effective; however finite volume methods are more detailed. Indoor environments can be simulated using zonal, multi-zonal or computational fluid dynamics (CFD) models (Chen, 2009). However, in cases with large indoor spaces, the International Energy Agency (IEA) suggests that the air-flow inside the space is crucial, and recommends the use of CFD for performance evaluations (Heiselberg *et al.*, 1998). Thus, for the purpose of this study, CFD will be used to model both the phase change process and the indoor space of the airport terminal, in order to improve on the accuracy of the simulation results.

3.2 Common Phase Change Models

Phase change consists of a heat transfer process involving sensible and latent heat, within a quasi-constant temperature range. Based on the first law of thermodynamics; the conservation of energy, Eq. (3.1), is employed to model the heat transfer process involved in phase change.

Governing Energy Equation:

$$\frac{\partial}{\partial t}(\rho c_p T) + \frac{\partial}{\partial x_j}(\rho c_p u_j T) = \frac{\partial}{\partial x_j} \left(\lambda \frac{\partial T}{\partial x_j} \right) + S_E \quad (3.1)$$

Referring to Eq. (3.1), in the Eulerian context;

$\frac{\partial}{\partial t}(\rho c_p T)$ accounts for the total energy of the fluid in the control volume

$\frac{\partial}{\partial x_j}(\rho c_p u_j T)$ accounts for the energy transfer due to movement of fluid into and out of the control volume (convection)

$\frac{\partial}{\partial x_j} \left[\lambda \frac{dT}{dx_j} \right]$ accounts for the heat transfer by conduction at the surfaces of the control volume

S_E accounts for other energy sources such as chemical, electrical, etc

In a non-phase change problem, a solution can be obtained relatively simply by applying the boundary and initial conditions to the discretised energy equation. However, in problems involving phase changes, there exists additional boundary conditions at the phase change interface (Kowalewski and Gobin, 2004), as shown in Fig. 3.1 for a one dimensional problem.

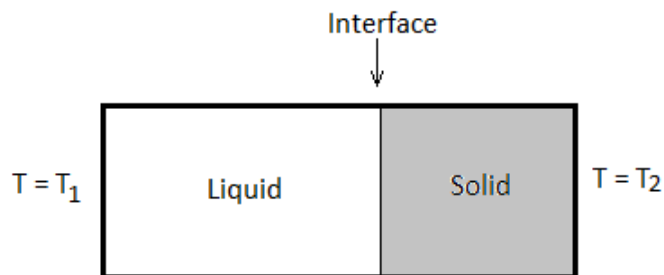


Fig. 3.1 Solid-liquid interface

For such problems, it is commonly assumed that the heat transfer at the interface is by conduction only, perpendicular to the interface, and that the homogeneous material has a single melting temperature. These are known as the Stefan conditions (Eq. (3.2)) for phase change, expressed as (Kowalewski and Gobin, 2004):

$$T_{liq} = T_{sol} = T_m \quad (3.2a)$$

$$\lambda \frac{\partial T_{sol}}{\partial x} - \lambda \frac{\partial T_{liq}}{\partial x} = \rho L_f \frac{ds}{dt} \quad (3.2b)$$

The Stefan conditions represent the energy conservation at the phase change interface, and relate to discrete phase change temperatures. The solution of the energy equation with these additional boundary conditions would describe the temperature distribution within the material. However, the ambiguity with this process is that the boundary conditions at the interface are constantly changing with the progression of phase change, implying that they have to be found as part of the final solution (Esen and Kutluay, 2004). This is known as the Stefan problem. Analytical solutions of the Stefan problem such as the Neumann solution do exist, but are limited to simple situations (Esen and Kutluay, 2004). In practical applications, the boundary conditions are more stochastic and the phase change region is mushy, therefore limiting the use of simplified analytical solutions, and preventing the use of the Stefan problem in its classical form.

More recently, an increasing number of numerical methods have attempted to avoid explicitly tracking the phase change interface in numerical models. However, although these methods have simplified the modelling of phase change, the numerical simulations still remain a challenging task, especially with regards to hysteresis, sub-cooling and nucleation. Common ‘non-explicit’ phase change tracking models include the enthalpy-porosity method and the effective heat capacity method, described in sections 3.2.1 and 3.2.2, respectively.

3.2.1 The Enthalpy-Porosity Method

The enthalpy of a material refers to the energy contained in a certain amount of that material, relative to a reference temperature. The enthalpy-porosity method does not aim at explicitly tracking the location of the phase change interface as proposed by the

classical Stefan problem, but instead uses a defined enthalpy-temperature relation, $\Delta H = f(T)$, to model the effect of phase change (Voller and Shadabi, 1984). This simplification has considerably increased the popularity of this method.

Early research by Voller and Shadabi (1984) mainly focused on materials with discrete phase change temperatures, where the enthalpy-temperature relation was a step function (see Fig 3.2). However, as most materials possess a phase change temperature range (i.e. a mushy region), with the enthalpy changing with different temperatures within the mushy region (see Fig 3.2), the problem becomes more complex.

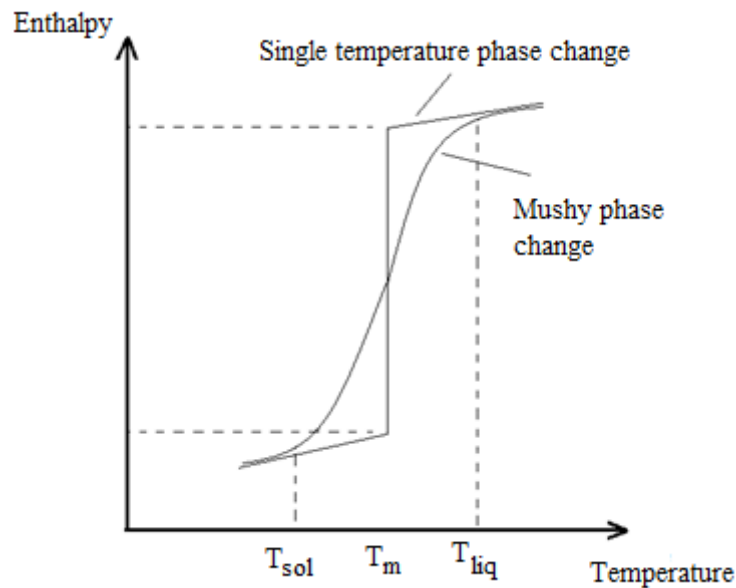


Fig. 3.2 Enthalpy-temperature relation

The effects of the mushy region are modelled through a parameter known as the liquid fraction (β) proposed by Voller and Prakash (1987), which has been adopted by various commercial packages, such as ANSYS FLUENT®. The liquid fraction is defined as:

$$\begin{aligned}
 \beta &= 0 && \text{if } T < T_{sol} \\
 \beta &= 1 && \text{if } T > T_{liq} \\
 \beta &= \frac{T - T_{sol}}{T_{liq} - T_{sol}} && \text{if } T_{sol} \leq T \leq T_{liq}
 \end{aligned} \tag{3.3}$$

From Eq. (3.3), β is obtained by the lever rule and the latent heat content of the material can be expressed as $\Delta H = \beta \cdot L_f$ (where L_f is the total latent heat). The lever rule assumes

that the enthalpy-temperature relation is linear, as opposed to the actual curvature obtained from experimental data.

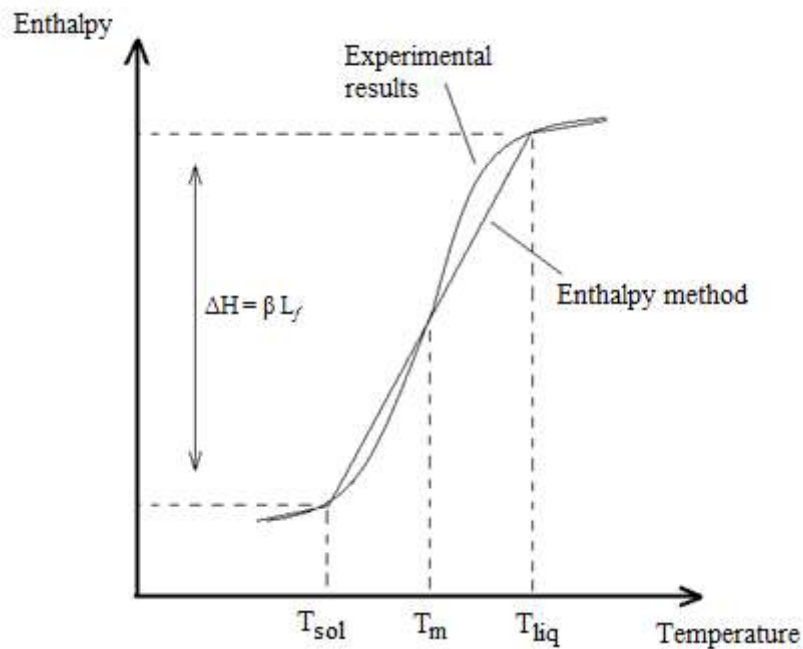


Fig. 3.3. The Enthalpy method of representing phase change

Fig. 3.3 shows that the linear approximation of the enthalpy-temperature relation may be satisfactory in some cases. However, as the enthalpy curvature for the actual material increases, the validity of the lever rule may then become questionable. Hence, the critical aspect to the accuracy of the method relates to the determination of an accurate enthalpy-temperature relation of the PCM, which can be obtained through heat analysis techniques such as the DSC or T-history method (Rady, 2009), described in section 2.1.3.

As previously explained, the additional thermal effect of phase change is the introduction of the latent heat, which refers to an additional heat storage capacity in the differential control volume. The latent heat can therefore be incorporated into the governing energy equation (Eq. (3.1)) as follows (ANSYS FLUENT theory guide, 2010):

The total energy in the control volume with phase change is given by:

$$H = h_{ref} + \int_{T_{ref}}^T c_p dT + \beta L_f \quad (3.4)$$

Hence by replacing Eq. (3.4) into the governing energy equation (Eq. (3.1)), the effect of phase change can be modelled as follows:

$$\frac{\partial}{\partial t} (\rho H) + \nabla(\rho u_j H) = \nabla(\lambda \nabla T) \pm S_E \quad (3.5)$$

In the case of FLUENT®, the solver operates by iterating between equations Eqs. (3.3), (3.4) and (3.5). The effect of convection during phase change can also be appropriately modelled using the enthalpy-porosity model (Voller and Prakash, 1987).

3.2.2 The Effective Heat Capacity Method

The effective heat capacity method was proposed by Poirier and Salcudean (1988) to simulate phase change. The basis for this method is similar to the enthalpy-porosity method, but instead of directly influencing the enthalpy of the PCM as in Eq. (3.4), it models phase change as a sensible process with an increased (effective) heat capacity. This can be visualised in Fig 3.4.

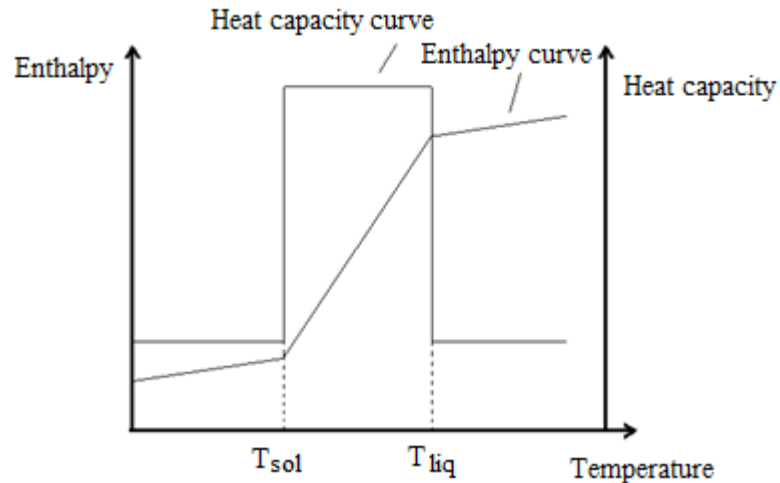


Fig 3.4. Effective heat capacity curve ($c_{p\ liq} = c_{p\ sol}$)

The effective heat capacity method, similar to the enthalpy-porosity method, defines a new parameter known as the ‘effective heat capacity’ ($c_{p\ eff}$) as follows (Yang and He, 2010):

$$\begin{aligned}
c_{p\,eff} &= c_{p\,sol} && \text{if } T < T_{sol} \\
c_{p\,eff} &= c_{p\,liq} && \text{if } T > T_{liq} \\
c_{p\,eff} &= [(1 - \beta)c_{p\,sol} + \beta c_{p\,liq}] + \left[\frac{L_f}{T_{liq} - T_{sol}} \right] && \text{if } T_{sol} < T < T_{liq}
\end{aligned} \tag{3.6}$$

Where ' β ' is the liquid fraction defined by Eq. (3.3).

Thus by substituting Eq. (3.6) into Eq. (3.1), the following expression can be obtained:

$$\frac{\partial}{\partial t} (\rho c_{eff} T) + \nabla(\rho c_{eff} u_j T) = \nabla(\lambda \nabla T) \pm S_E \tag{3.7}$$

As a result, another method of simulating a numerical phase change problem without explicitly tracking the phase front can be obtained by iterating between Eqs. (3.3), (3.6) and (3.7).

A limitation of the effective heat capacity method is that in the event that the total phase change occurs in one time-step, its effect will not be captured. Thus, small time steps are required, increasing the computational time. Furthermore, for materials with single phase change temperature, a virtual temperature range must be used, leading to poor results and simulation distortion of the real problem (Hu and Argyropoulos, 1996).

The choice of using either the enthalpy method or the heat capacity method is largely based on the numerical package used to solve the problem. For instance, it is recommended to use the enthalpy method with COMSOL® (Srinivas and Ananthasuresh, 2006), the effective heat capacity method with FEMLAB® (Lamberg *et al*, 2004a), either technique with ESP-r® (Heim, 2005), while FLUENT® only uses the enthalpy-porosity method. Both methods are physically and thermally valid, with the only distinctions relating to the stability and convergence of the numerical solution.

3.3 Enhancements to Phase Change Models

Two common limitations in both the enthalpy-porosity and the effective heat capacity methods, although employed in various studies such as: Susman *et al.* (2010), Sharma *et al.* (2006), Silva *et al.* (2012) or Chen *et al.* (2008), are that in their default states, they assume a linear enthalpy/cp – temperature relationship and no hysteresis in the PCM. Hysteresis refers to the phenomenon whereby the PCM melts and freezes in different temperature ranges and with different enthalpies, i.e. different temperature–enthalpy curves for melting and freezing. Hysteresis is related to the chemical and kinetic properties of the material (Mehling and Cabeza, 2008).

Although these two assumptions used in the previously described methods may be justified for certain PCMs; they do not represent the actual heat transfer process within the material. As portrayed in the works of Kuznik and Virgone (2009a, b) and Dolado *et al.* (2011), these effects are crucial in the appropriate performance evaluation of PCM systems, especially since a large proportion of PCMs available for building applications shows hysteresis in the charge and discharge cycles (Soares *et al.*, 2013). As a result, this shows the importance of developing new phase change simulation models, such as the sigmoid function based smooth effective heat capacity by Yang *et al.* (2010) or the continuous-properties model by Egolf and Manz (1994), and the need for further work in evaluating the real performance of PCMs (Soares *et al.*, 2013).

The following section 3.3.1 depicts a model developed as part of this study, which aims at improving the simulation of phase change in commercial PCM systems. It focuses on the simulation of PCM boards or panels, where thermal conduction is the dominant heat transfer process. This model is further documented in Gowreesunker *et al.* (2012).

3.3.1 Enhanced Phase Change Conduction Model

As elaborated in section 2.1, PCM boards and panels constitute a large proportion of passive PCM systems employed in buildings. Being a passive system, where the actual conditioning of the indoor environment is based solely on the thermodynamics of the boards, the appropriate representation of the phase change process is crucial in determining the overall performance of PCM boards.

The model developed in this section enhances the conventional enthalpy-porosity and effective heat capacity methods, by allowing user defined enthalpy-temperature curves to be separately defined for melting and freezing processes. In doing so, both the non-linearity and hysteresis involved in phase change processes can be modelled. This method was inspired by similar works performed on evaporation/condensation by De Schepper *et al.* (2009). The works of De Schepper *et al.* (2009) focused on a single phase change temperature, incorporating source terms in the energy and momentum equations to simulate phase change in pure water. This study, on the other hand, focuses on phase change mushy regions and only influences the energy equation. The method may be thought of as an extrapolation of the enthalpy-porosity method, but instead of explicitly calculating the enthalpy of the PCM at each time-step, it relies on the addition of a heat source term S_E in Eq. (3.1) to account for the extra latent energy involved in the melting and solidification processes. At this moment, this method has been developed for conduction dominant phase change processes only, as is the case in PCM boards.

The source terms for the melting and solidification processes are defined in Table 3.1. The functions $f(T)_m$ and $f(T)_f$ relates to the amount of heat stored/released by the PCM at each temperature during the melting and freezing processes, respectively. They can be obtained from heat analysis techniques such as DSC or the T-history method. For completeness, the source terms must be defined for all the conditions described in Table 3.1.

Table 3.1. User defined source terms required to fully defining the conduction phase change process

Heat sink conditions for Melting ($T_{t-1} < T_t$)	
$(T_t \leq T_{liq, m}) \ \& \ (T_{t-1} \geq T_{sol, m})$	$S_{E, m} = - \frac{\rho}{\Delta t} \int_{T_{t-1}}^{T_t} f(T)_m \ dT$ Eq.(3.8)
$(T_t > T_{liq, m}) \ \& \ (T_{t-1} < T_{sol, m})$	$S_{E, m} = - \frac{\rho}{\Delta t} L_f$ Eq.(3.9)
$(T_{sol, m} \leq T_t \leq T_{liq, m}) \ \& \ (T_{t-1} < T_{sol, m})$	$S_{E, m} = - \frac{\rho}{\Delta t} \int_{T_{sol}}^{T_t} f(T)_m \ dT$ Eq.(3.10)
$(T_t > T_{liq, m}) \ \& \ (T_{sol, m} \leq T_{t-1} \leq T_{liq, m})$	$S_{E, m} = - \frac{\rho}{\Delta t} \int_{T_{t-1}}^{T_{liq}} f(T)_m \ dT$ Eq.(3.11)
Heat source conditions for Freezing ($T_{t-1} > T_t$)	
$(T_t \geq T_{sol, f}) \ \& \ (T_{t-1} \leq T_{liq, f})$	$S_{E, f} = \frac{\rho}{\Delta t} \int_{T_{t-1}}^{T_t} f(T)_f \ dT$ Eq.(3.12)
$(T_t < T_{sol, f}) \ \& \ (T_{t-1} > T_{liq, f})$	$S_{E, f} = \frac{\rho}{\Delta t} L_f$ Eq.(3.13)
$(T_{sol, f} \leq T_t \leq T_{liq, f}) \ \& \ (T_{t-1} > T_{liq, f})$	$S_{E, f} = \frac{\rho}{\Delta t} \int_{T_{liq}}^{T_t} f(T)_f \ dT$ Eq.(3.14)
$(T_t < T_{sol, f}) \ \& \ (T_{sol, f} \leq T_{t-1} \leq T_{liq, f})$	$S_{E, f} = \frac{\rho}{\Delta t} \int_{T_{t-1}}^{T_{sol}} f(T)_f \ dT$ Eq.(3.15)

3.3.2 Validity of Model

This model was validated with 0.5 kg of macro-encapsulated PCM encased in a 100×70×80 mm thin aluminium box. The sample was a composite of low density polyethylene and organic PCM with phase change behaviour shown in Fig. 3.5, obtained via DSC.

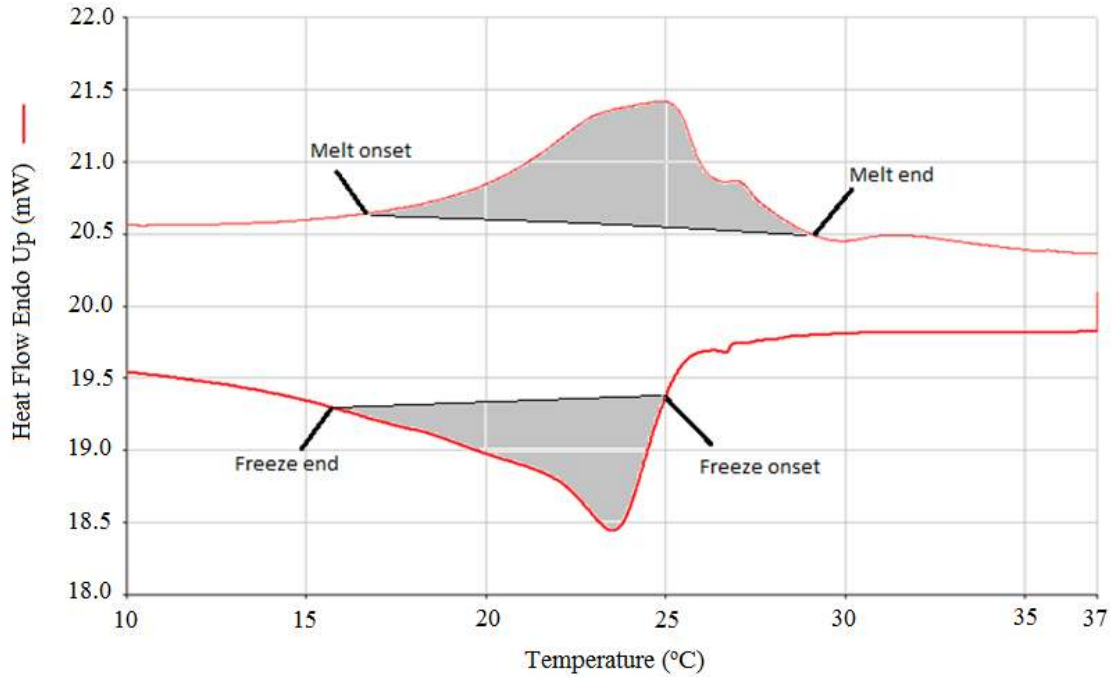


Fig. 3.5. DSC graph of investigated PCM composite (More details in Appendix A)

The shaded areas within the curves in Fig 3.5 depict the latent enthalpies of the composite. Note that freezing is slightly underestimated to show the effect of inaccurately defining the phase change parameters. The encased sample was placed in a controlled environment where the air temperature was varied from below the solidus line and above the liquidus line, as shown in Fig. A1.1 (Appendix A).

The experimental temperature within the composite was measured at four points (see Fig. A1.3), at intervals of 5s, using T-type thermocouples (uncertainty of $\pm 0.2^{\circ}\text{C}$), and the numerical validation of the developed method was performed using the CFD simulation package FLUENT[®]. The source terms defined in Table 3.1 were incorporated in the simulations via User-Defined-Functions (UDF), and the enthalpy-temperature relations employed are described in Fig. A1.2, Eq. (A1.6) and Eq. (A1.7).

The validation study consisted of simulating the temperature progression within the PCM composite for both the melting and freezing phase changes, under similar conditions as the experimental setup, and comparing the simulated temperature with the experimental data. The CFD model (see Fig. A1.3) consisted of $\sim 12,000$ hexahedral cells, and a time-step of 10s was employed for all simulations. The validation results are shown in Fig. 3.6a and 3.6b.

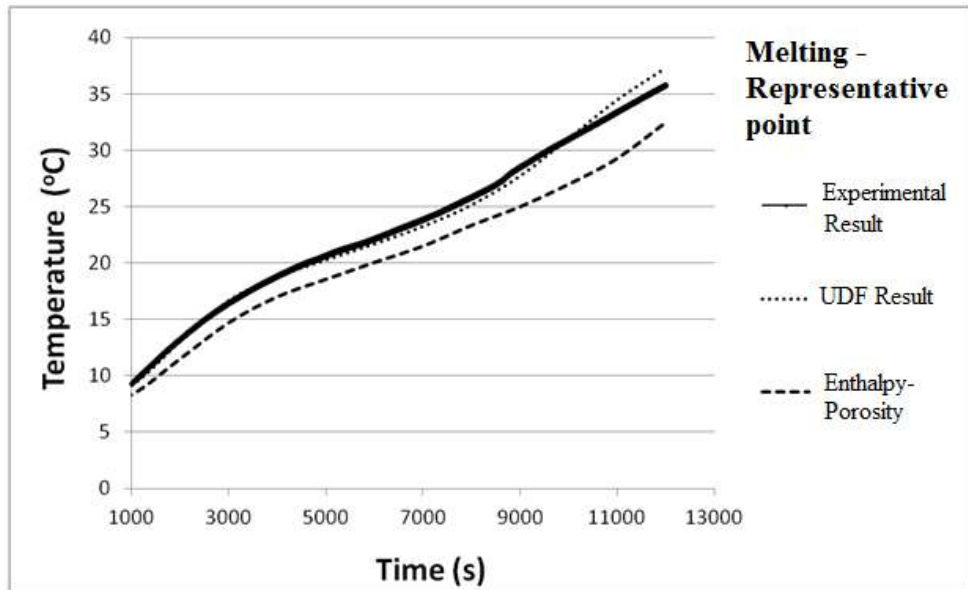


Fig. 3.6(a). Experimental, UDF and Enthalpy-porosity temperatures of a representative point during the melting process

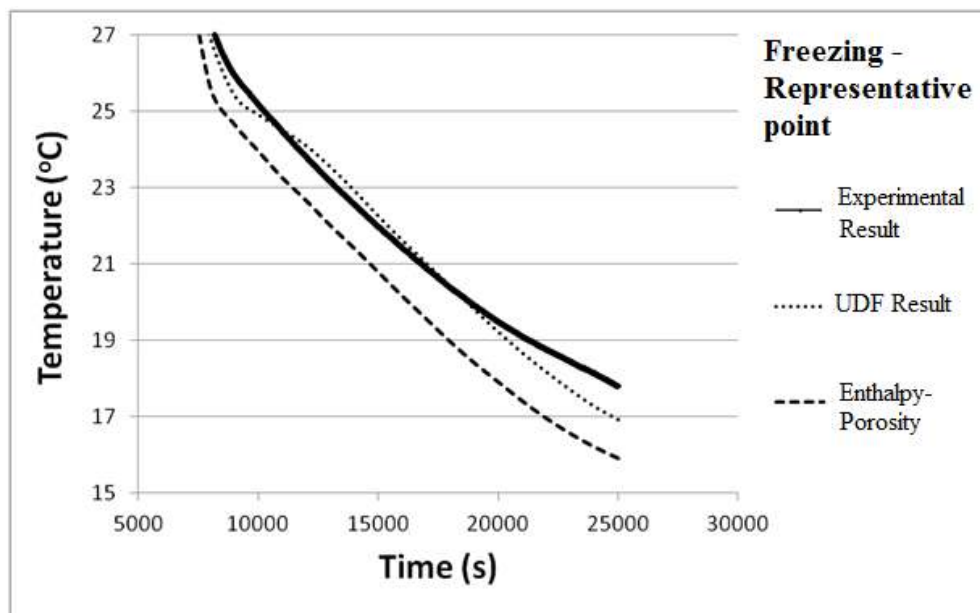


Fig. 3.6(b). Experimental, UDF and Enthalpy-porosity temperatures of a representative point during the freezing process

(The details of the simulations are given in Appendix A)

Fig. 3.6 shows that the User Defined Function (UDF) models more accurately predict the temperature trends in both the melting and freezing cases than the enthalpy-porosity model. In the melting case, the UDF model produces a more gradual change in the temperature trend due to the smoothness in the enthalpy-temperature relationship described in Fig. A1.2a, compared to the enthalpy porosity method which assumes the

linear relationship. Overall, for the melting case, the UDF model produced a Root Mean Square (RMS) error of 1.3% (0.36K), whilst the enthalpy-porosity model produced a higher RMS error of 12.3% (3.5K), calculated using Eq. (A1.8) and Eq. (A1.9).

In the freezing case, Fig. 3.6b shows that the experimental approximation of the enthalpy-temperature curve in Fig. A1.2b and Eq. (A1.7) is not accurate enough to predict the exact temperature trend in the composite material. This is due to the deliberate slightly inaccurate freezing onset and end temperatures, and curvatures employed in the simulations. The results showed that for the freezing case, employing the UDF model produces an RMS error of 0.5% (0.2K), while the default enthalpy-porosity model produces a higher error of 6.3% (2.6K).

In general, it was found that employing the UDF model, which accounts for the enthalpy-temperature curvature and hysteresis in the PCM during phase change is more accurate than the default enthalpy-porosity method employed in FLUENT®. Furthermore, the validation study showed that the predicted temperature trends are dependent on the thermal properties of phase change, but also on the curvatures assigned to the S_E equations. For instance in the freezing case, because of the higher gradient in the $f(T)_f$ curve (see Fig. A1.2b) at the freezing onset, relative to the DSC curve, the temperature trend is different at the start of freezing. These effects are particularly important when simulating the cyclic operation (charge/discharge) of PCM systems.

3.4 Summary of Chapter 3

This chapter provides an understanding of the numerical modelling of phase change processes. The enthalpy-porosity method and the effective-heat capacity method are described, and their limitations in terms of the linear evaluation of the liquid fraction are emphasised. For the case of phase change processes where thermal conduction is dominant, such as in PCM boards, an enhanced method of simulation is presented. This method employs User Defined Functions (UDF) obtained from experimental phase change characterisation techniques to mimic the enthalpy-temperature relationships of the PCM during phase change. The overall simulation errors were reduced when employing the enhanced method, due to the more accurate representation of phase change.

This method is fully documented in Gowreesunker *et al.* (2012), and more details are given in Appendix A. The following chapter describes the numerical procedure used to account for air-movement in indoor spaces, and depicts the application and validation of the enhanced conduction-dominant phase change model described in this chapter, in a CFD environment.

CHAPTER 4 – MODELLING OF INDOOR THERMAL ENVIRONMENT AND PCM

4.1 Introduction to Computational Fluid Dynamics (CFD)

Indoor thermal environments can be simulated with zonal, multi-zonal or Computational Fluid Dynamics (CFD) models. Zonal or multi-zonal modelling refers to the situation where the properties of a macroscopic volume of air are concentrated at one node in the investigated zone. It assumes that the volume of air for this node is fully mixed, and the properties are uniform throughout the zone. For large and open spaces, such as Airport Terminals, the International Energy Agency (IEA) recommends the use of CFD because of the importance of air-flow within the building (Heiselberg *et al*, 1998). CFD is a finite volume method that solves the discretised form of the governing Navier-Stokes equations in order to produce solution fields describing the fluid motion, heat transfer and/or chemical reactions in a particular domain.

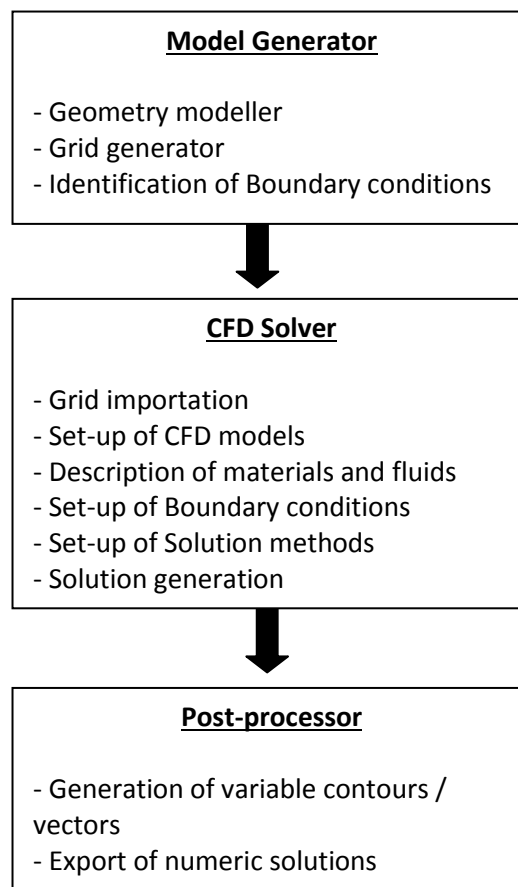


Fig. 4.1. Schematic of CFD solution process

The general set-up for a CFD simulation consists of a model generator, a CFD solver and a post-processor, schematically represented in Fig 4.1. In this study, ANSYS FLUENT® is used as the CFD solver. The aims of using CFD are to obtain a localised solution of the variables (pressure, temperature, density and velocities) and to obtain an adequate visualisation of the variable fields in the solution domain, otherwise not possible in zonal models. The potential of CFD extends into many disciplines, and has been employed in research studies, ranging from oxygen generation (Matsui *et al*, 2004), thermal comfort in buildings (Tye-Gingras and Gosselin, 2012) and atmospheric simulations (Gousseau *et al*, 2011).

The level of precision possible from CFD varies depending on the level of grid and model refinement, whereby increasing the level of details increases the computing costs. For instance, the number of grid cells required to calculate the smallest eddies in a turbulent flow with Re in the order of 10^4 , would be of the order of 10^8 cells and would require a supercomputer (Stribling, 2000). Generally, for engineering problems, it is more important to obtain a solution where the general numerical solution accuracy is within the real-life uncertainties of the adequate sensors (Gowreesunker *et al*, 2013a), as opposed to having a solution with very small-scale details. This allows for a quicker and more efficient use of the CFD tool for engineering purposes.

4.1.1 Governing Equations

The main variables involved in the governing equations are pressure (P), temperature (T), density (ρ) and velocities (u, v, w), and therefore six equations are required to describe a particular flow problem. These equations are known as the Navier-Stokes set of equations (Eqs. 4.1-4.3) and the equation of state (Eq. 4.4). The Navier-Stokes equations are non-linear, coupled and partial differential equations which represent the physical laws governing the motion of fluids. They are difficult to solve using conventional mathematical methods, and are therefore discretised, linearised, and solved in a CFD solver through iterative methods. Convergence of a solution is obtained after the residuals between successive iterations are within the limits defined in the solver.

Momentum equation:

$$\frac{\partial}{\partial t}(\rho u_j) + \frac{\partial}{\partial x_j}(\rho u_i u_j) = -\frac{\partial P}{\partial x_j} + \frac{\partial}{\partial x_i} \left[\mu \left(\frac{\partial u_j}{\partial x_i} \right) \right] + \rho g_j \quad (4.1)$$

Continuity equation:

$$\frac{\partial \rho}{\partial t} + \frac{\partial}{\partial x_j}(\rho u_j) = S_m \quad (4.2)$$

Energy equation:

$$\frac{\partial}{\partial t}(\rho c_p T) + \frac{\partial}{\partial x_j}(\rho c_p u_j T) = \frac{\partial}{\partial x_j} \left(\lambda \frac{\partial T}{\partial x_j} \right) + S_E \quad (4.3)$$

Equation of state:

$$\rho = \frac{P}{RT} \quad (4.4)$$

Discretisation refers to the process of breaking down the terms of the governing equations into simpler discrete algebraic forms. It can also refer to the breaking down of the flow domain into separate control volumes, i.e. meshes, as shown in Fig. 4.2, which allows the production of localised solution fields for a particular domain.

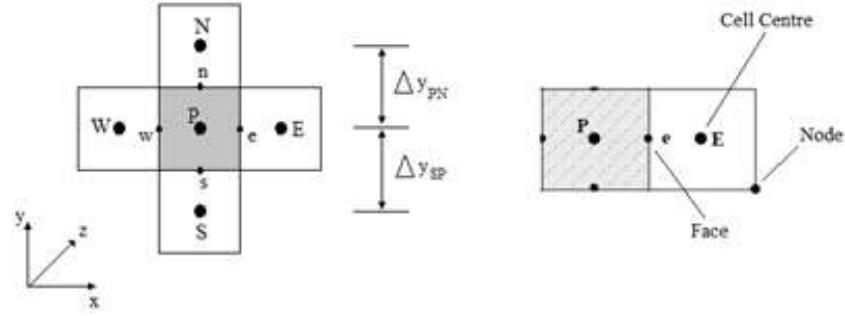


Fig. 4.2. Grid discretisation schematic

In Fig. 4.2, the cell centre values are noted by block letters (P, E, N, W, S), while the face values are denoted by the small-case letters (e, n, w, s). The approximate form of the governing equations is applied to each control volume and the face values are required to obtain a solution.

The following shows a simple example of the discretisation for the diffusion term in the governing energy equation (Eq. 4.3) with respect to the y-direction for the control volume in Fig 4.2 (Beausoleil-Morrison, 2000).

$$\int_{\Delta V} \frac{\partial}{\partial y} \left(\lambda \frac{\partial T}{\partial y} \right) dV = \int_x \int_y \int_z \frac{\partial}{\partial y} \left(\lambda \frac{\partial T}{\partial y} \right) dx dy dz \quad (4.5)$$

$$= [dx dz] \left[\left(\lambda \frac{\partial T}{\partial y} \right)_n - \left(\lambda \frac{\partial T}{\partial y} \right)_s \right]$$

Eq. (4.3) is given in terms of the face values. However, CFD stores cell-centre values as opposed to face values. Thus, in order to appropriately use the governing equations, the face values have to be computed from the cell centre values (ANSYS FLUENT theory guide, 2010). This is accomplished by a linearisation process, which simplifies the governing equation terms into linear algebraic terms through various gradient computation schemes. For instance, the least-square cell based gradient assumes a linear variation of the surrounding cell variables with respect to the control volume (P), as shown by Eq. (4.6).

$$\left(\lambda \frac{\partial T}{\partial y} \right)_n \approx \left(\frac{\lambda_n}{\Delta y_{PN}} \right) \cdot (T_N - T_P) \quad (4.6a)$$

$$\left(\lambda \frac{\partial T}{\partial y}\right)_s \approx \left(\frac{\lambda_s}{\Delta y_{SP}}\right) \cdot (T_P - T_S) \quad (4.6b)$$

Applying the results from Eq. (4.6) to Eq. (4.5), we obtain the following Eq. (4.7):

$$\begin{aligned} \int_{\Delta V} \frac{\partial}{\partial y} \left(\lambda \frac{\partial T}{\partial y} \right) dV &\approx [dx dz] \left[\left\{ \left(\frac{\lambda_n}{\Delta y_{PN}} \right) \cdot (T_N - T_P) \right\} - \left\{ \left(\frac{\lambda_s}{\Delta y_{SP}} \right) \cdot (T_P - T_S) \right\} \right] \\ &= a_N T_N + a_S T_S - a_P T_P \end{aligned} \quad (4.7)$$

The general form of the discretised equation is given as Eq. (4.8) (Fluent theory guide, 2010):

$$a_P \phi_P = \sum_{nc} a_{nc} \phi_{nc} + b \quad (4.8)$$

Where ‘ nc ’ represents the neighbouring cell, ‘ a ’ are linearised coefficients and ‘ ϕ ’ is the scalar quantity at the cell centre. The processes of discretisation and linearisation can both be commonly referred to as ‘discretisation’, and will henceforth be implied in this manner for this study. Thus, this discretised form of the governing equations is employed in the CFD solver to generate solution fields for a specified problem.

4.1.2 Turbulence Modelling

Air-flows inside built environments consist of different flow regimes ranging from low-Reynolds flows (wall boundary layers) to more turbulent flows (near HVAC inlets/outlets) (Heiselberg *et al*, 1998). The adequate modelling of turbulence is therefore one of the most important aspects in appropriately defining the velocities and stresses involved in the flow, and thus the actual building air movement itself. Turbulence is a complex phenomenon, referring to small scale random variations in fluid motion, for which the direct simulation is not possible under the current level of technology (ANSYS FLUENT theory guide, 2010). Its modelling is instead conducted with the Reynolds-Averaged Navier-Stokes (RANS) or the Large Eddy Simulation (LES) methods, through a filter which limits the size of turbulence in the flow domain. In the case of LES, eddies larger than the size of the filter are explicitly resolved to improve accuracy, at the expense of large computational costs. The RANS models separate the solution variables into mean (time-averaged) and fluctuating components as shown in Fig. 4.3 and Eq. (4.9). Both the RANS and LES models introduce additional unknowns in the approximate form of the governing equations, which must be solved to close the overall system of equations (Fluent theory guide, 2010).

The following sections focus on the RANS turbulence models, which are more commonly employed because of the relatively lower computational effort required.

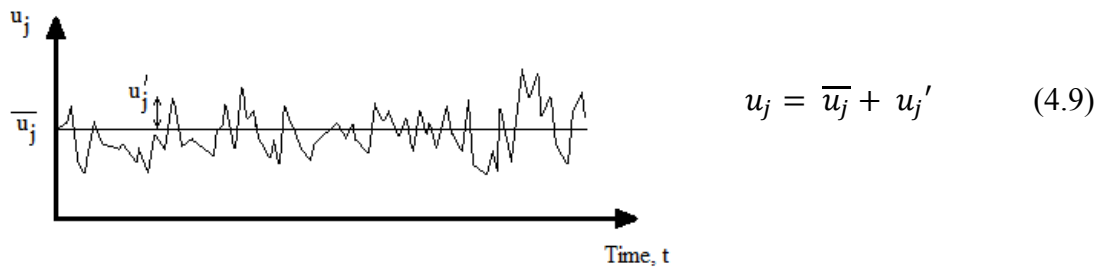


Fig 4.3. Velocity fluctuations

The velocities at a point in time and space are defined by u_j , with a time-averaged value of \bar{u}_j and fluctuation of u_j' , as defined by Eq. (4.9). This averaging process introduces some new unknowns – known as the Reynolds stresses – into the governing equations (ANSYS FLUENT theory guide, 2010) – Reynolds Stresses: $-\rho \overline{u_i' u_j'}$.

These stresses represent the rate at which momentum is transported or diffused by turbulent fluctuations, and they have to be solved in order to satisfy ‘closure’ of the system of equations. The Reynolds stresses can be evaluated by two methods: the Eddy viscosity models or the Reynolds Stress Models (RSM). The Eddy-viscosity models relate the Reynolds stresses to the mean velocity gradient and produce a relatively low computationally expensive process. Examples of the Eddy-viscosity models are the Spalart-Allmaras model, the $k-\varepsilon$ models and the $k-\omega$ models. The alternative Reynolds Stress Model aims at solving the differential transport equations for each term in the Reynolds stresses, considerably increasing the solution complexity and computational time (ANSYS FLUENT theory guide, 2010).

Various studies have employed CFD to simulate the air-flows in built environments, and because of the different flow regimes encountered in buildings, the choice of a turbulence model is crucial, as elaborated by the following studies. Zhang *et al.* (2007) evaluated eight turbulence models, including the Re-Normalisation Group (RNG) $k-\varepsilon$, the low-Reynolds number $k-\varepsilon$ and the Shear-Stress Transport (SST) $k-\omega$ models, in the prediction of air-flow, temperature and turbulence in four indoor geometries, under forced, natural and mixed forced/natural convection. They found that in general, LES provides the most detailed flow features, but considerably increases the computational time relative to the RANS models. Among the RANS models, the V^2-f and the RNG $k-\varepsilon$ models have the best accuracy, computing effort and robustness. The authors stress that each airflow category favours a particular turbulence model, but recommend the V^2-f and the RNG $k-\varepsilon$ models for indoor airflow simulations.

Gebremedhin and Wu (2003) studied the airflow characteristics of a ventilated cattle facility to evaluate the thermal interaction between the cattle and the indoor environment. The standard $k-\varepsilon$ model, the RNG $k-\varepsilon$ model, the Low-Reynolds number $k-\varepsilon$ model, the $k-\omega$ model and the Reynolds stress model (RSM) were employed in the CFD simulations. The authors concluded that the RNG $k-\varepsilon$ model provided the most accurate, stable and computationally efficient solution.

Rohdin and Moshfegh (2007) compared the standard $k-\varepsilon$, RNG $k-\varepsilon$ and realizable $k-\varepsilon$ models for the temperature and air-flow simulation in a mechanically ventilated large and complex industrial facility. The comparison was relative to field measurements. They found that the RNG $k-\varepsilon$ turbulence model produced the lowest validation errors in

the simulation, with deviations of 0.04 m/s and 0.3 °C from the experimental results, at the expense of slightly higher computational time than the other models.

Hara and Kato (2004) validated a CFD simulation for the movement of smoke in a fire using the standard k- ϵ model. Deviations of 5% were obtained for both the velocity and temperature fields in the simulations, with respect to experimental correlations. They showed that modifying the buoyancy production term of the turbulence dissipation (ϵ) equation does not significantly affect the results, but an appropriate grid near the heat source is crucial for the accurate representation of the thermal plume.

Leenknecht *et al.* (2012) conducted a sensitivity analysis for the convective heat exchange between the room air and the envelope thermal mass. The standard, realizable and RNG k- ϵ models, and the standard and SST k- ω models were studied in their analysis. The authors showed that similar results are obtained for the standard and RNG k- ϵ models, as well as the standard and SST k- ω models, respectively. The RNG k- ϵ model was adopted for the final model, based on the results of their literature survey.

Hussain *et al.* (2012) investigated six RANS models, including the one-equation model (Spallart–Allamaras), together with the Discrete Transfer Radiation Model (DTRM) in the natural and forced ventilation simulation of atria. In comparison with experimental results, they concluded that the two equation models (the standard k- ϵ , RNG k- ϵ , realizable k- ϵ , standard k- ω and SST k- ω models) provided better results compared to the one-equation model, and that SST k- ω model showed relatively better prediction than the other models.

Awbi (1998) investigated the natural convection heat transfer coefficients for walls, ceiling and floor of a building space, using the standard k- ϵ model with logarithmic wall function and the low-Reynolds number k- ϵ model. The author found that the standard k- ϵ model does not generally predict accurate heat transfer, whilst the low-Reynolds number k- ϵ model performs much better. The low-Reynolds turbulence model however requires fine grid points which increases computational time. The author suggests finding the convective heat transfer coefficients from empirical equations, and applying them directly to the simulation, instead of calculating them for every iteration.

Kuznik *et al.* (2007) conducted a steady-state validation study of a mechanically ventilated test cell, using the realizable k- ϵ , RNG k- ϵ , standard k- ω and SST k- ω

turbulence models. They found that only the realizable k- ϵ and the k- ω models provided appropriate numerical results, of which the k- ω model was in better agreement with the experimental temperature progression. Furthermore, the realizable k- ϵ and the k- ω models also appropriately predicted the jet expansion rate of the inlet fan, whilst none of the models properly predicted the jet profiles.

Tanasic *et al.* (2011) investigated the airflow in a mechanically ventilated large industrial hall, including buoyancy, using the standard k- ϵ model for turbulence. They concluded that the model did not provide adequate quantitative results as the simulation values differed significantly from the measured values.

Suarez *et al.* (2011) investigated the forced/buoyant airflow in a glazed gallery using the RNG k- ϵ , standard k- ϵ and the k- ω models. They concluded that there were no major air-flow differences between the models, and on the basis of stability and simulation time, the RNG k- ϵ model was employed in their final simulations.

Gowreesunker and Tassou (2013a) investigated the performance of PCM boards in a test cell using the RNG k- ϵ model. The model's air and surface temperatures were compared to experimental data, and were found to have a mean error of 1.0 °C for a total of 23 thermocouples. Local absolute errors in the air temperature values varied between 0.6-1.5 °C, including the uncertainty in the thermocouples. The models were considered to be accurate enough based on the relative errors obtained in the study.

Zhai *et al.* (2007) studied turbulence models for enclosed indoor environments. They identified that each turbulence model has its advantages and limitations under different situations, and that no universal turbulence model exists for indoor airflow simulations.

This literature survey shows that the most popular and accurate RANS models are the RNG k- ϵ and the SST k- ω turbulence models, although each model may provide relatively different results in some cases. Generally, the RNG k- ϵ turbulence model was found to be equally valid for both low and strong turbulence flows, due to various improvements from the standard model, resulting in a better modelling of separating and near-wall flows (Leenknecht et al, 2012). Thus, even though there is not a universal turbulence model, there is a general consensus from the literature that the RNG k- ϵ model produces adequate flow fields for simulations involving buoyant, forced or forced/buoyant flows in buildings, under reasonable simulation times (Gowreesunker and Tassou, 2013a; Chen, 1995; Zhang *et al*, 2007).

4.1.3 Renormalisation Group (RNG) k-ε Turbulence Model

This section describes the RNG k-ε turbulence model which is employed in this study. Following the Boussinesq approach for the k-ε turbulence models, two additional sets of equations are to be solved: one for the turbulent kinetic energy (k); and one for the dissipation rate of kinetic energy (ε) (Launder and Spalding, 1972), which are then used to obtain the turbulent/eddy viscosity (μ_t) of the flow, as shown by Eq. (4.10).

$$\frac{\partial}{\partial t}(\rho k) + \frac{\partial}{\partial x_j}(\rho u_j k) = \frac{\partial}{\partial x_j} \left(\left(\mu + \frac{\mu_t}{\sigma_k} \right) \frac{\partial k}{\partial x_j} \right) + G_k + G_b - \rho \varepsilon \quad (4.10a)$$

$$\frac{\partial}{\partial t}(\rho \varepsilon) + \frac{\partial}{\partial x_j}(\rho u_j \varepsilon) = \frac{\partial}{\partial x_j} \left(\left(\mu + \frac{\mu_t}{\sigma_\varepsilon} \right) \frac{\partial \varepsilon}{\partial x_j} \right) + C_{1\varepsilon} \frac{\varepsilon}{k} (G_k + C_{3\varepsilon} G_b) - C_{2\varepsilon} \rho \frac{\varepsilon^2}{k} \quad (4.10b)$$

$$\mu_t = \rho C_\mu \frac{k^2}{\varepsilon} \quad (4.10c)$$

The coefficients $C_{1\varepsilon}$, $C_{2\varepsilon}$, $C_{3\varepsilon}$ and C_μ are empirical constants; σ_k and σ_ε are the inverse effective Prandtl numbers for the turbulent kinetic energy and dissipation rate, respectively; G_b is the turbulent kinetic energy generation due to buoyancy; G_k is the kinetic energy generation due to the mean velocity gradients; and μ_t is the eddy viscosity. The default values for the coefficients are 1.42, 1.68, 0.0, 0.0845, 0.7178 and 0.7178 for $C_{1\varepsilon}$, $C_{2\varepsilon}$, $C_{3\varepsilon}$, C_μ , σ_k and σ_ε , respectively (Rohdin and Moshfegh, 2007).

The RNG k-ε turbulence model has been developed following a statistical study known as the renormalisation group theory. It filters out small scale turbulence to a degree that the remaining scales can be resolved (Rohdin and Moshfegh, 2007). The turbulence dissipation rate (ε) equation is modified as shown by Eq. (4.11a) and R_ε is defined by Eq. (4.11b).

$$\frac{\partial}{\partial t}(\rho \varepsilon) + \frac{\partial}{\partial x_j}(\rho u_j \varepsilon) = \frac{\partial}{\partial x_j} \left(\left(\mu + \frac{\mu_t}{\sigma_\varepsilon} \right) \frac{\partial \varepsilon}{\partial x_j} \right) + C_{1\varepsilon} \frac{\varepsilon}{k} (G_k + C_{3\varepsilon} G_b) - C_{2\varepsilon} \rho \frac{\varepsilon^2}{k} - R_\varepsilon \quad (4.11a)$$

$$R_\varepsilon = \frac{C_\mu \rho \eta^3 (1 - \frac{\eta}{\eta_0})}{1 + \beta_0 \eta^3} \frac{\varepsilon^2}{k} \quad (4.11b)$$

The values of the additional constants in Eq. (4.11) are 0.012 and 4.38 for β_0 and η_0 , respectively. The RNG k- ε model enhances the standard model, through the use of an analytically derived function to calculate the effective turbulent viscosity, separating low Re-number flows from high Re-number flows. This allows a more accurate representation of turbulence for different types of flows, instead of assuming high Re-number flows for all types flows, as in the case of the standard model (ANSYS FLUENT theory guide, 2010).

4.1.4 Near-Wall Treatment

Wall functions are empirical relationships that are used to simplify the prediction of flows within the boundary layer at the near wall grid cells. Instead of attempting to resolve the different flow regimes within the boundary layer through the use of many grid cells, wall functions allow a relaxation of the grid size near the wall by permitting the near wall grid points to be relatively further from the wall.

The standard wall functions simplify the near wall flows into two distinct regions: laminar dominated flow and the log-law region, requiring different empirical relationships. These two regions are separated based on the dimensionless distance from the wall (y^+).

$$y^+ = \frac{\rho u_\tau y}{\mu} \quad (4.12)$$

$$\text{Where: } u_\tau = \sqrt{\frac{\tau_w}{\rho}} \quad (4.13)$$

By appropriately placing grid points in the respective regions of the boundary layers, the near-wall model employ different methods to obtain an equilibrium solution. For cases where ($y^+ > 11.225$), the standard wall model employs the logarithmic law:

$$\frac{u}{u_\tau} = \frac{1}{\kappa} \ln(Ey^+) \quad (4.14)$$

For cases where ($y^+ < 11.225$), the following laminar stress-strain relationship is employed:

$$\frac{u}{u_\tau} = y^+ \quad (4.15)$$

κ is the Von Kármán constant (0.4187), E is an empirical constant (9.793), u is the mean fluid velocity, τ_w is the wall shear stress and u_τ is the friction velocity. Although, the standard model represents an ideal approach to modelling the near-wall phenomena, it has been found to work well with various wall-bounded flows (ANSYS FLUENT User guide, 2010) and in some building simulations (Blocken and Carmeliet, 2007). Nonetheless, FLUENT also offers various other near-wall treatments, including the enhanced-wall treatment which is more suited to different flow regimes, as explained in the ANSYS FLUENT theory and user guides (2010).

4.2 Modelling of Indoor Environment and PCM boards

In this study, in order to further validate the use of CFD in the simulation of indoor thermal environments, its effectiveness was extended to the simulation of PCM boards within the built environment. Hence, the next section depicts the experimental validation and usefulness of CFD when employed in the performance evaluation of PCM boards applied to a test-cell's walls.

PCM boards are becoming a popular passive method for controlling the indoor temperature, as confirmed by the number of commercial products available on the market. They are being currently marketed as an energy-efficient alternative to gypsum plasterboards, with the PCM preventing overheating and reducing the temperature swings in thermally lightweight buildings. Conventionally, commercial simulation tools such as ESP-r (Heim and Clarke, 2003) and TRNSYS (Bony and Citherlet, 2007), amongst others, possess phase change modelling capabilities. However, in addition to not allowing for detailed air-flow analyses, the percentage of PCM being used cannot be determined with these default multi-zonal models. Thus, in order to appropriately evaluate the performance of PCM boards and the indoor environment air-flow, both aspects should be simultaneously simulated in a CFD environment. The validation of such simulations has not been previously reported in the literature.

To accomplish this validation study, the test cell shown in Fig. 4.4 was constructed with internal dimensions of $1.3 \times 0.8 \times 1.4$ m and a glazed area of 1.3×0.8 m. This test cell was then placed inside an environmental chamber where the air temperature was controlled. In essence, the test cell represents a built environment whilst the environmental chamber provides the ambient conditions. The material configuration of the walls provided an overall U-value of $0.21 \text{ W/m}^2\text{K}$, a decrement factor of 0.81 and a time lag of 4.8h, which is similar to a timber frame wall with plasterboard (CIBSE A, 2006). The glazing U-value is $1.2 \text{ W/m}^2\text{K}$.

(Refer to Appendix B for more construction and experimental details)

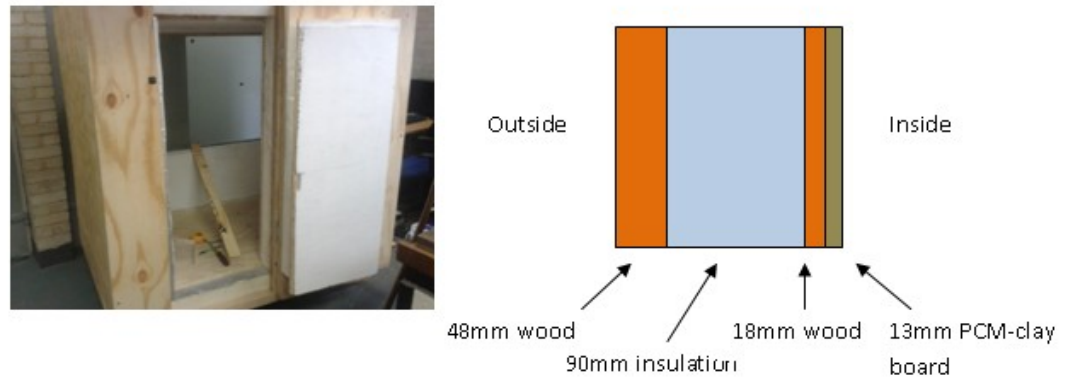


Fig. 4.4a. Experimental test cell and wall construction

Twenty three type-T thermocouples were uniformly distributed inside the test cell and on the walls (see Fig B1.2). The air sensors were placed 5cm from the wall and the surface sensors were covered with a thin layer of plaster. The test cell was assumed to be intermittently occupied and a 200×100 mm, 100 W mica plate heater was employed to produce the internal heat gains during the day-time occupied hours. During night-time, the heater was turned off.

Day-time was defined as the hours where the external ambient temperature increases, and vice-versa for night-time, as shown in Fig. 4.5. Two sets of experiments were performed: a non-ventilated case where the inlet and outlet were closed during night-time; and a ventilated case, where external air was blown into the test cell during night-time at a rate of 0.045 kg/s via the 100 mm diameter inlet shown in Fig. B1.2. The air velocity was measured with a TSI hot-wire velocity meter with an accuracy of ± 0.015 m/s. The two different ventilation scenarios were investigated in order to show the importance of night charging on the performance of the PCM boards. Before each experiment was started, it was ensured that all temperatures in the test-cell were at the same steady value, for the valid initialisation of the CFD models. Each experiment recorded the temperatures at locations shown in Fig. 4.4b, at intervals of 30 s for 24 h using Pico data loggers.

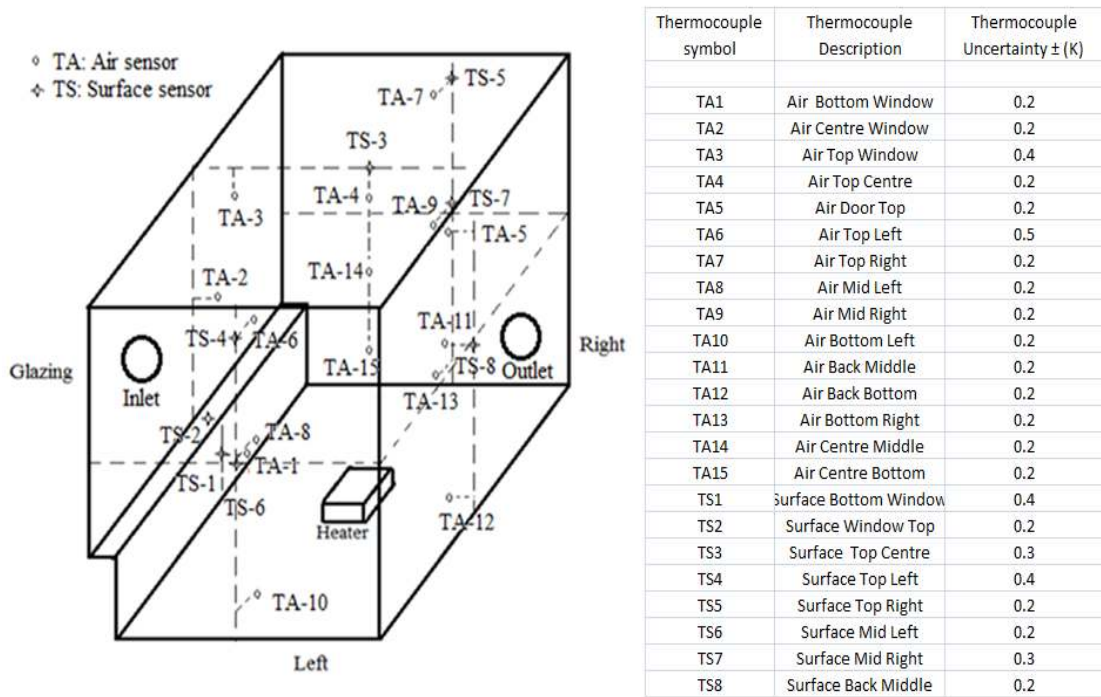


Fig. 4.4b. Locations of temperature sensors in experimental test cell

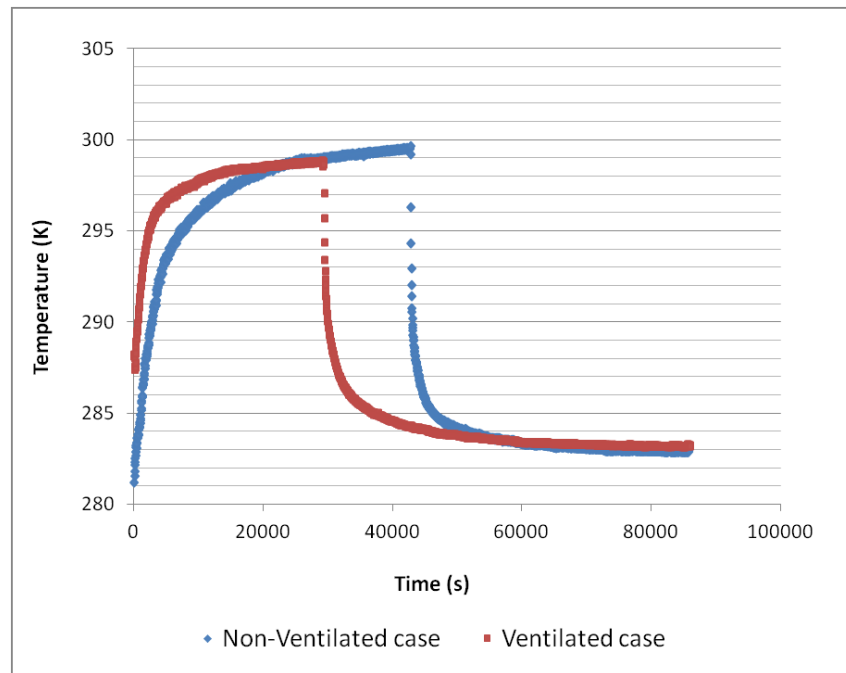


Fig. 4.5. Environmental chamber/ External air temperature

The PCM board investigated in this study is a commercial 13 mm clay board impregnated with 21% (by volume) Micronal® PCM. These EBB™ PCM clay boards are manufactured by mixing the PCM microcapsules and clay, before being compacted and embedded in a polythene matrix. As a result, this does not always result in a uniform distribution of the PCM granules in the board. Three random sample locations were therefore chosen from the boards to conduct the DSC characterisation analysis, shown in Table 4.1.

Table 4.1. PCM DSC enthalpy, onset and end temperatures for different PCM-Clay board samples and heating/cooling rates

Heating / cooling Rate	Melting			Freezing		
	Onset Temperature (K)	End Temperature (K)	Enthalpy (kJ/kg)	Onset Temperature (K)	End Temperature (K)	Enthalpy (kJ/kg)
1 st Sample (S-1)						
0.5 K/min	285.4	295.5	14.7	295.4	284.4	17.0
1 K/min	285.3	295.5	14.8	295.3	284.2	17.1
2 K/min	284.9	296.0	15.6	294.8	283.8	17.7
2 nd Sample (S-2)						
0.5 K/min	284.9	296.1	16.3	294.9	284.9	17.9
1 K/min	284.8	295.9	16.3	294.9	284.8	18.0
2 K/min	284.1	296.4	17.0	293.8	283.8	18.8
3 rd Sample (S-3)						
0.5 K/min	285.2	295.8	15.6	295.2	284.7	17.4
1 K/min	285.1	295.9	15.7	295.1	284.6	17.5
2 K/min	284.5	296.3	16.1	294.6	283.8	18.5
Enthalpy Porosity Model						
-	284.9	295.5	16.5	295.5	284.9	16.5

Table 4.1 shows that as the heating/cooling rates of each sample are lowered, the melting/freezing enthalpy and phase change temperatures tend towards a constant value. The lowest investigated heating/cooling rate of 0.5 K/min provides values which are within the uncertainty of ± 0.1 K and $\pm 2\%$ of the enthalpy change for the DSC, and are therefore considered for further analysis. Between the 3 samples at 0.5 K/min, a mean melting enthalpy of 15.6 kJ/kg and mean freezing enthalpy of 17.4 kJ/kg are obtained, with a deviation of ± 0.9 kJ/kg between samples. A mean melting onset temperature of

285.2 K, and end temperature of 295.8 K are obtained, while a mean freezing onset temperature of 295.2 K and end temperature of 284.7 K are obtained. The deviation in temperature between the 3 samples is ± 0.6 K. The enthalpy–porosity model is defined as the average values of the onset and end temperatures, and enthalpy of all the samples at 0.5 K/min for both freezing and melting.

4.3 Validity of CFD

The validation study was conducted in ANSYS FLUENT® where all the domains of the test-cell were modelled. The final mesh was obtained following an L_2 norm study to test for the spatial and temporal convergence of the model (see Appendix B), and is shown in Fig. 4.6. The external surfaces of the test-cell are bounded by convective heat transfer conditions, which were determined by a separate CFD investigation, modelling the external surface of the test-cell and the environmental chamber. This resulted in values of $5.3 \text{ W/m}^2 \text{ K}$ for the bottom and right surfaces, $2.8 \text{ W/m}^2 \text{ K}$ for the glazing, left and top surfaces, and $2.4 \text{ W/m}^2 \text{ K}$ for the back surface, with reference to Fig. B1.2. A heat generation rate of $500,000 \text{ W/m}^3$ is applied to model the 10 mm thick plate heater. The mass-flow inlet and pressure outlet are closed during the day-time heating period. The RNG $k\text{--}\epsilon$ turbulence model, with non-slip enhanced wall functions were used and air was considered as an ideal gas. The body-force weighted discretisation scheme was employed for pressure, and the second order upwind scheme was used for momentum, density and energy. The SIMPLE algorithm was used for the pressure–velocity coupling.

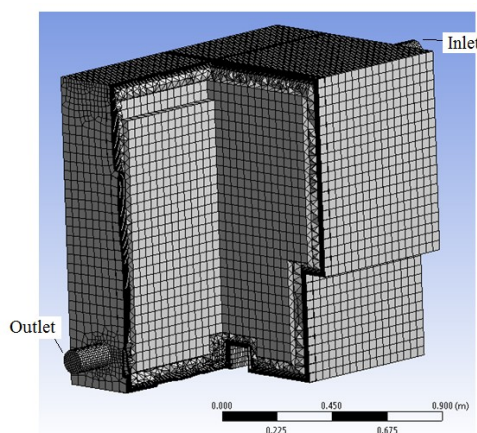


Fig. 4.6(a). Mesh in main air-domain

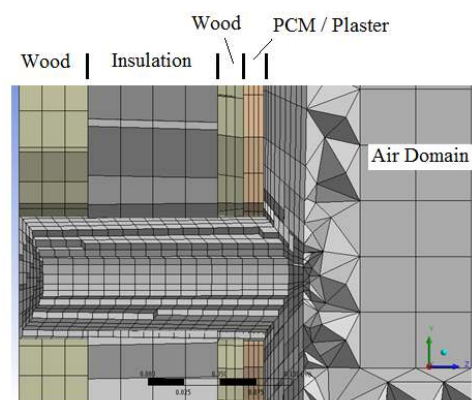


Fig. 4.6(b). Mesh distribution in walls and air boundary layer

The mesh was designed using the in-built ANSYS design modeller meshing algorithm, and the resulting mesh comprised of hexahedral cells in the near-wall inflated layers and wall domains, with tetrahedral and hexahedral cells in the air domain. Eight inflation layers were used near the walls, with a first grid size of 2 mm and growth ratio of 1.3. The mesh size increases towards the bulk of the air domain to 40 mm. The wall-solid domains contain 3–4 mesh intervals along the thickness, with a face cell size of 20–50 mm. The inlet and outlet domains contain four inflation layers with a first grid size of 1.5 mm, growth ratio of 1.2 and an average of 10 mm cells in the main fluid flow. The mesh at the heater has a face size of 10 mm and 8 inflation layers with a first grid size of 1.5 mm and growth ratio of 1.1. The enhanced phase change model described in chapter 3 is employed to simulate the boards (the equations for the S-3 enthalpy-temperature curves are given by Eq. (B1.2) and Eq. (B1.3) in Appendix B).

The validation errors from the simulations are shown in Fig. 4.7 and Fig. 4.8. The validity of the models was based on the relative RMS errors of each model with respect to the experimental data. (Refer to Appendix B for details of the error calculations)

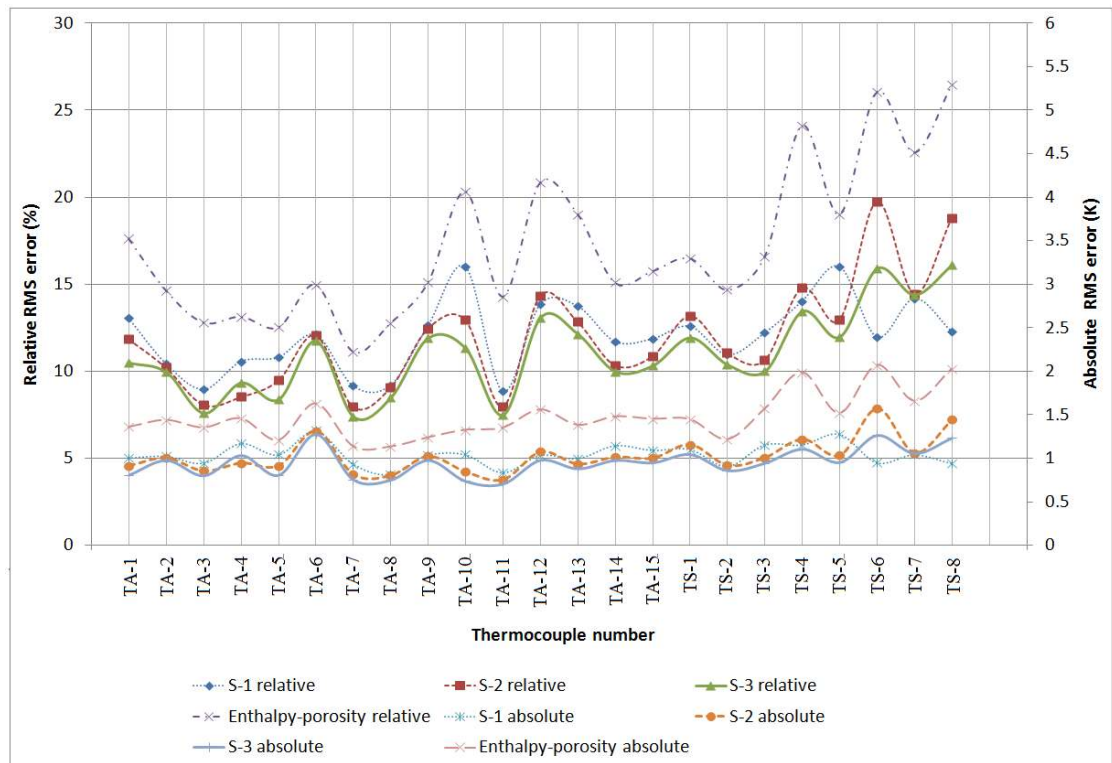


Fig. 4.7. Local error analysis for non-ventilated scenario

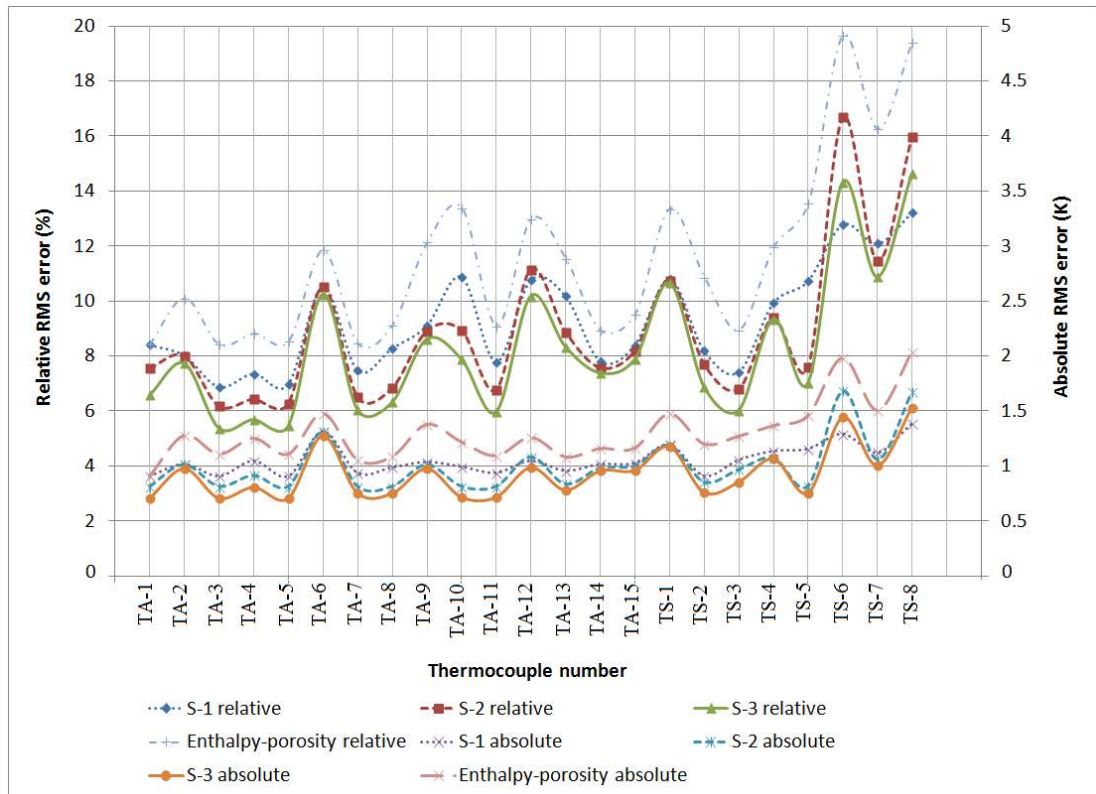


Fig. 4.8. Local error analysis for ventilated scenario

In the non-ventilated case (see Fig 4.7), the absolute errors vary between 0.7-1.5 K and 0.8-2.1 K, corresponding to relative errors of 7.3-20.8% and 8.5-27 %, for the air and surface temperatures, respectively. The higher errors for surface temperatures can be attributed to the uneven distribution of PCM in the boards. Overall mean errors of 11.92% (1.07 K), 11.73% (1.02 K) and 10.8% (0.96 K) are obtained for sample-1 (S-1), sample-2 (S-2) and sample-3 (S-3), respectively. It can also be seen from Fig. 4.7 that the enthalpy-porosity model produces higher errors of 11-27% with a mean of 18.5% (1.5 K), than the UDF models that incorporates the hysteresis and non-linearity effects in the PCM simulation.

For the ventilated case (see Fig 4.8), the local absolute error varies between 0.7-1.5 K and 0.8-2.0 K, corresponding to relative errors of 5.4-13.4% and 6.0-19.6 % for the air and surface temperatures, respectively. Similarly in this case, the higher surface errors can be attributed to the uneven distribution of PCM in the boards. The overall mean errors are found to be 9.25% (1.03 K), 8.8% (0.97 K) and 8.06% (0.91 K) for S-1, S-2 and S-3, respectively, while the mean error for the enthalpy porosity model is again higher, at 12.5% (1.3 K), than the curved-fit models. As the relative errors in both scenarios are lower than 30%, using a similar justification as proposed in the works of

Zhang *et al.* (2007), the validation of the CFD modelling study is considered acceptable (Gowreesunker and Tassou, 2013a).

It is interesting to note that the choice of PCM sample does not impact heavily the overall errors when the UDF models are used. However, a mean improvement of 0.5 K is obtained with the implementation of the S-3 model relative to the enthalpy–porosity model. Depending on the type of building, with different comfort temperature ranges, the importance of appropriately simulating phase change will become higher as the building temperature range becomes smaller. These errors should therefore be carefully considered when applying CFD to the thermal evaluation of built environments with PCM. In this validation study, the main errors can be attributed to: the uncertainty in the thermocouples (see Fig. B1.2); the uncertainty in the curve-fits for the external air temperature, PCM enthalpy and temperature data (see Table B1.3); the non-uniformity in PCM distribution; the uncertainty in the ventilation flow rate; and the non-consideration of radiation.

4.4 Effectiveness of CFD

As mentioned previously, passive PCM systems rely on cool night ventilation for adequate charging. This section describes the effectiveness of CFD to predict the performance of PCM boards for the more popular ventilated case, in terms of: the impact of the PCM boards in the test-cell, the heat transfer rates with different night ventilation rates, and the effective use of PCM boards. The results are for the PCM sample S-3 which produced the lowest errors in the validation study.

4.4.1 Impact of PCM boards

The test cell was closed during the heating period, and thus buoyancy due to the heater is the dominant force in the indoor air flow, as shown in the temperature contours of Fig 4.9. The experimental study from Hunt *et al.* (2001) suggests that an aspect ratio (height/width) <1 causes stable stratification, as the propensity for turbulent mixing and overturning at the top of the air domain is lower. In this study, the aspect ratios of the test cell were 1.08 and 1.75. The qualitative results from Fig. 4.9 therefore abide by the empirical observations made by Hunt *et al.* (2001), as although the aspect ratios of the cell are slightly higher than 1, they are not high enough to completely destroy stratification. Thus, both stratification and a slight overturning near the walls are observed in this simulation.

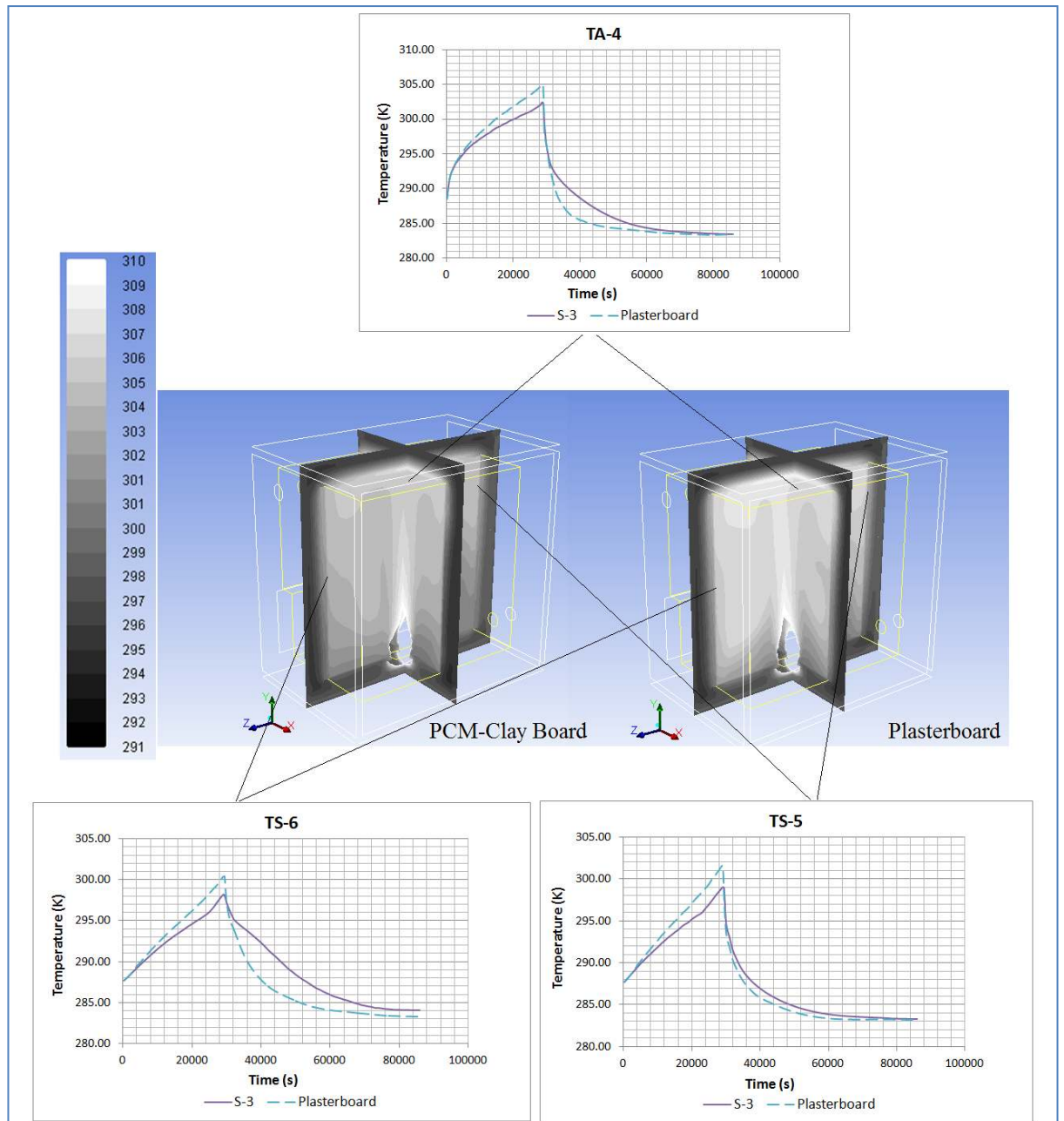


Fig. 4.9. Comparison of Temperature evolutions at 3 points in the test cell, and Temperature contours (K) at the end of the heating period with PCM-Clay board and Plasterboard on the walls

It can also be observed from Fig 4.9 that a reduction of 3 K in the peak air temperature and a lower temperature swing are obtained with the addition of the PCM-Clay board, relative to plasterboard. Vertical temperature stratification in the air domain of the PCM cell is ~ 3 K/m compared to ~ 4 K/m in the plasterboard cell, and stratification in the PCM cell is more uniform compared to the plasterboard cell. A more uniform and less stratified environment in the occupied zone provides better thermal comfort (Chao and

Wan, 2004). Furthermore, the determination of the velocity, temperature and turbulence fields from the CFD results may improve the evaluation of local thermal comfort (ANSI/ASHRAE 55-2004), which is otherwise not available for zonal models.

4.4.2 Ventilation heat transfer rates

While conduction is the dominant heat transfer mechanism within the boards, convection occurs between the boards and the air domain (natural convection during the heating/occupied period and forced convection during the night ventilation period). Fig. 4.10 shows the area-weighted heat flux on the internal side of the test cell walls, which aims at determining the energy impact of PCM-clay boards and plasterboards during the day, and the effects of different ventilation rates on the PCM boards during night ventilation charging.

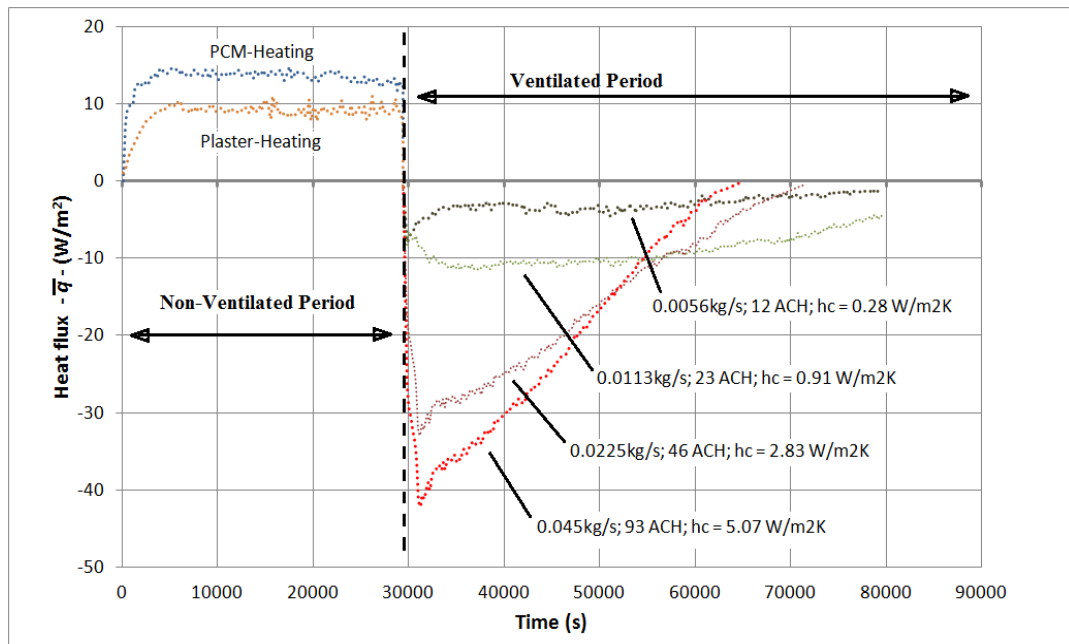


Fig. 4.10. Area-weighted wall heat flux with PCM and plaster boards, and with different night ventilation rates for PCM boards only (The calculation method for 'hc' is given in Appendix B)

Fig. 4.10 shows that in the heating phase, the heat flux to the PCM wall is higher than the plasterboard wall, due to the lower wall temperatures of the PCM board during phase change. The average increase in wall heat flux into the walls of 5W/m^2 with the

addition of the PCM-board signifies that the building envelope is providing an extra 5W/m^2 of cooling, compared to plasterboard. This corresponds to an extra cooling effect of 25W for this test cell, compared to plasterboards, with an internal heat gain of 100W and without air-conditioning systems. Fig. 4.10 also depicts the impact of night ventilation on the PCM boards. As the wall heat transfer coefficient, h_c , increases with increasing ventilation rates, the heat flux out of the walls also increases. This corresponds to a faster re-charge of the PCM boards, improving their efficiency. By employing heat transfer coefficients of 5.07 , 2.83 , 0.91 and $0.28\text{ W/m}^2\text{K}$, the PCM boards are fully recharged after 9 , 11 , 17 and 23 hrs, respectively (Note that the last two charging times have been linearly extrapolated).

In this study, as the externally blown air is just below the freezing end temperature of the PCM, $\bar{q} = 0$ can be used to justify full-recharge of the boards. In other cases, monitoring the liquid fraction may be more appropriate. The relatively low reduction in charging times as h_c increases from 2.83 to $5.07\text{ W/m}^2\text{K}$ is explained by the fact that as h_c increases, the low thermal diffusivity of the PCM board becomes more dominant and limits the heat transfer rates in the boards. In this case, a wall heat transfer coefficient greater than $2.83\text{ W/m}^2\text{K}$ (46 ACH) would be adequate, as it would completely recharge the PCM boards before the end of the simulation period.

4.4.3 Effective use of PCM boards

In order to extract the full potential of PCM boards, they have to be suitably placed within the building, and the liquid fraction is a useful parameter to quantify their effective use.

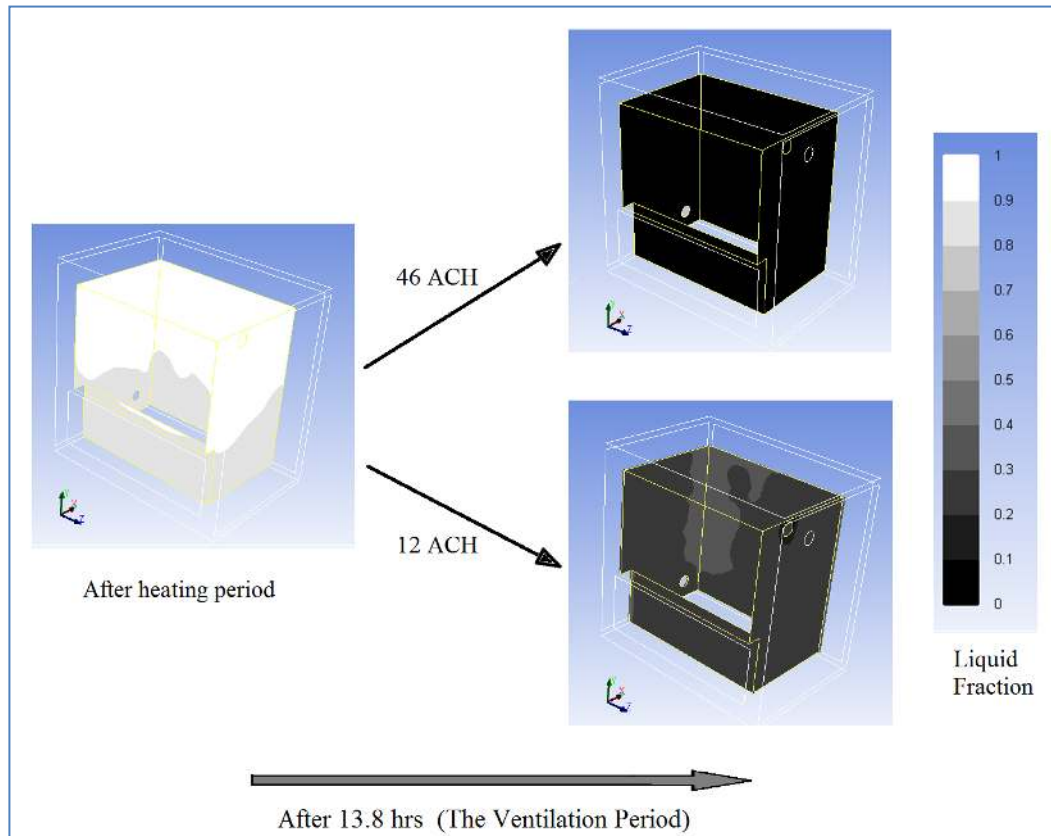


Fig. 4.11. Liquid fraction change for different ventilation rates

The qualitative observations from Fig. 4.11 infer that the top part of the test-cell undergoes full phase change after the heating period. The liquid fraction in the lower portion of the cell is 0.8-0.9, signifying that only 80-90% of the PCM has been used in the cooling process. This is due to temperature stratification in the space. In order to optimise the boards' performance, air mixing strategies can be considered for the space or the PCM could be concentrated at the top part of the wall and ceiling of the cell.

Fig. 4.11 also shows the re-charging effects of different ventilation rates at the end of the simulations. Using 46 ACH reduces the overall liquid fraction to 0, and hence completely recharges the PCM boards. Conversely, using 12ACH recharges the PCM to 30-50% for the same time period. For this latter ventilation rate, the wall temperatures

near the outlet are affected by the airflow, as shown by an area of higher liquid fraction in Fig. 4.11.

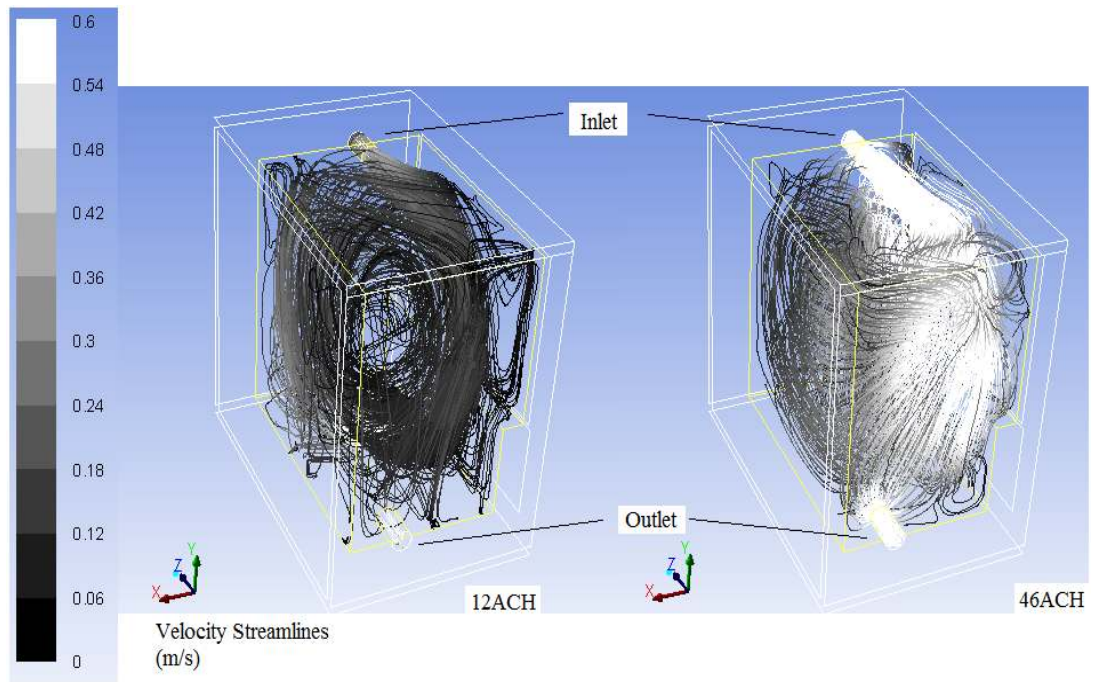


Fig. 4.12. Velocity streams for ventilation rates of 12 ACH and 46 ACH

Fig. 4.12 shows that the air movement at this area near the outlet is low at 12ACH compared to the mixing propensity of 46ACH, and hence the low heat transfer from the wall. The ventilation rate can therefore be increased or an air inlet with swirl diffusers can be used to generate mixing in the space at 12 ACH, and further reduce the liquid fraction in the recharging process.

4.5 Summary of Chapter 4

This chapter describes the use of CFD in the simulation of indoor environments and also validates the application of the enhanced conduction-dominant phase change model developed in chapter 3. The experimental tests used for the validation study were conducted in a test cell, placed inside an environmental chamber, where the ambient conditions of the test cell were controlled and monitored. In general, the results showed that:

- the PCM clay wall boards can provide up to 3 K reduction in the peak temperature of indoor spaces compared to conventional plasterboard, and can prevent overheating. The performance depends on the quantity of PCM used, the characteristics of the building fabric and the internal and external heat gains.
- the performance of the CFD simulations depends to a certain extent on the approach used for the simulation of the PCM in the board. Using the enhanced phase change model improves the simulation accuracy compared to the standard enthalpy–porosity by a mean 0.5 K.
- the average absolute error in the simulations compared to the experimental results was found to be 1.0 K, including the uncertainties of the thermocouples. These errors are acceptable judged by other studies and uncertainties in the measurements.
- the qualitative results show that the temperature stratification effects can be adequately predicted with CFD models and together with the liquid fraction term, can enable more efficient building design using PCM boards for both natural and forced convection scenarios.
- due to the extensive simulation times required, CFD can mainly be used as a design tool to determine areas of concern and to investigate improvements in the design with PCM boards over a short period of time. A number of discrete time dependent simulations, however, can be used with different weather data to gain an understanding of the influence of the variation in external conditions on the thermal response of indoor spaces equipped with PCM boards.

Furthermore, this chapter shows that the RNG k- ϵ turbulence model can be successfully used in the air-flow modelling within built environments, as suggested by past literature, and demonstrates the higher potential of CFD for detailed analysis, relative to zonal or multi-zonal models. This research is further documented in Gowreesunker *et al.* (2013a)

The next chapter extends the application of PCM modelling further, to large glazed buildings, with relatively low thermal mass. It addresses the performance of PCM-glazed units, and provides various relationships that can be employed in the numerical modelling of such systems.

CHAPTER 5 – OPTICAL MODELLING OF PCM

The low thermal mass or capacitance of building envelopes is progressively becoming a growing issue due to the increasing trend of designing buildings with maximum exposure to the outdoor environment (Bostick, 2009), such as for airport terminal buildings. One approach to increasing the thermal mass of low thermal mass buildings is to incorporate PCM in the glazing structure (Goia *et al*, 2012).

Weinläder *et al.* (2005) investigated the optical properties of RT25®, S27® and L30®, placed in transparent plastic containers behind a double glazed window. The optical tests revealed that the PCMs have higher transmittance values in the liquid state than the solid states. In the liquid phase, the PCMs are clear, transparent and non-scattering, while the solid phase is translucent and scattering. Nonetheless, the colour of the transmitted light is constant for all phases, making PCMs viable options for day-lighting purposes. The authors also numerically showed that a PCM façade reduces the overall heat gains by 25 % and provides a lower indoor temperature relative to conventional double glazed units in a German summer condition, whilst it increases the insulating effect during winter.

Regarding the optical modelling of the PCM, Weinläder *et al.* (2005) assumed identical refractive indices for the solid and liquid phases, which varied with the radiation wavelength; and found that the radiation scattering coefficient is a function of only the PCM thickness. The numerical model employed in their study is unclear, and the authors do not comment on the variation of the optical properties as the PCM changes phase.

Ismail and Henriquez (2002) adopted a 1-D mathematical model to simulate the behaviour of a PCM-glazed unit. The PCM was placed within the gap of a double glazed unit, where it was assumed to have constant thermophysical properties, a single phase change temperature and no convection in the liquid phase. The optical modelling was relatively simple as the optical properties were considered constant during phase change, and the scattering effects were neglected. Nonetheless, the authors claim that the model was validated with experimental data.

Goia *et al.* (2012) also investigated the 1-D mathematical modelling of a PCM double glazed unit. The thermophysical properties of the PCM were considered constant in all phases, convection was ignored in the liquid phase and phase change was simulated using the effective heat capacity method. The optical properties of the PCM were constant in the fully liquid and solid phases, but varied with the temperature during phase change. This variation in optical properties with temperature/ liquid-fraction was an assumption from the authors. The PCM domain was segmented into different nodes, each with lumped value parameters. The model showed good validity with respect to experimental data, but the authors acknowledge the limitations associated with their assumptions. They further suggest the need for a better and more reliable modelling of short wave radiation within the PCM.

As seen in section 2.1.8 and as depicted by the previously referred literature, PCM glazed units have received relatively less research attention compared to other PCM systems. However more recently, new commercially available types of glazing such as Delta Cool-28® or GlassX®, which incorporate PCMs, have been developed, which indicates an increasing market interest for more thermally massive glazing. As a result, the accurate modelling of radiation through PCMs is growing in importance, especially with regards to the appropriate performance evaluation of PCM-glazed units.

One of the limiting aspects of PCM optical modelling encountered in the literature is the inability of the models to fully simulate the radiation behaviour of PCMs during the phase change process. Thus, in order to understand and improve the performance/modelling of PCMs in glazed structures, knowledge of the optical properties (scattering and absorption) during phase change is required. These properties are characterised as follows.

5.1 Development of Optical Model

This model was largely developed from empirical data from a spectroscopy analysis and an actual double glazed unit. It aims at defining the variation of the extinction coefficient (i.e. sum of the scattering and absorption coefficients) of the PCM during phase change. This model is published in Gowreesunker *et al.* (2013c).

The optical characterisation of the PCM was first performed with a spectrophotometer, which measured the spectral radiation transmittance for different PCM phases, as shown in Fig. 5.1. However, due to the inability to control and monitor the temperature within the spectrophotometer, a specific spectrum could only be assigned to the fully solid and liquid phases (under visual inspection), while the spectrum for the mushy region only depicts the relative differences. The investigated PCM was RT27[®].

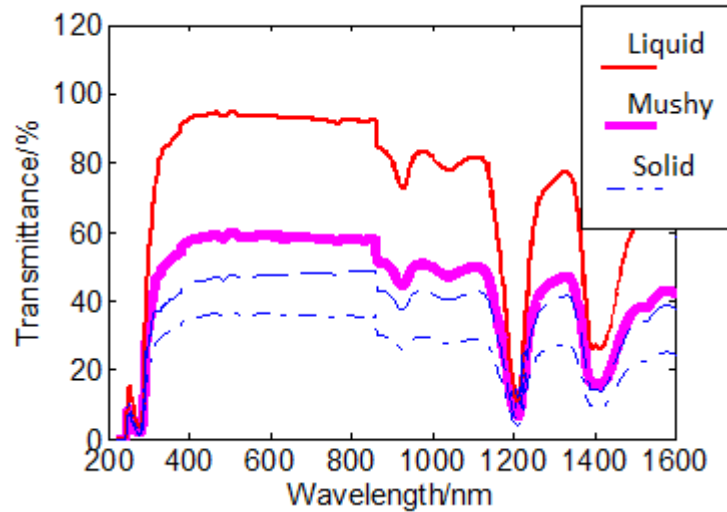


Fig 5.1. Spectral transmittance of RT27 in solid, liquid and mushy phases (The measurement uncertainty is $\pm 2\%$ for the liquid samples and $\pm 10\%$ for the solid samples) (Gowreesunker et al, 2013c)

Using Fig. 5.1, it was estimated that the extinction coefficients for the solid and liquid phases of RT27[®] were 30.1-52.3 m^{-1} and 3.6-5.5 m^{-1} , respectively, (using Eq. (C1.7)) for the visible range (350-850 nm) of the spectrum. Furthermore, it was also observed that in the visible range, the transmittance / optical thickness is nearly independent of the wavelength. This accounts for the unchanged colour in the transmitted light (therefore, suitable for day-lighting), and also allows for gray modelling of PCM in the visible range.

Due to the lack of temperature control in the spectrophotometer, the following experimental setup was therefore devised in order to quantify the variation in the optical properties during phase change (see Fig. 5.2).

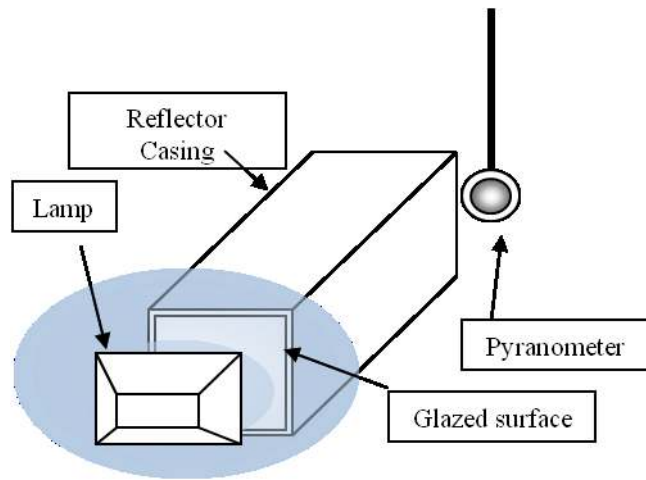


Fig. 5.2(a). Schematic of Experimental setup

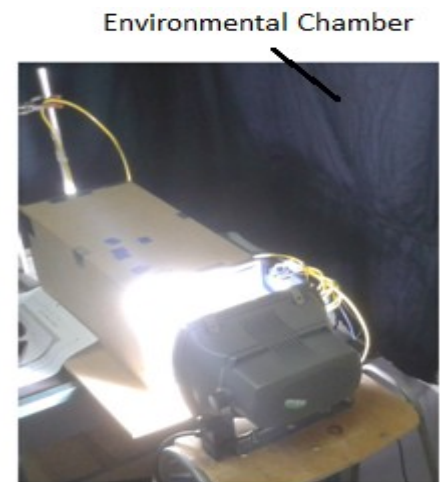


Fig. 5.2(b). Actual setup in Environmental chamber

The entire setup was placed inside an environmental chamber where the air temperature was controlled. A Kipp & Zonen CMA-6[®] pyranometer was used to measure the radiation heat flux (W/m^2) transmitted through the glazed surface test specimens. A 150 W metal halide (Iodide discharge) lamp producing a diffuse light with a spectrum ranging mainly from 350 nm to 850 nm was employed. The irradiation intensity was varied by varying the distance between the glazing and the lamp. Three types of surfaces were investigated: a standard double-glazed unit, a PCM-double glazed unit (PCM within glazing) and ‘no-glazing’. The main objective was to measure the gray radiation transmission for the different surfaces at different temperatures during phase change, and using the procedure described in Appendix C to obtain the variation in absorption, scattering and extinction coefficients of RT27[®].

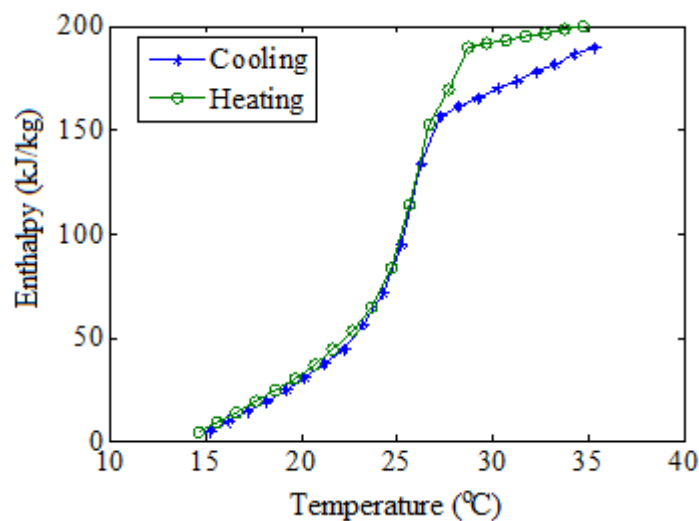


Fig. 5.3. Enthalpy-temperature curve of RT27(Gowreesunker et al, 2013c)

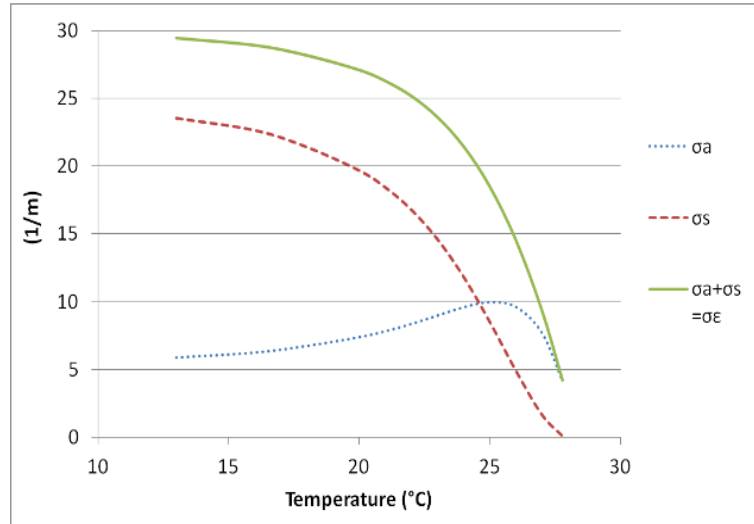


Fig. 5.4. Absorption (σ_a), scattering (σ_s) and extinction (σ_e) coefficients during phase change

Fig. 5.3 shows that the latent heat capacities of RT27[®] were found to be 165 kJ/kg and 191 kJ/kg for the cooling and heating cycles, respectively, evaluated between 15 and 27.8 °C using the T-history method (Appendix C). Correspondingly, Fig. 5.4 shows the variation in the absorption, scattering and extinction coefficients during the phase change process of RT27 (Gowreesunker *et al.*, 2013c). As anticipated from previous studies (Weinläder *et al.* 2005 and Goia *et al.* 2012), the scattering coefficient is more prominent in the solid phase, while absorption dominates in the liquid phase. Within the mushy phase, the scattering effect is higher for the major part until a temperature 24.5 °C, after which, absorption dominates until phase change is complete.

The relationships developed are as follows:

$$\sigma_e = (\beta \cdot \sigma_{e,liq}) + (1-\beta) \cdot (\sigma_{e,sol}) \quad (5.1)$$

$$\sigma_a = (\sigma_e)[\delta\beta + (1 - \delta)] \quad (5.2)$$

$$\sigma_s = (\sigma_e) - \sigma_a \quad (5.3)$$

Where:

$$\delta = \frac{\tau_{liq} - \tau_{sol}}{1 - \tau_{sol}} \quad (5.4)$$

δ defines the ratio between the absorption and scattering coefficients for the fully solid phase of the PCM. Eqs. (5.1-5.4) describe the change in optical properties as a PCM

changes phase. They employ the liquid fraction term or temperature (as $\beta=f(T)$) to vary the optical properties, and therefore portray the importance of the thermal characterisation of the PCM. The following section shows the implication and validation of Eqs. (5.1-5.4) in an actual PCM-glazed unit.

5.2 Validity of Optical Model

The numerical validation of the optical model / relations developed (Eqs. 5.1-5.4) was performed using the CFD package FLUENT®. The PCM-double glazed unit was simulated at an irradiation level of 950 W/m² and a surrounding temperature of 13°C, until the PCM completely changed phase from solid to liquid. The overall gray transmittance value was the main variable monitored for validation.

The effective heat capacity method was employed to simulate the phase change process: because of the relative ease to incorporate the variation of specific heat capacity with a temperature profile in FLUENT using UDF and; to account for the effect of natural convection. The variation in c_p is determined from Eqs. (5.5) and (5.6). The derivation of the equations is detailed in Appendix C. In addition, the density and viscosity of the PCM were varied in the simulations as shown in Table 5.1. The thermal conductivity of RT27® is 0.2 W/mK.

Table 5.1. Viscosity and density variation of RT27® during phase change (Gowreesunker et al. 2013c)

Temperature range	Viscosity (Pa·s)	Density (kg/m ³)
$T < T_{sol}$	-	880
$T_{sol} \leq T \leq T_{liq}$	0.031	$880 - (120 \cdot \beta)$
$T > T_{liq}$	$0.01 \exp \left(-4.8 + \frac{1790}{T + 273.15} \right)$	$\frac{760}{[0.001 \times (T - T_{liq})] + 1}$

For $15^\circ\text{C} \leq T < 26^\circ\text{C}$;

$$c_p(T) = 0.012 T^4 - 0.911 T^3 + 25.835 T^2 - 323.96 T + 1519.21 \quad (\text{kJ/kg}\cdot\text{K}) \quad (5.5)$$

$(R^2 = 0.994)$

$$\text{For } 26\text{ }^{\circ}\text{C} \leq T \leq 27.94\text{ }^{\circ}\text{C}; \quad c_p(T) = -7.34 T^2 + 376.55 T - 4786.72 \quad (\text{kJ/kg}\cdot\text{K}) \quad (5.6)$$

$$(R^2=1.000)$$

The change in viscosity in the liquid phase was obtained using the approach employed by Reid *et al.* (1987), which suggests a form of $\exp(A + (B/T))$, whilst the change in liquid density is obtained from the works of Ye *et al.* (2012).

The radiation modelling of the glazed unit was performed using the gray Discrete-Ordinates (DO) radiation model as it is the most detailed model in FLUENT. It allows for the simulation of radiation scattering and absorption effects, and is applicable for a wide range of optical thicknesses. The DO model solves the radiation heat transfer equation for a finite number of discrete solid angles by transforming it into a transport equation for radiation intensity (ANSYS FLUENT theory guide, 2010). The angular discretisation for radiation transport was separated into 3×3 divisions and 2×2 pixels, and the irradiation is diffuse and gray. The two glass layers in the double glazed window were modelled as thin walls, with thermal conductivity of 1.3 W/mK, density of 140 kg/m³, specific heat capacity of 840 J/kgK, σ_a of 19 m⁻¹, non-scattering properties and a constant refractive index of 1.5. The equations of the absorption and scattering coefficients for the PCM are implemented as UDFs, varying with the temperature of the cells. The refractive index of the PCM was constant at 1.3.

The front and back faces were defined as semi-transparent walls, with convective thermal boundary conditions to the ambient environmental chamber air. A heat transfer coefficient of 5.1 W/m²K was applied to the front face, while 1.1 W/m²K was used for the back face (These coefficients were obtained from a separate simulation between the experimental setup and the environment chamber). The sides of the glazed units were assumed to be adiabatic and reflective. A time-step of 10s was employed for the simulation and the model consisted of 10,000 structured hexahedral cells (see Fig. 5.5).

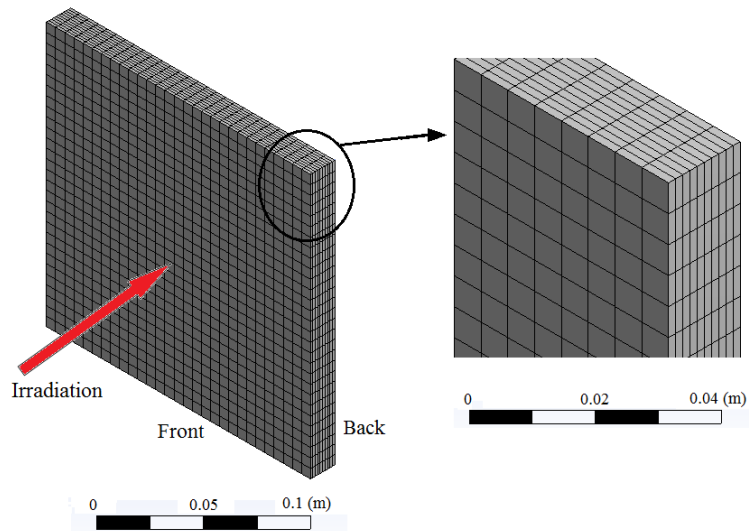


Fig. 5.5. PCM finite volume model in PCM-glazed unit

Fig. 5.6a shows the progression of the transmittance (τ_{gl-PCM}) of the PCM filled glazed unit, and portrays a comparison with the experimental results. Fig. 5.6b shows the numerical volume weighted temperature of the PCM, depicting the state of the PCM.

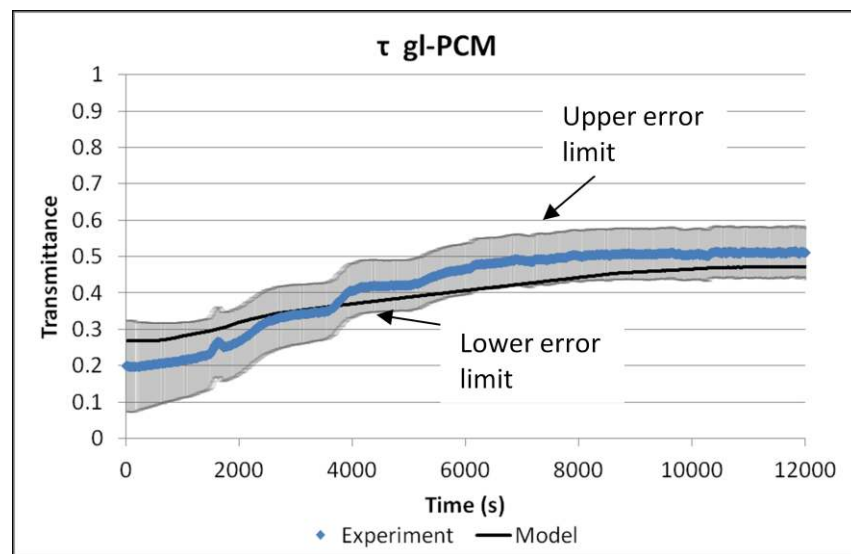


Fig. 5.6(a). Transmittance (with experimental error bars) of the PCM filled glazing under 950 W/m^2 irradiation and 13°C

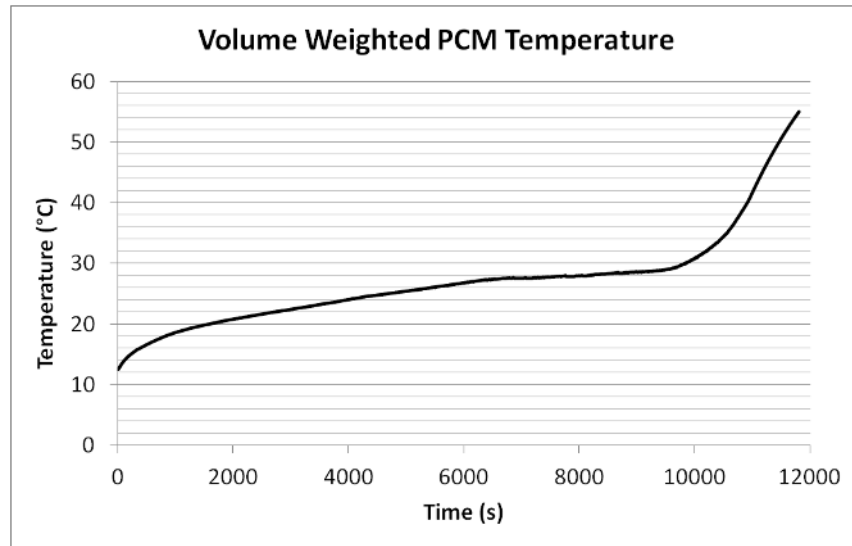


Fig. 5.6(b). Numerical progression of PCM Temperature

Fig. 5.6a shows that at the beginning of the experiment, the transmittance value of the PCM glazing is lowest due to the opacity associated with the solid PCM. In the solid state, the scattering effect dominates as described in Fig. 5.4, and thus most irradiation is reflected. The relatively small absorption effect of $\sim 6 \text{ m}^{-1}$ allows the temperature to gradually increase until the phase change onset temperature of 15°C (at $\sim 750\text{s}$). In the beginning of phase change, the absorption effects are constant, while the change in the scattering coefficient is relatively more pronounced. Therefore, in the early stages of phase change, the change in transmittance can be mainly associated to scattering.

Subsequently, upon reaching a temperature of $\sim 20^\circ\text{C}$ (at $\sim 2000\text{s}$) the rate of increase in transmittance decreases due to a lower rate of temperature increase, whereby the phase change effect of the PCM becomes more evident. In this temperature range, although the optical thickness has a high rate of change (see Fig. 5.4), the variation in effective heat capacity of the PCM dominates the overall change in transmittance. In the final stages of phase change (between $25\text{-}28^\circ\text{C}$), where the effective heat capacity of the PCM is at its maximum, the rate of increase of both the temperature and the transmittance decreases further. Fig. 5.6a shows that the transmittance values obtained from the simulation are within the errors of the experimental results, and that the trends are also similar. As the numerical results match the experimental data within the error limits, the model is considered to be valid.

5.3 Design Implications

The purpose of incorporating PCM within a glazed unit is to increase the thermal mass of the glazed system. However, because of the transparency of glazed units, the radiation effects of the PCM are also crucial. This section aims at comparing the performance of a PCM-glazed unit with an ordinary double glazed unit.

The application of PCM increases the overall heat capacity within a double glazed unit. In this case, with a mean effective heat capacity of 10 kJ/kgK for RT27[®] during phase change, the decrement delay of the overall PCM-glazed unit is approximately 2h (decrement factor of 0.9), compared to 0.03h (decrement factor of 1.0) for an ordinary double glazed unit, calculated using the CIBSE admittance method. These imply that employing PCM within a glazed unit will improve the thermal mass by delaying the impact and reducing the effect of the outdoor conditions on the indoor environment.

As elaborated in section 5.2, the reduction in transmittance of the PCM-glazed unit during phase change is mainly due to the scattering and absorption properties of the PCM. However, when the PCM is melted, radiation absorption is then the dominant effect resulting in an increase in the temperature of the unit. On the other hand, in a standard double glazed unit, the radiation absorption properties of air in the cavity are negligible, and the dominant effect resulting in the reduction in transmittance is the reflection due to changes in refractive indices and the radiation absorption properties of the glass. The differences in behaviour for these two systems are shown in Fig. 5.7. The standard glazing temperature profile is obtained from a separate CFD simulation, with similar parameters to those described in section 5.2, but with an air-cavity.

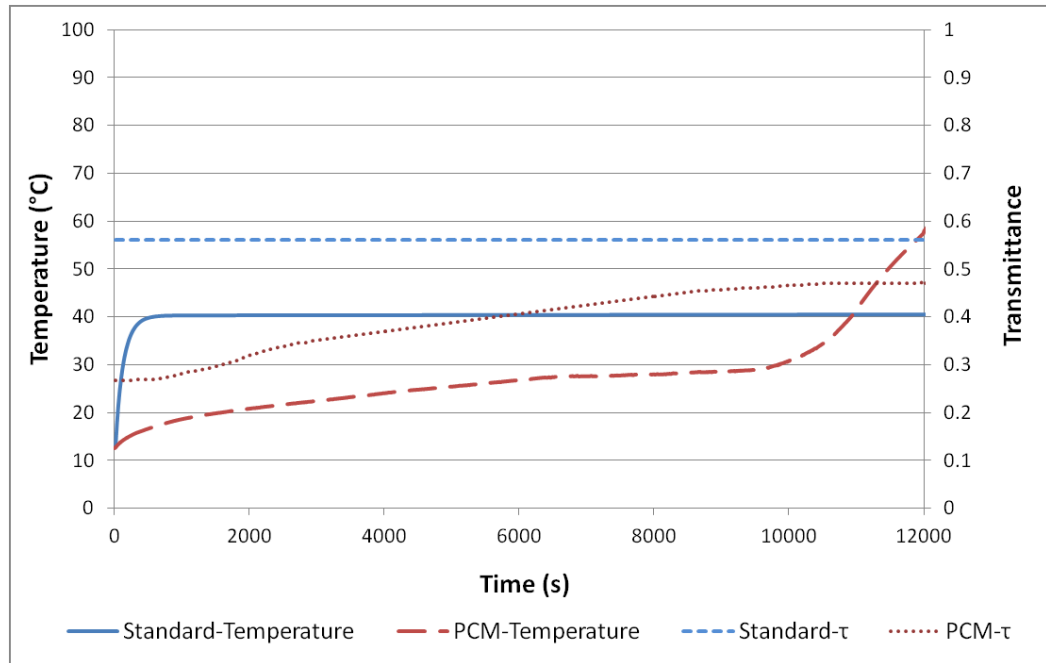


Fig. 5.7. Model Temperature and transmittance progression for a PCM-glazed and a standard double glazed unit under 950 W/m^2 irradiation and 13°C air/initial glazing temperature.

Fig. 5.7 shows that in the phase change region of the PCM-glazed unit, the PCM provides a higher reduction in transmittance and a lower rise in temperature than the standard double glazed unit. This implies that the radiation heat transfer rate is reduced and the effect of the extra thermal mass due to the PCM can be clearly observed. The discrepancy in the glazing performance occurs after the phase change process, where the temperature of the PCM increases above that of standard glazing. This is due to the constant radiation absorption coefficient (4 m^{-1}) of the PCM in the liquid phase, as opposed to no absorption by the air-cavity. As a result, a steady-state temperature of 40°C is obtained for the standard glazing, while a higher steady temperature of 70°C is obtained for the PCM-glazed unit after the phase change process.

Furthermore, it can be seen that the steady-state transmittance of the PCM-glazed (0.47) and standard glazed units (0.56) are relatively close, even though more radiation is absorbed by the liquid PCM. This similarity in transmittance can be explained with reference to the different refractive indices of a normal glazing and PCM-filled glazing. In the case of the standard glazing, the greater difference between the refractive indices of the glass ($n=1.5$) and air-cavity ($n\approx 1$) implies that the overall diffuse reflection propensity of the glazed unit is higher (Siegel and Spuckler, 1994). Conversely, as the difference in refractive indices between the PCM ($n=1.3$) and the glass ($n=1.5$) in the

PCM-glazing is lower, less reflection is induced. Thus, although the steady-state transmittances are similar, the dominant radiation effects are different; the irradiation is mostly absorbed in the liquid PCM (leading to increase in temperatures), whilst it is mainly reflected in a normal air-cavity glazing. This therefore stresses the importance of proper sizing of such PCM-systems in order to avoid overheating.

Moreover, the visual aspect of a PCM-glazed unit is also very important with regards to aesthetics. As observed in this study, PCMs are fully transparent in the liquid phase, but are translucent in the solid/mushy phase, as shown in Fig. 5.8.

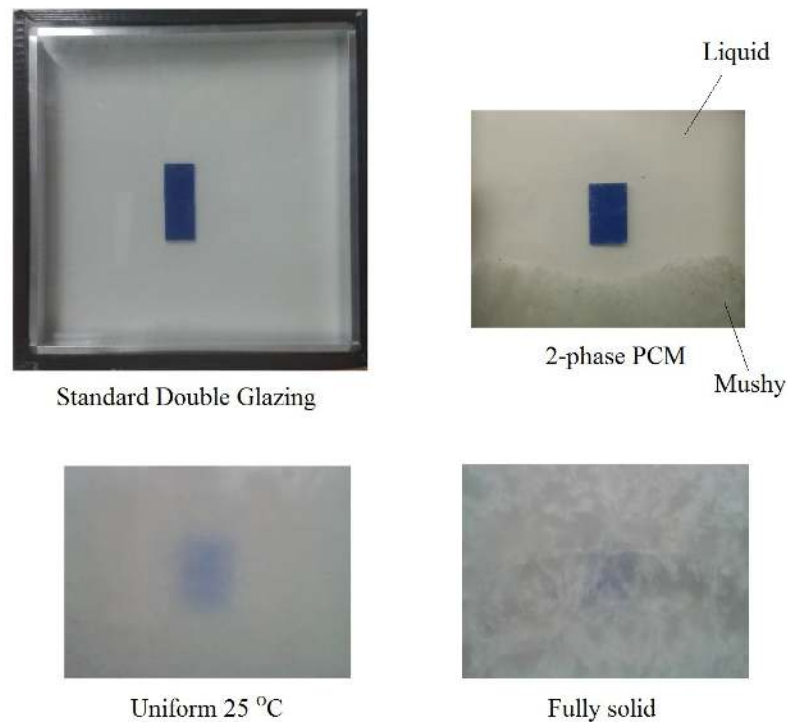


Fig. 5.8. Visual aspect of phase change

The colour of the transmitted light is the same at any phase of the PCM as the spectral distribution in Fig. 5.1 is the same at all phases, making it acceptable for daylight purposes. However the radiation intensity is different. Furthermore, the change in opacity and scattering of light can be an architectural drawback. This can however be minimised by employing concealing measures such as screen-prints or translucent containers (Weinlader et al, 2005), if the application permits it.

5.4 Summary of Chapter 5

This chapter analysed the optical and thermal aspects of a PCM-glazed unit with RT27[®], and compared its performance with a standard double glazed unit. The optical properties were evaluated using spectrophotometry and a custom-built experimental setup, whilst the thermal properties were evaluated using the T-history method. Various relationships were developed based on observations from the experimental results, which allowed the description and modelling of the optical aspects of PCM during phase change. The experimental results and relationships developed were also employed in a finite volume model, which was validated over the entire phase change process. This research is further documented in Gowreesunker *et al.* (2013c).

The main results showed that:

- during rapid changes in temperature or phase of the PCM, the transmittance spectra are unstable. Conversely, under stable conditions, visual transmittance values of 90 % and 40 % are obtained for the liquid and solid phases, respectively. It was also observed that the changes in transmittance spectrum at different PCM phases are quasi-uniform under stable conditions.
- the scattering effects are more prominent in the solid phase, while absorption dominates in the liquid phase. Within the mushy phase, the optical properties of PCM that are non-scattering in the liquid phase can be described with relation to the liquid fraction.
- employing the relationships developed from this study allows a successful and valid representation of the radiation propagation within a PCM, over the entire phase change range.
- the use of PCM within a double-glazed unit improves the thermal mass during phase change, relative to a standard double glazed unit. After phase change, although providing a similar transmittance to a standard glazed unit, the absorption process dominates in the PCM-glazed unit, compared to reflection in the standard glazed unit. Thus, in using PCM-glazed units, adequate emphasis must be placed on the overheating aspects of PCM-glazed units after the PCM has melted.

- the PCM visual aspect changes as the material changes phase. It is translucent in the solid phase and transparent in the liquid phase. Thus, depending on the application, this may be acceptable, or the PCM may have to be concealed.

This next chapter describes the methodology used for the performance evaluation of the different PCM systems in the airport terminal space. It describes the coupling between the CFD tool and the Energy Simulation (ES) tool.

CHAPTER 6 – NUMERICAL CONSIDERATIONS FOR AIRPORT TERMINAL

6.1 Overview of Modelling Strategy

As alluded to in the previous chapter, a coupled simulation method will be employed in this study. This is particularly important in order to accurately represent the air-movement within the airport terminal and calculate the HVAC energy impact of the different PCM systems. This study focused on a case similar to London Heathrow Terminal 5 departure hall which is a large and open space, with a glazed envelope. The departure hall is fitted with displacement conditioning (DC) diffusers on the floor, which provide both heating and cooling.

This study investigated the relative energy saving potential of PCM systems in the airport DC system. The input parameters used were obtained from the validated works of other authors and CIBSE and ASHRAE guides, as described in the following sections. The accuracy of the models was obtained from an L_2 norm study using the widely validated RNG k- ϵ turbulence model for buildings. The coupling strategy is similar to that employed in the models of Zhai and Chen (2005), and Fan and Ito (2012). The PCM models have all been validated as discussed in Chapters 3 to 5 and using the data from the works of Dolado *et al.* (2011).

In effect, the modelling strategy employs several validated models (including the validated phase change models from this study) to quantify the performance of each PCM system when employed in the airport terminal. The results from this study will be used for comparative analyses rather than the absolute characterisation of the energy performance of the HVAC system. A similar approach can be found in the works of Oikonomou *et al.* (2012).

In the coupled simulations for this study, the departure hall and PCM systems are simulated in FLUENT. TRNSYS is used to simulate the control system, provide the necessary boundary conditions required by the FLUENT model, and calculate the energy requirements of the building.

6.2 Introduction to TRNSYS

TRNSYS® (TRaNsient SYstem Simulation) is a modular simulation program that allows the evaluation of various energy systems, including HVAC analysis and sizing, multi-zone airflow analyses, electric power simulation, building thermal performance, and analysis of control schemes. It consists of a Graphical User Interface (GUI), a simulation kernel and different simulation components (Types). The kernel reads the project description file or deck file (*.dck), and adjusts the simulation components' order so as to ensure adequate transfer of information between the components.

The components used in TRNSYS can be written in various languages such as FORTRAN, PASCAL or C++, that allows the creation of a Windows DLL (Dynamic Link Library, *.dll). These components contain the programming subroutines which describe the function of the component. The DLL refers to a shared library with the main TRNSYS kernel, and because of the modular approach employed in TRNSYS, the new component DLL can be externally incorporated into the simulation without the need for recompiling the entire TRNSYS software for each new component added. This provides the flexibility for the user to easily create different simulation components which are not present in the default simulation studio.

The components in TRNSYS are interlinked in the graphical interface, whereby the solution can be obtained either through the successive substitution method or the Powell's method (TRNEdit, 2010). The successive substitution method refers to the method where the outputs of a component are fed/ substituted as the inputs to another component. A component is called only if its inputs change during a particular time-step, and convergence is reached when the outputs vary within the tolerance limits defined in the deck file. The successive substitution method calls a component as many times as required by the simulation during a time-step and then proceeds to the next time-step after convergence. The Powell's method, on the other hand, has been developed for back-solving and oscillatory data limitations of the successive substitution method. This latter method is mainly used for controller research (TRNEdit, 2010). The time-stepping in TRNSYS is constant during a simulation, and, the successive substitution method is used in this study.

The incorporation of weather files, different control systems, HVAC systems, different scheduling strategy and the modelling of multi-zone buildings makes TRNSYS a complete and powerful tool in the evaluation of building energy systems. Nonetheless, similar to other multi-zone simulation tools, it is not recommended for cases where the geometry and size of a building largely influence the performance of the HVAC systems, such as in Atria, Airports, or other large open spaces. In these cases, the modelling of air-flow in the building is crucial and therefore zonal representations do not provide adequate results (Heiselberg *et al*, 2008; Gowreesunker and Tassou, 2013a).

6.3 Coupling of CFD & TRNSYS

Common simulation tools such as TRNSYS®, EnergyPlus® and ESP-r® typically employ zonal or multi-zonal models to simulate buildings and HVAC systems. This approach eliminates the necessity to model the airflow distribution in the zone, considerably simplifying the model through the use of empirical equations to mimic air-flow. These simulation tools have been more focused on the simulation of building services systems than the air flow and temperature variation within a space. In doing so, the simulation times and computer costs are kept low, at the expense of accuracy in the determination of air flow and temperature in the building.

On the other hand, CFD tools such as ANSYS FLUENT® or CFX® have been mainly developed as general purpose simulation softwares. These tools employ the finite volume principle, which requires the generation and discretisation of the building volume and solution of the approximate form of the Navier-Stokes equations. The simulation results can therefore be of high accuracy, at the expense of high computing time and costs.

It can thus be claimed that CFD provides detailed air-flow simulations, whilst TRNSYS provides the platform to simulate the mechanical systems used for indoor thermal environment control. In other words, the benefits provided by one tool are missing in the other tool, such that an ‘optimum’ model would be the complement of both tools, requiring a coupling strategy (Zhai and Chen, 2005). As a result, some commercial simulation packages such as Integrated Environmental Solution Virtual Environment® (IES-VE) (IES, 2012) and Design builder® (DesignBuilder, 2012) have introduced CFD components to their interface. The CFD capability on these tools, is however simpler than actual CFD solvers, but the resulting simulation outputs are more detailed than those of zonal models. The limitations of these packages are that: i) the grids are uniform hexahedral cells, suited mainly to rectangular geometries; ii) there are limitations in the turbulence models employed; and iii) the coupling between the building space and the control systems is done at the end of the simulation (Gowreesunker et al, 2013b).

In this study, the advantages of both TRNSYS and CFD modelling are utilised through the development of a coupling code that dynamically links TRNSYS to the CFD

package FLUENT. At the moment, because of the respective architecture of the softwares, it is simpler to allow TRNSYS to control the entire coupling, as it is easier to integrate new components in TRNSYS than to modify the FLUENT kernel. This coupling can be done via a script and results file (Arias, 2006; Fan and Ito, 2012).

A script file is a *.in file, created by TRNSYS, which is read by FLUENT. It contains the journal file with all the inputs to the CFD simulation which include: specific models to be used, boundary conditions, and which outputs to be produced. A results file is a *.txt file, created by FLUENT, containing the outputs from the CFD tool which can be read by TRNSYS. These outputs can be localised or mean values.

Zhai and Chen (2005) generally classified the coupling methods as either static or dynamic. A static coupling consists of ‘one-step’ or ‘two-step’ data exchange between the CFD and the Energy Simulation (ES) tools. This is suitable for cases where the solution is not very sensitive to the data being exchanged. Alternatively, a dynamic coupling strategy is proposed, which refers to a continuous exchange of data for each time-step in the simulation. The latter strategy can be further sub-divided into quasi-dynamic and fully-dynamic coupling.

A quasi-dynamic coupling involves no iterations between ES and CFD at each time-step. Instead CFD receives the boundary conditions from the ES time-step (t^{th}), and returns the results to the ES tool for the next time-step $(t+1)^{th}$. Conversely, a fully-dynamic coupling iterates ES and CFD a number of times during each time-step, until a converged coupled solution is reached, before moving to the next time-step. The latter method is more time-consuming because of the relatively higher number of coupled iterations between the ES and CFD tools during each time-step.

A quasi-dynamic coupling strategy is employed in this study so as to minimise the computational effort of the coupled simulation. However, when using such a strategy, it is important that the accuracy of the models is not sacrificed to an extent where the results become non-representative of the actual scenario. Sections 6.6 and 6.7 therefore depict the numerical considerations for operating such coupled simulations in the performance evaluation of PCM systems in the Airport Terminal.

6.4 CFD Numerical Considerations

FLUENT was used to simulate the indoor environment because of its ability to solve the discretised form of the Navier-Stokes equations, and provide velocity and temperature fields within the terminal space. The London Heathrow Terminal 5 is shown in Fig. 6.1.



Fig. 6.1. London Heathrow Terminal 5 Departure Hall

An accurate model of the airport terminal, generated in FLUENT must capture the essential aspects of such a space, which includes: a high ceiling space; a large glazed envelope and a large open floor space. These characteristic aspects can also be found in several other modern airports such as Bangkok International Airport (Simmonds *et al*, 2000), Chengdu Shuangliu International Airport (Liu *et al*, 2009) and Dubai International Airport, amongst others. As a result, a 2D transient model of the departure hall which includes these characteristic features was developed. The 2D analysis is justified based on the constant cross-sectional area of the departure hall, and to minimise computational effort. The 2D depth of the model is 1 m, however, each diffuser actually serves a depth of 12 m at London Heathrow Terminal 5.

The CFD model boundary of the airport terminal is shown in Fig. 6.2.

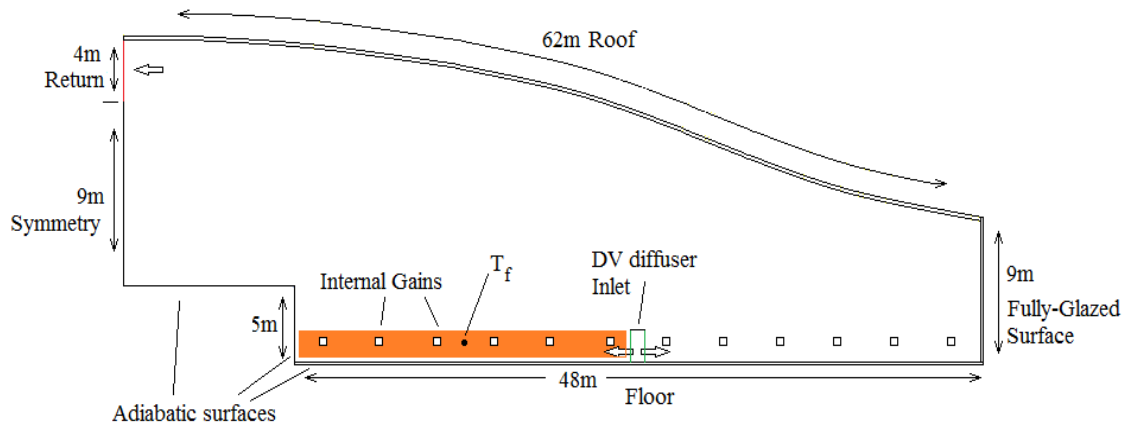


Fig. 6.2. CFD representation of investigated airport departure hall

The geometry consists of a fully glazed surface at one extremity, a partially glazed roof and tiled floor. All the domains (Air/Roof/Floor/Glazing) are explicitly modelled and discretised in FLUENT so as to account for their thermal inertia. The roof is assumed to be 25% glazed; the external surface of the roof and glazing are bounded by convection and radiation conditions and the floor external surface is adiabatic. The external convection heat transfer coefficient is $25 \text{ W/m}^2\text{K}$ (CIBSE A, 2006), with a mean annual wind speed of $\sim 5 \text{ ms}^{-1}$ at London Heathrow (DECC, 2013). The internal occupancy heat gains are mimicked by each square (0.25 m^2), with the uniform heat flux boundary conditions shown in Fig. 6.3. The passenger zone spreads along half of the floor area at a height of 2 m, as shown by the shaded area in Fig. 6.2, and consists of the crucial part of the departure hall to be conditioned (Liu *et al*, 2009). As a result, T_f , the feedback temperature node for the HVAC control system is located within this conditioned space.

Owing to the chaotic nature of passenger traffic within the terminal building, the occupancy heat gain schedule is shown in Fig. 6.3. This schedule is adapted from Parker *et al*. (2011), with the heat fluxes obtained from Simmonds *et al*. (2000).

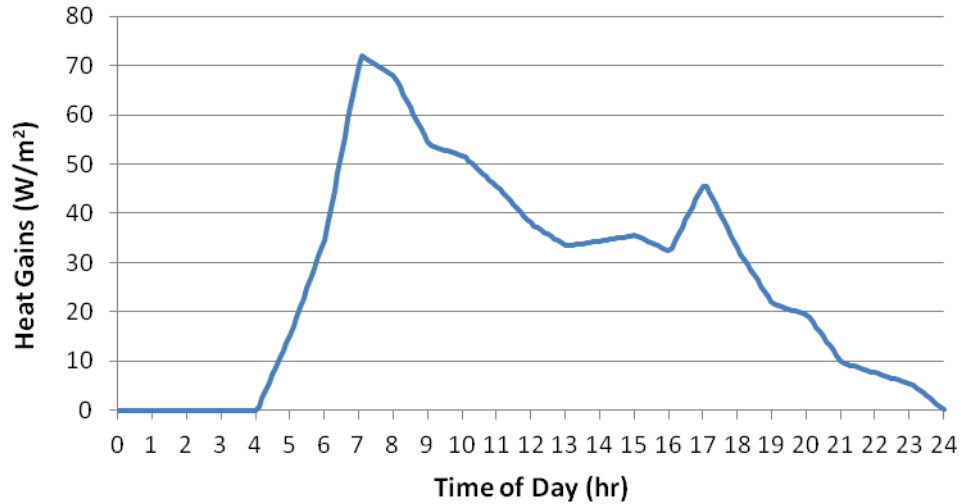


Fig. 6.3. Internal heat gains schedule (Parker *et al*, 2011; Simmonds *et al*, 2000)

The lighting gain is constant at 5 W/m^2 during the occupied hours and is applied at the internal surface of the roof (Simmonds *et al*, 2000). The DC diffuser inlet has a height of 2m and is bounded by a ‘mass-flow inlet’ condition. The return/ exhaust from the airport terminal has a height of 4m and is bounded by an ‘outwards mass-flux inlet’ conditions, with a total mass flow rate equal to the inlet mass flow rate, so as to allow for conservation of mass.

As elaborated in sections 4.1 and 4.3, the RNG $k-\epsilon$ turbulence model has been shown to be appropriate in a number of air-flow simulations in buildings, and will thus be employed in this study. The walls are considered non-slip. Air is modelled as an ideal gas to account for the buoyancy effects within the space. The effect of humidity is neglected in this study because PCM systems only affect the sensible load of a building.

The SIMPLE algorithm is used for the pressure-velocity coupling and the Body-Force Weighted pressure interpolation scheme is employed to account for the buoyancy effects. These assumptions are based on the recommendations of ANSYS FLUENT® (FLUENT User guide, 2010) for problems involving large body forces (such as natural convection), and the work of Gowreesunker and Tassou (2013a), Schellen *et al*. (2013) and Schellen *et al*. (2012). The enhanced wall treatment is used to model the near-wall flows, because the enhanced-wall function in FLUENT allows an adequate representation of the velocity and thermal profiles for different near-wall flow regimes, including the buffer region ($3 < y^+ < 10$) (ANSYS FLUENT Theory guide, 2010).

The material properties of the building envelope are given in Table. 6.1, and are obtained from a combination of CIBSE Guide A (2006) and the works of Simmonds *et al.* (2000).

Table 6.1. Building envelope physical and thermal properties

	Thickness (mm)	ρ (kg/m ³)	λ (W/mK)	c_p (J/kgK)	ϵ_{ext}	ϵ_{int}	τ
Floor	13	1700	0.8	850	-	0.5	-
Glazing	30	140	0.03	840	0.16	0.2	0.5
Roof	30	140	0.03	840	0.16	0.2	0.01

All radiation properties are based on Kirchhoff's radiation law, which states that at equilibrium, the emissivity equals the absorptivity of a surface (Modest, 2003).

6.4.1 Radiation Modelling

Five different radiation models are available in FLUENT. In this study, the Discrete Ordinate (DO) radiation model is employed to simulate the radiation heat exchange between the airport terminal internal surfaces, as it is a more generic radiation model and is more accommodating to complex geometries (ANSYS FLUENT theory guide, 2010). This model solves the radiative heat transfer equation Eq. (6.1) for a finite number of discrete solid angles.

$$\frac{dI(\vec{r}, \vec{s})}{ds} + (\sigma_a + \sigma_s)I(\vec{r}, \vec{s}) = \alpha n^2 \frac{T^4}{\pi} + \frac{\sigma_s}{4\pi} \int_0^{4\pi} I(\vec{r}, \vec{s}') \phi(\vec{s} \cdot \vec{s}') d\Omega' \quad (6.1)$$

All surfaces are treated as opaque and diffuse in CFD, and the effect of solar radiation is incorporated in the form of heat fluxes and generation rates in the building envelope, as recommended by the International Energy Agency (IEA) Task 12 Report (Bryn and Schiefloe, 2006). An explicit modelling of radiation propagation through the building envelope would result in the inappropriate representation of long-wave radiation at night, and would require the non-gray segmentation of radiation. This is beyond the scope of this study. Instead, Kirchhoff's law is used to account for the radiation exchange between the external surface of the airport terminal and the sky, whilst the

DO-model is used to calculate the radiation exchange between the internal surfaces of the airport terminal. The radiative properties are given in Table 6.1.

The radiative heat exchange between the external surface and the sky is obtained from Eq. (6.2).

$$q_{rad,ext} = \sigma \varepsilon_{ext} (T_{sky}^4 - T_{ext}^4) \quad (6.2)$$

Where T_{sky} is obtained from TRNSYS:

At night; from TRNSYS Type 69b which calculates the night-sky temperature based on the dry bulb and dew point temperatures.

During the day (based on the assumption that the external surface temperature is close to the ambient temperature);

$$T_{sky} = \sqrt[4]{\frac{G}{\sigma} + T_{amb}^4} \quad (6.3)$$

The total heat exchange between the external surface and the ambient environment is therefore given by Eq. (6.4):

$$q_{ext} = h_c (T_{amb} - T_{ext}) + \varepsilon \sigma (T_{sky}^4 - T_{ext}^4) \quad (6.4)$$

Furthermore, the heat load on the floor due to the transmitted solar radiation from the roof and side glazing is calculated from Eq. (6.5), and applied to the internal side of the floor as a heat generation rate:

$$A_{fl} q_{fl,rad} = \alpha_{fl} G [(\tau_{gl} A_{gl}) + (\tau_{ro} A_{ro})] \quad (6.5)$$

It should be noted that all radiation properties are gray.

6.5 TRNSYS HVAC System

The HVAC system simulated in TRNSYS is a constant air volume system, whereby the conditioning of the airport terminal is done via adjustments of the supply air temperature. The overall system is schematically shown in Fig. 6.4.

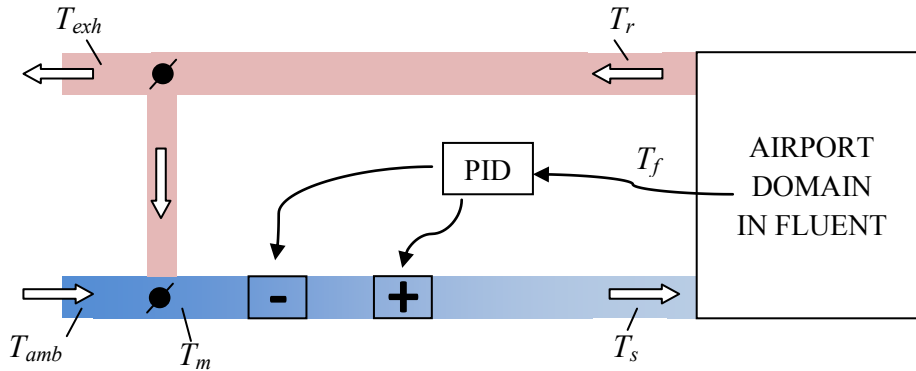


Fig. 6.4. Schematic of HVAC system

Return air at temperature T_r is extracted from the airport and partially mixed with incoming ambient air at temperature T_{amb} . The mixed air at temperature T_m then passes through the heating and cooling coils, where the PID control system adjusts the amount of either cooling or heating required by the space, based on the feedback temperature T_f . The sensor position for T_f can be found in Fig. 6.2. Thus, the PID controller is effectively providing thermal comfort in the space by adjusting the supply temperature T_s . The PID set point temperature is maintained at 21 °C, and the integral, derivative and gain constants are 0.1 hour, 0.1 hour and 10% respectively, for all simulations. The PID set point temperature is maintained constant for all seasons, as it can be considered a mean optimum thermal comfort temperature condition (Auliciems and Szokolay, 2007). This was verified for the case of an airport terminal space in the UK, based on: 1.15 clo, 1.4 met and air velocity of 0.15 ms⁻¹ for winter conditions; and 0.65 clo, 1.4 met and air velocity of 0.15 ms⁻¹ for summer conditions (CIBSE A, 2006); whereby a temperature of 21 °C is found to provide an adequate PMV of ± 0.5 for the occupants in both seasons, using the Fanger's equation of thermal comfort (Fanger, 1970).

The mode of operation of the HVAC system and the PID controller is as follows; where $T_{c,l}$ and $T_{c,u}$ are the lower and upper limits of comfort temperature, respectively.

If $T_f > T_{c,u}$; The PID controller will calculate a supply temperature $T_s < 21^\circ\text{C}$ so as

to satisfy the cooling requirement of the space.

If $T_{c,l} \leq T_f \leq T_{c,u}$;

The PID controller is non-operational and air is supplied at T_m to the space, in order to reduce the HVAC energy consumption.

If $T_f < T_{c,l}$;

The PID controller will calculate a supply temperature $T_s > 21^\circ\text{C}$ so as to satisfy the heating load.

During its normal mode, the HVAC system is operational only during the occupied hours, i.e. between 04:00 and 24:00 (see Fig. 6.3), whilst the entire airport is assumed closed during the non-occupied hours. For the case of the 2D geometry shown in Fig. 6.2, the total inlet ventilation flow rate is 0.5 kg/s, comprising of 0.2 kg/s fresh air flow rate. This mixing ratio is constant. This results in a heating and cooling capacity of 4 kW each, with a temperature difference of 8K across the units. Note that the cross-sectional thickness of the 2D geometry is 1m and that the HVAC sizing methodology is more thoroughly described in Appendix D.

6.6 L₂ Norm – CFD Temporal and Spatial Convergence Study

The CFD model of the airport terminal space simulated in FLUENT is the more important part of the coupled simulation, because the temperature data obtained from the FLUENT building model controls the entire simulation. As a result, it is important to ensure that the data obtained from FLUENT is accurate enough, so that it represents the actual behaviour of the airport terminal space.

The validity of CFD in building simulations has already been confirmed in a wide range of studies, described in section 4.1, as well as the validation study conducted in section 4.3. However, because of the influence of the mesh size and time-step on the final results of a particular geometry (Gowreesunker *et al*, 2013 a, b), it is important to design a CFD model whereby the errors associated with these aforementioned parameters are justified within the limits of accuracy and adequate computing power.

This error analysis is performed following an L₂ norm study for the temperature and velocities in the model. The L₂ norm study is essentially a sensitivity analysis of the mesh size and time-step, with the temperature and velocities variables as the monitored parameters. It quantifies the errors in the model based on the difference between the exact solution of the governing differential equations and the solution of the discrete governing equations. However as the exact solution of the governing equations is not known, the results of a simulation with a uniformly very fine mesh and small time-step are taken as the benchmark (Gowreesunker and Tassou, 2013a; Alauzet *et al*, 2007). The L₂ norm errors are calculated from Eq. (6.6) (Veluri *et al*, 2012):

$$L_2 \text{ norm} = \left[\frac{\sum [V_i (\phi_{discrete} - \phi_{exact})_i^2]}{\sum V_i} \right]^{1/2} \quad (6.6)$$

The inputs to the L₂ norm simulation are described in Figs. 6.5, representing typical values for airports (Parker *et al*, 2011; Simmonds *et al*, 2000).

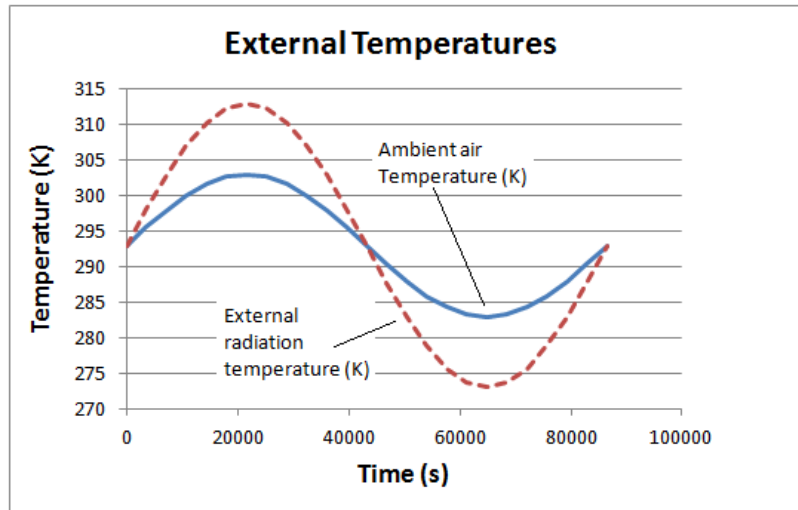


Fig. 6.5(a). External temperatures schedule input for L_2 norm study

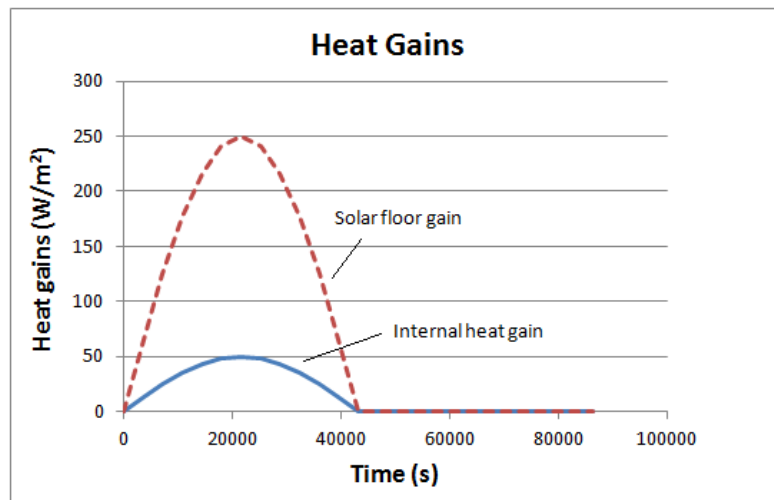


Fig. 6.5(b). Heat gains schedule input for L_2 norm study

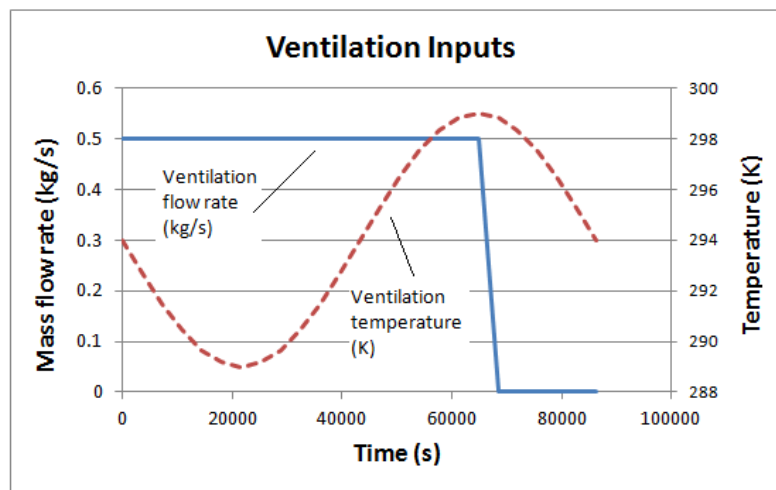


Fig. 6.5(c). Ventilation input schedule for L_2 norm study

In this case, the results of a simulation with very fine-uniform mesh (307,000) and time-step (10 s) are taken as the benchmark. This benchmark model employs second-order discretisation schemes (as proposed by Ramponi and Blocken (2012)), has a mean y^+ value of 3.2 and a global Courant number of 1.55. Furthermore, the scaled residuals are 10^{-4} for continuity; 10^{-5} for x/y velocities, k and ϵ ; and 10^{-7} for energy and DO intensity, as shown in Fig. 6.6.

Three meshes: coarse ($\approx 26,000$ cells), medium ($\approx 40,000$ cells) and fine ($\approx 61,000$ cells); and four time-steps: 60s, 120s, 360s and 720s were evaluated in this model independence study. Mesh refinement was performed by varying all mesh sizes by the same ratio. Apart from the benchmark model simulation, the default FLUENT residual convergence criteria and first-order discretisation schemes were employed for all other investigated models. Furthermore, air is modelled as an ideal gas to account for buoyancy effects, the body-force weighted scheme was used for the pressure discretisation, the RNG k- ϵ model non-slip wall conditions were used for turbulence and the SIMPLE algorithm was used for the pressure-velocity coupling. The enhanced wall treatment is used to model the near-wall flows, because the enhanced-wall function in FLUENT allows an adequate representation of the velocity and thermal profiles for different flow regimes, including in the buffer region ($3 < y^+ < 10$) (ANSYS FLUENT theory guide, 2010).

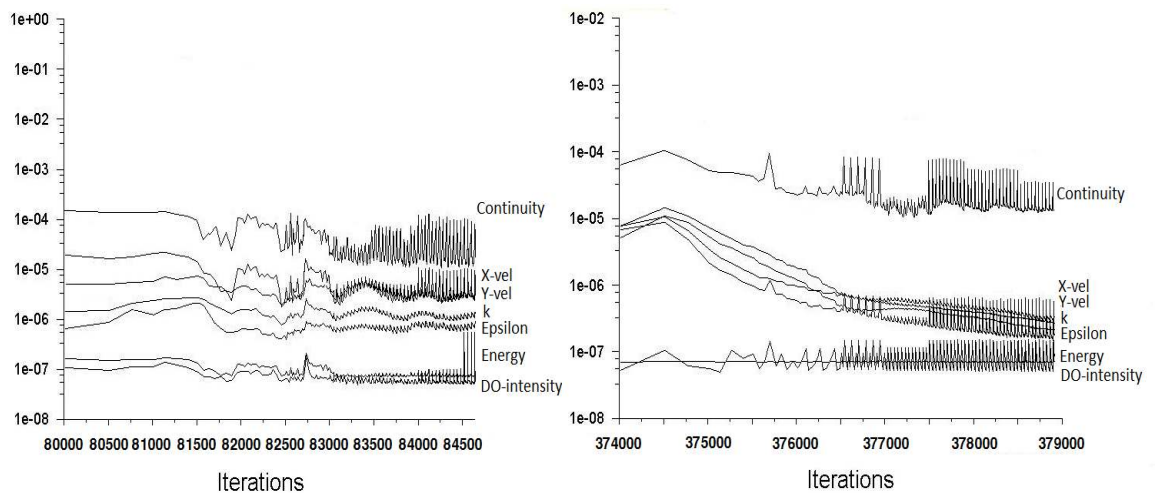


Fig. 6.6. Scaled residuals for the benchmark model only, over the course of the simulation

The mean errors and standard deviations from the L_2 norm study shown in Figs. 6.7 are determined from 36 uniformly distributed points in the comfort zone at heights of 0.3 m, 1.2 m, and 2 m, and time intervals of 1 hour.

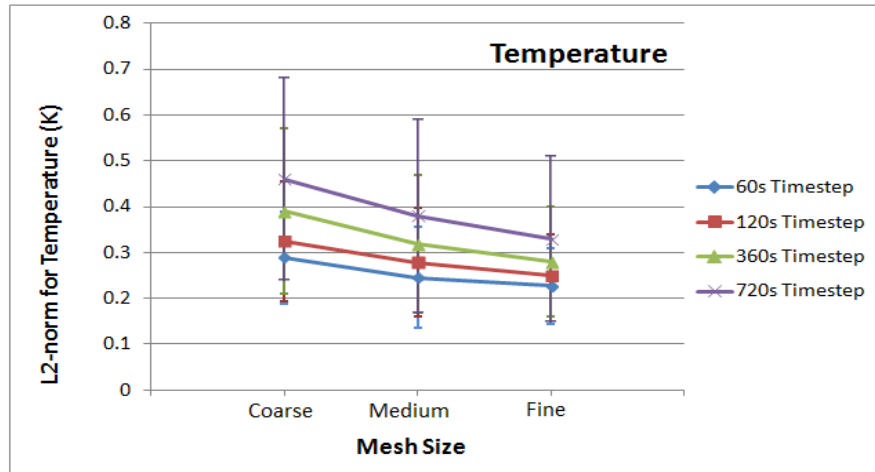


Fig. 6.7(a). L_2 norm for Temperature

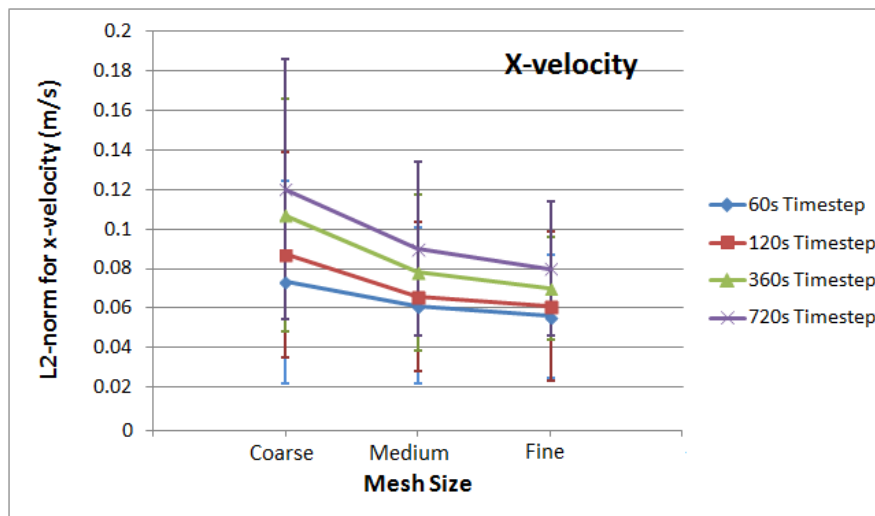


Fig. 6.7(b). L_2 norm for x-velocity

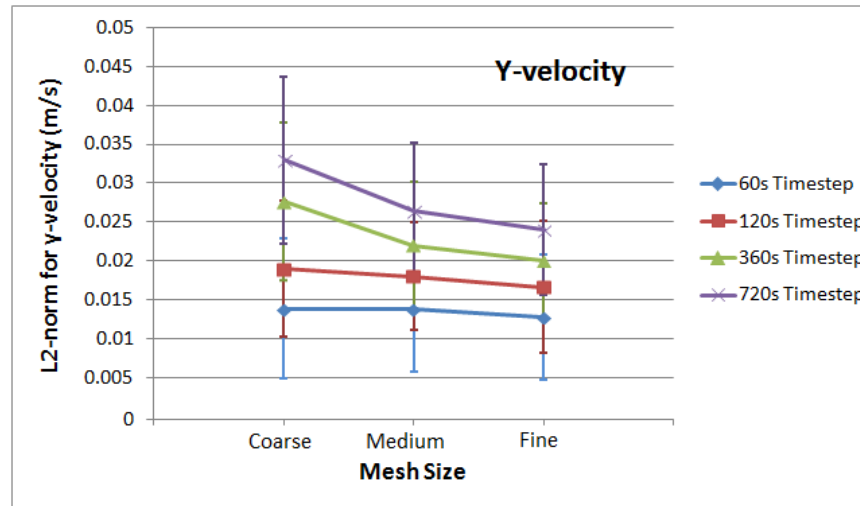


Fig. 6.7(c). L_2 norm for y-velocity

In order to enhance the practicality and realism of this study, the maximum errors are taken to be similar to the uncertainty of real-life sensors. Hence, the error requirements are taken to be 0.5K (similar to errors in K-type thermocouples) and 0.15 m/s (similar to errors in the TSI VelociCalc 8386® Pitot-tube velocity meter). Figs. 6.7 show that although the scaled residuals convergence criteria is relaxed for the investigated models, relative to the benchmark model, the errors for the different mesh sizes and time-steps are still within reasonable margins. The use of first order discretisation schemes in the investigated models improved the residual convergence stability in this case.

For the case of the simulated models, the velocity error requirement is satisfied with the Coarse-60s/120s, and all the medium and fine configurations. However, the temperature error requirement is only satisfied with the Coarse-60s/120s, Medium-60s/120s/360s and Fine-60s/120s/360s configurations. As a result, the medium mesh with 360s time-step was finally chosen for the CFD model, on the basis of a temperature error level lower than 0.5K and the relatively lower computing times. The resulting CFD grid is shown in Fig. 6.8 (Gowreesunker et al, 2013b).

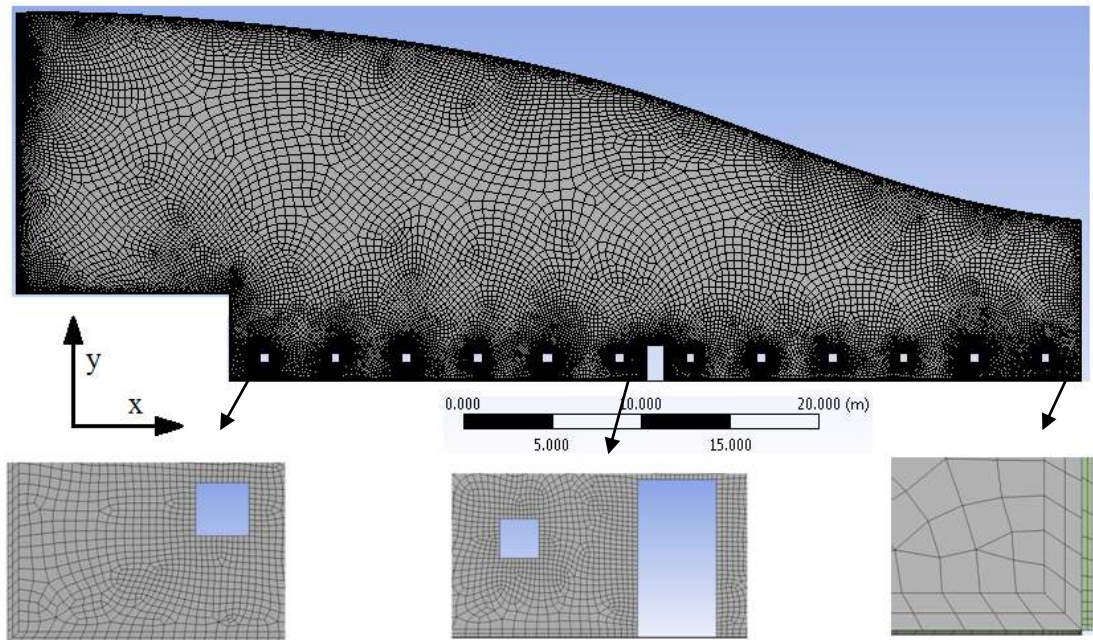


Fig. 6.8. Airport Terminal Space Model Grid

The mesh shown in Fig. 6.8 is designed using the in-built ANSYS® design modeller meshing algorithm, and consists of mainly hexahedral cells. The air domain is made of unstructured mesh, with a face cell size of 5 cm and growth rate of 1.1 at the internal gains; a face cell size of 10 cm and growth rate of 1.05 at the envelope surfaces, producing a first inflated layer of 4 cm; and a face cell size at the inlet and outlet of 6 cm. The mesh gradually increases towards the bulk of the air domain producing a maximum cell size of 75 cm. The roof, glazing and floor domains are made of structured hexahedral cells ranging from 3 cm to 10 cm, with 2-5 mesh intervals, with the finest meshes in the floor domain to appropriately account for the solar heat fluxes.

6.7 Coupled Model

As elaborated in section 6.3, the coupling between an ES tool (TRNSYS) and a CFD package (FLUENT) is essential in order to account for the impact of air-movement in the airport terminal space on the energy consumption of the HVAC system. This coupling can be accomplished through the use of a script and results file which transfers the required information between the two software. At present, it is simpler to allow TRNSYS to control the entire coupling, due to the ease of incorporating a user-built component in its architecture. Modifying the FLUENT kernel would be beyond the scope of this study.

A quasi-dynamic coupling method is employed in this study, where the transfer of information between the two tools is done at the end of each time-step. This method is chosen based on its practicality of use and much lower simulation times than fully-dynamic simulations. Furthermore, as shown in the works of Zhai and Chen (2006), quasi-dynamic coupling can provide very similar results to fully-dynamic coupling for cases where the thermal behaviour of the building does not change significantly within a time-step. It is therefore important to determine the maximum time-steps allowed in the simulations, whereby the prediction errors are acceptable.

In this study, it has already been confirmed in section 6.6 that a time-step of 360s in CFD is appropriate for the terminal space, because the temperature and velocity norms vary within the error limits of actual sensors. The coupled simulation should however also ensure a small enough time-step so that the switching effects of the PID controller are accounted for in the simulations. This is also justified with regards to the performance of real-life sensors, such as the Siemens REV200® or the REV23RF® PID building temperature controllers. These controllers are employed for both massive and lightweight structures, and operate with switching cycles of 360s or 720s, depending on the size and thermal response of the building (Siemens, 2001). This implies that the time-step of the TRNSYS PID controller should also be in the range of 360s to 720s, so that the effect of the switching cycles of the PID controller is not lost in the quasi-dynamic coupling. Thus, considering the maximum time-step of the CFD model and the switching cycles of the PID controller, 360s (0.1 hr) is chosen as the time-step for both the CFD and TRNSYS models.

The general transfer of information between the two simulation tools is shown in Fig. 6.9.

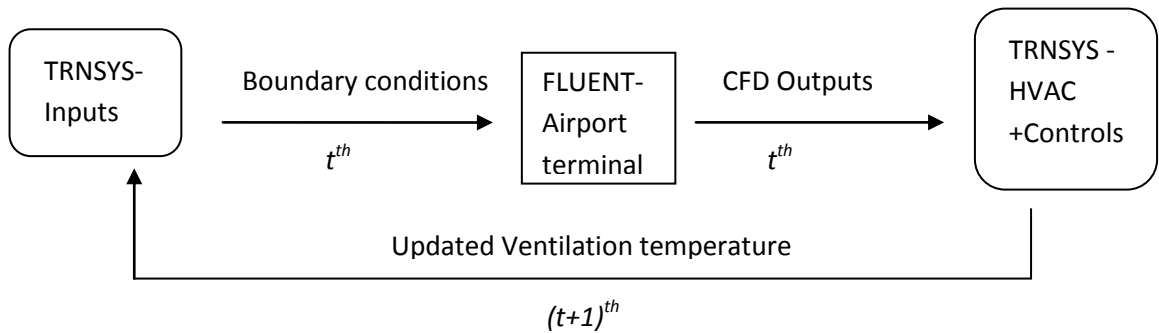


Fig. 6.9. Generic flow of information in TRNSYS-FLUENT coupling for normal HVAC system

The ‘inputs’ from TRNSYS at time t^{th} are passed as boundary conditions to the FLUENT model, where the latter solves the discretised governing equations, and the ‘CFD-outputs’ results are returned to TRNSYS at t^{th} . However, because of the successive substitution method used by TRNSYS, the ‘CFD-outputs’ are actually used at time $t+1^{\text{th}}$ for the ‘updated ventilation temperature’, hence completing the information loop.

Table 6.2. Information exchanged in coupled simulation

TRNSYS inputs (Boundary conditions) - (Script file)	CFD Outputs - (Results file)
Linearly interpolated weather data (ambient temperature (T_{amb}), sky temperatures (T_{sky}), floor solar gains)	Feedback temperature (T_f)
Internal heat gains (lighting, occupancy gain)	Return air temperature (T_r)
Ventilation conditions (supply air temperature (T_s), supply air mass flow rate)	

The TRNSYS screen-shot and program files can be found in Appendix D. This coupled model is also described in Gowreesunker et al (2013b).

6.8 Summary of Chapter 6

This chapter explains the quasi-dynamic coupling method employed between FLUENT and TRNSYS. It describes the L_2 norm procedure used to obtain a CFD model of the airport terminal space, where the errors associated with the time-steps and mesh sizes are within the uncertainties of real-life sensors. It also describes the flow of information between the two simulation tools, as well as the parameters exchanged. Furthermore, the HVAC and control systems are also described.

The chapter also provides the settings employed in the quasi-dynamic simulations of the airport terminal in order to determine the energy consumption. Further details of the TRNSYS model are provided in Appendix D. The following chapter describes the actual PCM systems and models investigated in this study which includes two passive systems and a semi-active system. The parameters exchanged and the flow of information between the simulation tools can be slightly different depending on the PCM system investigated.

CHAPTER 7 – AIRPORT PCM SYSTEMS

Although the number of passengers travelling through UK airports keeps increasing, existing airport terminals will continue to be in operations due to land space constraints (CAA, 2011). It can therefore be anticipated that refurbishment of these existing airports will become more frequent, emphasising the importance of retrofitting using novel energy saving systems. Thus, in addition to providing adequate energy savings to the airport terminal, the ease of retrofitting the PCM systems into existing airports was also considered in the choice of the investigated PCM systems.

This chapter describes the different PCM systems investigated for the airport terminal space described in Chapter 6. Two passive systems, PCM floor tiles and a PCM glazing envelope, as well as a semi-active PCM heat-exchanger system are investigated. These systems are studied for the case of displacement conditioning, which is more popular for large indoor spaces with high ceilings, due to their lower cooling energy consumption (Gowreesunker and Tassou, 2013 **d, e**).

Each of the PCM systems are modelled in FLUENT using the phase change models described later in this chapter. The PCMs are discretised in order to obtain a more accurate representation of the internal heat transfer processes. The flow of information and parameters exchanged in the TRNSYS-FLUENT coupling may differ depending on the particular PCM system modelled.

Additionally, because the FLUENT model requires extensive simulation times, discrete time-dependent simulations will be performed for generic weather patterns. The yearly energy demands are determined using the concept of Degree Days, as explained in section 7.5. Sections 7.1 to 7.3 describe the models of the PCM tiles, PCM glazing and PCM-HX system, respectively.

7.1 PCM Floor Tiles

The use of the PCM floor tiles implies replacing the normal floor tiles described in Table 6.1 by modified floor tiles impregnated with PCM. The PCM tiles are explicitly discretised in the FLUENT model as shown in Fig. 7.1, and the enhanced phase change conduction model described in section 3.3 is used to simulate the thermal performance. This enhanced phase change method is employed here, because such passive systems operate mainly on the thermodynamics of the PCM, in order to dampen the indoor temperature fluctuations (Zhou *et al*, 2012), and therefore require a detailed representation of phase change.

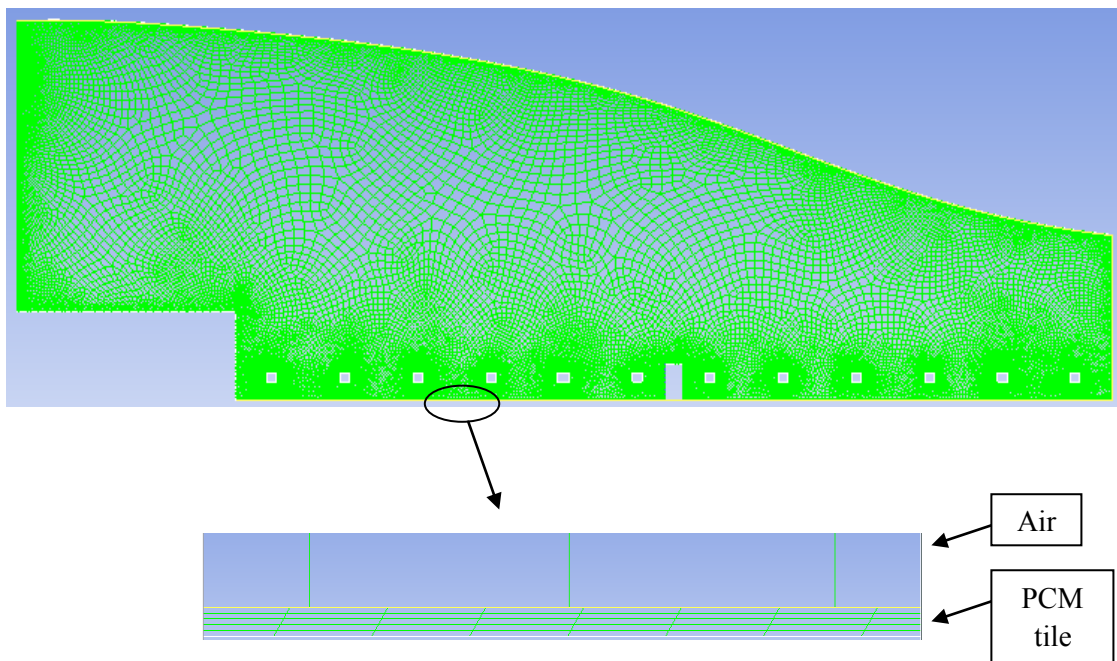


Fig. 7.1 PCM tiles grid

The phase change characteristics of the tiles are the same as commercial PCM products, such as the EBB-PCM-Clay[®] boards (as used in section 4.2) and the Dupont Energain[®], but have the same physical dimensions as the normal floor tiles. These products have been chosen as the peak phase change temperature is near the optimum comfort temperature of 21°C and the overall phase change temperature range spans the comfort temperature range. However, the two PCM tiles have relatively different latent heat capacity. The physical and thermal characteristics of the different floor tiles are shown in Table 7.1.

Table 7.1. Floor tiles physical and thermal characteristics

	Thickness (mm)	ρ (kg/m ³)	λ (W/mK)	c_p (J/kgK)	ϵ_{ext}	ϵ_{int}	τ
Normal Tiles	13	1700	0.8	850	-	0.5	-
Ebb-PCM® Tiles	13	1430	0.14	1240	-	0.5	-
‘Energain’® Tiles	13	1430	0.14	1240	-	0.5	-

Note that the Energain tiles properties from Table 7.1 are similar to the Ebb-PCM tiles, but the two tiles have different phase change properties. The fictitious Energain® tile has been used to show the energy impact of using a different PCM in the tiles. The phase change characteristics of the PCMs are given below (obtained from DSC measurements at 0.5 K/min), and are applied to the FLUENT model via UDFs.

Ebb-PCM tiles (Temperatures in equations in K):

Melting: 285.2 K (12.05°C) < T < 295.8 K (22.65°C) ; Enthalpy: 15.6 kJ/kg

$$S_{E, m} = 12.781736 T^3 - 10932.541511 T^2 + 3117074.922039 T - 296256708.8957 \quad (7.1)$$

$(R^2 = 0.999)$

Freezing: 295.2 K (22.05°C) < T < 284.7 K (11.55°C) ; Enthalpy: 17.4 kJ/kg

$$-S_{E, f} = 13.026531 T^3 - 11055.072091 T^2 + 3129090.962073 T - 295246573.26512 \quad (7.2)$$

$(R^2 = 0.998)$

Energain tiles (Temperatures in equations in K):

Melting: 281.55 K (8.4°C) < T < 299.05 K (25.9°C) ; Enthalpy: 56.4 kJ/kg

$$S_{E, m} = -0.189779 T^5 + 272.61369 T^4 - 156615.961029 T^3 + 44980610.444 T^2 - 6458295211.7616T + 370856404172.359 \quad (7.3)$$

$(R^2 = 0.999)$

Freezing: 296.79 K (23.64°C) < T < 276.15 K (3.0°C) ; Enthalpy: 69.3 kJ/kg

$$-S_{E, f} = 0.04292 T^5 - 63.0934T^4 + 37056.44153 T^3 - 10870156.565 T^2 + 1592636432.2822 T - 93242273523.9778 \quad (7.4)$$

$(R^2 = 0.999)$

Furthermore, two night ventilation recharge strategies are investigated for the recharge of the PCM tiles: no-night ventilation; and night ventilation during the non-occupied hours of the airport (between 24:00 and 04:00). As the PCM tiles are located within the terminal space, the ventilated night air must pass through the indoor space in order to re-charge the tiles (i.e. flush the airport indoor space). Hence, during the summer or intermediate periods, outdoor air is assumed to pass through the airport at night; and during the winter period, the indoor air is re-circulated through the DC diffuser to provide air movement in the terminal space to re-charge the tiles. The night ventilation rate through the diffuser for the 2D airport geometry is maintained at 0.5 kg/s for all cases.

For the PCM tiles simulations, the TRNSYS-FLUENT coupling is similar to the normal DC simulation described in section 6.7, and the phase change effect is accounted for in the FLUENT model.

7.2 PCM Glazing Envelope

As indicated in chapter 5, past research in the field of PCM glazing has been relatively scarce. However more recently, with the advent of commercial PCM glazed units, it has generated renewed attention. Thus, because of the large glazed areas in Airport terminal buildings, the energy performance of such systems is of interest to this study.

7.2.1 PCM Glazing Model

A PCM glazing envelope involves replacing the partly-glazed roof and side-glazing of the terminal space with modified glazing units with PCM. Hence, the 30 mm thick glazing and roof units described in Table 6.1 are replaced with double glazing units with two 8 mm glass encapsulation panels and PCM RT27[®] in the 30 mm cavity, (in a similar manner to Fig. 5.8). This configuration is similar to commercial structural glazing products such as the SunGuard[®] (Guardian Industries Corp., 2012), which roughly uses glass dimensions twice the size of conventional double glazing units for structural purposes. The PCM RT27[®] is employed here based on the specifications of commercial products such as the Delta-Cool 28[®], which employ PCM with phase change temperatures in the range of 26 – 30 °C, and which were shown to be adequate for the European climate (DELTA, 2013).

The modelling of PCM glazing is more complex than ordinary PCM systems (such as PCM tiles) because the heat transfer process within the PCM constitutes of both conduction and radiation. Convection within the PCM is neglected in this case because the two 8mm glass panels provide the dominant thermal resistance in the overall glazing unit. The validated method described in chapter 5 and Gowreesunker *et al.* (2013c) is employed to simulate the thermal and optical aspects of the PCM glazing envelope. The thermophysical and phase change properties of RT27[®] can be found in chapter 5, and the glass properties in Table 6.1, noting that $\varepsilon = \alpha$ according to Kirchhoff's Radiation law (Siegel and Spuckler, 1994).

It should be noted that because radiation transfer between the sky and the external surface of the glazing is not explicitly modelled in FLUENT, the relationships for the radiation properties (scattering, absorption and extinction coefficients) of the PCM

described by Eqs. (5.1-5.3) are not used. Instead, a more lumped approach is employed, as described by Eqs. (7.5-7.8) (Gowreesunker *et al*, 2013c):

The transmittance of the PCM is:

$$\tau_{PCM} = 10^{-d} \quad (7.5)$$

$$\text{where } d = [\beta \cdot \sigma_{e,liq} + (1-\beta) \cdot \sigma_{e,sol}] \cdot s \quad (7.6)$$

The absorption of the PCM is:

$$\alpha_{PCM} = [\delta \cdot \beta + (1-\delta)] \cdot (1-\tau_{PCM}) \quad (7.7)$$

The reflectance of the PCM due to scattering is:

$$\rho_{PCM} = [\delta - \delta \cdot \beta] \cdot (1-\tau_{PCM}) \quad (7.8)$$

Referring to Fig. 5.1, with a transmittance value of 0.4 and 0.9 for the solid and liquid phases, respectively, δ is found to be 0.83 using Eq. (5.4). The physical thickness ‘s’ of the PCM is 30 mm; the extinction coefficients are 30 m^{-1} and 4 m^{-1} for the solid ($\sigma_{e,sol}$) and liquid phases ($\sigma_{e,liq}$), respectively obtained from Fig. 5.4, and the variation of the liquid fraction term (β) is obtained from Eq. (C1.6) in Appendix C.

The overall transmittance and absorptance of the glazing units are obtained according to the conservation of energy principle, as follows:

$$\text{Transmittance of overall glazing unit } (\tau_{unit}) = (\tau_{gl} \cdot \tau_{PCM}) \quad (7.9)$$

$$\text{Absorptance of overall glazing unit } (\alpha_{unit}) = (\alpha_{gl} + \alpha_{PCM} - \alpha_{gl} \cdot \alpha_{PCM}) \quad (7.10)$$

The transmitted energy is applied as a heat generation rate on the floor of the terminal space, whilst the absorbed radiation in the glazed units is implemented as described in section 6.4.1. The glazing and roof radiation properties are modified according to Eqs. (7.9 and 7.10). At night, emission from the glazing and roof surfaces occurs according the external surface emittance only, as described in section 6.4.1, and the radiation interaction between different PCM phases is ignored.

Phase change is simulated with the effective heat capacity method, according to the variation of c_p obtained from Eqs. (C1.4 - 1.5) in Appendix C. The variation of c_p is implemented as User Defined Function (UDF) in FLUENT.

7.2.2 TRNSYS-FLUENT Coupling for PCM Glazing

In this case, because the solar heat fluxes and the radiation boundary conditions are calculated directly in TRNSYS and then passed to FLUENT, the radiation characteristics of the PCM were also calculated in TRNSYS. As a result, although the overall coupling strategy remained unchanged from the normal DC case, the exchanged parameters are different as shown in Fig. 7.2.

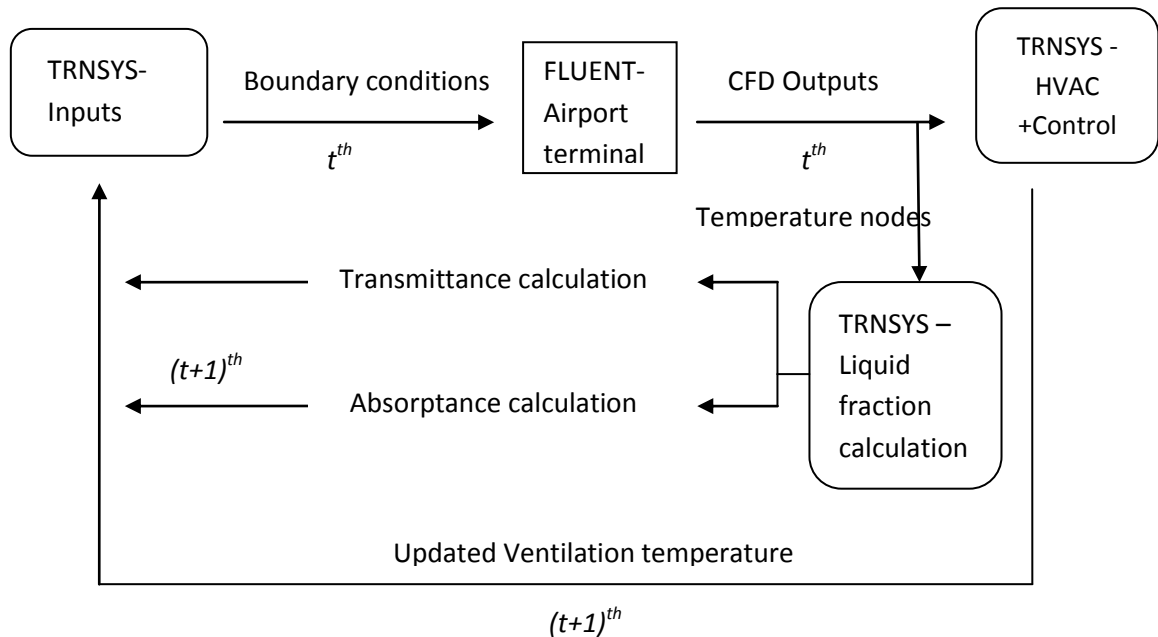


Fig. 7.2. Flow of information in TRNSYS-FLUENT coupling for the PCM-glazed model

Furthermore, expanding on the lumped-radiation modelling approach of the PCM, the temperature at 11 segments/ nodes inside the roof and glazing are used in the calculation of the radiation characteristics of the PCM-glazed envelope. The nodes shown in Fig. 7.3 are chosen for segments where the temperatures are observed to be quasi-uniform (i.e. $<0.4^{\circ}\text{C}$ difference). The roof and glazing domains were refined to 6 mesh intervals in order to increase the simulation accuracy for the phase change.

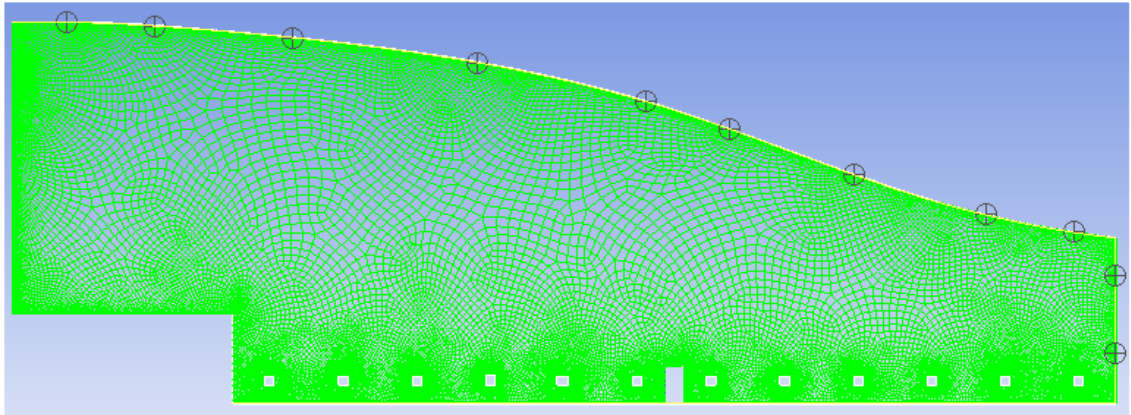


Fig. 7.3. Temperature nodes used in calculating the radiation properties of RT27

Referring to Fig. 7.2, in addition to the normal parameters produced by FLUENT at t^{th} , the 11 extra temperatures from the nodes in Fig. 7.3 are also returned to TRNSYS. TRNSYS then employs these temperatures at t^{th} to calculate the liquid fraction of the PCM for each node using Eq. (C1.6), and subsequently, the transmittance and absorptance of the glazing units, using Eq. (7.9) and Eq. (7.10). These radiation parameters are then used to adjust the floor solar heat flux and external surface absorptivities for the FLUENT model at $(t+1)^{th}$, therefore completing the information loop. Note that the surface absorptances are separately supplied by TRNSYS to each segment in the FLUENT model, and that the overall transmitted radiation is uniformly distributed on the floor. Furthermore, the two night ventilation recharge strategies employed for the PCM tiles are also used for this PCM-glazed envelope.

In essence, TRNSYS is used to calculate the radiation transmittance and absorptance of the PCM-glazed envelope for every PCM state, and to provide the floor solar heat flux. FLUENT simulates the phase change process of the PCM and the indoor air movement. It can be argued that the lumped approach used to simulate radiation in the PCM is limited by the fact that it assumes uniform properties for each node. However, referring to Fig. C1.2b, where the uncertainty in the temperature values is $\pm 0.4^{\circ}\text{C}$, this approach can be justified as the temperature difference over each segment in the model is also within this uncertainty margin.

7.3 PCM Heat-Exchanger (PCM-HX)

This PCM-HX system represents a semi-active arrangement to provide free conditioning of the airport space. The arrangement consists of the Rubitherm GmbH CSM[®] plates (see Fig. 7.4) retrofitted inside the displacement DC diffuser in the airport departure hall shown in Fig. 7.5. The plates are symmetrically arranged as shown in Fig. 7.6.

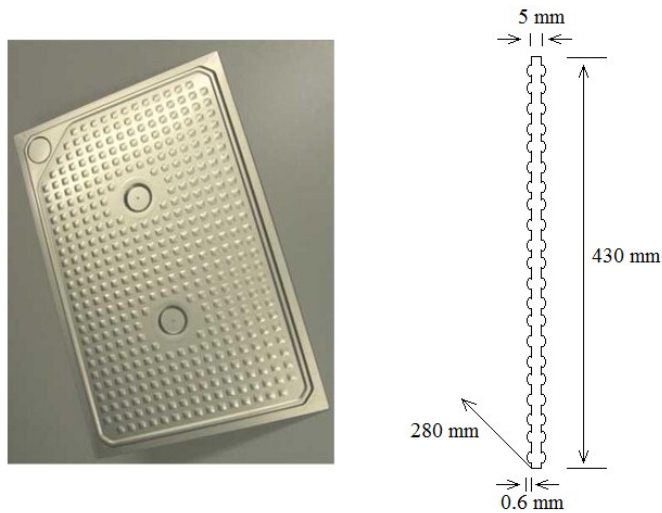


Fig. 7.4. Rubitherm GmbH CSM[®] plate



Fig. 7.5. Actual Heathrow Terminal 5 diffuser

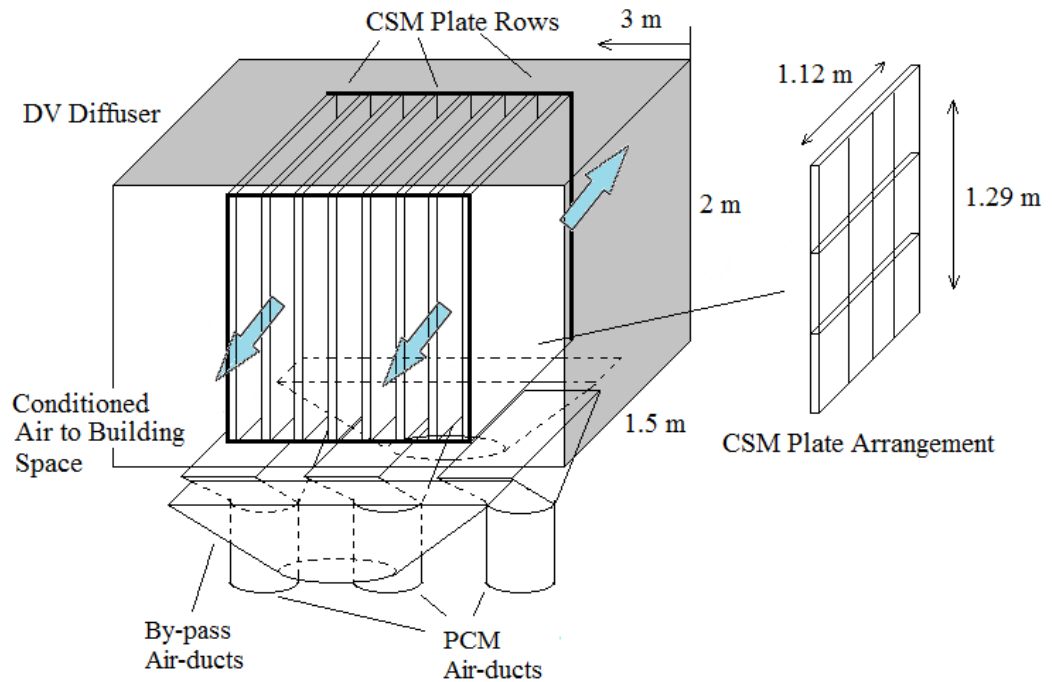


Fig. 7.6. Schematic of DV diffuser, CSM plate arrangement, and supply and by-pass ducts inside diffuser

Due to the large air volume flow rate supplied by each diffuser to the space, the surface area of the diffusers has to be large in order to satisfy the low velocity requirements of displacement ventilation system (CIBSE B, 2006). The volume inside the diffuser is however mainly empty space, which provides the opportunity to retrofit the PCM-HX system.

7.3.1 PCM-HX Model

Due to the symmetry of the PCM-HX arrangement, a 2D model of the PCM plates is employed. The protrusions of the plate surface into the air stream, shown in Fig. 7.4, are crucial in the heat transfer calculations from the plates, and are incorporated as a surface roughness of 0.25 mm in the FLUENT model (Dolado *et al*, 2011).

The mesh employed in the CSM® plate model consists of structured 1.0×3.0 mm hexahedral cells in the PCM domain, and hexahedral cells with a face size of 2mm with growth ratio of 1.2 in the air domain, as shown in Fig. 7.7. The RNG k-ε turbulence model was used, as it is adaptable to both high and low turbulence scenarios. The phase

change process was modelled with the enthalpy porosity method, and the properties of the PCM used are: $\lambda = 0.2 \text{ W/mK}$; $\rho = 820 \text{ kg/m}^3$; $c_p = 2100 \text{ J/kgK}$; phase change range = $16 - 25 \text{ }^\circ\text{C}$; and latent enthalpy = 180 kJ/kg , similar to the phase change properties of RT25[®] used in the experimental free-cooling system of Zalba *et al.* (2004). Furthermore, the adequacy of the enthalpy-porosity method for PCM heat exchanger systems is confirmed by the studies of Ye *et al.* (2011).

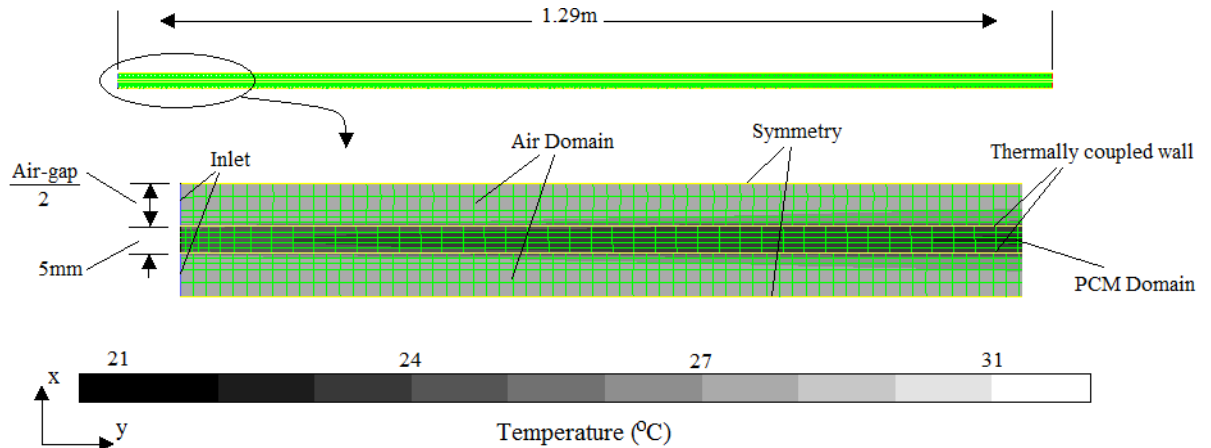


Fig. 7.7. Model description of CSM Plate

To allow for appropriate residual convergence, a time-step of 20 s was employed for the plate model. Hence, for one time-step in the Airport-CFD and TRNSYS models, 18 sub time-steps were performed for the PCM plate model to ensure that all the simulation components were at the same time, i.e. to produce a coherent overall time-step of 360 s.

In order to size the system, the following set of simulations was performed to gain an understanding of the heat transfer rates associated with the plate arrangements within the diffuser. This was done by varying the air gap between the plates in the model of Fig. 7.7, and computing the total heat transfer rate for an entire diffuser, according to the scenario presented in Fig. 7.6. The results are shown in Fig. 7.8.

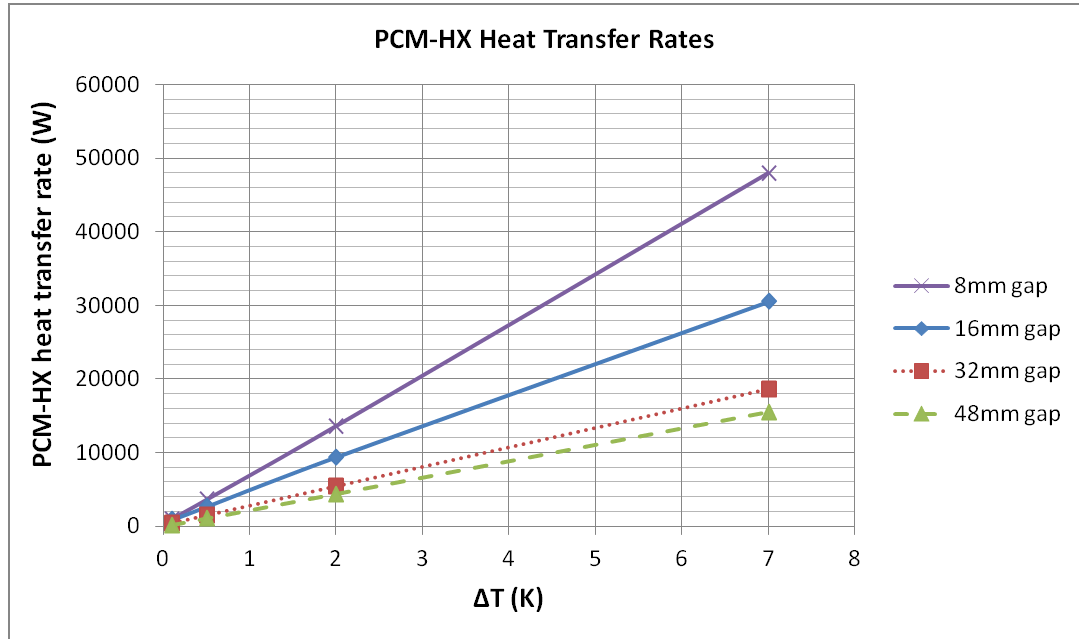


Fig. 7.8. Heat transfer rates of PCM-HX unit for different air-gaps between plates at a total mass flow rate of 6 kg/s (i.e. (0.5 kg/s/m in the 2D geometry) × (12m served by 1 diffuser)). ΔT is the temperature difference between the incoming air and the PCM plate.

According to the HVAC size in section 6.5, 48 kW of conditioning is required per diffuser to fully satisfy the conditioning load of the airport terminal. Fig. 7.8 shows that employing an air-gap of 8mm produces a heat transfer rate of 47.9kW per diffuser, while using an air-gap of 16mm produces a heat transfer rate of 30 kW, at a temperature difference of 7K. Hence, an air-gap of 8mm should be adequate for this study.

However, for completeness, an air-gap of 16mm is also studied so as to investigate the energy impact of adequately sizing the PCM-HX. This amounts to a total PCM latent heat capacity of 202MJ (190 rows) and 133MJ (125 rows) for air-gaps of 8mm and 16mm, respectively. The air convection heat transfer coefficient for the plates in the 16mm air gap configuration is 14.3 W/m²K and in the 8mm air gap configuration is 16.05 W/m²K. Furthermore, the pressure drops across the plates with an air-gap of 8mm and 16mm are 45Pa and 10Pa, respectively.

As the HVAC system is a constant air-volume system, the air-mass flow rate passing through the PCM plate arrangement is also constant. This amounts to 0.048 kg/s (i.e. 6 kg/s ÷ 125 rows) and 0.032 kg/s (i.e. 6 kg/s ÷ 190 rows) per row, for each air-gap case. These mass flow rates are applied to the model in Fig. 7.7.

7.3.2 TRNSYS-FLUENT Coupling for PCM-HX

The TRNSYS-FLUENT coupling for the PCM-HX system is done via a secondary custom built component in TRNSYS that transfers the required parameters to the separate PCM plate FLUENT model (see Fig. 7.7). The flow of information is shown in Fig. 7.9.

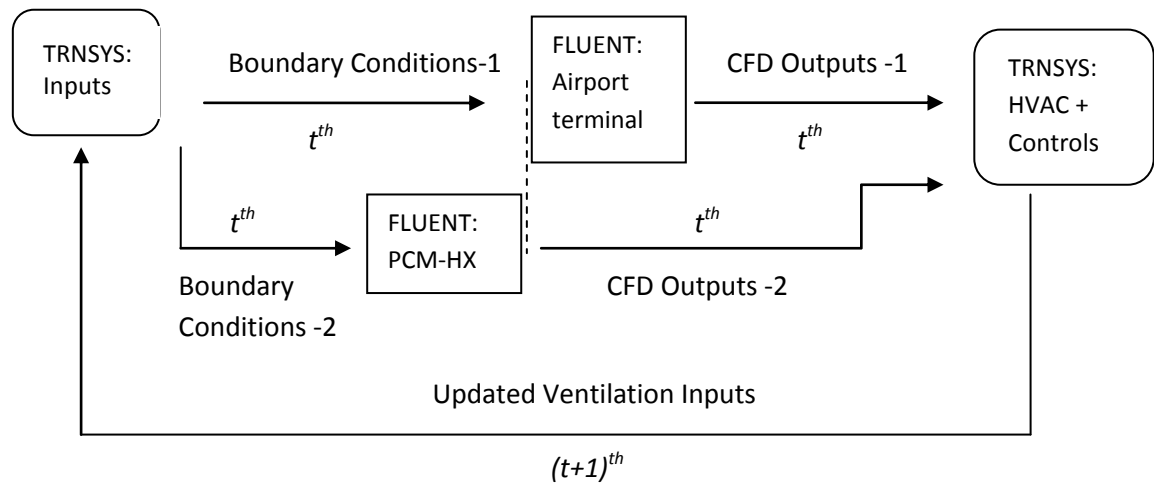


Fig. 7.9. Modified information flow for DC with PCM-HX

Fig 7.9 shows that the flow of information consists of the similar exchange of parameters as in the normal DC case described in Fig. 6.9, but additionally includes the ‘Boundary Conditions-2’ and ‘CFD Outputs-2’ with the PCM-HX plate model. Boundary Conditions-2 comprises the air mass flow rate and the mixed air temperature T_m (see Fig. 6.4), while CFD Outputs-2 consists of the PCM mean temperature and the outlet air temperature from the PCM-HX.

In this case, TRNSYS provides the boundary conditions for both the airport model and the PCM-HX model, and uses the CFD outputs to control both the airport and the PCM-HX system, as described in the next section. FLUENT is used to simulate both the building and the PCM-HX model, including the phase change process.

Due to the successive substitution method, each CFD component built in TRNSYS is simulated sequentially. Thus, the overall simulation time in running the airport model with the PCM-HX model is the addition of the individual simulation times of the two custom-built CFD components.

7.3.3 PCM-HX Control Strategies

The PCM-HX system is employed here for free-conditioning the airport terminal space. This generally refers to relying on the PCM plate arrangement to adequately condition the mixed air at temperature T_m (see Fig. 6.4), without the need for auxiliary heating or cooling. However, as the PCM-HX system is located in the diffuser, at the end of the HVAC line, and because of the irregularities in the internal heat gains, the air temperature leaving the PCM-HX is unpredictable. Hence, for this case, the following control strategies were employed:

If $T_f > T_{c,u}$; The PID controller will calculate a supply temperature $T_s < 21^\circ\text{C}$ to satisfy the cooling load, and the supply air bypasses the PCM-HX (see Fig. 7.6).

If $T_{c,l} \leq T_f \leq T_{c,u}$; The heating/cooling coils are non-operational, and air at T_m passes through the PCM-HX before being supplied to the space.

If $T_f < T_{c,l}$; The PID controller will calculate a supply temperature $T_s > 21^\circ\text{C}$ to satisfy the heating load, and the supply air bypasses the PCM-HX.

The PCM-HX is effectively used only when the indoor temperature is within the comfort level, where the PCM-HX aims at prolonging the duration of comfort, by providing suitable temperature dampening effects. An indication of the air-by-pass route inside the diffuser can be observed in Fig. 7.6.

In this study, three different night charging strategies are investigated for the PCM-HX when the airport terminal building is closed between 24:00 and 04:00: i) no night ventilation; ii) ‘non-stop’ full ventilation; and iii) a limiting ventilation control. During the summer and intermediate periods, cold ambient air is used for charging. The limiting control is done by monitoring the PCM temperature, and stopping night ventilation when the PCM temperature drops below the lower comfort level. The night outdoor-recharge air is used to simply flush the PCM-HX in the diffuser, and does not affect the indoor airport terminal space at night.

During winter, the return air from the airport is re-circulated through the PCM-HX to store the extra heat from the space (i.e. flushing the airport indoor space). In the winter case, the limiting control is performed by monitoring the difference between the return air temperature (T_r) and the mean PCM temperature (T_{pcm}), such that night ventilation is active only when there is a net positive heat transfer into the PCM, i.e. $T_r > T_{pcm}$. As mentioned earlier, the night ventilation rate for the 2D geometry is maintained at 0.5 kg/s for all cases.

7.4 Pressure Drop Calculations

The boundary used to calculate the pressure drops across the HVAC ducts is shown in Fig. 7.10.

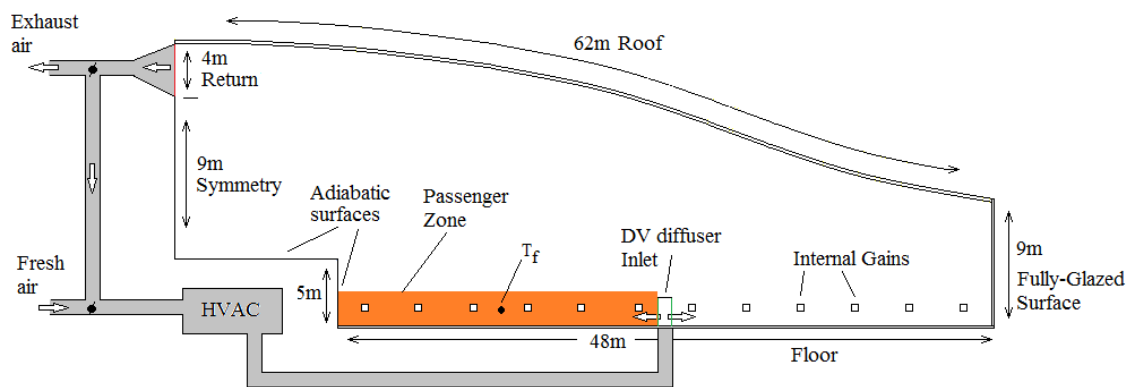


Fig. 7.10. HVAC ducting for airport terminal space

The sizing of the ducts was based on the velocity criteria provided by CIBSE guide B (2006), and the pressure drops are calculated from equations given in Idelchik (1994). A velocity of 15 m/s was used for the main ducts giving a diameter of 0.65 m, and a velocity of 10 m/s with a duct diameter of 0.45 m was used for the 3 final ducts run to the diffuser, as shown in Fig. 7.6. The detailed pressure drop calculations are shown in Appendix E.

Note that the air duct design serves only as an approximate means of quantifying the pressure drop for the different DC configurations, and that the same ducting configuration is employed for all DC and PCM system cases in order to abide by the comparative nature of this study.

7.5 Total Annual Energy Demand

The annual HVAC energy demand is obtained through the concept of Heating Degree Days (HDD) and Cooling Degree Days (CDD), as proposed by CIBSE TM-41 (Day, 2006). Degree days are a measure of how much (in degrees), and for how long (in days), the external air temperature is lower than a specific base temperature in the case of heating or above a specific base temperature in the case of cooling. It is used as a means of estimating the amount cooling/heating required by a building, as well as for energy management purposes (Day, 2006).

The key issue in employing this method relates to the choice of the base temperatures (i.e. reference temperatures), which allows the determination of the energy consumption of the building (Day, 2006). The base temperature refers to the external ambient temperature whereby the building does not require any energy to maintain the indoor comfort conditions. Hence, for HDD, the base temperature will be the ambient temperature above which heating is not required, and for CDD, it will be the ambient temperature below which cooling is not required.

This method is employed here mainly due to the extensive computing times associated with the CFD models, whereby the running of yearly simulations in CFD would be impractical. As suggested in Gowreesunker and Tassou (2013a), discrete and generic time dependent situations can be simulated to quantify the behaviour of the building and the HVAC system. The energy demand per degree day can be calculated for each of these simulated periods, and the total annual HDD and CDD are then used to extrapolate for the yearly energy demand. The base temperatures are obtained by analysing the energy demand and ambient temperature patterns of the stand-alone DC cases.

The simulations are therefore run for peak summer and winter conditions, and an intermediate condition, as described in Table 7.2 and Fig. 7.11, in order to obtain the behaviour of the building under different weather conditions. The Meteonorm C-37790 weather files for London are used for the simulations, and the weather data values for the 360s time-steps employed in this study are linearly interpolated between the hourly values. The intermediate conditions are obtained based on a probabilistic study of the

most frequent ambient air temperature ranges occurring during the year; which was found to be in the range of 10-23°C for this weather file.

Table 7.2 Discrete Simulation times

Intermediate	4500 – 4600 hrs
Summer	5434 – 5534 hrs
Winter	8576 – 8676 hrs

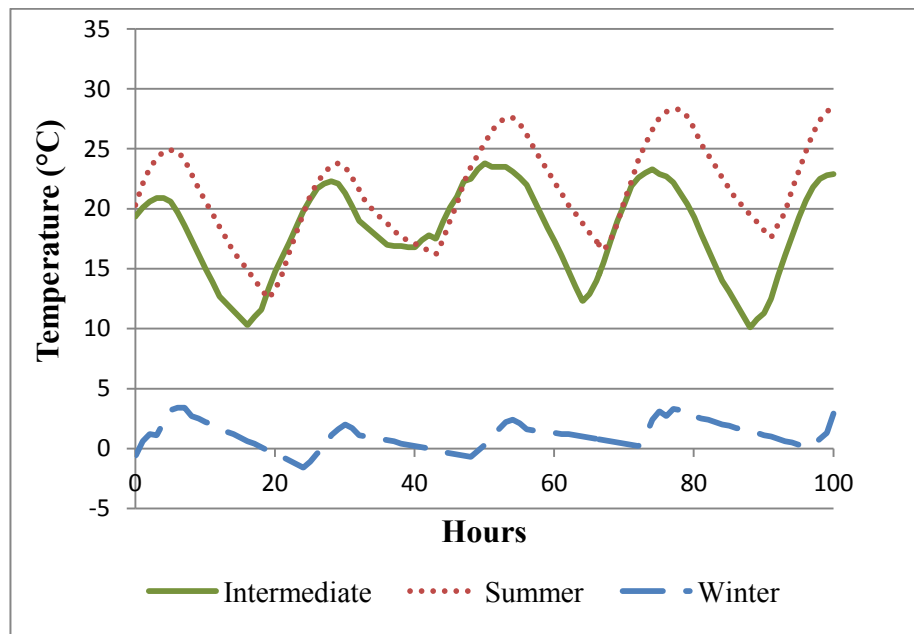


Fig. 7.11. Generic ambient temperatures for the different seasons

*Table. 7.3. Simulated and yearly Degree days for 15°C and 18°C base temperatures
(The base temperatures presented in Table 7.3 are obtained based on the energy demands, as explained in Appendix F)*

Seasons	HDD	CDD
Simulated Winter	46.35	0.00
Simulated Summer	0.29	13.79
Simulated Intermediate	2.49	6.27
Entire Year	1859.12	120.10

HDD and CDD have been employed in several studies such as Kolokotroni *et al.* (2010) and Bolatturk (2008), in the prediction of building energy consumption. This is due to its simplicity and speed of use, as well as the possibility to easily estimate the building energy performance for different weather conditions. This concept is therefore adopted for this study as it is an adequate method to estimate the annual energy demand for simulations requiring long computing times. It is also adequate for comparative analyses.

7.6 Summary of Chapter 7

This chapter describes the numerical models of the PCM systems studied for the airport terminal space. Two passive and one semi-active system are presented, which have been chosen based on their energy storage potential as well as suitability and ease-of-retrofit in the airport terminal. The implementation of the PCM tiles, PCM glazing and PCM-HX systems in the respective models, the thermo-physical properties of the PCMs, and the flow of information in the TRNSYS-FLUENT coupling are described. Furthermore, the control strategies involved with each system in terms of both the HVAC control system and the night recharge methods are also explained.

The layout for the air ducts is presented in section 7.4, and is maintained for all simulation scenarios, for comparative purposes. The pressure drops involved with each PCM system can be found in Appendix E. Because of the extensive simulation times involved in the CFD models, the concept of Degree Days was employed in the annual energy calculations.

The next chapter describes the air conditioning performance of the stand-alone DC system as well as each PCM system, when employed in the airport terminal space.

CHAPTER 8 – PERFORMANCE OF PCM SYSTEMS IN AIRPORT TERMINAL SPACE

This chapter presents a case study, depicting the numerical results obtained using the previously described models in the airport terminal space, with the TRNSYS-FLUENT coupled simulation method. The comfort temperature range is taken to be 18-23°C, as defined in Table 2.6 (CIBSE A, 2006). The HVAC mode of operation, described in section 6.5, allows the indoor temperature to closely follow the ambient conditions, and improve both the energy consumption and thermal comfort of the space, by providing the flexibility of the occupants to adapt to the indoor conditions.

In addition it also shows the thermal performance of the conventional stand-alone Displacement Conditioning (DC) system, and each of the PCM systems, namely: the PCM tiles ('Ebb' and 'Energain' tiles), the PCM-glazed envelope, and the retrofitted PCM-HX system (with 8mm and 16mm air gaps), described in Chapter 7. The simulations are run for discrete weather conditions and the annual energy demands are computed using the Degree Day concept. The first day of each simulation is neglected in the analysis, so as to avoid initialisation errors. The results include the indoor temperature progression as well as the energy demand trends for each system. These results are aimed at providing the relative energy performances of each PCM system.

8.1 Seasonal Performance of stand-alone DC system

This scenario involves the modelling of the conventional DC system using the CFD and TRNSYS HVAC models, without the use of PCM systems. A time-step of 360s was used for both TRNSYS and CFD, as explained in section 6.7, with an average of 40 iterations per time-step for the CFD simulation to satisfy the convergence criteria. All simulations are initialised at 21°C, and the overall actual simulation time for each season was 13 hrs with a 3GHz i7 processor. The results are given in Fig. 8.1.

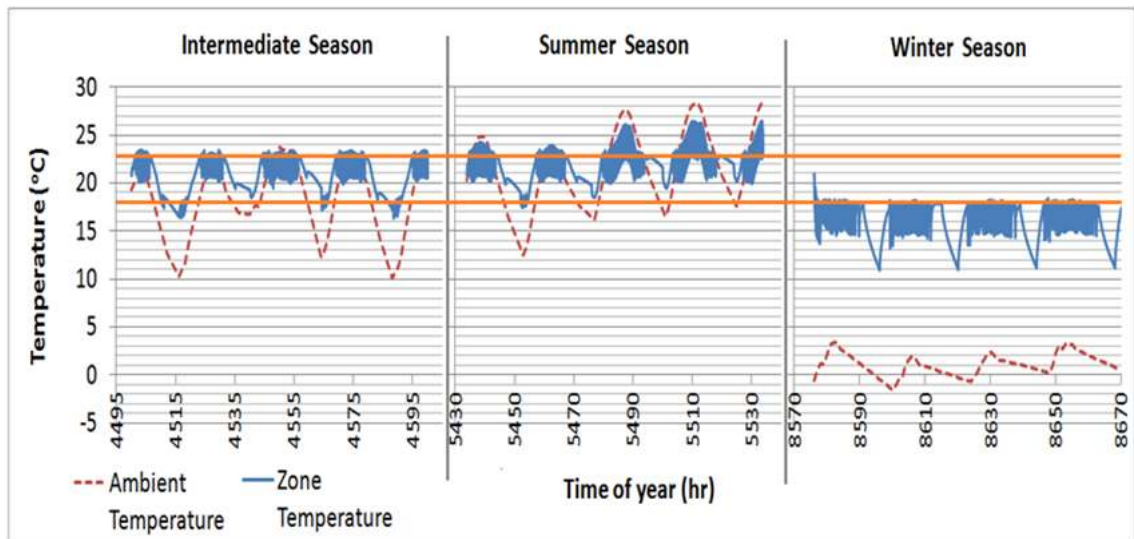


Fig. 8.1(a). Ambient and zone temperature (T_f) profiles for the three distinct seasons in 'DC-only' Case

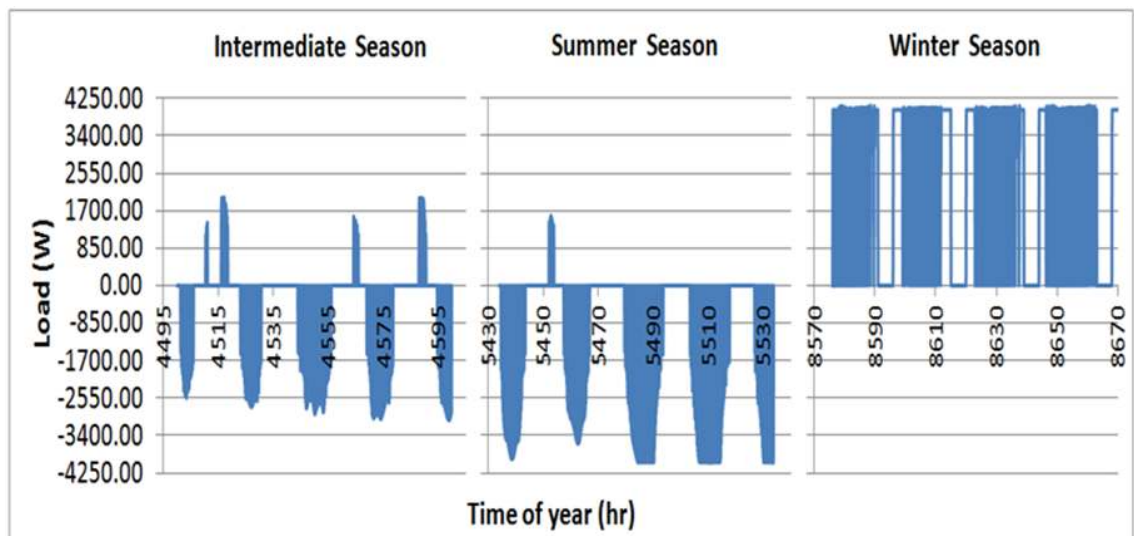


Fig. 8.1(b). Heating (+) and cooling (-) energy load Profile for 'DC-only' case for 2D geometry

During the intermediate period, the DC system successfully controls T_f within the comfort temperature range of 18-23 °C. The majority of the energy requirement is for cooling, with a relatively small amount for heating during the early hours of the morning. During the summer period, the zone temperature is less effectively controlled compared to the intermediate season, where the temperature reaches ~26 °C at mid-day. Similar to the intermediate season, the majority of the load is for cooling during summer, but heating is also required on a small number of occasions when the ambient temperature is low during early mornings.

During winter, only heating is required by the space. However, Fig. 8.1(a) shows that based on the control strategy used, the DC system is unable to satisfy the comfort requirements in winter; where the zone temperature varies between 15 °C and 18 °C. This anomaly is further explained in section 8.5.2.

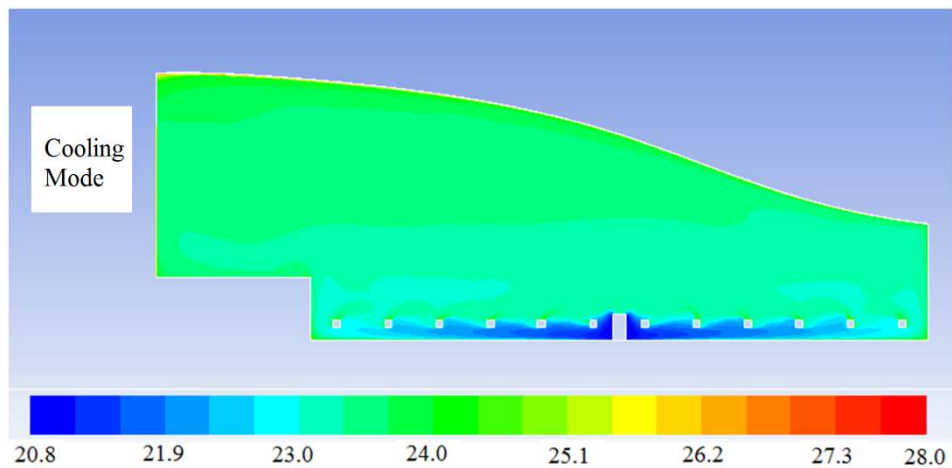


Fig. 8.2(a). Temperature contour (°C) still-frame during the DC unit cooling mode

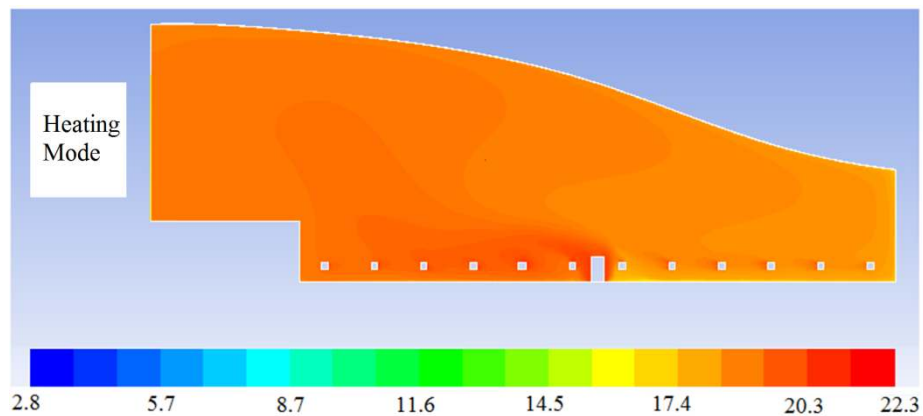


Fig. 8.2(b). Temperature contour (°C) still-frame during the DC unit heating mode

Fig. 8.2 demonstrates why DC is more suitable for cooling purposes, rather than heating large spaces. During the cooling mode, Fig. 8.2 (a) shows the buoyancy effects of the DC system enhance cooling in the space, with the cold air spreading on the floor until it reaches a heat source. This enables the cooling potential of the DC system to be specifically directed to the occupied space and avoid unnecessary conditioning of unoccupied areas. Furthermore, the temperature stratification effect in the space prevents further heat gains from the higher levels in the building envelope by reducing the temperature difference with the external conditions. In the case of heating, the DC system behaviour resembles a mixed ventilation system (Gowreesunker *et al*, 2013d). Fig. 8.2(b) shows that the warm air supplied by the displacement diffuser rises quickly and mixes with the indoor air due to its dominant buoyant force, hence failing to establish the temperature stratification benefits in the space.

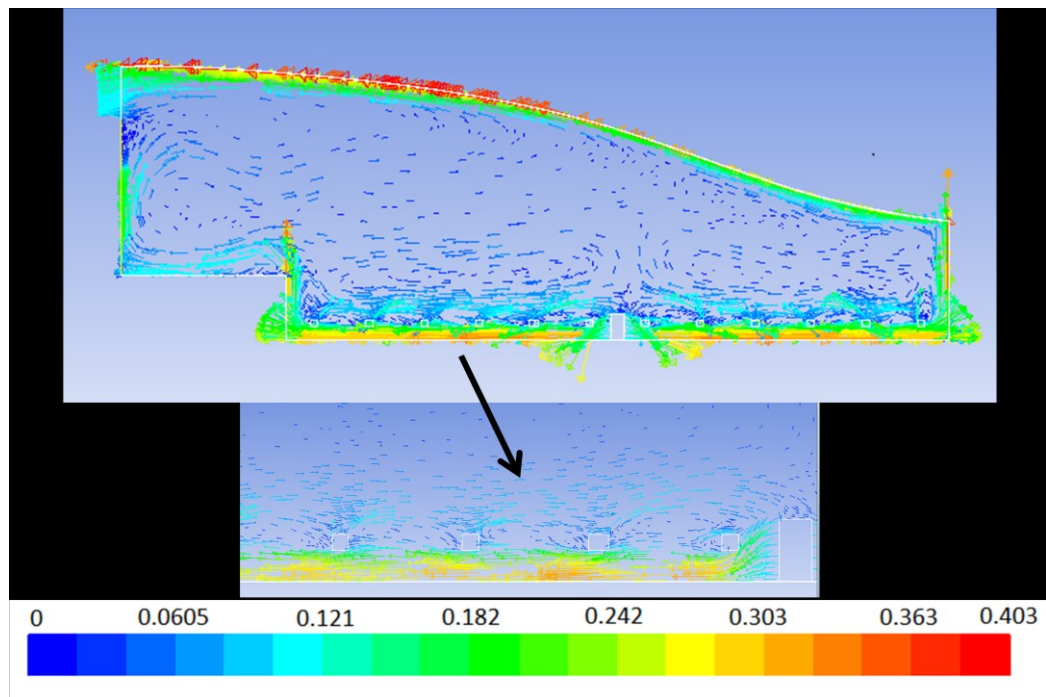


Fig. 8.3(a). Velocity vectors (m/s) in airport domain during DC cooling mode

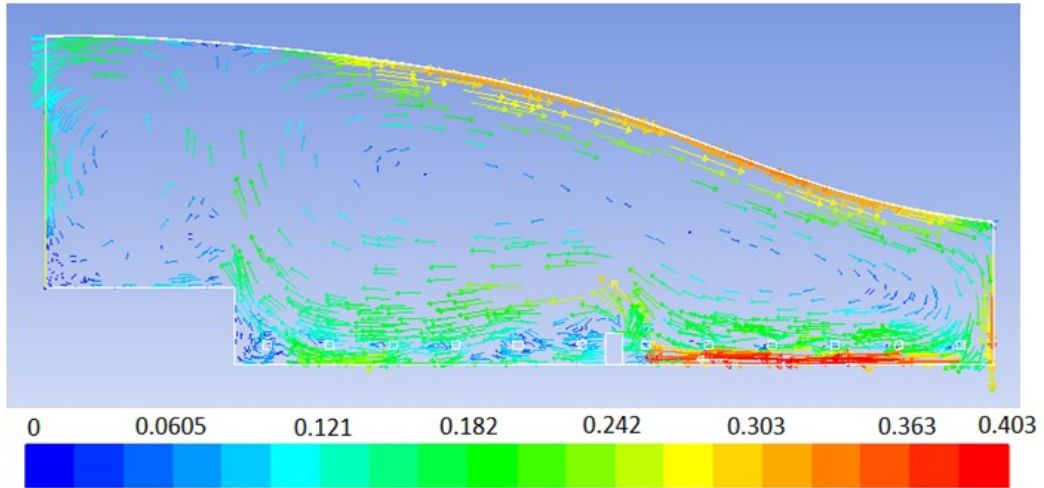


Fig. 8.3(b). Velocity vectors (m/s) in airport domain during DC heating mode

Additionally, Fig. 8.3 shows the velocity vectors in the entire airport domain and in the conditioned zone, which is naturally influenced by the geometry of the airport. The main observation from this velocity plot relates to the air velocities in the conditioned zone, which was found to be in the range of 0.1 - 0.3 m/s, hence abiding by the velocity comfort criteria of < 0.5 m/s, described in section 2.2.1. Being a constant air volume HVAC system, the temperature and velocity plots from Figs. 8.2 and 8.3 are similar for all systems, and hence these plots can be taken as the generic air-movement plots for the airport terminal.

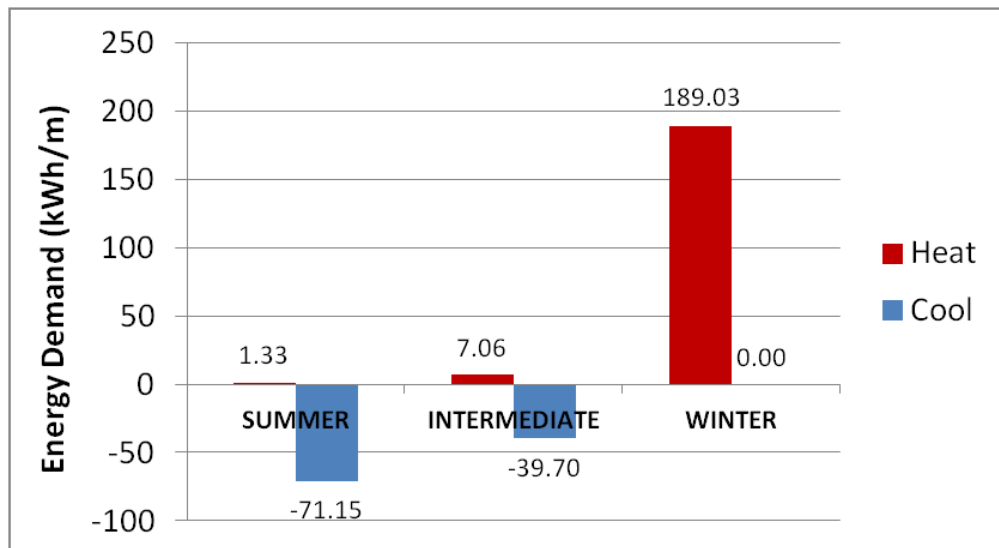


Fig. 8.4. Seasonal heating (+) and cooling (-) demands of the airport space for stand-alone DC case

It can be observed from Fig. 8.4 that the space requires heating for all three seasons: during the early morning hours of the day for the summer and intermediate season (due to the airport operating hours described in Fig. 6.3), and for the entire day in the winter season. Consequently, cooling is required only during the mid hours of the day for the summer and intermediate periods. Hence for the 'DC-only' case, it can be observed that under UK weather conditions, heating is more prominent than cooling, and that the indoor stratification benefits associated with the DC cooling mode can only be obtained for the summer and intermediate weather conditions.

8.2 Seasonal Performance of DC system and PCM Tiles

This section depicts the energy impact of the PCM floor tiles on the airport terminal space, and is divided into the performance of the Ebb[®] tiles and the Energain[®] tiles. A time-step of 360s is employed for both the CFD and TRNSYS models, with an average of 40 iterations per time-step for the CFD model. The simulation time for each season was 14 hours with a 3GHz i7 processor. The contour and vector plots for the indoor air-movement are similar to Figs. 8.2 and 8.3.

8.2.1 'Ebb' Tiles

The Ebb tiles are placed on the floor of the airport terminal space as described in section 7.1, and the enhanced phase change model developed in this study is used to simulate phase change. The temperature and load trends of the zone, with the Ebb floor tiles, are shown in Fig. 8.5.

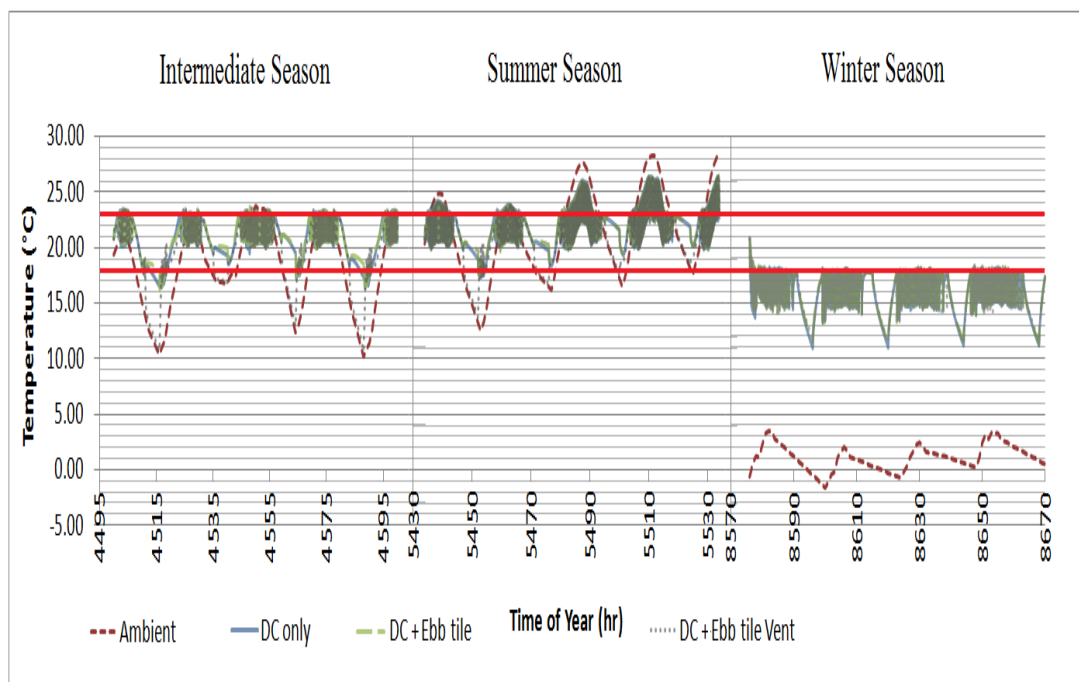


Fig. 8.5(a). Ambient and zone temperature (T_f) profiles with and without night ventilation for the Ebb-Tiles' case

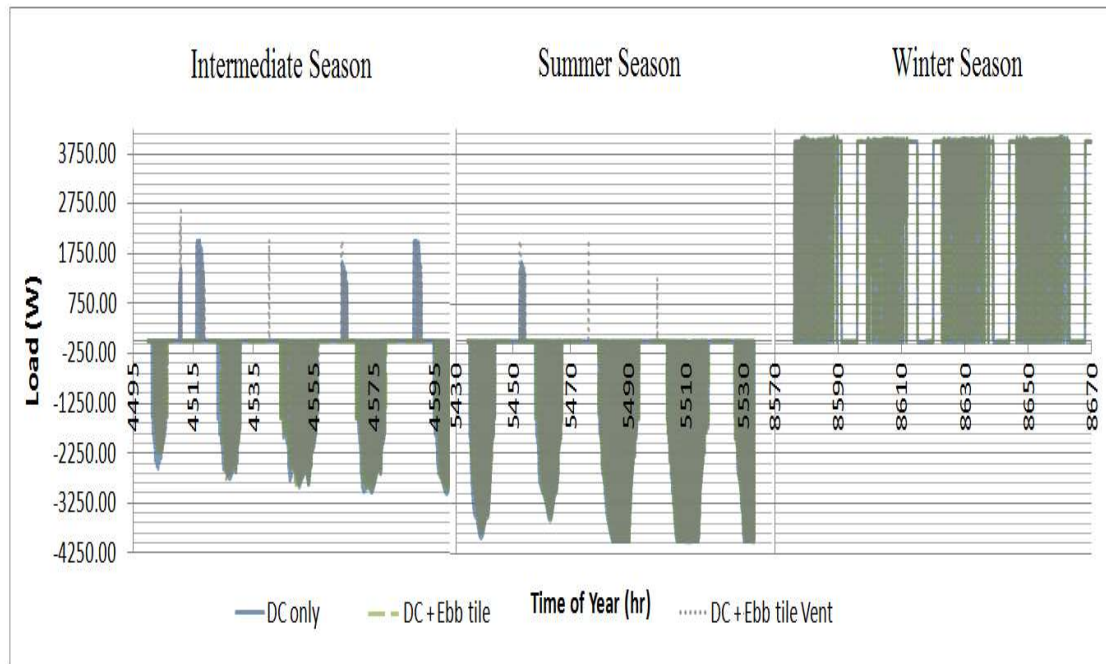


Fig. 8.5(b). Heating (+) and cooling (-) load profiles for the Ebb-Tiles' case, with/ without night ventilation, for 2D geometry

It can be observed from Fig 8.5(a) that the general temperature trends for the Ebb tiles' for all seasons are similar to the 'DC-only' case, whereby: the indoor space is maintained in the comfort range only for the intermediate season; whilst the space overheats for part of the summer. The temperature impact of the PCM tiles in the summer can be quantified by the fact that the indoor space overheats (i.e. $T_f > 23^\circ\text{C}$) for 22% and 21.5% of the time for the non ventilated 'DC + Ebb tiles' and the 'DC + Ebb tiles Vent' cases, respectively, compared to 23% for the 'DC-only' case. Furthermore, the zone temperature during the winter season is below the comfort requirements, similar to the 'DC-only' case.

The load profiles for both the 'DC-only' and the non-ventilated 'DC + Ebb tiles' cases are very similar, as shown in Fig. 8.5(b). During the intermediate season, heating is required during the early morning hours, while cooling dominates during the day. During summer, heating may be required, but cooling is most prominent, whilst in winter, the airport terminal requires only heating. For the 'DC + Ebb tiles Vent' case, a noticeable change in the load profile can be observed. The time of maximum cooling load for both the summer and intermediate seasons is found to shift by an average of 0.8 hrs, whilst the heating load for these two seasons is found to increase in the early

morning hours compared to the ‘DC-only’ and ‘DC + Ebb tiles’ cases. During winter, the heating load trends for all configurations are similar.

Thus, the addition of the Ebb tiles without ventilation is found not to have a major impact on both the temperature and energy load profiles of the airport terminal, whilst recharging the Ebb tiles through night-ventilation shifts the time of maximum cooling load during the day by 0.8 hours during the intermediate and summer seasons. However, night-ventilating the indoor space also increases the heating load required by the space during the early morning hours in the intermediate and summer seasons. Hence, although the percentage overheating time in the summer is similar for the non-ventilated and ventilated cases, the overheating of the space occurs 0.8 hrs later when ventilating the indoor space at night. There is no apparent impact of the Ebb tiles during the winter season.

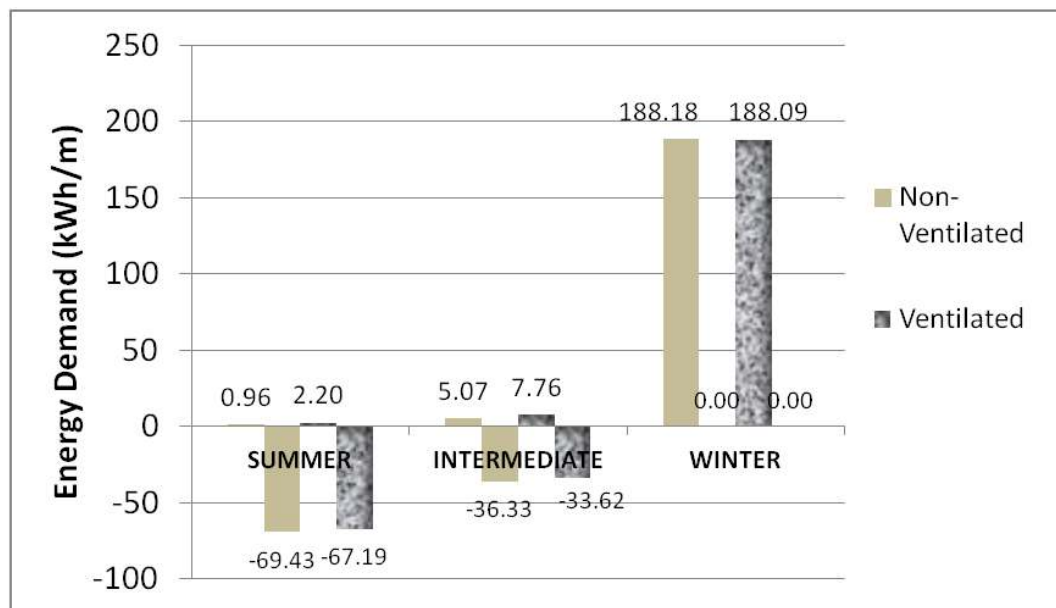


Fig. 8.6. Heating (+) and cooling (-) demands with and without night ventilation, with Ebb floor tiles

Fig. 8.6 shows that employing night ventilation in the space reduces slightly the cooling demand during the summer and intermediate seasons, but at the same time, increases the heating demand. Thus, night ventilation is effectively shifting the load from cooling to heating, and therefore the annual energy savings will depend on the balance between the two opposing loads. Furthermore, compared to the ‘DC-only’ case from Fig. 8.4, it can be observed that the cooling loads are lower when employing the Ebb floor tiles, whilst

heating load increases when using night ventilation with the Ebb floor tiles. During winter, the heating loads for the Ebb floor tiles are slightly lower compared to the ‘DC-only’ case.

8.2.2 ‘Energain’ Tiles

The thermophysical properties of the Energain tiles are given in section 7.1. This tile is used to show the impact of floor tiles with higher latent enthalpy than the Ebb tile, on the energy performance of the indoor space. The temperature and load trends of the zone for the Energain floor tiles are shown in Fig. 8.7.

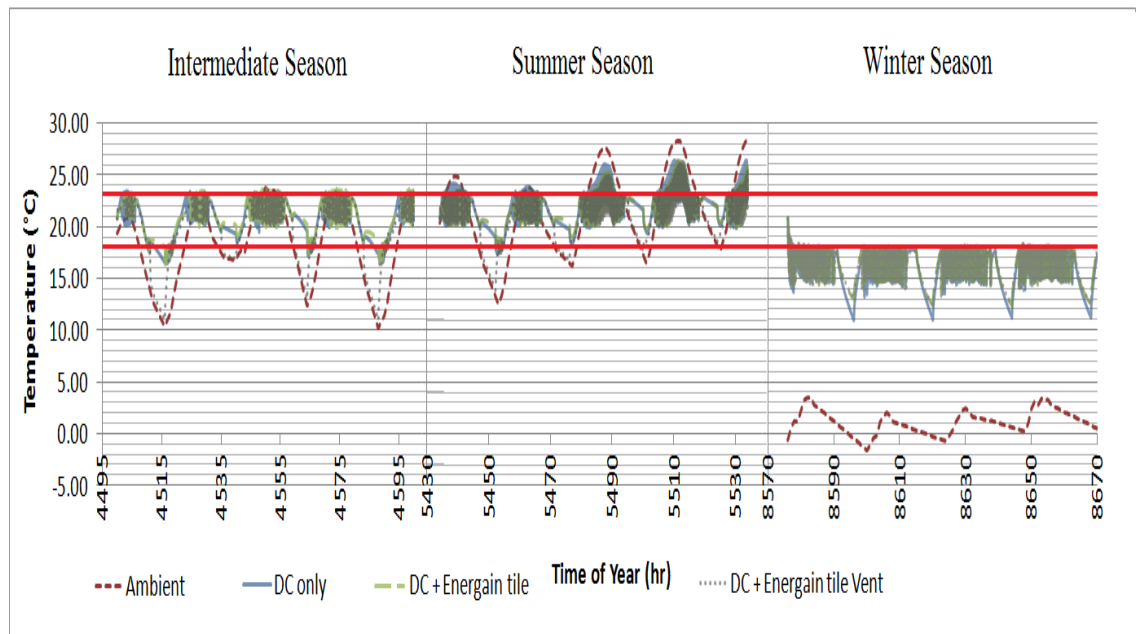


Fig. 8.7(a). Ambient and zone temperature (T_f) profiles with and without night ventilation for the Energain-Tiles’ case

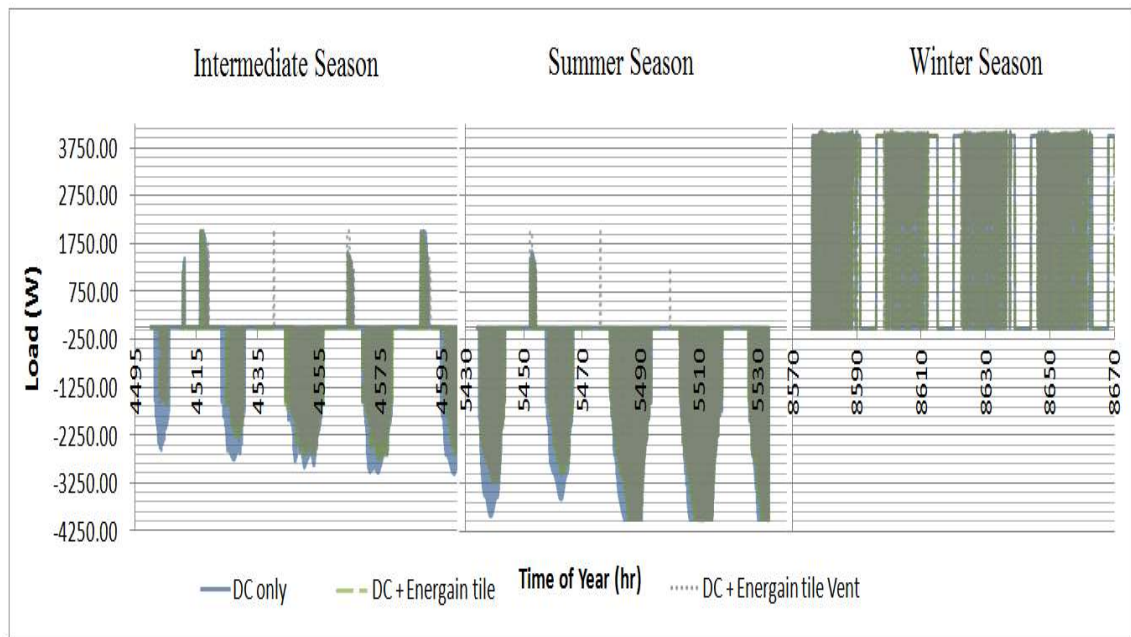


Fig. 8.7(b). Heating (+) and cooling (-) load profiles for the Energain-Tiles' case, with and without night ventilation, for 2D geometry

The general observations from the trends in Fig. 8.7 are similar to the Ebb tiles' case, that is: the comfort conditions are satisfied for the intermediate season; there is overheating in the summer; and the indoor temperatures are below the comfort requirements during winter. However, the swing in the indoor temperature is more noticeable when employing the Energain floor tiles. For instance, the summer indoor temperatures are found to increase at a slower rate compared to the 'DC-only' case, whilst the reduction in the winter indoor temperatures during the night is lower when the Energain tiles are used, compared to the 'DC-only' case.

Consequently, the temperature impact of the PCM tiles in the summer can be quantified by the fact that the indoor space overheats (i.e. $T_f > 23^\circ\text{C}$) for 19.7% and 19.0% of the time for the non ventilated 'DC + Energain tiles' and the 'DC + Energain tiles Vent' cases, respectively, compared to 23% for the 'DC-only' case. This also shows an improvement in indoor thermal comfort, compared to using the Ebb floor tiles.

Similar to the Ebb tiles case, the heating energy load is found to increase (when night ventilating the space) in the early morning due to the higher thermal mass of the building that needs heating, while the cooling energy decreases during the day, compared to the 'DC-only' case. However, when using the Energain tiles, the reduction in cooling energy during the day is more prominent for both the non-ventilated and

ventilated cases, compared to both the ‘DC-only’ and Ebb-tile cases. Additionally, the time of maximum cooling load is found to shift by an average of 1.3 hrs for both the non-ventilated and ventilated scenarios, compared to the ‘DC-only’ case. During winter, there are no apparent changes in the energy demand for the space.

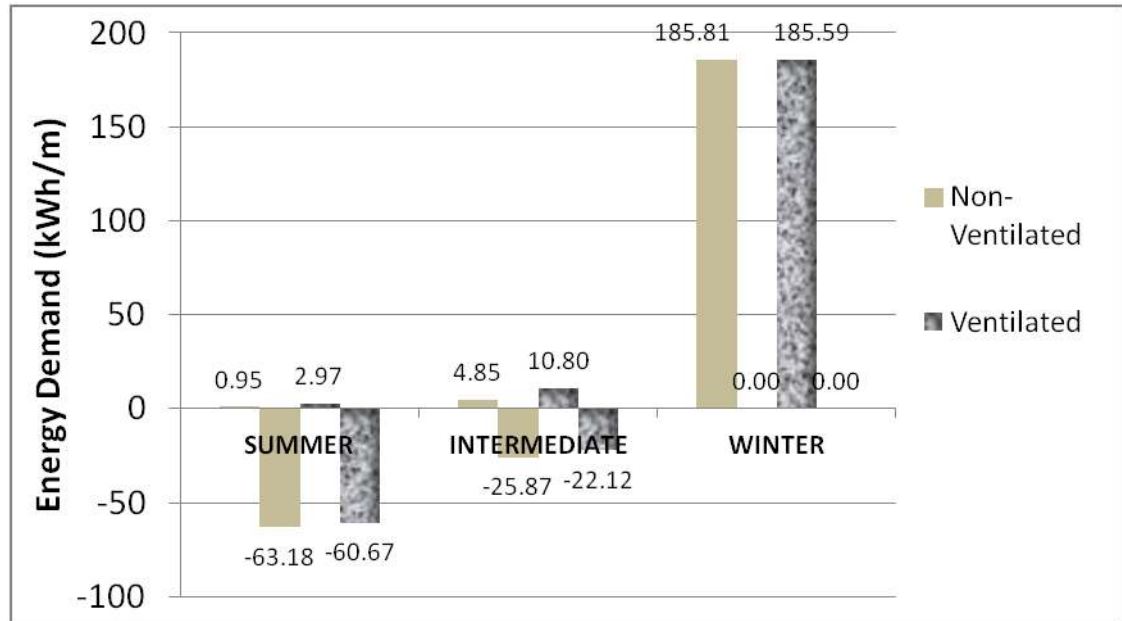


Fig. 8.8. Heating (+) and cooling (-) demands with and without night ventilation, with Energain floor tiles

Fig. 8.8 shows that similar to the Ebb tiles, using the Energain tiles reduces the cooling load during the day for the intermediate and summer seasons, compared to the ‘DC-only’ case. However, the reduction in cooling load is more pronounced when using the Energain tiles, due to the higher latent heat capacity of the PCM. The heating demand for the summer and intermediate seasons is reduced when employing the Energain tiles in the non-ventilated mode, whilst ventilation significantly increases the heating load, compared to the ‘DC-only’ case. It can also be observed that the winter heating load is reduced when employing the Energain tiles, compared to both the Ebb-tiles and the ‘DC-only’ cases.

Generally, it was found that increasing the latent heat capacity of the floor tiles reduces the cooling load during the summer and intermediate seasons, but ventilating the space at night increases the heating loads for these two seasons. In winter, the heating load also decreases with the use of higher latent heat capacity PCM in the floor tiles, and ventilating the space at night has a very low impact on the heating energy demand of the space.

8.3 Seasonal Performance of DC system and PCM Glazing

This section describes the performance of the PCM-glazed envelope. A time-step of 360s is employed for both the CFD and TRNSYS models, with an average of 50 iterations per time-step for the CFD model. The simulation time for each season was 17 hours with a 3GHz i7 processor. The thermophysical properties of the PCM-glazing are detailed in section 7.2. Fig 8.9 shows the temperature and load trends of the zone, with a PCM glazed envelope.

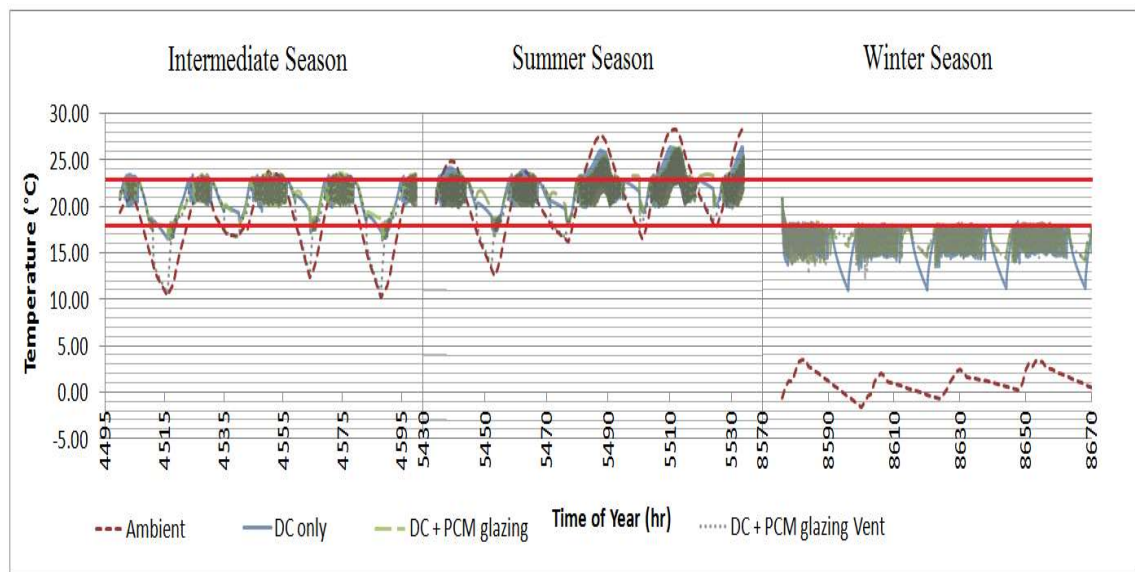


Fig. 8.9(a). Ambient and zone temperature (T_f) profiles with and without night ventilation for the PCM-glazing's case

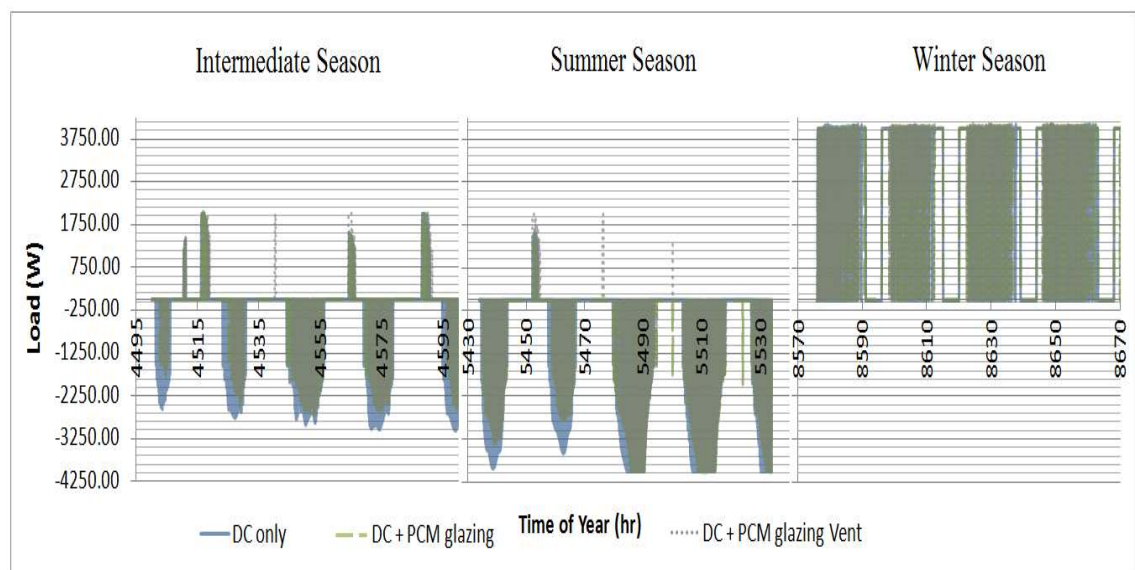


Fig. 8.9(b). Heating (+) and cooling (-) load profiles for the PCM glazing's case, with and without night ventilation, for 2D geometry

The overall temperature trends obtained from using the PCM-glazed envelope are similar to the trends when using the Energain tiles, i.e. there is a noticeable reduction in the rate of increase of temperature during the summer and intermediate seasons, as well as relatively higher night temperatures during winter, compared to the ‘DC-only’ case. Furthermore, the %-overheating hours (i.e. $T_f > 23^\circ\text{C}$) during summer is also reduced to 20.3% and 18.1%, for the non-night ventilated and night ventilated PCM-glazing cases, respectively.

The heating energy load during the intermediate and summer seasons is found to increase in the early morning hours, similar to the ‘PCM floor tiles’ cases, due to the higher thermal mass of the building that requires heating, compared to the ‘DC-only’ case. During the day, the cooling load is found to decrease relative to the ‘DC-only’ case, portraying the effectiveness of the PCM. Furthermore, the time of maximum cooling energy load during the intermediate and summer days is shifted to later in the day by an average of 1.6 hrs, for both the ventilated and non-ventilated cases, compared to the ‘DC-only’ case. During winter, there is no apparent change in the heating energy demand, when using the PCM-glazed envelope.

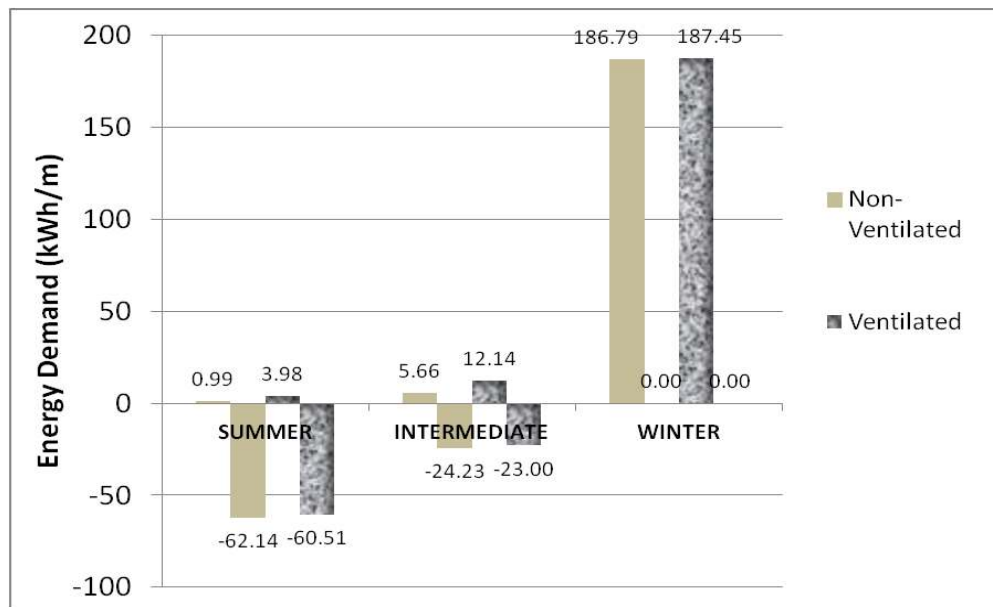


Fig. 8.10. Heating (+) and cooling (-) demands with and without night ventilation, with the PCM-glazing envelope

Fig. 8.10 shows that the summer and intermediate cooling loads are reduced with the use of the PCM-glazing compared to the 'DC-only' case, because of the higher solar radiation absorption rate of the PCM compared to the normal glazing; and that the employment of night ventilation has a beneficial impact in this regard. Night ventilation however also increases the heating loads for these two seasons. During winter, the heating energy demand also decreases with the use of the PCM-glazing compared to the 'DC-only' case, due to the lower heat loss rates through the glazed envelopes. However, using night ventilation in winter increases the heating load compared to a non-ventilated case. The latter observation can be explained by the fact that compared to the floor tiles; the PCM-glazing envelope has a direct contact with the external ambient air conditions. Hence, increasing convection within the building also increases the heat transfer with the outdoor air which increases the heating requirement during the winter occupied hours.

8.4 Seasonal Performance of DC system with retrofitted PCM-HX

This section describes the impact of retrofitting the PCM heat exchanger (PCM-HX) system in the displacement diffuser of the airport terminal. Compared to the PCM tiles and glazing, this is a semi-active system, whereby the PCM influences the air supplied into the space. The control strategies are described in section 7.3.3, and both configurations of the PCM-HX, i.e. the 16mm and the 8mm air gaps between successive PCM plate rows, are evaluated in this section. In this case, the airport CFD model employed a time-step of 360s and 40 iterations per time-step, and the PCM-HX CFD model employed a time-step of 20s to satisfy the convergence criteria. Thus for every time-step of the airport model, 18 sub time-steps were performed for the PCM plate in order to allow coherency in the simulation times. The overall computing time was 19 hrs for each season, with a 3GHz i7 processor.

8.4.1 DC-PCM-HX-16mm

Fig. 8.11 shows the temperature and energy trends for the different seasons using a 16mm air gap for the PCM-HX, and the different night charging strategies described in section 7.3.3.

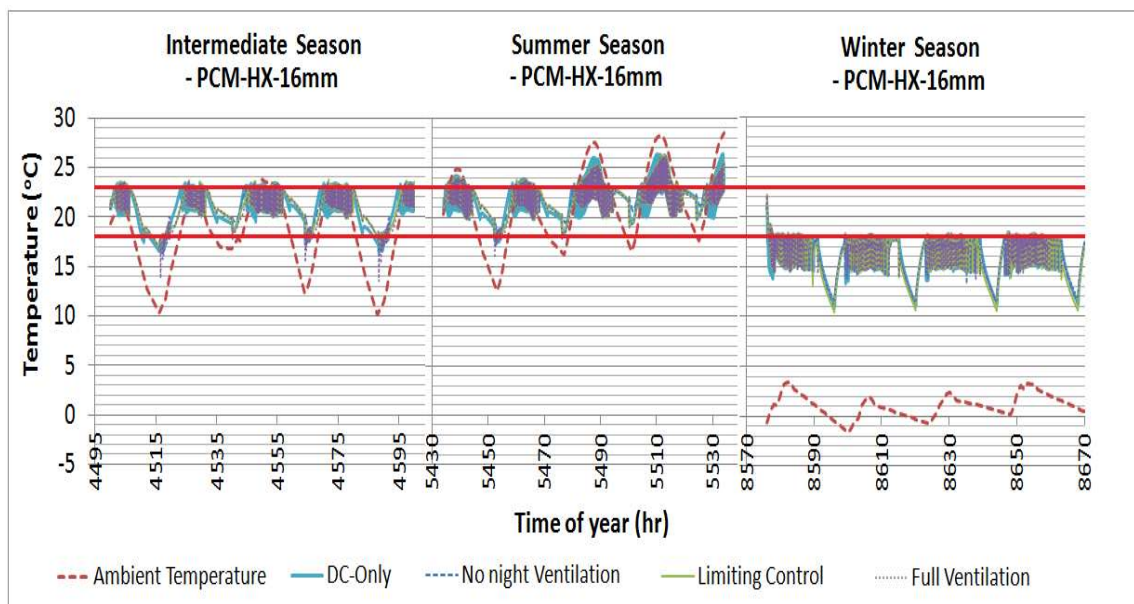


Fig. 8.11(a). Ambient and zone temperature (T_z) profiles, with different night ventilation charging strategies for the PCM-HX-16mm case

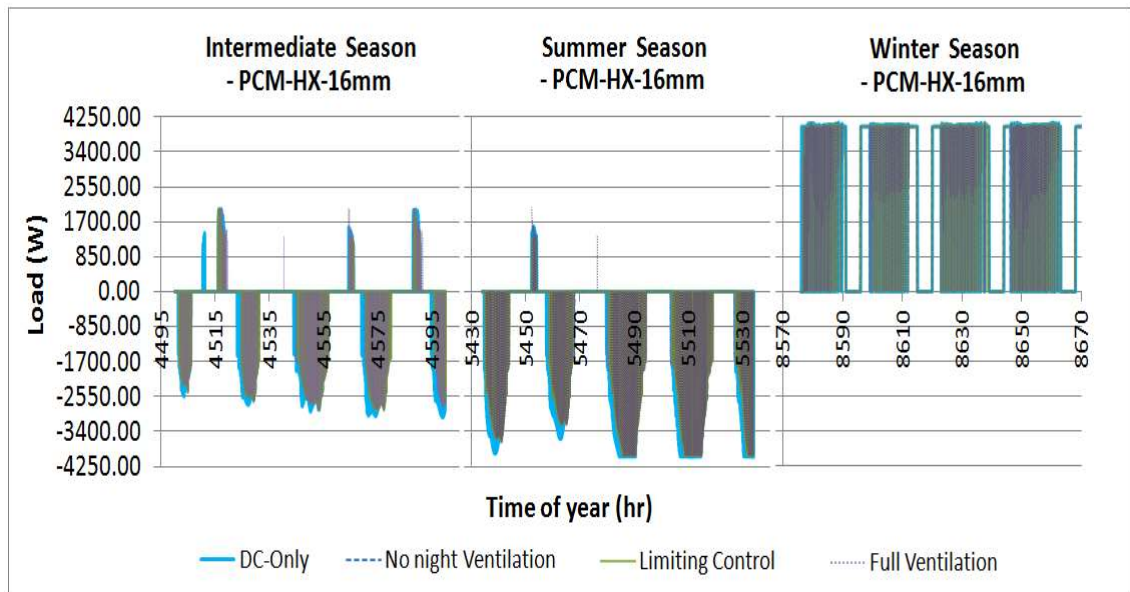


Fig. 8.11(b). Heating (+) and cooling (-) load profiles for the PCM-HX-16mm case, with different night ventilation charging strategies, for 2D geometry

Fig. 8.11(a) shows that the PCM-HX-16mm system is able to satisfy the comfort conditions only during the intermediate season whilst produces slight overheating during the summer, and the temperature during the winter drops outside the comfort region. The overall temperature performance of the three control strategies is very similar. The employment of the PCM-HX-16mm shows an average shift of 1.8 hrs in the intermediate and summer peak temperatures, as well as lower peak summer temperatures, compared to the ‘DC-only’ case. The %-overheating summer hours (i.e. $T_f > 23^\circ\text{C}$) are 21.6%, 21.5% and 21.1% for the ‘noVent’, ‘limiting control’ and ‘full ventilation’ night charging strategies, respectively, compared to 23% for the ‘DC-only’ case.

With regards to energy demand (see Fig. 8.11(b)), it can be seen that the ‘full ventilation’ strategy increases the early morning peak heating demands during both the intermediate and summer periods due to PCM over-cooling at night, relative to the other strategies. The use of the PCM-HX-16mm produces an average shift of 1.8 hrs in the time of peak cooling energy demand, compared to the ‘DC-only’ case. The winter heating load trends are similar for all control strategies.

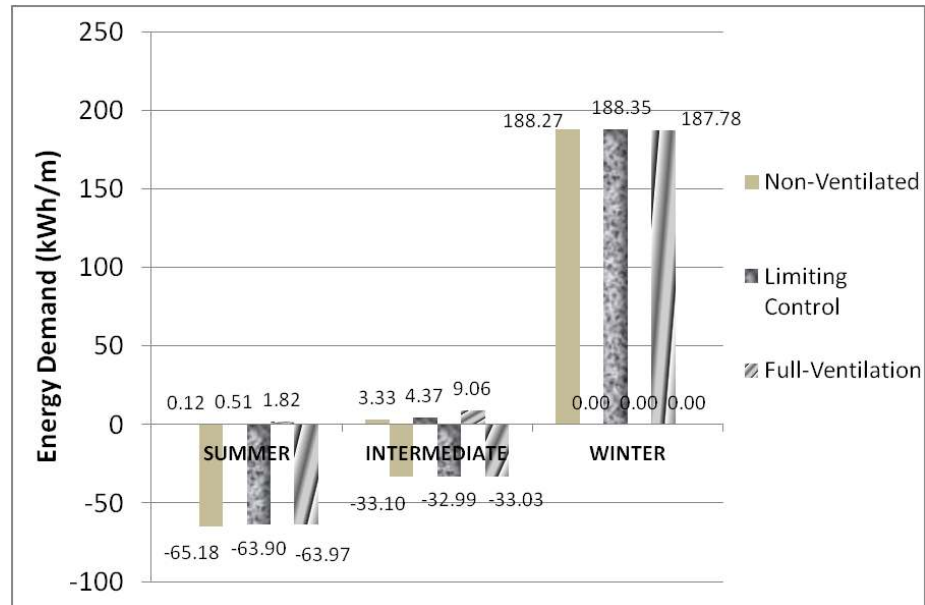


Fig. 8.12. Heating (+) and cooling (-) demands with different night ventilation strategies, with PCM-HX-16mm

Fig. 8.12 shows that the night charging strategies of the PCM-HX-16mm have a greater relative effect on the heating energy requirement than the cooling energy requirement, in the summer and intermediate seasons. It can be seen that reducing night ventilation to recharge the PCM, reduces the heating demand in the intermediate and summer periods as overcooling in the morning is reduced. The use of the PCM-HX-16mm has little effect on the heating demand in winter, due to the fact that the temperature of the air (T_m or T_r , in Fig. 6.4) passing through the PCM-HX-16mm is in the lower range (15-18°C) of the PCM phase change temperature range of 16-26 °C, as shown in Fig. 8.11(a). The latent storage capacity of the PCM is therefore inefficiently used during winter.

On the other hand, the cooling demand in both the summer and intermediate seasons is reduced with the addition of the PCM-HX-16mm, relative to the ‘DC-only’ system. However, the different ventilation charging strategies do not significantly affect the cooling performance. Previous studies have primarily shown that PCM free-conditioning systems mainly reduce cooling demands and temperature swings in intermittently occupied buildings. However, as the airport schedule is less uniform and different to intermittently occupied buildings, this study shows that the PCM-HX-16mm has a higher impact on the heating demand of the space during the intermediate and summer periods. This is explained below.

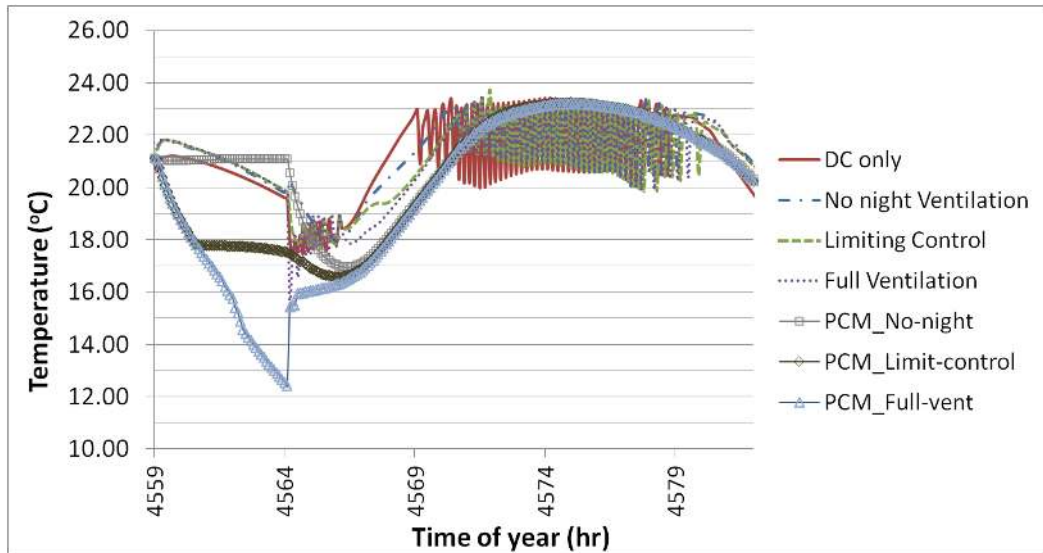


Fig. 8.13(a). Zone temperatures (T_z) and PCM mean temperatures during one day in the intermediate season

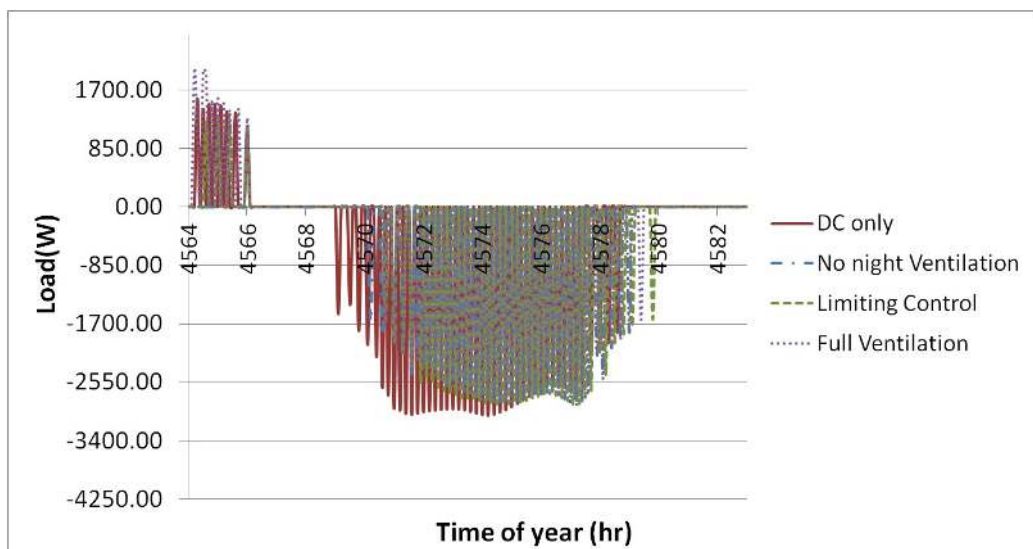


Fig. 8.13(b). Heating (+) and cooling (-) load trends for one day in the intermediate season

(Note that: (4559-4564) hrs is the night charging/ ventilation period; the daytime period is during (4565-4579) hrs; and (4583) hrs is 24:00, when the airport closes. The specifics of the weather data can be obtained from the Meteonorm C-37790 weather files for London)

Fig. 8.13(a) shows that during the early hours of the morning, the zone temperature for most cases is less than the lower comfort limit of 18°C, with the space requiring heating. Employing a full night ventilation charging strategy implies that the

temperature being supplied to the space from the PCM-HX-16mm in the early morning hours is lower compared to the other configurations, hence increasing the heating demands. Preventing night ventilation or limiting the PCM temperature to 18°C will reduce the need for heating in the early hours (from 4564 hr) of the morning, because of the relatively higher supply temperature compared to the full ventilation strategy. Furthermore, Fig. 8.13(a) shows that the use of the PCM-HX-16mm shifts the occurrence of high space temperature from the morning to later hours, reducing the cooling energy requirements in the morning (see Fig. 8.13(b)), but increasing it in the late afternoon hours. Nonetheless, as shown by Figs. 8.12 and 8.4, the overall cooling energy requirement of the space is reduced with the use of the PCM-HX-16mm compared to a ‘DC-only’ system.

8.4.2 DC-PCM-HX-8mm

Fig. 8.14 shows the temperature and energy trends for the different seasons using an 8mm air gap for the PCM-HX, including the different night charging strategies.

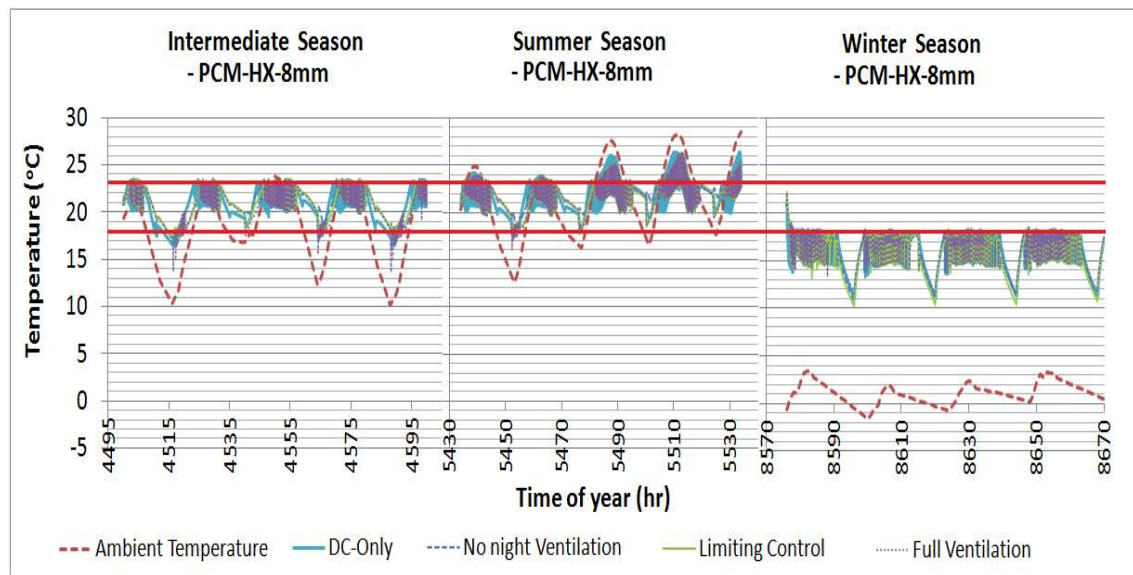


Fig. 8.14(a). Ambient and zone temperature (T_f) profiles, with different night ventilation charging strategies for the PCM-HX-8mm case

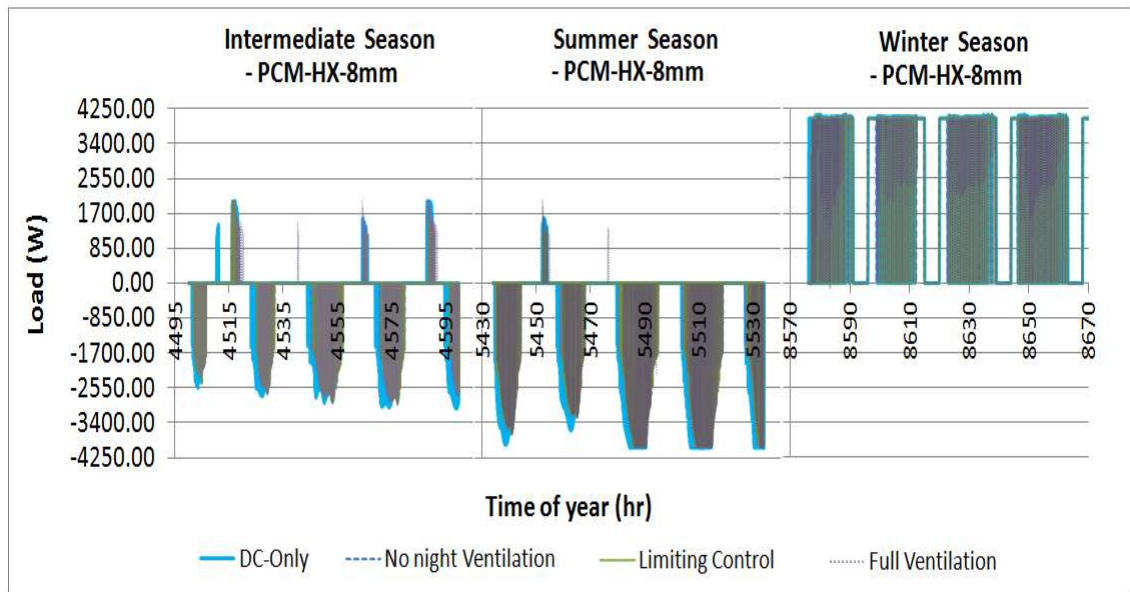


Fig. 8.14(b). Heating (+) and cooling (-) load profiles for the PCM-HX-8mm case, with different night ventilation charging strategies, for 2D geometry

The observations for the temperature and energy trends of the PCM-HX-8mm case are similar to the PCM-HX-16mm case, where: the comfort conditions are satisfied only for the intermediate season; overheating occurs in the summer; the indoor temperatures are below the comfort criteria for winter; there is a reduction in the peak summer temperatures, relative to the ‘DC-only’ case; and a shift in the time for peak cooling demand by 2.0 hrs, compared to the ‘DC-only’ case. There is also no major change in the winter temperature and energy trends when using the PCM-HX-8mm.

Furthermore, the %-overheating summer hours (i.e. $T_f > 23^\circ\text{C}$) are 21.4%, 21.1% and 19.5% for the ‘noVent’, ‘limiting control’ and ‘full ventilation’ night charging strategies, respectively.

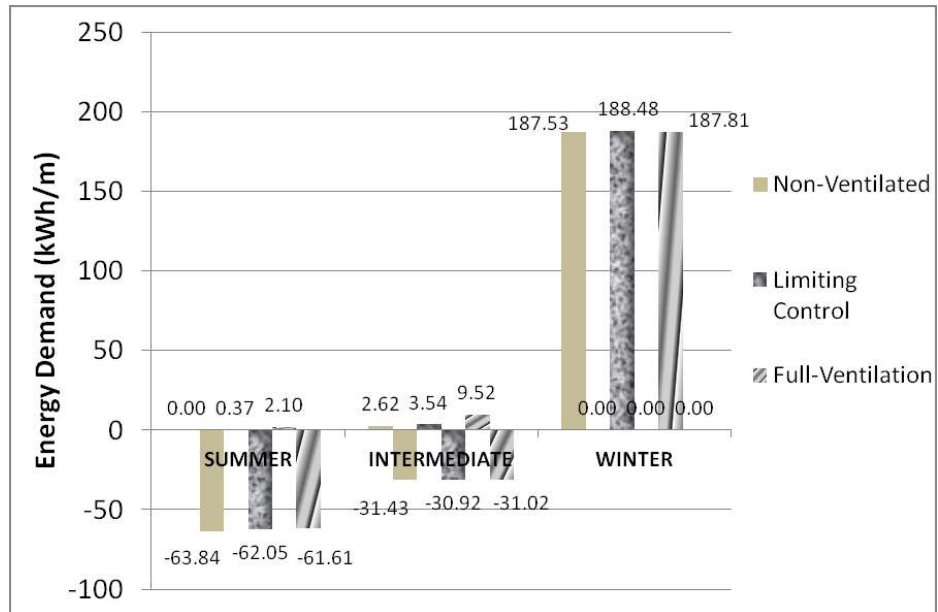


Fig. 8.15. Heating (+) and cooling (-) demands with different night ventilation strategies, with PCM-HX-16mm

The observations from Fig. 8.15 imply that the effect of the PCM-HX-8mm on the energy performance of the DC system is again similar to the PCM-HX-16mm case. However, the cooling loads of the PCM-HX-8mm are relatively lower than the PCM-HX-16mm configuration in the summer and intermediate seasons, whilst the PCM-HX-8mm configuration improves the heating performance only for the ‘non-ventilated’ and ‘limiting control’ night charging strategies, compared to the PCM-HX-16mm for the summer and intermediate seasons. There is no major difference in the performance of the PCM-HX-8mm and PCM-HX-16mm during winter, because the indoor temperature fluctuates in the lower levels of the phase change temperature range, inefficiently exploiting the energy storage potential of the PCM, as explained in section 8.4.1.

Thus, in general, the PCM-HX-8mm is found to have a similar impact on the Airport space as the PCM-HX-16mm case, except that the effects are more prominent due to the higher latent heat capacity of the PCM-HX-8mm configuration. This observation is exemplified in Fig. 8.16, for the case of limiting night ventilation control.

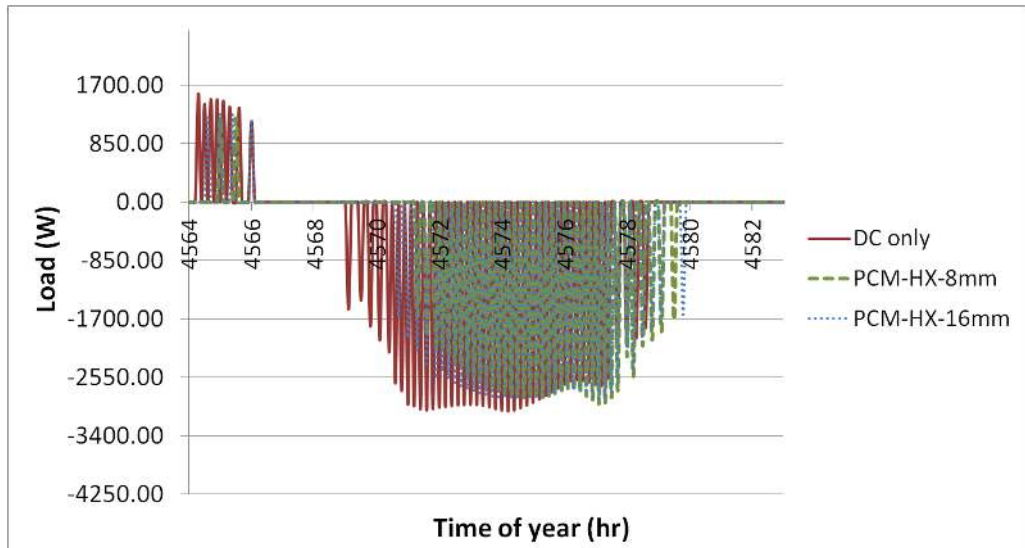


Fig. 8.16. Load comparison of PCM-HX-8mm and PCM-HX-16mm for a day in the intermediate season, under the limiting night control ventilation charging strategy

It can be observed from Fig. 8.16 that: employing the PCM-HX systems reduces the heating load during the early morning hours; and employing a higher latent heat capacity in the diffuser, in the form of the PCM-HX-8mm configuration, improves the heating energy demand even further. This is explained by the fact that due to the higher heat capacity of the diffuser, the PCM temperature is maintained closer to the lower limit of comfort during the early morning hours, requiring less auxiliary heating when the HVAC system starts to operate (from 4564 hr).

During the day, there is a shift in the peak cooling load from the early morning hours to later hours in the day when using the DC-PCM-HX system, relative to the ‘DC-only’ case. Furthermore, there is a net reduction in the cooling loads when employing the DC-PCM-HX system relative to the ‘DC-only’ system, due to the increased thermal mass. This increase in heat capacity is effectively prolonging the period for which the indoor temperature is within the comfort region of 18-23 °C. In this regard, increasing the latent heat capacity of the system from the PCM-HX-16mm to PCM-HX-8mm configuration improves this effect and reduces the cooling loads even further, as shown in Fig. 8.16.

8.5 Annual Energy Performance

This section presents the annual energy demands of the space when using each PCM system. The energy is divided into annual heating and cooling load, extrapolated using the Degree Day concept explained in section 7.5, and the fan powers described in Appendix E. (The annual energy calculation method is explained in Appendix F)

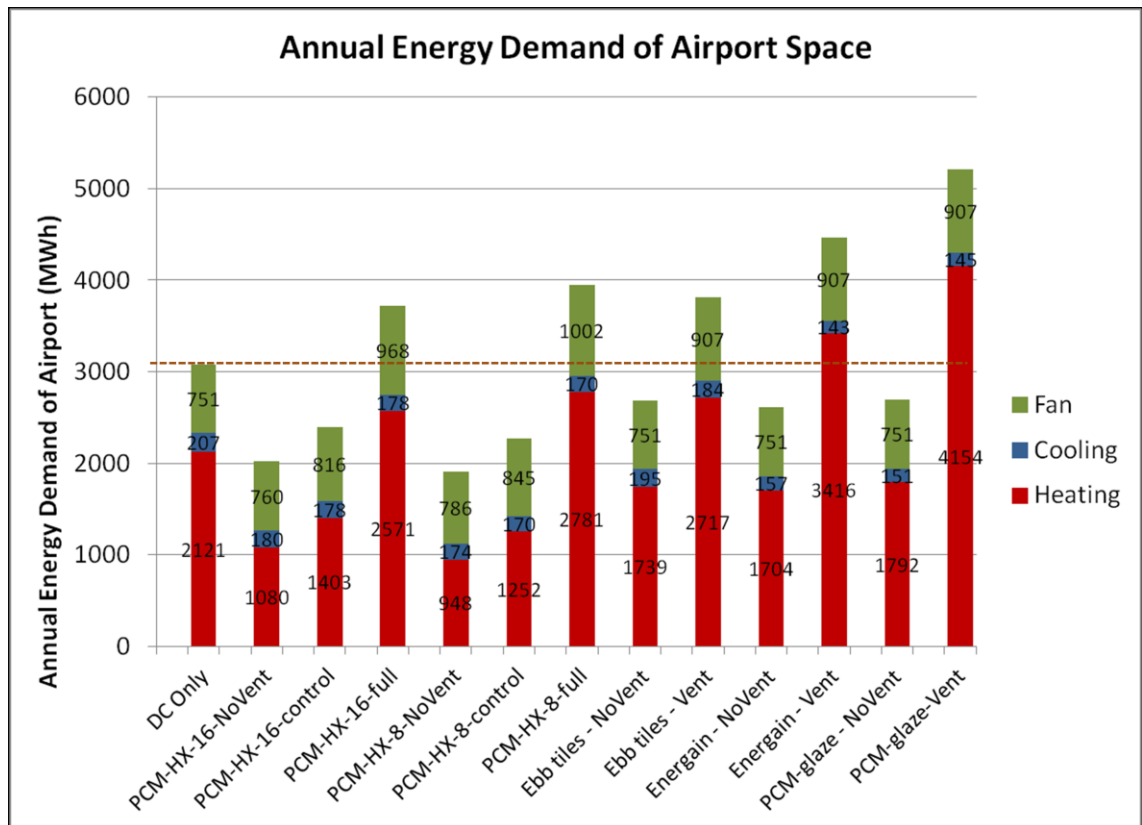


Fig. 8.17. Annual energy demand of the entire Airport Terminal Space for the different PCM system configurations

Fig. 8.17 shows that heating constitute a major portion of the annual energy demand for the airport terminal space in UK weather conditions, whilst cooling is the least significant portion of the annual energy demand. This is due to the relatively higher number of annual Heating Degree Days (HDD) compared to Cooling Degree Days (CDD) for the UK weather conditions (see Table 7.3). As a result, in order to significantly influence the energy performance of the airport space, the PCM system must influence the heating load of the building relatively more than the cooling load.

This is a rather counter-intuitive ideology, because PCMs have been mainly appreciated in past studies for their cooling energy savings potential.

From the previous sections, it has been observed that employing the PCM systems during winter has a relatively low influence on the heating demand. Hence, in order to improve the annual total energy demand, the heating loads during the summer and intermediate seasons must instead be reduced. For these two latter seasons, heating is mainly required during the early morning hours when the airport opens. Thus, an efficient PCM system would either limit the reduction in temperatures during the night or satisfy the early morning heating requirements, reducing the dependency on energy-consuming auxiliary heating units.

Fig. 8.17 shows that employing full night ventilation for recharge actually reduces the energy saving potential of the PCM systems. This is because night-ventilating the PCM systems without any control produces lower temperatures during the early hours of the morning, which have to be compensated through the use of increased amount of auxiliary heating. Conversely, not providing night ventilation, provides the maximum heating energy savings potential as the morning supply/indoor temperatures are higher.

In cases without night-ventilation, the recharging process of the PCM systems adequately occurs within the operating hours of the airport. For instance, referring to Fig. 8.13(a), it can be seen that the PCM temperature decreases during the early occupied hours of the day, when the airport starts to operate (i.e. the PCM charging phase). Although the PCM temperature decreases to a slightly higher value without night-ventilation, compared to the night-ventilation strategies, the PCM is still adequately recharged to ~80% without any ventilation in the intermediate season. Thus, using the non-ventilated strategies allows a reduced heating load in the early morning (due to the higher PCM temperatures), without extensively sacrificing the cooling potential of the PCM during the day. This observation is confirmed in the annual energy demands of the different PCM configurations, whereby not employing night ventilation provides energy savings for all the investigated PCM systems.

8.5.1 Relative Energy Performance

In order to analyse the energy impact of the different PCM systems, Fig. 8.18 shows the energy performance of the PCM systems relative to the ‘DC-only’ case.

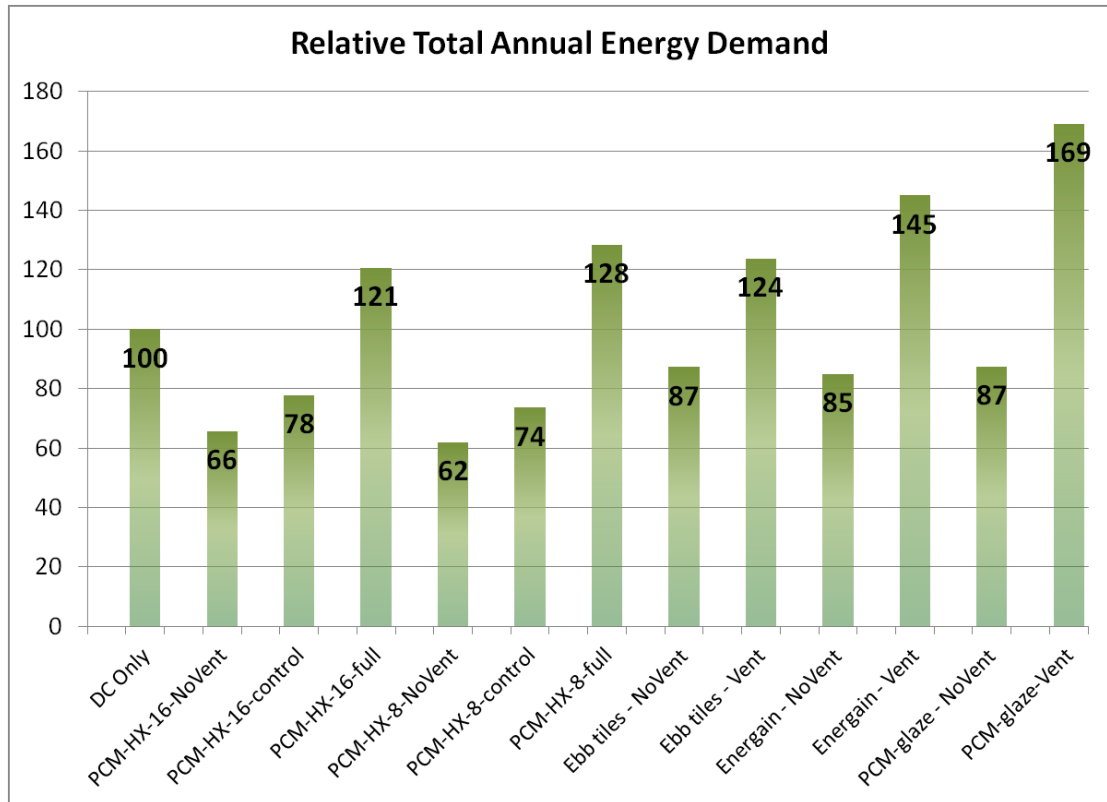


Fig. 8.18. Total annual energy demands of PCM System configurations relative to the ‘DC-only’ case

Employing the retrofitted PCM-HX configurations reduces the annual energy demands only for the cases of ‘noVent’ and ‘Limiting control’ night ventilation strategies. These cases reduce the heating requirements in the early morning hours of the summer and intermediate seasons, and thus provide with the highest energy savings compared to the ‘Full’ night ventilation strategy. Employing the latter night charging strategy produces annual energy losses. Additionally, using the PCM-HX-8mm configuration produces higher energy savings compared to the PCM-HX-16mm configuration due its higher latent heat capacity, even though the fan power is higher for the PCM-HX-8mm configuration. Thus, in this case, employing an extra 150% latent heat capacity in the PCM-HX system of the DC diffuser produces an extra annual energy savings of 4%.

Using PCM floor tiles also produces energy savings only for the cases where night ventilation is not employed. The energy saving potential of the tiles is less than the PCM-HX systems, partly because of the relatively lower latent heat capacity of the tiles, and partly due to the passive nature of the PCM system. Using a passive system produces a lower heat transfer rate due to the lower air velocities (heat transfer coefficients) with the PCM. Additionally, using a PCM tile with higher latent heat capacity produces higher energy savings. However, Fig. 8.18 shows that employing a PCM tile that contains about an extra 350% latent heat capacity, only produces a supplementary reduction of 2% in the annual energy demand.

Similarly, utilising the PCM glazed envelope produces energy savings only for the case without night ventilation. In this case, the energy saving potential is similar to using the non ventilated Ebb floor tiles, and lower than the other PCM configurations. This can be explained by the fact that although the higher thermal mass and the lower solar transmission of the PCM glazing reduces the cooling energy load during the day, a higher thermal mass also requires relatively higher heating in the early morning hours, compared to the other PCM systems. Also, because the PCM glazed envelope is located adjacent to the external air, the entire PCM thermal mass is not solely employed in the conditioning of the indoor space, but is also directly influenced by the external conditions. Conversely, ventilating the PCM-glazed system at night significantly amplifies the early morning heating load (especially during the summer and intermediate seasons), making the combination of PCM glazing and night ventilation the worst annual energy performing configuration. (The optical change in the PCM during phase change must also be considered in the application of such PCM-glazed structures.)

Thus, for the PCM system configurations studied, employing the PCM-HX-8mm without night ventilation provides the highest energy savings of 38%, whilst employing the PCM glazing with night ventilation produces the highest energy losses of 69%, compared to the 'DC-only' case. The employment of PCM systems, without night ventilation is found to shift the peak cooling energy demand to later hours in the day, while also reducing the early morning heating and overall energy demands.

8.5.2 Assessment of the Control Method

The use of the PID controller and the HVAC control strategy described in section 6.5, leads to a poor performance for the displacement conditioning system during the winter season (i.e. the indoor temperatures are below the comfort requirements) and the overheating propensity during the summer season. This is explained with reference to Fig. 8.19.

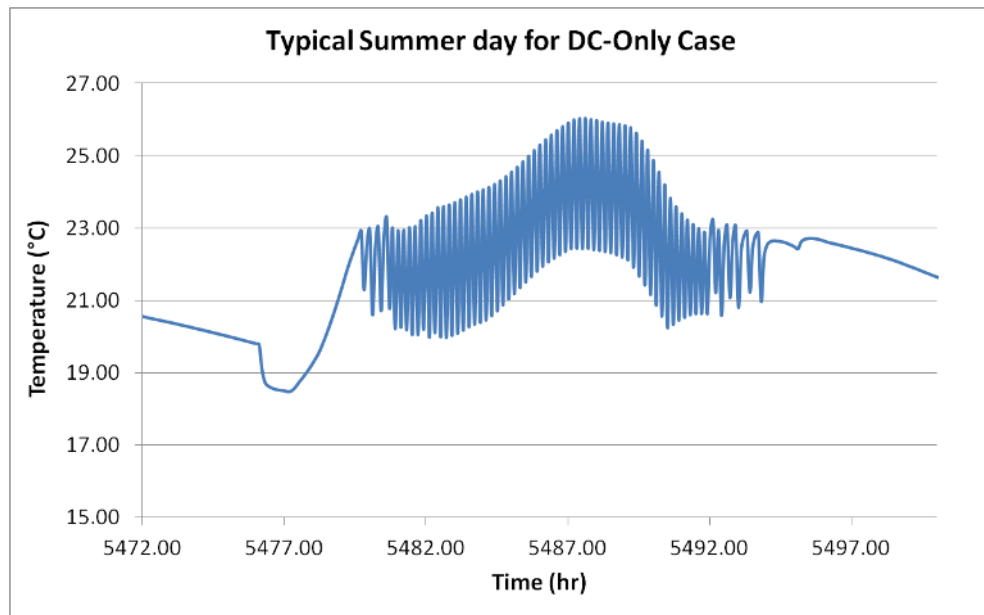


Fig. 8.19. Indoor temperature (T_i) for a typical summer day for the 'DC-only' case (Airport opens at 5476 hrs and closes at 5495 hrs)

As observed in Fig. 8.19, the cooling capacity of the HVAC system at 4 kW for the section considered, is justified by the fact that when the indoor temperature is outside the comfort range, providing 4kW of cooling brings the indoor temperature back to within comfort. Overheating occurs due to the cyclic behaviour of the PID controller and HVAC control strategy, whereby when the indoor temperature reaches the comfort conditions of 18 – 23 °C, cooling is switched off, and the mixed air at temperature (T_m – see Fig. 6.4) is then supplied to the space. The same explanation applies to the poor heating performance during the winter season. This combination of PID and HVAC control method represents a relatively simple control strategy, and was adopted mainly to allow free-conditioning of the space within the comfort temperature range and to reduce the energy demand.

Nonetheless, although the indoor temperatures in the peak summer and winter seasons are slightly out of the comfort requirements, they can be justified based on the adaptive thermal comfort approach employed by CIBSE guide A (2006). This approach allows an overheating of 3°C (i.e. indoor temperatures of up to 26°C) for summer days, which corresponds to a relaxation of the Percentage of People Dissatisfied (PPD) value to 20% (Holmes and Hacker, 2008). Similarly, for the thermal conditions of 1.15 clo, 1.4 met and 0.2 m/s (i.e. the winter criteria for airport check-in areas – set by CIBSE guide A (2006)), a PPD value of 20% (PMV of ± 0.8) allows a minimum temperature of $\sim 15^\circ\text{C}$ (Fanger, 1970), i.e. an undercooling of 3°C, to account for the adaptive thermal comfort aspect of the occupants.

8.5.3 Cost and CO₂ Emissions Analysis

This section describes the payback periods and CO₂ emissions for each of the investigated PCM systems. The analysis is based on the additional costs of the PCM in the individual systems and the energy cost savings provided by each system, with respect to the DC-only case.

The costs and CO₂ emissions analysis are shown in Table 8.1. More details can be found in Appendix G.

Table 8.1. Payback period and CO₂ emissions of PCM systems for the entire airport

	Total running costs (£/year)	Savings (£/year)	Additional PCM Investment (£)	Payback (years)	Annual CO₂ emissions (kgCO₂)	CO₂ emissions reduction (%)
DC Only	293,788	-	-	-	1,066,777	-
PCM-HX-16-NoVent	234,546	59,243	495,360	8.36	829,889	22
PCM-HX-16-control	250,932	42,856	495,360	11.56	945,360	11
PCM-HX-16-full	352,054	- 58,266	495,360	NA	1,327,929	- 24
PCM-HX-8-NoVent	232,312	61,477	752,947	12.25	817,637	23
PCM-HX-8-control	247,956	45,832	752,947	16.43	931,266	13
PCM-HX-8-full	370,856	- 77,068	752,947	NA	1,400,526	- 31
Ebb tiles - NoVent	271,242	22,546	150,703	6.68	977,107	8
Ebb tiles - Vent	348,363	- 54,575	150,703	NA	1,317,627	- 24
Energain - NoVent	268,064	25,725	572,670	22.26	965,152	10
Energain - Vent	387,592	- 93,804	572,670	NA	1,474,815	- 38
PCM-glaze - NoVent	272,966	20,822	2,449,607	117.64	984,813	8
PCM-glaze-Vent	430,495	- 136,706	2,449,607	NA	1,645,827	- 54

CO₂ emissions reduction is calculated relative to the ‘DC-only’ case. The calculations assume that heating is done with gas boilers with efficiency of 80% (Energy Saving Trust, 2013), cooling is done by chillers with COP of 5.0 (source:

www.mitsubishirenewables.eu, 2013), and the efficiency of the fan is 70% (CIBSE B, 2006). CO₂ emission factors for natural gas and electricity are 0.517 kgCO₂/kWh and 0.185 kgCO₂/kWh, respectively (Energy Saving Trust, 2013).

Table 8.1 shows that the Ebb tiles have the shortest payback period, whilst the PCM glazing units have the highest payback period. It can be seen that the semi-active PCM system configurations of 'PCM-HX-16-NoVent' and 'PCM-HX-8-NoVent' produce the lowest CO₂ emissions as well as the highest energy savings, and have relatively average payback periods, compared to the other systems. The 'Ebb tiles-NoVent' produces higher CO₂ emissions than the PCM-HX systems. This may present a dilemma: whereby if CO₂ emissions are crucial, then the 'PCM-HX-8-NoVent' is the most appropriate system; whilst if payback is more important, the 'Ebb tiles-NoVent' system may be the more appropriate system.

Nonetheless, considering both the carbon emissions and energy demand of the airport to be the crucial parameters, the 'PCM-HX-8-NoVent' system configuration is the most energy efficient system, producing a reasonable payback period of 12.25 years. This configuration also produces about 23% lower annual CO₂ emissions compared to the DC-only case. Furthermore, it is also expected that as the quantities of PCM purchased increase and PCM technologies become more mature, the investment costs and payback periods will also decrease.

8.6 Summary of Chapter 8

This chapter presents a case study of the energy performance obtained from applying the different PCM configurations to an airport terminal space. The results are obtained from the numerical models described in Chapters 6 and 7. In general, it was found that using night ventilation as a charging strategy when the airport is closed, has a negative impact on the PCM system performances because of the higher heating requirements in the early morning hours. The use of the semi-active PCM-HX systems provides higher energy savings compared to the passive PCM floor tiles and glazing envelope, and the PCM-HX-8mm without night ventilation is found to be the most energy efficient configuration. This chapter also presents the results of a simplified cost and CO₂ emissions analysis of the different PCM systems.

Chapter 9 will summarise the results and findings obtained from this study, and provide recommendations for future research.

CHAPTER 9 – CONCLUSIONS AND RECOMMENDATIONS FOR FUTURE WORK

Airport terminal spaces can be generally classified as large open spaces with high ceilings and glazed envelope, resulting in a thermally lightweight building structure. For UK weather conditions, thermal mass has been found to be advantageous as it reduces thermal comfort by limiting the temperature fluctuations in the indoor environment, thus keeping the HVAC energy costs and associated carbon emissions low.

In this study, Phase Change Material (PCM) systems have been proposed to increase the thermal mass of airport terminal spaces, without significantly affecting the aesthetics and design of the building. Three systems: PCM tile; PCM glazed unit; and a retrofitted PCM-HX system were investigated. This thesis describes the numerical procedure employed to determine the performance of these systems and presents a case study of the associated HVAC and PCM energy performance in an airport terminal space.

A quasi-dynamic coupled TRNSYS and FLUENT simulation approach was used to evaluate the performance of the PCM systems. The use of computational fluid dynamics (CFD - FLUENT) was imperative in this study due to the large indoor space of airport terminals, whereby the indoor air movement is a significant factor in the energy demand of the HVAC system. Hence, an in-house coupling code was developed and used to enhance the potential of the multi-zonal simulation software TRNSYS, where the HVAC and control system was simulated.

The phase change processes in the PCM systems were simulated in FLUENT, due to the flexibility and accuracy provided by finite volume methods. An improved simulation method was developed to simulate the conduction dominant phase change process in PCM tiles; a novel simulation method, describing the impact of incident radiation on PCMs, was developed to evaluate the performance of the PCM-glazed unit, and the enthalpy-porosity method was used to simulate the PCM-HX behaviour. The phase change models developed in this study have been experimentally validated, and were found to improve the prediction results compared to more conventional simulation methods.

The work carried out as part of this thesis can be summarised as follows:

- A literature review of the different types, benefits and drawbacks of commercial and experimental PCMs and PCM systems that are employed in the thermal conditioning of buildings is presented in Chapter 2.
- An enhanced phase change conduction model was developed in Chapter 3, specifically aimed at the simulations of PCM boards or tiles, and was experimentally validated. This model allows the simulation of non-linear enthalpy-temperature relationships as well as hysteresis, and is published in Gowreesunker *et al.* (2012).
- The effectiveness of CFD in the prediction of air-flow in indoor environments has been explored in Chapter 4. The extended potential and benefits of CFD in determining the impact of PCM boards on the indoor environment has also been explored and validated in a test cell environment. This is published in Gowreesunker and Tassou (2013a).
- Due to the large glazed structure of airport terminals, the behaviour of PCMs under incident radiation was also investigated in Chapter 5. This resulted in the development of a model to define the radiation and thermal behaviour of PCMs in a PCM-glazed structure. This model has been experimentally validated in a PCM-glazed unit, and is published in Gowreesunker *et al.* (2013c).
- Employing these validated phase change models and the conventional enthalpy-porosity model, the energy performance of two PCM tile systems, a PCM-glazed envelope, and two retrofitted PCM-HX systems were numerically evaluated for the airport terminal space. The simulations were performed using a quasi-dynamic coupled TRNSYS-FLUENT method, via a coupling code developed in this study. The coupling strategies and PCM systems are described in Chapters 6 and 7. The general coupled modelling approach is published in Gowreesunker *et al.* (2013b).
- The impact of each PCM system in the airport terminal space under displacement conditioning, was evaluated in terms of the indoor temperature and energy demands trends for three distinct seasons. The overall impacts were then evaluated based on their relative annual energy demands, computed using the degree day concept, and the associated CO₂ emissions. This is described in Chapter 8.

9.1 Concluding Remarks

1. The literature survey showed that PCM systems have been largely investigated for relatively small indoor spaces, such as offices, and for intermittently occupied buildings. The high heat content at a narrow range of temperatures supports the use of PCMs to improve the thermal mass of lightweight buildings, but other thermophysical, kinetic and chemical properties are also important for the proper implementation of PCM systems. The limitations of certain properties can be overcome through adequate system design. In general, the literature survey showed that:

- a. PCMs with phase change temperatures in the range of 18°C to 25°C have been deemed appropriate for both passive and free-conditioning of spaces.
- b. Although the T-history method has been proposed as more accurate for the thermal characterisation of PCMs due to the larger sample size, the use of Differential Scanning Calorimetry (DSC) has also been found to be satisfactory for engineering purposes, when evaluating the overall performance of PCM systems.
- c. PCM systems have been mainly found to reduce the temperature swing in free-floating indoor spaces, and reduce energy consumption in air-conditioned buildings. However, PCMs have to be recharged to allow the repetitive functioning of the system. This has mainly been done through the use of outdoor night air ventilation for cooling, or through the storage of excess heat for heating purposes.
- d. PCM boards and panels have been the most extensively studied passive systems in the literature, and have resulted in various commercial products. Similarly, PCM heat exchanger (PCM-HX) type systems have been the most widely studied semi-active systems and have also resulted in several commercial products. PCM-glazed units have only recently attracted both research and commercial attention. Semi-active systems offer more flexibility in operation, compared to passive systems.
- e. Numerical modelling is important for the energy evaluation of PCM systems in buildings, because of the large number of variables encountered in system design and control.

2. The adequate modelling of phase change is essential in determining the performance of PCM systems, especially for passive systems, where the thermodynamics of the PCM is solely responsible for the overall performance of the system. Hence, the phase change conduction model developed as part of this study was aimed at improving the simulations of such passive systems, through the consideration of non-linear enthalpy-temperature relationships and hysteresis of the PCM, using User Defined Functions (UDF) in FLUENT. The model was experimentally validated, and the results showed that:

- a. For a PCM with temperature hysteresis of 2°C, the RMS prediction errors for melting were found to be 0.36°C for the UDF models, compared to 3.5°C for the enthalpy-porosity model.
- b. For freezing, the RMS prediction errors were found to be 0.2°C for the UDF models, compared to the 2.6°C for the enthalpy-porosity model.
- c. The PCM temperature trends were also found to be more accurate when employing the UDF models, compared to the conventional enthalpy-porosity model.

3. Due to the renewed research and commercial attention on PCM-glazed units, and the typical large glazed envelope of airport terminal spaces, the impact of a PCM-glazed envelope was considered to be of interest for this study. However, as the behaviour of PCMs under an incident radiation has not been extensively studied and reported in the literature, the radiation and thermal aspects of PCM RT27® was also explored in more detail in this thesis. The main outcomes of this analysis showed that:

- a. Radiation scattering is more prominent in the solid phase of the PCM, while radiation absorption dominates in the liquid phase. In the mushy phase, the radiation scattering and absorption behaviours can be described by the liquid fraction term.
- b. The models developed in this study are able to adequately predict the radiation and thermal behaviour of the PCM as it undergoes phase change. The simulation results were successfully validated with experimental data.

- c. The use of PCM within a double-glazed unit increases the thermal mass during phase change relative to a standard double glazed unit. After phase change, although providing a similar overall transmittance value to a standard glazed unit, the absorption process dominates in the PCM-glazed unit, compared to reflection in a standard glazed unit. Thus, when using PCM-glazed units, adequate emphasis must be placed on the overheating aspects after the PCM has melted.
- d. The PCM visual aspect changes as the material changes phase. It is translucent in the solid phase and transparent in the liquid phase. Thus, depending on its application, this may be acceptable, or should be considered in greater detail in architectural design.

4. Airport environments require the use of CFD to predict the indoor air-flow which is required for the appropriate energy evaluation of HVAC systems for large spaces. In this regard, although several past studies have shown the adequacy of CFD to predict indoor air-flows, the effectiveness of CFD in this study is further extended to the simulation of indoor air-flow and PCM boards. This was done by applying the PCM boards on the internal sides of the walls of an experimental test-cell, and monitoring the indoor air and surface temperatures for different ventilation configurations, in order to validate the CFD model. The results showed that:

- a. The performance of the CFD simulations depends to a certain extent on the approach used for the simulation of the PCM in the board. Using the enhanced phase change conduction model improves the simulation accuracy compared to the standard enthalpy–porosity by about 0.5 °C.
- b. The qualitative results show that the temperature stratification effects can be adequately predicted with CFD models, and the liquid fraction term can enable more efficient building design using PCM boards for both natural and forced convection scenarios.
- c. Due to the extensive simulation times required, CFD can mainly be used as a design tool to determine areas of concern and to investigate improvements in building design over a short period of time. A number of discrete time dependent simulations, can however be used with different weather data to gain

an understanding of the influence of the variation in external conditions on the thermal response of indoor spaces equipped with PCM boards.

5. The performance evaluation of the PCM systems in the airport terminal space was carried out using a numerical approach, whereby the main aim was to obtain the relative performance of the different systems instead of their absolute quantifiable performances.

Furthermore, because of the requirement to simulate the indoor air-flow, multi-zonal simulation tools could not be employed in isolation due to their simplistic approach to air-flow modelling. As a result, a coupled simulation approach was adopted to study the performance of the PCM systems in the airport terminal space. The CFD model was developed following an L_2 norm approach in order to adequately relax and justify the errors encountered in the simulations. It was found that using such a coupled simulation approach provides a greater flexibility in terms of: designing different PCM systems, control systems and indoor geometries; implementing detailed simulation models and boundary conditions; combining different mechanical systems and CFD; and providing a detailed visualisation and understanding of the heat transfer processes involved in both the building and the HVAC system.

6. The performance evaluation of the DC (Displacement Conditioning) system was done in terms of the heating and cooling energy demands of the building, the fan power required by the DC system, and the indoor temperature trends. The results showed that:

- a. The use of DC is more effective for cooling purposes rather than heating purposes. This is due to the stratification benefits provided by the buoyancy effects of cold supply air, compared to the mixing propensity of hot supply air. Temperature stratification allows the cooling potential of the supply air to be specifically targeted to the conditioned zone and to reduce the heat gains from higher levels in the building envelope, improving the air distribution in the indoor space and reducing the overall HVAC energy demand.

- b. The combination of the cyclic operation of the PID controller and the free-conditioning HVAC control strategy used in this study was able to satisfy the comfort conditions only during the intermediate seasons. Slight over-heating was noted during summer, whilst slight under-cooling was obtained in winter. Nonetheless, the indoor temperatures can still be justified based on the adaptive thermal comfort approach by CIBSE. This control strategy represents a relatively simple control method, and was mainly adopted to allow free-conditioning of the space and reduce energy requirements.
- c. The majority of the annual energy demand is for heating the space. This was mainly due to the: operating hours of the airport terminal building, whereby heating was sometimes required even during the early morning hours in the summer; and the UK weather conditions. As a result, it was observed that in order to significantly reduce the energy demand of the airport terminal space, the PCM systems must influence the heating demand of the building relatively more than the cooling demand.

7. Three different PCM systems were studied for this airport terminal space, together with different night charging strategies for each system. The relative performance of the systems was then compared to each other, and with the 'DC-only' diffuser. The results showed that:

- a. The use of the retrofitted semi-active PCM-HX system in the DC diffuser improves the overall performance of the HVAC system by providing the intended improved free-conditioning aspect. The indoor temperature within the comfort range of 18-23°C is thus effectively prolonged as the supply air is kept closer to the comfort temperature range for a longer duration of time, compared to the 'DC-only' case. Hence, it was found that by increasing the overall heat capacity of the PCM-HX configuration from PCM-HX-16mm to PCM-HX-8mm, the temperature swing in the space was further reduced and the overall energy demand improved, even though the fan power increased.
- b. The use of passive PCM floor tiles was found to increase the overall thermal mass of the building envelope. In doing so, the cooling energy demand of the building is reduced, and depending on the night charging strategy employed,

heating demand can also be reduced, compared to the ‘DC-only’ case. It was also found that increasing the latent heat capacity of the PCM floor tiles simply made a more pronounced reduction in the space overheating and overall energy demand.

- c. The use of the passive PCM-glazed envelope slightly improved the indoor temperature swing compared to the PCM floor tiles during the summer and intermediate periods. Similarly, the cooling loads also reduced for the majority of cases, relative to the PCM floor tiles and ‘DC-only’ case, mainly due to the lower solar transmission. In winter, the heating loads reduced compared to the ‘DC-only’ case, depicting the insulating effect of the PCM in the glazing. The optical change of the PCM during phase change must also be taken into account when applying such PCM-glazed structures to the building envelopes.
- d. In general, employing night ventilation produced a negative impact on the annual energy demand of the airport terminal space when using the PCM systems. This is due to the early morning heating demands of the building; ventilating the PCM at night without any control, produces lower PCM temperatures in the morning, requiring additional heating. Conversely, avoiding or limiting night ventilation increases the PCM temperatures in the morning, reducing the early morning heating demand and overall fan power. The recharge of the PCM systems can be adequately implemented within the early operating hours of the airport terminal space.

8. The use of the PCM systems investigated in this study smoothed out the variation of energy demand across the operating hours of the airport. This was observed by the fact that both the early morning heating demands and the cooling demands during daytime were reduced with the use of the PCM systems without night-ventilation, in the summer and intermediate periods. Additionally, there was a net shift of the peak temperatures to later in the day when using the PCM systems.

During winter, the PCM systems were found to have a relatively lower impact on both the indoor temperature and heating demands, compared to the summer and intermediate periods. This was mainly due to the fact that the phase change temperatures of the PCMs were slightly outside the indoor temperature fluctuation range, resulting in the

slightly inefficient use of the latent heat capacity. This shows the importance of appropriately choosing the PCM for each investigated scenario.

This study generally showed that employing PCMs in an airport terminal space can be beneficial, depending on the type of system and the night recharge strategy employed. Using the semi-active PCM-HX system without night ventilation can provide up to 38% and 23% in annual energy and CO₂ emissions savings, respectively, whilst using the passive PCM floor tiles and PCM-glazed envelope without night-ventilation can provide up to 15% and 10% in annual energy and CO₂ emissions savings, relative to the 'DC-only' case. Employing 'full night' ventilation strategies produces energy losses for all PCM systems, whilst using controlled night ventilation strategies provides relatively lower energy savings compared to 'noVent' ventilation strategies.

For the case of this airport departure hall, this study showed that the use of the semi-active 'PCM-HX-8mm' system without night ventilation produces the lowest energy demand (38%), lowest CO₂ emissions (23%) and a payback period of 12.25 years, compared to the 'DC-only' case.

9.2 Recommendations for Future Work

The modelling approaches to simulate phase change processes are constantly being improved, especially with regards to simulating convection, hysteresis and nucleation. The enhanced phase change model developed in this study is currently limited to conduction dominant phase change only, due to the nature of the UDF equations employed in the model. This model can however be improved by adequately modifying these UDF equations to account for convection, and by undergoing further validation studies. Nucleation, on the other hand, is a more design dependent problem and may require the use of statistical approaches to quantify the surface parameters.

The test cell and environmental chamber facilities developed as part of this study may be used to provide further experimental results to validate different numerical scenarios, not limited to PCM boards. For instance, the large glazed surface in the test cell can be used to study radiation models such as the Discrete Ordinates or Surface-2-Surface models. Because of the growing use of numerical models in the design process, engineers and manufacturers are constantly looking for simpler and more accurate models to quickly evaluate the impact of different building phenomena (such as stratification, dynamic heat transfer rates or thermal mass). The developed facilities can be therefore used to validate such simple models, in order to facilitate the design process. Validation studies are very important in order to improve confidence in numerical modelling approaches.

The PCM radiation modelling approach developed in this study is aimed at primarily providing a method to quantify the radiation performance of PCMs, but also to provide a platform for further research in this field. The relationships developed can be further verified for a wider range of PCMs and wavelengths, or be further improved by accounting for the radiation transfer between different phases at the material phase change interface. Additionally, the behaviour of PCM-glazed units during night cooling can also be further explored, or the model can be employed in the design of thermally massive glazed units with PCM.

The coupled simulation approach between TRNSYS and FLUENT provides a very flexible simulation tool to analyse different complex scenarios, because it combines the zonal approach of TRNSYS with the finite volume method of FLUENT. However, at

the moment, due to extensive computing times, this coupled approach is limited to research studies, and even then, requires some simplifications to make it practical. These simplifications can introduce uncertainties with the real situation and can therefore be further improved. For instance: a more explicit modelling of radiation through the glazing structure, considering the absorption, scattering and reflection properties of the glass can be used, instead of employing the lumped parameters; the simulation domain can be extended from 2D to 3D; or longer time periods can be simulated to improve the prediction accuracy of the Degree Day concept. The effects of these simplifications can be further investigated, in the form of parametric analyses of the different simulation variables.

This study provides a platform for investigating the relative performance of PCM systems for large and thermally lightweight indoor spaces. The performance of the PCM systems can however be further investigated for various different scenarios, including: different ventilation systems; different comfort temperature ranges; different night control strategies, including pre-heating of the airport in the morning; different heat gain profiles; intelligent HVAC control systems; different heating and cooling set-points; different PCMs for summer, intermediate and winter seasons; and different PCM configurations or inter-operation of different PCM systems. Furthermore, a more extensive costs and CO₂ emissions analysis can be performed, depending on the quality of information available.

REFERENCES

- Airports Council International – ACI (2009), ACI Policies and Recommended Practices Handbook, Seventh Edition, ACI, Geneva
- Airports Council International – ACI, Green Flight Times, Edition 4 (Sept-Nov 2010)
- Alauzet F, Frey PJ, George PL, Mohammadi B (2007), 3D transient fixed point mesh adaptation for time-dependent problems: application to CFD simulations, *Journal of Computational Physics* 222: 592-623
- Ander GD (2003), *Daylighting performance and design*, John Wiley & Sons, Inc. 2nd Edition. USA. ISBN: 0-471-26299-4.
- ANSI/ASHRAE Standard 55-2004: Thermal environmental conditions for human occupancy (2004) pp. 8
- ANSYS FLUENT theory guide (Nov 2010), Release 13.0.
- ANSYS FLUENT user guide (Nov 2010), Release 13.0.
- Arias DA (2006), Advances on the coupling between a commercial CFD package and a component-based simulation program, Second National IBPSA-USA Conference (SimBuild 2006), Cambridge, MA, August 2-4, 2006
- Athienitis AK, Liu C, Hawes D, Banu D, Feldman D (1997), Investigation of the thermal performance of a passive solar test-room with wall latent heat storage, *Building and Environment* 2(5):3405–3410
- Auliciems A, Szokolay SV (2007). *Thermal comfort: Passive and low energy Architecture International design tools and techniques*, PLEA Note 3. ISBN: 0867767294. 2nd Edition. The University of Queensland; 2007
- Awbi HB (1998), Calculation of convective heat transfer coefficients of room surfaces for natural convection, *Energy and Buildings* 28: 219–227
- Barbour SL, Krahn J (2004), Numerical modelling – Prediction or Process?, *Geotechnical News*, December Issue, pp. 44-52
- BATA-The Voice of UK Airlines, *The Environment, Fuel and Fuel Efficiency* (2008), 5 pgs
- Beausoleil-Morrison I (2000), *The adaptive coupling of heat and air flow modelling within dynamic whole-building simulation*, PhD Thesis, University of Strathclyde, Glasgow UK.
- Bentz DP, Turpin R (2007), Potential applications of phase change materials in concrete technology, *Cement & Concrete composites*, 29, 527 – 532

- Bershtein VA, Egorov VM (1994), *Differential Scanning Calorimetry of polymers*, Ellis Horwood, ISBN: 0-13-218215-7
- Blocken B, Carmeliet J (2007), Validation of CFD simulations of wind-driven rain on a low-rise building façade, *Building and Environment* 42: 2530–2548
- Bo H, Gustafsson EM, Setterwall F (1999), Tetradecane and hexadecane binary mixtures as phase change materials for cool storage in district cooling systems, *Energy* 24(12): 1015 – 1028
- Boh B, Sumiga B (2008), Microencapsulation technology and its applications in building construction materials, *Materials and Geoenvironment*, 55(30): 329 – 344
- Bolatturk A (2008), Optimum insulation thickness for building walls with respect to cooling and heating degree-hours in the warmest zone of Turkey, *Building and Environment* 43: 1055-1064
- Bony J, Citherlet S (2007), Numerical model and experimental validation of heat storage with phase change materials *Energy and Buildings* 39: 1065–1072
- Bostick CW (2009), Architectural trend through the looking glass, In *Proceedings of the Glass performance days 2009*, Tampere, Finland, pp. 860-866
- Brager GS, De Dear RJ (1998), Thermal adaptation in the built environment: a literature review, *Energy and Buildings* 27: 83-96
- Bryn I, Schiefloe PA (2006), Atrium models for the analysis of thermal comfort and energy use, A report of the International Energy Agency (IEA) Task 12 – Building Energy analysis and design tools for solar applications, Project A.3, March 2006
- Building Research Establishment (BRE) – Carbon emissions from non-domestic buildings (BR442), Published in 2000.
- Callister WD (2006), *Materials Science and Engineering: An Introduction*, 6th Edition, Wiley International Edition
- Castell A, Martorell I, Medrano M, Perez G, Cabeza LF (2010), Experimental study of using PCM in brick constructive solutions for passive cooling, *Energy and Buildings* 42: 534–540
- Castellon C, Medrano M, Roca J, Nogues M, Castell A, Cabeza LF (2007), Use of microencapsulated phase change materials in building applications, *ASHRAE*, 2007
- Cerón I, Neila J, Khayet M (2011), Experimental tile with phase change materials (PCM) for building use, *Energy and Buildings* 43: 1869–1874

- Chao CYH, Wan MP (2004), Airflow and air temperature distribution in the occupied region of an underfloor ventilation system, *Building and Environment*, 39: 749–762
- Chartered Institute of Building Services Engineering (CIBSE) Guide A, 2006
- Chartered Institute of Building Services Engineering (CIBSE) Guide B, 2006
- Chen C, Guo H, Liu Y, Yue H, Wang C (2008), A new kind of phase change material (PCM) for energy-storing wallboard, *Energy and Buildings* 40(5): 882-890
- Chen Q (1995), Comparison of different k- ϵ models for indoor air flow computations, *Numerical Heat Transfer, Part B*, 28(3): 353-369
- Chen Q (2009), Ventilation performance prediction for buildings: A method overview and recent applications, *Building and Environment* 44(4): 848–858
- Chung DDL (2010), *Composite Materials – Science and Applications*, 2nd Edition, Springer Verlag (ISBN: 9781848828308)
- Citherlet BJ, Cabeza LF, Streicher W (2007), Laboratory prototypes of PCM storage units, Project report 4 of subtask C 2007, Solar Heating and cooling Programme
- Civil Aviation Authority – CAA (2011) – Airport market power assessments; UK Airports Market - General Context; Working Paper September 2011
- Day T (2006), Degree days: Theory and Applications, CIBSE TM-41
- De Dear R, Brager G, Cooper D (1997), Developing an adaptive model of thermal comfort and preference, Final Report, ASHRAE RP-884
- De Saulles T (2009), The Concrete Centre, Thermal mass explained, ISBN: 978-1-904818-71-7
- De Schepper SCK, Heynderickx GJ, Marin GB (2009), Modeling the evaporation of a hydrocarbon feedstock in the convection section of a steam cracker, *Computers and Chemical Engineering*, 33: 122-132
- Delgado M, Lázaro A, Mazo J, Zalba B (2011), Review on phase change material emulsions and microencapsulated phasechange material slurries: Materials, heat transfer studies and applications, *Renewable and Sustainable Energy Reviews* 16: 253– 273
- Dimaano MNR, Watanabe T (2002), Performance investigation of the capric and lauric acid mixture as latent heat energy storage for a cooling system, *Solar energy* 72(3): 205-215

- Dolado P, Lazaro A, Marin JM, Zalba B (2011), Characterization of melting and solidification in a real scale PCM-air heat exchanger: Numerical model and experimental validation, *Energy Conversion and Management* 52: 1890–1907
- Dolado P, Lazaro A, Zalba B, Marin JM, (2009) Numerical simulation of the thermal behaviour of an energy storage unit with phase change materials for air conditioning applications between 17°C and 40°C, *Thermal Engineering Division, Department of Mechanical Engineering, University of Zaragoza, Spain*
- Egolf PW, Manz H (1994), Theory and modeling of phase change materials with and without mushy regions, *International Journal of Heat Transfer*, 37(18): 2917-2924
- Esen A, Kutluay S (2004), A numerical solution of the Stefan problem with a Neumann-type boundary condition by enthalpy method, *Applied Mathematics and Computation* 148: 321–329
- Evola G, Marletta L, Sicurella F (2013), A methodology for investigating the effectiveness of PCM wallboards for summer thermal comfort in buildings, *Building and Environment* 59:517-527
- Fan Y, Ito K (2012), Energy consumption analysis intended for real office space with energy recovery ventilator by integrating BES and CFD approaches, *Building and Environment* 52: 57-67
- Fanger PO (1970), *Thermal Comfort: Analysis and applications in Environmental Engineering*, McGraw-Hill Book Company, USA
- Farid MM, Khudhair AM, Razack SAK, Hallaj SA (2004) A review on phase change energy storage: materials and applications, *Energy Conversion and Management* 45, 1597–1615
- Gagge AP, Stolwijk JAJ, Hardy JD (1967), Comfort and thermal responses at various ambient temperatures, *Environmental Research* 1(1): 1-20
- Gebremedhin KG, Wu BX (2003), Characterization of flow field in a ventilated space and simulation of heat exchange between cows and their environment, *Journal of Thermal Biology*, 28: 301–319
- Godarzi AA, Jalilian M, Samimi J, Jokar A, Vesaghi MA (2013), Design of a PCM storage system for a solar absorption chiller based on exergo-economic analysis and genetic algorithm, *International Journal of Refrigeration* 36: 88-101
- Goia F, Perino M, Haase M (2012), A numerical model to evaluate the thermal behaviour of PCM glazing system configurations, *Energy and Buildings* 54: 141–153

- Gousseau P, Blocken B, Stathopoulos T, van Heijst GJF (2011), CFD simulation of near-field pollutant dispersion on a high-resolution grid: A case study by LES and RANS for a building group in downtown Montreal, *Atmospheric Environment* 45(2): 428-438
- Gowreesunker BL, Tassou SA, Kolokotroni M (2012), Improved simulation of phase change processes in applications where conduction is the dominant heat transfer mode, *Energy and Buildings* 47: 353-359
- Gowreesunker BL and Tassou SA (2013a), Effectiveness of CFD simulation for the performance prediction of phase change building boards in the thermal environment control of indoor spaces, *Building and Environment* 59: 612-625
- Gowreesunker BL, Tassou SA, Kolokotroni M (2013b), Coupled TRNSYS-CFD simulations evaluating the performance of PCM plate heat exchangers in an Airport Terminal building displacement conditioning system, *Building and Environment* 65: 132-145
- Gowreesunker BL, Stankovic SB, Tassou SA, Kyriacou PA (2013c), Experimental and numerical investigations of the optical and thermal aspects of a PCM-Glazed unit, *Energy and Buildings* 61: 239-249
- Gowreesunker BL and Tassou SA (2013d), Evaluation of the energy impact of PCM tiles in an Airport Terminal Departure Hall, In *Proceedings of the CIBSE Technical Symposium 2013*, Liverpool John Moore's University, Liverpool, UK, 11-12 April 2013
- Gowreesunker BL and Tassou SA (2013e), A TRNSYS-FLUENT coupled simulation of the thermal environment of an airport terminal space with a mixing and displacement air conditioning system, *13th International Conference of the International Building Performance Simulation Association*, Chambéry, France, 25-28 August 2013.
- Gregori G (2010), Technology on Energy saving – Airports going green, “Leonardo da Vinci” Fiumicino Airport, Chicago Nov 2010
- Gunther E, Mehling H, Hiebler S (2007), Modeling the subcooling and solidification of phase change materials, *Modelling and Simulation in Materials Science and Engineering*. 15: 879-892, IOP Publishing
- Guobing Z, Yinping Z, Xin W, Kunping L, Wei X (2007), An assessment of mixed type PCM-gypsum and shape-stabilized PCM plates in a building for passive solar heating, *Solar Energy*, 81(11), 1351-1360
- Gutiérrez-Montes C, Sanmiguel-Rojas E, Kaiser AS, Viedma A (2008), Numerical model and validation experiments of atrium enclosure fire in a new fire test facility, *Building and Environment* 43(11): 1912-1928

- Hara T, Kato S (2004), Numerical simulation of thermal plumes in free space using the standard k-ε model, *Fire Safety Journal* 39: 105-129
- Heim D (2005), Two solution methods of heat transfer with phase change within whole building dynamic simulation, *Building Simulation 2005, Ninth International IBPSA Conference*, Montreal, Canada, 15-18 August 2005
- Heim D, Clarke J (2003), Numerical modelling and thermal simulation of phase change materials within ESP-r. In: *Eighth international IBPSA conference*, Eindhoven, Netherlands, August 11–14, 2003
- Heiselberg P, Murakami S, Roulet CA (1998), Ventilation of large spaces in building – Analysis and prediction techniques, *International Energy Agency (IEA) Energy Conservation in Buildings and Community systems, Annex 26: Energy Efficient Ventilation of Large Enclosures*, 1998
- Holmes M, Hacker J (2008), The problem of summertime overheating prediction, *Proceedings of Conference: Air Conditioning and the Low Carbon Cooling Challenge*, Cumberland Lodge, Windsor, UK, 27-29 July 2008. London: Network for Comfort and Energy Use in Buildings
- <http://glassx.ch/index.php?id=314>, Accessed on 09 Jan. 2013
- http://pedia.educdz.com/Encyclopedia_of_Chemical_Physics_and_Physical_Chemistry/b1_27.htm, Accessed on 12 Oct. 2010
- Weisstein EW (2010), <http://scienceworld.wolfram.com/chemistry/IncongruentMelting.html>, Accessed on 09 Oct. 2010
- SkyCool Pty (2011), <http://www.airport-technology.com/contractors/terminal/skycool/>, Accessed on 17 Mar. 2011
- DELTA (2013), <http://www.cosella-dorken.com/bvf-ca-en/products/pcm/products/cool28.php>, Accessed on 09 Jan. 2013
- Cristopia Co Ltd (2010), <http://www.cristopia.com/cristopia/english/products/indproducts.html>, Accessed on 16 Oct. 2010
- DECC – UK Department of Energy and Climate Change (2009), http://www.decc.gov.uk/en/content/cms/what_we_do/lc_uk/lc_uk.aspx, Accessed on 06 Oct. 2009
- DesignBuilder (2012), <http://www.designbuilder.co.uk/content/view/40/61/>, Accessed on 22 Dec. 2012

Designbuild-network (2012), <http://www.designbuild-network.com/projects/terminal-5-heathrow/terminal-5-heathrow4.html> , Accessed on 20 Sep. 2012

DFPNI – UK Department of Finance and Personnel (2010), <http://www.dfpni.gov.uk/energy-performance-of-buildings>, Accessed on 06 Oct. 2010

Energy Saving Trust (2013), <http://www.energysavingtrust.org.uk/Energy-Saving-Trust/Our-calculations>, Accessed on 15 Apr. 2013

IES (2012), <http://www.iesve.com/news>, Accessed on 22 Dec. 2012

<http://www.malaysiaairports.com.my/index.php/environment/534>, Accessed on 28 Mar. 2013

<http://www.mitsubishirenewables.eu/downloads.php>, Accessed on the 16 Apr. 2013

MONODRAUGHT Ltd (2013), <http://www.monodraught.com/>, Accessed on 08 Jan. 2013

MRFN – Materials Research Facilities Network (2010), <http://www.mrfn.org/ucsb/polym/DSC-Manual.pdf>, Accessed on 12 Oct. 2010

NPL – National Physical Laboratory (2010), <http://www.npl.co.uk/engineering-measurements/thermal/temperature/faqs>, Accessed on 12 Oct. 2010

PCM Products Ltd (2010), http://www.pcmproducts.net/products_pcm_solutions.htm, Accessed on 11 Oct. 2010

Ye P, McCorkle J, Cassel B (2010), <http://www.perkinelmer.co.uk>, Accessed on 12 Oct. 2010

Roper, LD (2010), <http://www.roperld.com/science/minerals/fossilfuels.htm>, Accessed on 06 Oct. 2010

Rubitherm GmbH (2010), <http://www.rubitherm.com/english/index.htm>, Accessed on 19 Oct. 2010

BASF (2010), http://www.basf.com/group/corporate/en_GB/brand/MICRONAL_PCM , Accessed on 19 Oct. 2010

ScienceDirect (2013), <http://www.sciencedirect.com>, Accessed on the 01 Feb. 2013

Guardian Industries Corporation (2012), <http://www.sunguardglass.co.uk/SpecificationsResources/ProductSpecifications/index.htm>, Accessed on 24 Aug. 2012

TROX UK Ltd (2013), http://www.troxuk.co.uk/uk/service/download_center/structure/technical_documents/air_water_systems/index.html, Accessed on 22 Jan. 2013

- DECC-UK Department of Energy and Climate Change (2013), [https://restats.decc.gov.uk /cms/ annual-mean-wind-speed-map](https://restats.decc.gov.uk/cms/annual-mean-wind-speed-map), Accessed on 14 Mar. 2013
- Hu H, Argyropoulos SA (1996), Mathematical modelling of solidification and melting: a review, *Modelling and Simulation in Materials Science and Engineering*. 4: 371-396
- Hung WY (2003), Architectural aspects of atrium, *International Journal on Engineering Performance-Based Fire Codes*, 5(4):131-137
- Hung WY and Chow WK (2001), A Review on Architectural Aspects of Atrium Buildings, *Architectural Science Review*, 44(3): 285-295
- Hunt GR, Cooper P, Linden PF (2001), Thermal stratification produced by plumes and jets in enclosed spaces, *Building and Environment* 36: 871–882
- Hussain S, Oosthuizen PH, Kalendar A (2012), Evaluation of various turbulence models for the prediction of the airflow and temperature distributions in atria, *Energy and Buildings* 48: 18-28
- Idelchik IE (1994), *Handbook of hydraulic resistance*. 3rd Edition. CRC Press; 1994
- HM Government (2009), *Investing in a Low Carbon Britain, initiative of ‘Building Britain’s Future’ 2009*, HM Government, Crown Copyright. URN 09D/544
- Ismail KAR, Henriquez JR (2002), Parametric study on composite and PCM glass systems, *Energy Conversion and Management* 43: 973–993
- Jahns E (2010), *Microencapsulated phase change material*, BASF AG, Germany
- Kelly R (2000), *Latent Heat Storage in Building Materials*, International Conference on Sustainable Building 2000, 22-25 October 2000, Maastricht, The Netherlands.
- Koca A, Oztop HF, Koyun T, Varol Y (2008), Energy and exergy analysis of a latent heat storage system with phase change materials for a solar collector, *Renewable Energy* 33(4):567-574
- Kolokotroni M, Davies M, Croxford B, Bhuiyan S, Mavrogianni A (2010), A validated methodology for the prediction of heating and cooling energy demand for buildings with the Urban Heat Island: Case-study of London, *Solar Energy* 84: 2246-2255
- Kondo T, Iwamoto T. *Research on using the PCM for ceiling board*. IEA ECESIA, Annex 17, 3rd workshop, Tokyo, Japan; 2002
- Koschenz M, Lehmann B (2004), Development of a thermally activated ceiling panel with PCM for application in lightweight and retrofitted buildings, *Energy and Buildings* 36: 567–578

- Kowalewski T. A., Gobin D. (2004) Phase change with convection: modelling and validation, Springer-Verlag Wien New York, ISBN: 3211208917
- Kravvaritis E D, Antonopoulos K A , Tzivanidis C (2010), Improvements to the measurement of the thermal properties of phase change materials, *Measurement Science and Technology* 21 (2010) 045103 (9pp)
- Kuznik F, Rusaouën G, Brau J (2007), Experimental and numerical study of a full scale ventilated enclosure: comparison of four two equations closure turbulence models, *Building and Environment* 42: 1043–1053
- Kuznik F, Virgone J (2009a), Experimental investigation of wallboard containing phase change material: Data for validation of numerical modelling, *Energy and Buildings* 41: 561–570
- Kuznik F, Virgone J (2009b), Experimental assessment of a phase change material for wall building use, *Applied Energy* 86: 2038–2046
- Lamberg P, Lehtiniemi R, Henell AM (2004a), Numerical and experimental investigation of melting and freezing processes in phase change materials storage, *International Journal of thermal Sciences* 43: 277-287
- Lamberg P (2004b), Approximate analytical model for two phase solidification problem in a finned phase-change-material storage, *Applied Energy* 77: 131-152
- Launder BE, Spalding DB (1972), *Lectures in Mathematical Models of Turbulence*, Academic Press, London, England.
- Leenknecht S, Wagemakers R, Bosschaerts W, Saelens D (2012), Numerical sensitivity study of transient surface convection during night cooling, *Energy and Buildings* 53: 85-95
- Li Y, Fazio P, Rap J (2012), Numerical investigation of the influence of room factors on HAM transport in a full-scale experimental room, *Building and Environment* 50: 114-124
- Lin K, Zhang Y, Di H, Yang R (2007), Study of an electrical heating system with ductless air supply and shape-stabilized PCM for thermal storage, *Energy Conversion and Management* 48: 2016–2024
- Liu J, Yu N, Lei B, Rong X, Yang L (2009), Research on indoor environment for the terminal 1 of Chengdu Shuangliu International airport, *Proceedings of the Eleventh International IBPSA Conference, Glasgow, Scotland, 27-30 July 2009*
- Matsui M, Takayanagi H, Oda Y, Komurasaki K, Arakawa Y (2004), Performance of arcjet-type atomic-oxygen generator by laser absorption spectroscopy and CFD analysis, *Vacuum* 73(3-4): 341-346

- McCartney KJ, Nicol JF (2002), Developing an adaptive control algorithm for Europe, *Energy and Buildings*, 34(6): 623-635
- McIntyre DA (1980), Design requirements for a comfortable environment, in: Cena K, Clark JA (Eds), *Bioengineering Thermal Physiology and Comfort*, Elsevier, Amsterdam: 157-168
- Medrano M, Yilmaz MO, Nogués M, Martorell I, Roca J, Cabeza LF (2009), Experimental evaluation of commercial heat exchangers for use as PCM thermal storage systems, *Applied Energy* 86: 2047–2055
- Medved S, Arkar C (2008), Correlation between the local climate and the free-cooling potential of latent heat storage, *Energy and Buildings* 40: 429–437
- Mehling H, Cabeza LF (2008), *Heat and cold storage with PCM: An up to date introduction into basics and applications*, Springer, ISBN: 978-3-540-68556-2
- Mehling H, Hiebler S, Cabeza LF (2002), News on the application of PCMs for heating and cooling of buildings, IEA, ECESIA Annex 17
- Meng Q, Li Q, Zhao L, Li L, Chen Y, Wang S (2007), Numerical study on airflow and temperature distribution in an airport terminal building under natural ventilation, 6th International Conference on Indoor Air Quality, Ventilation & Energy Conservation in Buildings IAQVEC 2007, Oct. 28 - 31 2007, Sendai, Japan
- Mettawee EBS, Assassa GMR (2006), Experimental study of a compact PCM solar collector, *Energy* 31(14): 2958-2968
- Miao C, Lu G, Yao Y, Tang G, Weng D (2007), Preparation of shape-stabilized phase change materials as temperature-adjusting powder, *Frontiers of materials science in China* 2007, 1(3): 284–287
- Milne GR (1995), The energy implications of a climate-based indoor air temperature standard, in: Nicol, Humphreys, Sykes, Roaf (Eds), *Standards for thermal comfort*, E and FN Spon, London, pp 182-189
- Modest MF (2003), *Radiative heat transfer*, 2nd Edition, Elsevier Science, USA
- Nagano K, Takeda S, Mochida T, Shimakura K, Nakamura T (2006), Study of a floor supply air conditioning system using granular phase change material to augment building mass thermal storage—Heat response in small scale experiments, *Energy and Buildings* 38: 436–446
- Oberkampf WL, Barone MF (2006), Measures of agreement between computation and experiment: validation metrics, *Journal of Computational Physics* 217(1): 5–36

- Oikonomou E, Davies M, Mavrogianni A, Biddulph P, Wilkinson P, Kolokotroni M (2012), Modelling the relative importance of the urban heat island and the thermal quality of dwellings for overheating in London, *Building and Environment* 57: 223-238
- Parker J, Cropper P, Shao L (2011), Using building simulation to evaluate low carbon refurbishment options for airport buildings, *Proceedings of Building Simulation 2011: 12th Conference of International Building Performance Simulation Association*, Sydney, 14-16 November 2011, pp. 554-561
- Parker J, Cropper P, Shao L (2012), Retrofit of airport terminals: Using building simulation to evaluate environmental and economic impacts. *Retrofit 2012*, Salford University, 24th – 26th January 2012. Available at: www.energy.salford.ac.uk (Accessed 28th March 2013)
- Piechowski M, Rowe A (2007), Building design for hot and humid climates – Implications on thermal comfort and energy efficiency, *Proceedings: Building Simulation 2007*
- Pochee H, Dawson G, Burgon P, Bentham T (2012), An analysis of the benefits and drawbacks of exposed thermal mass in modern, well-insulated buildings, *World Renewable Energy Forum*, Denver, Colorado, 13-17 May 2012, Paper 0964
- Poirier D, Salcudean M (1988), On numerical methods used in mathematical modelling of phase change in liquid metals, *ASME Journal of Heat Transfer* 110: 562–70
- Rady M (2009), Granular phase change materials for thermal energy storage: Experiments and numerical simulations, *Applied Thermal Engineering*, 29: 3149-3159
- Raj VAA, Velraj R (2010), Review on free cooling of buildings using phase change materials, *Renewable and Sustainable Energy Reviews* 14: 2819-2829
- Ramponi R, Blocken B (2012), CFD simulation of cross-ventilation for a generic isolated building: Impact of computational parameters, *Building and Environment* 53: 34–48
- Raoux S, Wuttig M (2008), *Phase change materials: Science and applications*, Springer
- Ravikumar M, Srinivasan PSS (2005), Phase change material as a thermal energy storage material for cooling of building, *Journal of Theoretical and Applied Information Technology*, 503-511
- Reid RC, Prausnitz JM, Poling BE (1987), *The Properties of Gases and Liquids*. McGraw-Hill, New York, 1987

- Rohdin P, Moshfegh B (2007), Numerical predictions of indoor climate in large industrial premises. A comparison between different k- ϵ models supported by field measurements, *Building and Environment* 42: 3872-3882
- Sandnes B, Rekstad J (2006), Supercooling salt hydrates: Stored enthalpy as a function of temperature, *Solar Energy* 80:616-625
- Schellen L, Loomans MGLC, Kingma RMN, de Wit MH, Frijns AJH, van Marken Lichtenbelt WD (2013), The use of a thermophysiological model in the built environment to predict thermal sensation: Coupling with the indoor environment and thermal sensation, *Building and Environment* 59: 10-22
- Schellen L, Timmers S, Loomans M, Nelissen E, Hensen JLM, van Marken Lichtenbelt W (2012), Draught assessment during design: Experimental and numerical evaluation of a rule of thumb, *Building and Environment* 57: 290-301
- Sharma A, Sharma SD, Buddhi D, Won LD (2006), Effect of thermo physical properties of heat exchanger material on the performance of latent heat storage system using an enthalpy method, *International Journal of Energy Research* 30 (3): 191–201
- Sharma SD, Kitano H, Sagara K (2004), Phase change materials for low temperature solar thermal applications, Department of Agricultural Engineering, Osaka University, Japan, Vol. 29, pp 31 – 64
- Shilei L, Guohui F, Neng Z, Li D (2007), Experimental study and evaluation of latent heat storage in phase change materials wallboards, *Energy and Buildings* 39: 1088–1091
- Siegel R, Spuckler CM (1994), Effects of refractive index and diffuse or specular boundaries on a radiating isothermal layer, *Journal of Heat Transfer* 116: 787-790
- Siemens REV200: Room Temperature Controller, CE1N2212en Data Sheet (2001)
- Silva T, Vicente R, Soares N, Ferreira V (2012) Experimental testing and numerical modelling of masonry wall solution with PCM incorporation: A passive construction solution, *Energy and Buildings* 49: 235-24
- Simmonds P, Gaw W (1996), Using a constant volume displacement ventilation system to create a micro climate in a large airport terminal in Bangkok, *Proceedings of the Tenth Symposium on Improving Building Systems in Hot and Humid Climates*, Fort Worth, TX, May 13-14, 1996, pp. 217-227
- Simmonds P, Holst S, Reuss S (2000), Using radiant cooled floors to condition large spaces and maintain comfort conditions, *ASHRAE Transactions* 106 (2000), pp. 695–701

- Soares N, Costa JJ, Gaspar AR, Santos P (2013), Review of passive PCM latent heat thermal energy storage systems towards buildings' energy efficiency, *Energy and Buildings* 59: 82-103
- Srinivas VSS, Ananthasuresh GK (2006), Analysis and Topology Optimization of Heat Sinks with a Phase Change Material on COMSOL Multiphysics™ Platform, Excerpt from the Proceedings of the COMSOL Users Conference 2006 Bangalore
- Stankovic SB, Kyriacou PA (2012), The effects of thermistor linearization techniques on the T-history characterization of phase change materials, *Applied Thermal Engineering* 44: 78–84
- Stansted Airport Energy Strategy 2011-2016: Renewing our approach to Energy Management, Published by London Stansted – Go Discover, Sept 2011
- Steicher W (2008), Laboratory prototypes of PCM storage units; A Report of IEA Solar Heating and Cooling programme - Task 32: Advanced storage concepts for solar and low energy buildings, Report C4 of Subtask C
- Strbac G, Aunedi M, Pudjianto D, Djapic P, Teng F, Sturt A, Jackravut D, Sansom R, Yufit V, Brandon N (2012), Strategic Assessment of the Role and Value of Energy Storage Systems in the UK Low Carbon Energy Future, Report for the Carbon Trust, Energy Futures Lab, Imperial College London.
- Stribling D, Tassou SA (2000), Investigation into the design and optimisation of multideck refrigerated display cases, PhD Thesis, Brunel University, UK
- Suarez MJ, Gutierrez AJ, Pistono J, Blanco E (2011), CFD analysis of heat collection in a glazed gallery, *Energy and Buildings* 43: 108-116
- Susman G, Dehouche Z, Cheechern T, Craig S (2010), Tests of prototype PCM 'sails' for office cooling, *Applied Thermal Engineering* 31(5): 717-726
- Tanasic N, Jankes G, Skistad H (2011), CFD analysis and airflow measurements to approach large industrial halls energy efficiency: A case study of a cardboard mill hall, *Energy and Buildings* 43: 1200-1206
- Tay NHS, Belusko M, Bruno F (2012), Experimental investigation of tubes in a phase change thermal energy storage system, *Applied Energy* 90: 288–297
- The Building Regulations 2010, Conservation of fuel and power, Part L2B, HM Government.
- Delay T, Farmer S, Jennings T (2009), Building the future, today. The Carbon Trust, Report No. CTC765.

- Ashcroft M, Rugg R (2013), <http://www.carbontrust.com/news/2012/05/building-for-the-future>, Accessed on the 10 April 2013.
- Thompson DE (2005), Verification, Validation, and Solution Quality in Computational Physics: CFD Methods Applied to Ice Sheet Physics, NASA/TM-2005-213453
- TRNSYS 17 Manual (2010), TRNEdit: Editing the input file and creating TRNSED application, Vol. 6
- Tye-Gingras M, Gosselin L (2012), Comfort and energy consumption of hydronic heating radiant ceilings and walls based on CFD analysis, *Building and Environment* 54: 1- 13
- Uddin MS, Zhu HJ, Hawlader MNA (2002) Effects of cyclic operation on the characteristics of a microencapsulated PCM storage material, *International Journal of Solar Energy*, 2002, 22(3-4),105–114
- UKTI - UK Trade & Investment, Sustainable airports: Benefitting from the UK's world-class expertise, Sept 2010, Crown Copyright.
- Vakilaltojjar SM, Saman W (2001), Analysis and modelling of a phase change storage system for air conditioning applications, *Applied Thermal Engineering* 21: 249-263
- Veluri SP, Roy CJ, Luke EA (2012), Comprehensive code verification techniques for finite volume CFD codes, *Computers & Fluids* 70: 59-72
- Verdonck E, Schaap K, Thomas LC (1999), A discussion of the principles and applications of Modulated Temperature DSC (MTDSC), *International Journal of Pharmaceutics* 192 (1999), 3–20
- Voller VR, Prakash C (1987), A fixed grid numerical modelling methodology for convection-diffusion mushy region phase-change problems, *International Journal of Heat and Mass Transfer* 30(8): 1709-1719
- Voller VR, Shadabi L (1984), Enthalpy methods for tracking a phase change boundary in two dimensions, *International Communications in Heat and Mass Transfer* 11(1): 239-249
- Waqas A, Din ZU (2013), Phase change material (PCM) storage for free cooling of buildings-A review, *Renewable and Sustainable Energy Reviews* 18: 607–625
- Weinläder H, Beck A, Fricke J (2005), PCM-façade-panel for daylighting and room heating, *Solar Energy* 78: 177-186
- Wunderlich B (2005), *Thermal Analysis of Polymeric Materials*, Springer, ISBN: 3540236295

- Yang H, He Y (2010), Solving heat transfer problems with phase change via smoothed effective heat capacity and element-free Galerkin methods, *International Communications in Heat and Mass Transfer*, 37: 385-392
- Ye WB, Zhu DS, Wang N (2011), Numerical simulation on phase-change thermal storage/release in a plate-fin unit, *Applied Thermal Engineering* 31: 3871-3884
- Ye WB, Zhu DS, Wang N (2012), Fluid flow and heat transfer in a latent thermal energy unit with different change material (PCM) cavity volume fractions, *Applied Thermal Engineering* 42: 49-57
- Yinping Z, Xu X, Hongfa D, Kunping L, Rui Y (2006), Experimental Study on the Thermal Performance of the Shape-Stabilized Phase Change Material Floor Used in Passive Solar Buildings, *J. Sol. Energy Eng.* 128(2): 255-257
- Yinping Z, Yi J and Yi J, (1999), A simple method, the T-history method, of determining the heat of fusion, specific heat and thermal conductivity of phase change materials, *Measurement Science and Technology*. 10 (1999) 201 – 205
- Zalba B, Marin JM, Cabeza LF, Mehling H (2004), Free-cooling of buildings with phase change materials, *International Journal of Refrigeration* 27: 839–849
- Zhai Z, Zhang Z, Zhang W, Chen Q (2007), Evaluation of various turbulence models in predicting air airflow and turbulence in enclosed environments by CFD. Part-1: Summary of prevent turbulence models, *HVAC&R Research* 13: 853-870
- Zhai ZJ, Chen QY (2005), Performance of coupled building energy and CFD simulations, *Energy and Buildings* 37: 333-344
- Zhai ZJ, Chen QY (2006), Sensitivity analysis and application guides for integrated building energy and CFD simulation, *Energy and Buildings* 38: 1060-1068
- Zhang Z, Zhang W, Zhai Z, Chen Q (2007), Evaluation of various turbulence models in predicting airflow and turbulence in enclosed environments by CFD. Part-2: Comparison with experimental data from literature, *HVAC&R Research* 13(6): 871-886
- Zhou D, Zhao CY, Tian Y (2012), Review on thermal energy storage with phase change materials (PCMs) in building applications, *Applied Energy* 92: 593–605
- Zhu N, Ma Z, Wang S (2009), Dynamic characteristics and energy performance of buildings using phase change materials: A review, *Energy Conversion and Management* 50: 3169–3181

Appendix A: Development of phase change conduction model

This appendix provides supporting information used in the development of the phase change conduction model described in Chapter 3.

A1. Surrounding air temperature

The surrounding air temperature employed in the experimental setup is shown in Fig. A1.1. The same temperature profiles are used in the validation study.

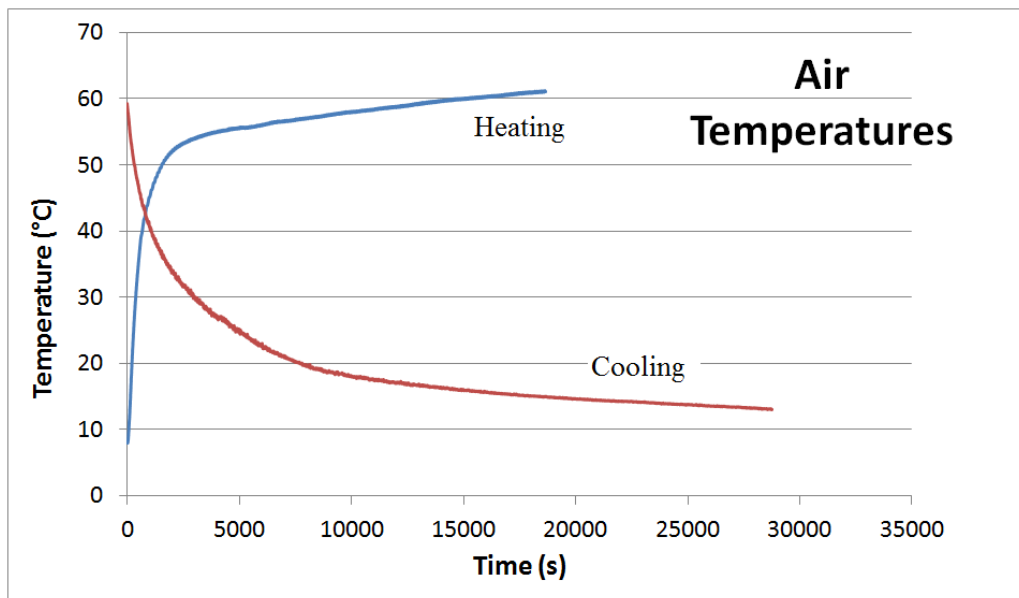


Fig. A1.1 – Environmental Chamber Air temperature surrounding the PCM composite sample

The heating curve air temperature equations are (Temperature in K):

$$\text{For: } 0 < t \leq 2000\text{s}; T = 0.000000012144889 t^3 - 0.000053128368077 t^2 + 0.081766346914520 t + 278.297052966762 \quad (R^2 = 0.997) \quad (\text{A1.1})$$

$$\text{For: } t > 2000\text{s}; T = 0.000460672416241 t + 326.288171300508 \quad (R^2 = 0.972) \quad (\text{A1.2})$$

The cooling curve air temperature equations are (Temperature in K):

$$\text{For } 0 < t \leq 3150\text{s}; T = -0.000000001487132 t^3 + 0.000009870224848 t^2 - 0.025669068823511 t + 330.967748978315 \quad (R^2 = 0.997) \quad (\text{A1.3})$$

$$\text{For } t > 3150\text{s}; T = -0.000000000002492 t^3 + 0.000000150684968 t^2 - 0.003125442202782 t + 310.139061137967 \quad (R^2 = 0.992) \quad (\text{A1.4})$$

A2. The enthalpy-temperature curves and PCM composite properties

The melting and freezing curves are obtained from the Differential Scanning Calorimetry (DSC) at a temperature rate of 0.5K/min. Heat flow DSCs provide the heat flow in the material in terms of mW. However, when extracting the numerical data from the Perkin Elmer DSC6000® curves, the values are given in terms of mW for every second. Hence, the final numerical value obtained from the DSC is equivalent to mJ.

The following procedure was then employed to obtain the enthalpy (J/kg) values for the PCM at each temperature.

$$\text{Enthalpy @ } T \text{ (in mJ/g or J/kg)} = q / m \quad (\text{A1.5})$$

Where:

- q: Energy (mJ)
- m: Mass of PCM sample in DSC (g)

Hence, the following enthalpy curves were obtained for the melting and freezing processes.

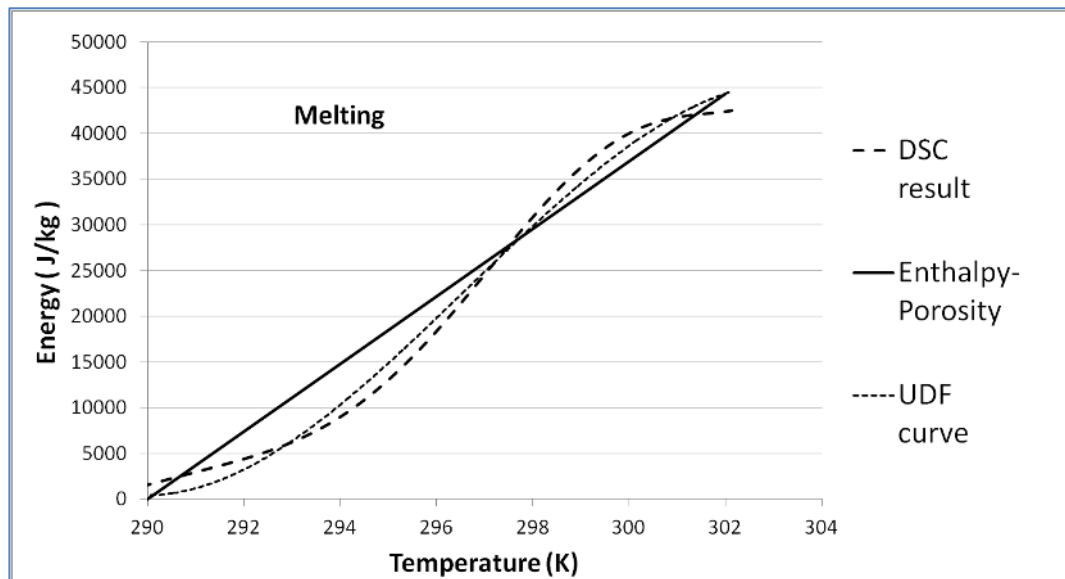


Fig. A1.2(a). DSC, UDF and Enthalpy-Porosity curves used in the simulations for the melting process

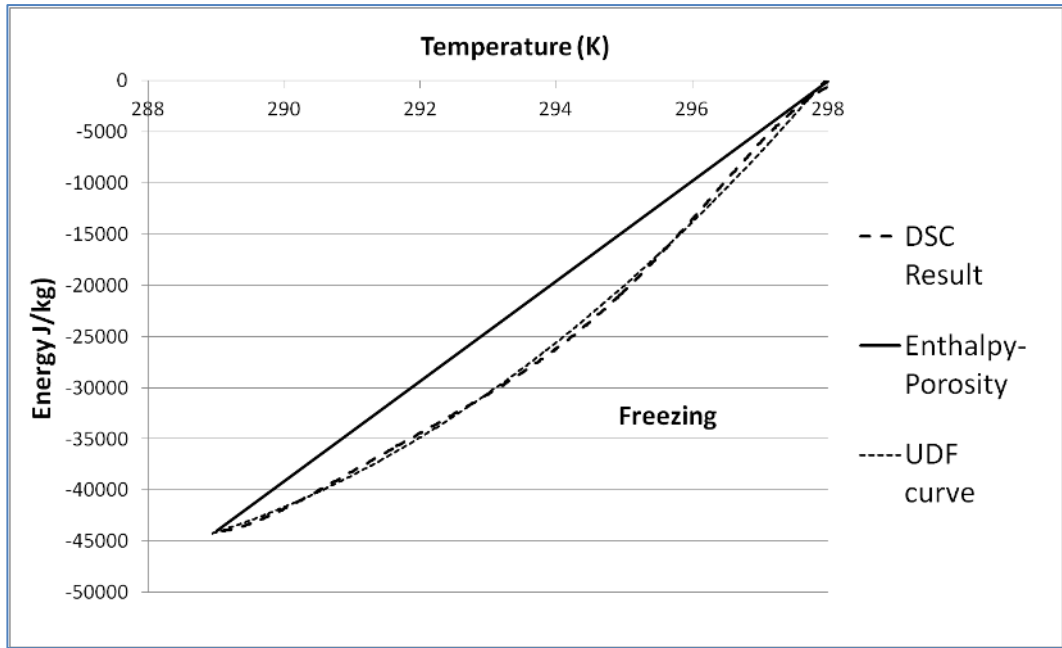


Fig. A1.2(b). DSC, UDF and Enthalpy-Porosity curves used in the simulations for the freezing process

The onset of melting is taken to be 290 K (16.85 °C) and the end temperature 302 K (28.85 °C), with a latent heat capacity of 44,360 J/kg, based on the original DSC curves in Fig. 3.5. The equation (J/kg) of the UDF curve is given by:

$$f(T)_m = -38.23834 T^3 + 34027.216359 T^2 - 10088202.17 T + 996484631.167432 \quad (A1.6)$$

(R²=0.992)

Similarly, the onset of freezing is taken to be 298.15 K (25 °C) and the end temperature at 289 K (15.85 °C), producing an average hysteresis of ≈2 K, based on the energy curves. The latent heat capacity for freezing is 44,117 J/kg. The equation of the UDF curve (J/kg) was determined to be:

$$-f(T)_f = -0.09683 T^3 + 394.481059 T^2 - 201586.679029 T + 27601496.324826 \quad (A1.7)$$

(R²=0.997)

The thermophysical properties of the PCM composite are given as: Density = 840 kg/m³; Specific heat capacity = 2400-2550 J/kgK; Thermal conductivity = 0.3 W/mK, which are obtained from the manufacturer.

A3. CFD model and simulation inputs

The CFD model consisted of 12,320 hexahedral cells and the time-step used in the simulation was 10s. The points A-D were monitored during both the experiments and simulations. Fig. 3.6(a) refers to the results for point A, while Fig. 3.6(b) refers to point C. These two points are presented as they represent the generic temperature trends for the overall model.

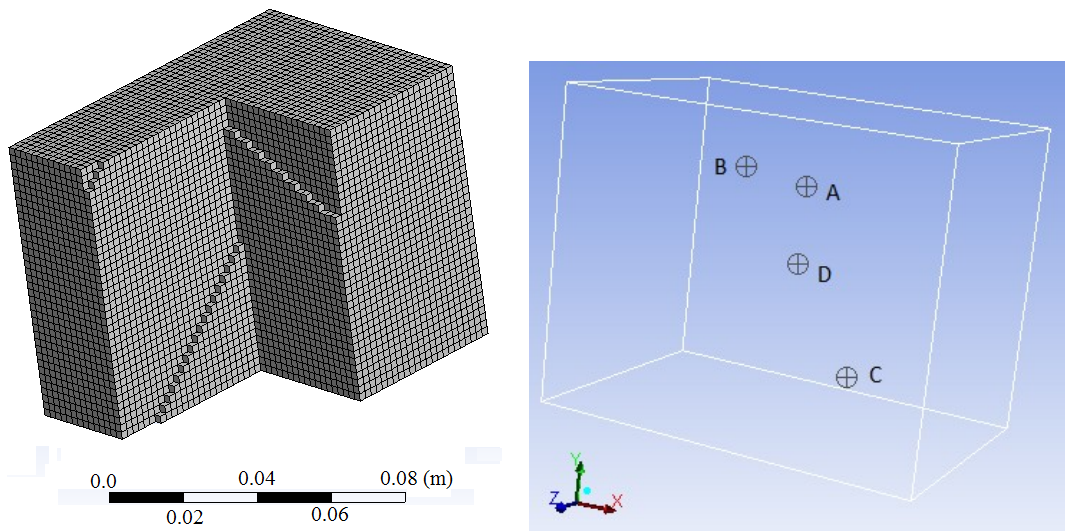


Fig. A1.3. CFD model grid and monitored points' locations

In addition to the UDF heat source terms, the PCM thermophysical properties, and the air temperature source codes, the following simulation inputs were also used.

Table A1.1. Additional CFD inputs

	Melting	Freezing
Initialisation temperature (°C)	8	59
Boundary convective heat transfer coefficients (W/m ² K)	5	8

The boundary convective heat transfer coefficients were obtained as part of the validation process.

A4. RMS error equations

The mean absolute RMS error is obtained by comparing the numerical (*num*) and experimental (*exp*) temperatures of the PCM for the same time (*t*).

$$\text{Mean absolute RMS error} = \left[\sqrt{\frac{\sum (T_{exp,t} - T_{num,t})^2}{n_p}} \right] \quad (\text{A1.8})$$

The mean relative RMS error was obtained by dividing the mean absolute RMS error by the mean absolute overall temperature difference over the four monitored points.

$$\text{Relative RMS error} = \left[\text{Mean absolute RMS error} / \frac{\sum |(T_{initial} - T_{final})_{exp}|_{n_p}}{n_p} \right] \times 100 \quad (\text{A1.9})$$

Where ' n_p ' refers to the points (A-D) monitored. In this case, the total number for $n_p = 4$.

Appendix B: Validity and effectiveness of CFD

This appendix provides supporting information on the validation study conducted in chapter 4. It describes the experimental procedure and the numerical model employed. (Note that this study is fully published in Gowreesunker and Tassou (2013a) – “Effectiveness of CFD simulation for the performance prediction of phase change building boards in the thermal environment control of indoor spaces”.

B1. Description of Experimental Test Cell

This test cell was constructed so as to provide experimental data to allow an appropriate validation of the CFD model. It was therefore constructed to closely match the thermal properties of an actual building.

One of the main aims of employing PCM panels is to enhance the thermal mass of a particular building. As a result, the choice of material combination for the test cell envelope was highly emphasised. The thermal mass was quantified in terms of the decrement factor and the time lag of the wall, calculated using the CIBSE admittance method. To simplify the calculation of the dynamic thermal properties, the Dynamic Thermal Property Calculator V1.0 (developed by ‘The Concrete Centre’) was employed. After various material combinations, the following wall configuration was chosen (see Fig. B1.1). The internal wall surfaces were plastered and painted white.

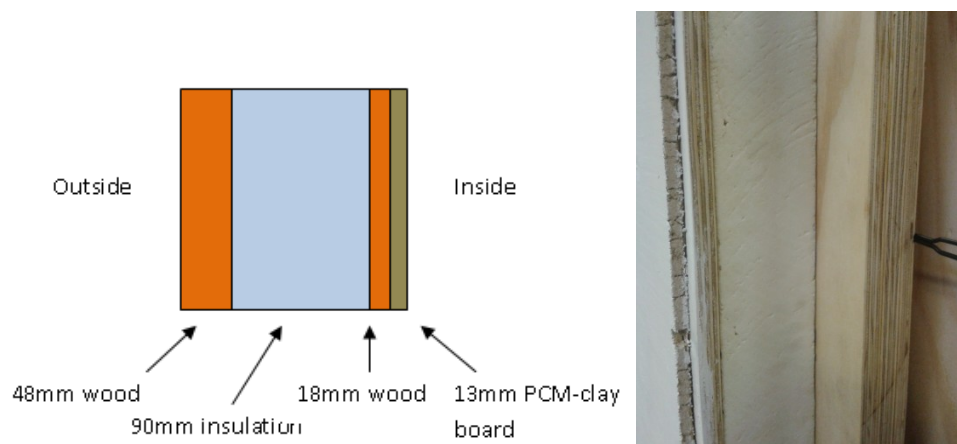


Fig. B1.1. Test Cell Wall Configuration

Adopting such material configuration provided thermal properties close to a Timber Frame Wall with plasterboard (CIBSE guide A, 2006), as shown in Table B1.1.

Table B1.1. Dynamic thermal properties of Walls

Thermal Properties	CIBSE Timber Frame Wall	Experimental Test Cell
U-value ($\text{W}/\text{m}^2\text{K}$)	1.14	0.21
Decrement Factor (-)	0.7	0.81
Time lag (hr)	4.9	4.8

Note that in this case, the U-value of the test cell walls was adjusted to abide by the 2010 Building Regulations Part L2A: Notional U-value of $< 0.26 \text{ W}/\text{m}^2\text{K}$ for non-dwellings' walls. Nonetheless, Table B1.1 shows that the dynamic properties of the test cell wall are relatively close to those of an actual wall.

A glazing of U-value $1.2 \text{ W}/\text{m}^2\text{K}$ (4-16-4 mm, Argon filled) was incorporated in the design in order to represent the large glazed areas usually found in Airport Terminals. The thermophysical properties of the materials are shown in Table B1.2.

Table B1.2. Material properties from manufacturer

Properties	PCM board	Wood	Rigid PIR Insulation	Glazing – 24mm (90% Ar filled)	Plaster
Density (kg/m^3)	1430	500	40	140	950
Specific heat capacity (J/kgK)	1240	1300	1600	840	840
Thermal conductivity (W/mK)	0.14	0.13	0.023	0.03	0.16

B2. Equipment used and Uncertainties

The main parameter monitored during the experiments was the surface and air temperatures, where various Type T thermocouples were uniformly placed within the test cell as shown in Fig. B1.2. The environmental chamber air temperature was also monitored using a Type T thermocouple with an error of $\pm 0.2\text{K}$.

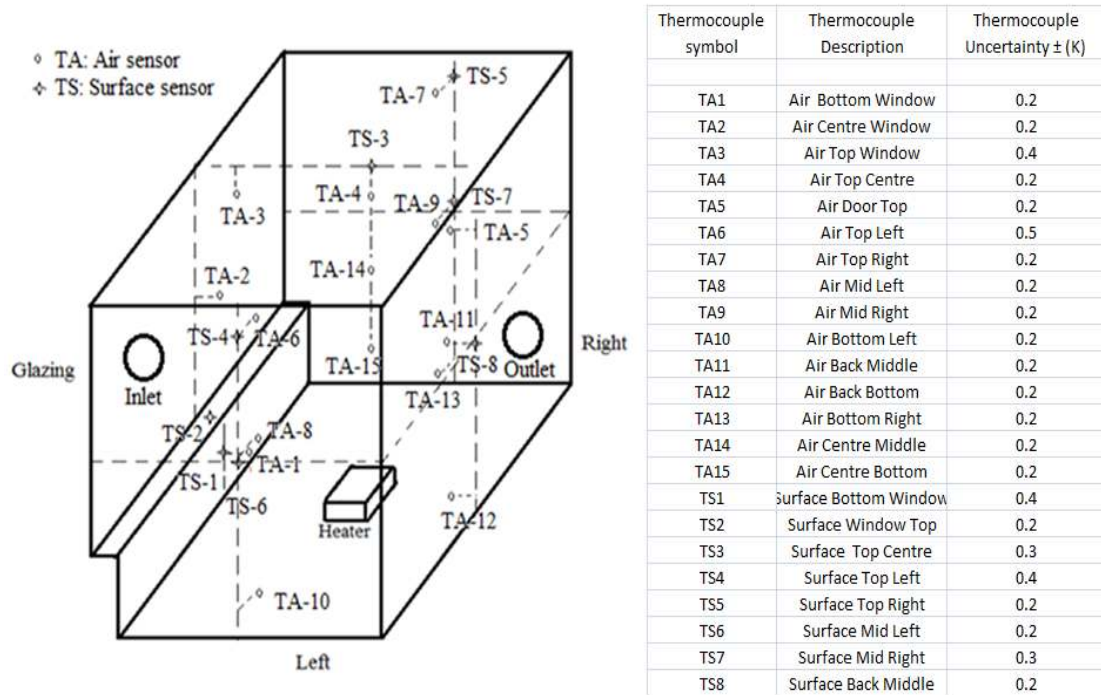


Fig. B1.2. Location, description and uncertainty of air and surface thermocouples

These thermocouples were calibrated together with their respective Pico TC-08® data loggers using a F250 mk2® precision thermometer ($\pm 0.1\text{K}$) in a water/glycol bath for a temperature range of 2-50 °C. The air thermocouples in the test cell were placed at 5cm from the wall surface, whilst the surface thermocouples were covered with a thin layer of plaster.

An axial fan was placed at the inlet to blow external air into the chamber for the night ventilation recharge. The air velocity was measured using a TSI hot-wire velocity meter with an accuracy of $\pm 0.015\text{m/s}$. The inlet and outlet were sealed during the heating period and the non-ventilated night condition.

B3. Phase change implementation of PCM board

Due to the non-uniform distribution of the Micronal® PCM granules in the clay board, three different random samples were taken from the boards and used in the DSC characterisation of the phase change. The phase change properties of the board were analysed using the Perkin Elmer DSC 6000®, which possess an uncertainty of ± 0.1 K for the temperature and ± 2 % of the enthalpy change. The DSC was industry calibrated using Indium and Zinc standards.

The DSC data for each sample are shown in Table 4.1. The phase change temperatures and enthalpies at a heating/cooling rate were considered for each sample, as the data were within the error limits of the DSC.

The enhanced phase change model described in chapter 3 and Appendix A was employed in this simulation. Polynomials were fitted to the melting and freezing curves of each sample, and were implemented in the CFD model as User Defined Functions (UDF). The errors associated with the curve fits are shown in Table B1.3.

Table B1.3. Regression coefficient, enthalpy uncertainty in h-T curve fits and total uncertainty in enthalpy at heating/cooling rate of 0.5 K/min

Sample	Melting			Freezing		
	R ²	$\Delta h_{\text{curve-fit}}$	Δh_{total}	R ²	$\Delta h_{\text{curve-fit}}$	Δh_{total}
S-1	0.999	± 0.065 kJ/kg	± 0.360 kJ/kg	0.998	± 0.350 kJ/kg	± 0.700 kJ/kg
S-2	0.999	± 0.073 kJ/kg	± 0.400 kJ/kg	0.998	± 0.343 kJ/kg	± 0.700 kJ/kg
S-3	0.999	± 0.061 kJ/kg	± 0.370 kJ/kg	0.998	± 0.340 kJ/kg	± 0.690 kJ/kg

$$\Delta h_{\text{total}} = \Delta h_{\text{curve-fit}} + \Delta h_{\text{DSC}} \quad (\text{B1.1})$$

Where:

$\Delta h_{\text{curve-fit}}$ = uncertainty in enthalpy associated with the curve fitting of the experimental DSC data for different samples over the phase change range. This is obtained through the comparison of the DSC data and data calculated by the curve-fit equation

Δh_{DSC} = uncertainty associated with the DSC or 2% of enthalpy value

The resulting enthalpy-temperature curves for sample S-3 (with the lowest errors) are given in Fig. B1.3.

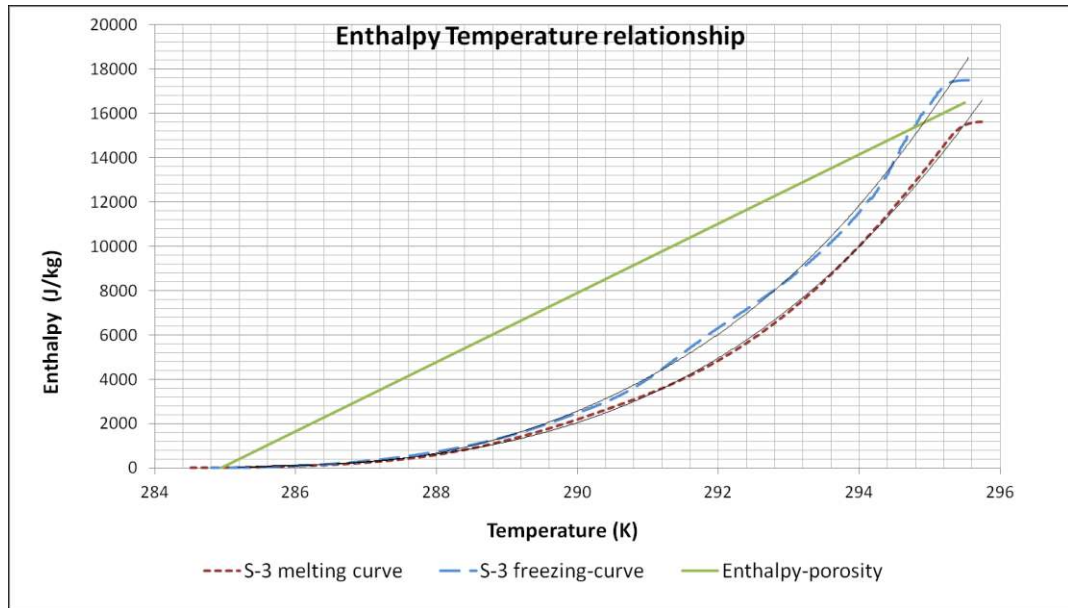


Fig. B1.3. Melting and freezing curves of sample S-3 and the enthalpy-porosity model

Correspondingly, the equations for the polynomial curves for S-3 h-T relations are:

$$f(T)_m = 12.781736 T^3 - 10932.541511 T^2 + 3117074.922039 T - 296256708.8957 \quad (R^2 = 0.999) \quad (B1.2)$$

$$-f(T)_f = 13.026531 T^3 - 11055.072091 T^2 + 3129090.962073 T - 295246573.26512 \quad (R^2 = 0.998) \quad (B1.3)$$

B4. L₂ norm study

In building simulations especially, because of the large spaces to be simulated, it is inconvenient to abide by the usual grid and time-step criteria of Courant number < 5 (FLUENT User guide, 2010), which often require very small grid size and small time-steps. These would significantly impact on the simulation times, or even make the use of CFD impractical.

The L₂ norm study is a grid and time-step sensitivity analysis to determine the appropriate mesh and time-step levels appropriate for a particular model. It was employed here to determine the errors associated with different grid sizes and time-

steps, and to justify the use of larger grid and time-step sizes. (The temperature and velocity norms are considered in this study)

$$L_2 \text{ norm} = \left[\frac{\sum [V_i (\phi_{discrete} - \phi_{exact})_i^2]}{\sum V_i} \right]^{1/2} \quad (\text{B1.4})$$

Where:

V_i = volume of cells

$\phi_{i \text{ discrete}}$ = Temperature or velocities obtained from the discretised Governing Equations

$\phi_{i \text{ exact}}$ = Temperature or velocities obtained from the exact solution of the Governing Equations

As the exact solution of the governing equations is not known, the results of a simulation with a uniformly very fine mesh (850,000 elements) and time step (10s) were taken as the benchmark. Three meshes: coarse (140,000 elements); medium (212,500 elements); and fine (283,000 elements), and three time-steps: 500s; 200s; and 100s were considered in this model independence study. Mesh refinement was performed by varying all mesh sizes by the same ratio, but maintaining the inflation parameters (Gowreesunker and Tassou, 2013a).

The L_2 norm was computed for uniformly distributed points, 0.2m apart, over the three planes (across the inlet, outlet and heater) shown in Fig. B1.4, and for 1000s intervals for the ventilated case, which consists of both buoyancy driven and forced convection flows. The default FLUENT residual convergence criteria were employed for all simulations.

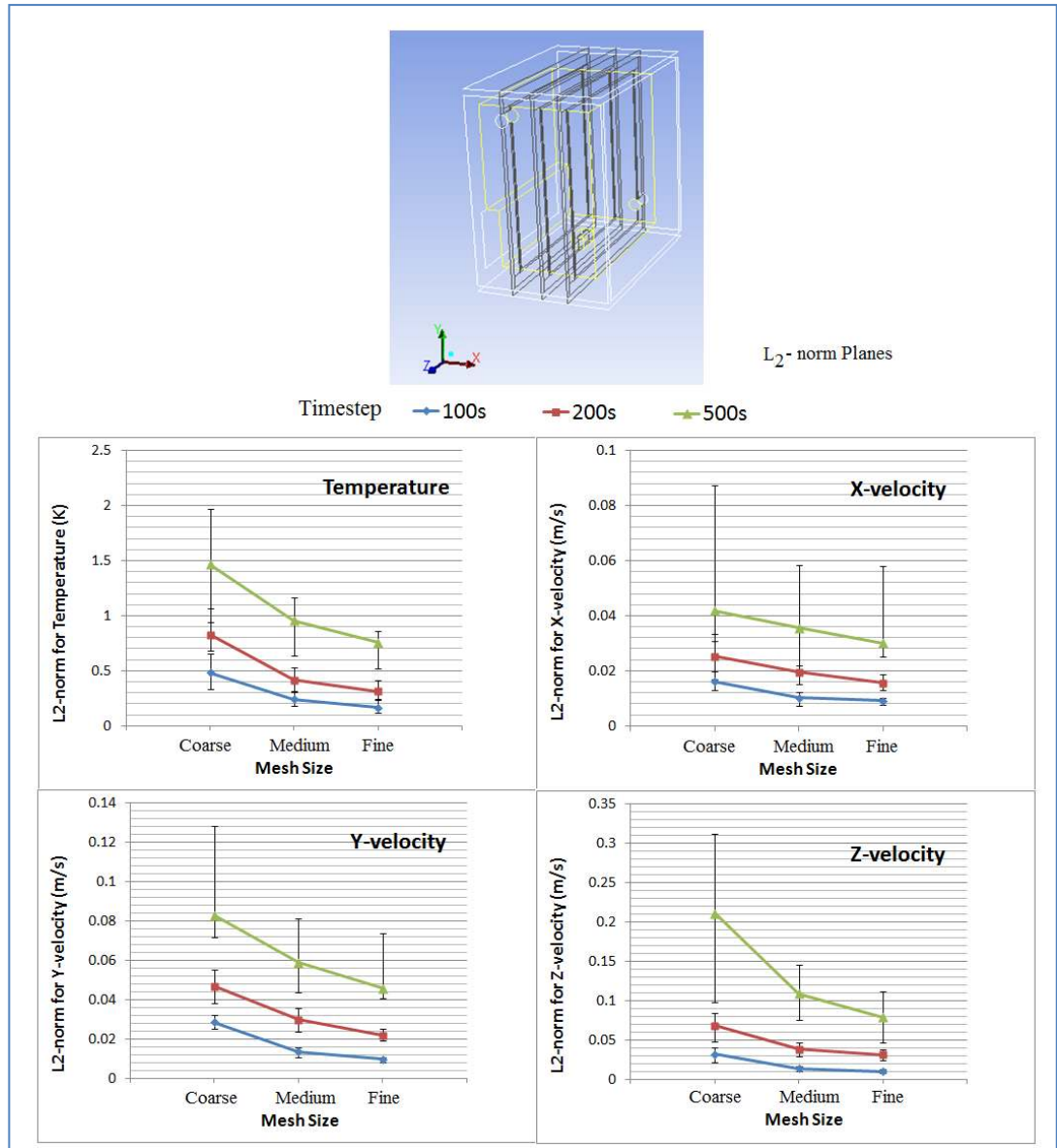


Fig. B1.4. L_2 -planes and L_2 -norm for temperature and velocities

Fig. B1.4 shows that the temperature and velocity norms are more dependent on the time-step than the mesh size. A temperature convergence criteria of 0.2-0.4 K was used, based on the uncertainty of the thermocouples, while 0.015 m/s was used for the velocity convergence criteria based on the accuracy of the TSI velocity meter used in the experiment. Under these conditions, the temperature criterion is satisfied with the Fine-100s, Fine-200s and Medium-100s setups, and the velocity criterion is satisfied by the Medium-100s and Fine-100s setups. Thus to minimise computational time, the Medium-100s setup was employed for the simulations. Both the ventilated and non-ventilated cases were simulated on the same grid with an average y^+ value of 6. The employed mesh is shown in Fig. 4.6.

B5. Numerical considerations

The validation errors were quantified in terms of the absolute Root Mean Square (RMS) error and the relative RMS errors, for each thermocouple and for each sample modelled.

$$\text{Local Absolute RMS error} = \left[\sqrt{\frac{\sum (T_{exp} - T_{num})_t^2}{N_t}} \right] + U_{thermocouple} \quad (\text{B1.5})$$

The relative error is defined by Eq. (B1.6):

$$\begin{aligned} \text{Local Relative RMS Error} \\ = \frac{\text{Local Absolute RMS error} * 100}{\text{Smallest Peak Local Experimental Temperature difference}} \end{aligned} \quad (\text{B1.6})$$

Where:

T_{exp} : Experimental Temperature (K or °C)

T_{num} : Numerical Temperature (K or °C)

$U_{thermocouple}$: Uncertainty of Local thermocouple (K or °C)

t : time (s)

N_t : Number of time-steps

The relative RMS error represents the overall local relative error in the transient simulation and is based on the smallest peak local experimental temperature difference obtained during the test cell heating/cooling cycle. This calculation method is analogous to the validation procedure used in Zhang *et al.* (2007), where the authors based the steady state relative errors on the temperature difference between the outlet/inlet, local/environment or cold/hot surfaces. However due to the transient nature of this study, the relative errors are hereby defined in a different way. The smallest local experimental temperature difference in Eq. (B1.6) refers to the smallest difference between the start/peak or peak/end temperatures of the experiment, where the ‘small’ nature of the difference provides a more conservative error evaluation. The errors can be found in Fig. 4.7 and Fig. 4.8.

Furthermore, the convective heat transfer coefficient for the ventilated night charging is given by Eq. (B1.7)

$$h_c = \left[\sum_{t=8.2 \text{ hrs}}^{t=24 \text{ hrs or } (\bar{q}=0)} \left(\frac{\bar{q}}{T_{inlet} - \overline{T_{surf}}} \right) \right] / N_t \quad (\text{B1.7})$$

Where:

\bar{q} : Area-weighted walls' heat flux (W/m²)

T_{inlet} : Air inlet/ Reference temperature (K)

$\overline{T_{surf}}$: Area-weighted walls' surface temperature (K)

N_t : Number of time-steps

Figs. B1.5 to B1.10 show some generic temperature trends obtained in the validation process.

For the Non-Ventilated Scenario:

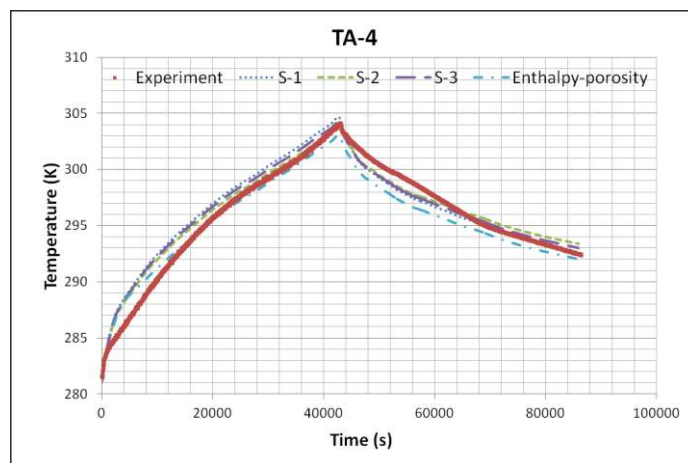


Fig. B1.5. TA-4 Non-ventilated experimental and simulated temperatures

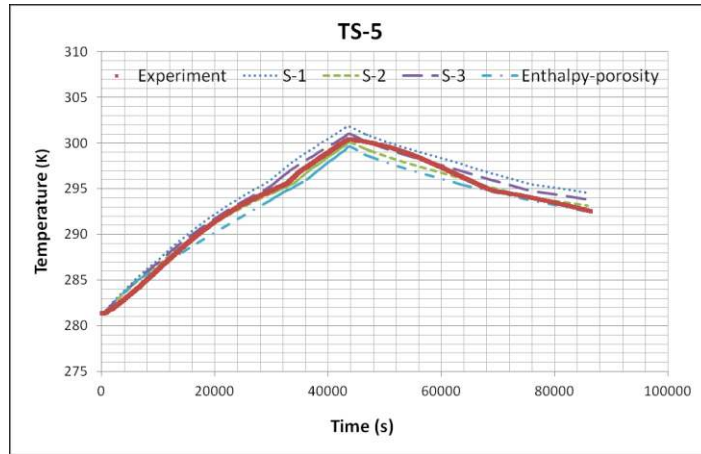


Fig. B1.6. TS-5 Non-ventilated experimental and simulated temperatures

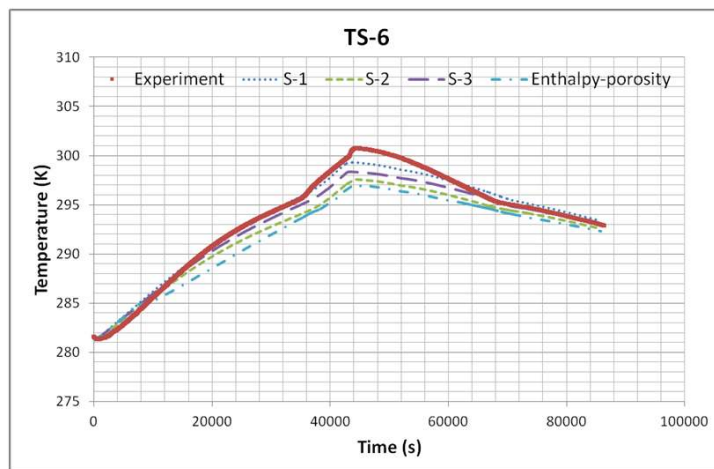


Fig. B1.7. TS-6 Non-ventilated experimental and simulated temperatures

For the Ventilated Scenarios:

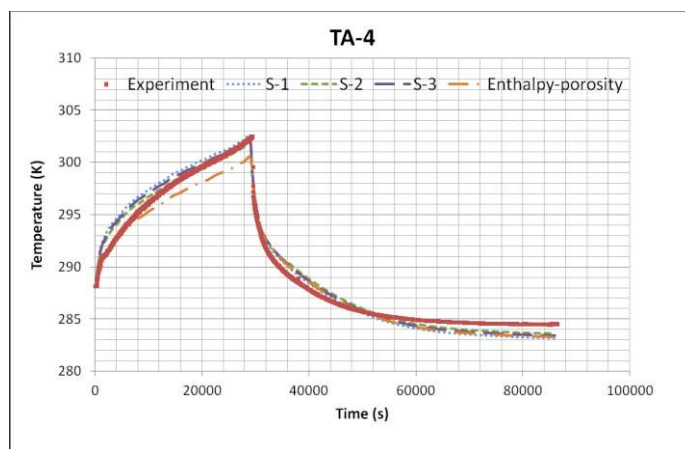


Fig. B1.8. TA-4 Ventilated experimental and simulated temperatures

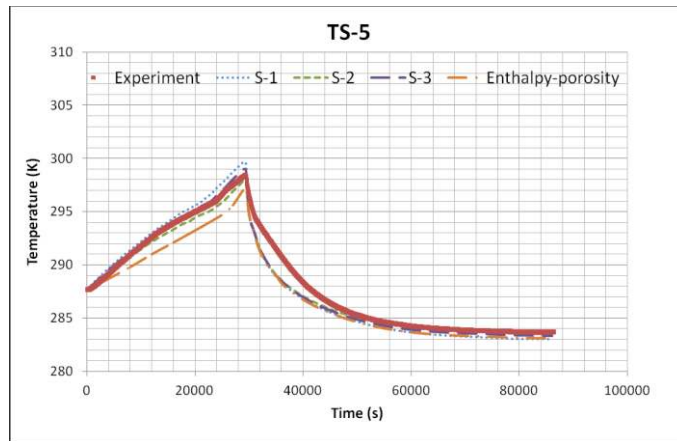


Fig. B1.9. TS-5 Ventilated experimental and simulated temperatures

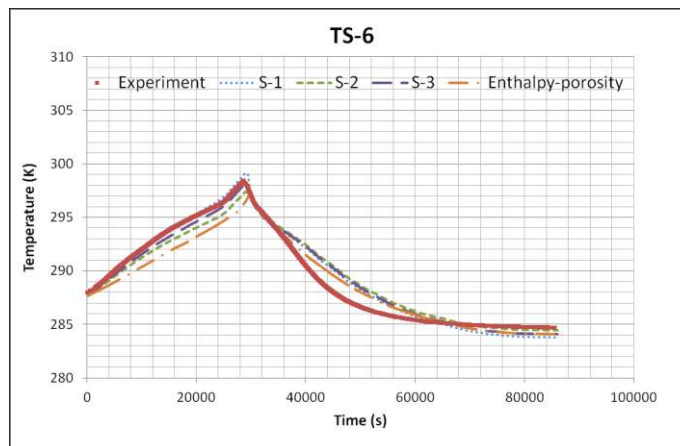


Fig. B1.10. TS-6 Ventilated experimental and simulated temperatures

Appendix C: Development of optical phase change model

This appendix provides supporting information used in the development of the optical phase change model described in chapter 5.

C1. Description of experimental setup and procedure

The experimental setup was devised in order to obtain the gray transmittance values of the PCM for different irradiation level and at different temperatures. The setup consisted of a 150W metal halide lamp, a reflector casing, a pyranometer and the investigated glazed surface, as shown in Fig. C1.1, placed inside an environmental chamber where the surrounding temperature was monitored and controlled. The internal side of the reflector casing had a dimension of 200×200×500mm, and was lined with reflective aluminium tape. The double glazing was air filled, with dimensions 4-16-4 mm and a U-value of 2.8 W/m²K. The purpose of the reflector casing was to limit the loss in radiation transfer between the glazed surface and the pyranometer. Furthermore, it also served to ‘focus’ the transmitted radiation to the pyranometer.

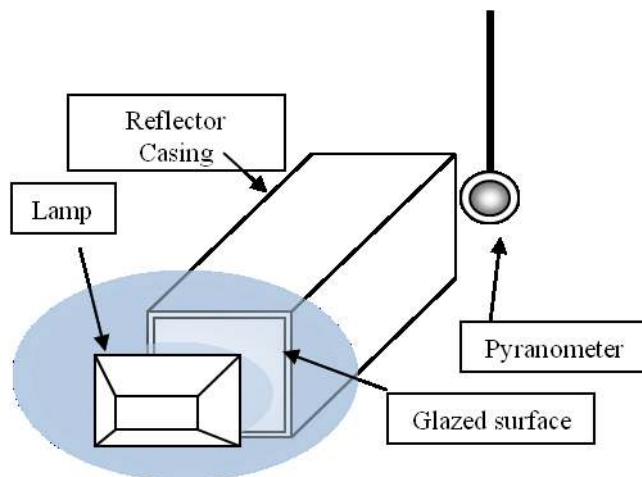


Fig. C1.1 Experimental setup for optical tests

The tests were conducted by placing the entire setup in the environmental chamber for 24 hours prior to the start of the test. This allowed the temperature of all the components to reach the same steady level, which is essential for the appropriate initialisation of the numerical model and to ensure that the temperature of the PCM is known. Note that there were no thermocouples within the PCM so as to avoid nucleation issues.

The irradiation levels were recorded with a ‘no-glazed’ surface, a standard double glazed unit and the PCM glazed unit (for a period varying between 5-9 hrs, or until steady state). The main parameter employed for the development of the model is the radiation transmittance, which is obtained from Eqs. C(1.1-1.3), where the transmitted radiation intensity for non-glazed/empty specimen, double glazed and PCM-glazed surfaces are (G) , $(G_{\tau-gl})$ and $(G_{\tau-gl-PCM})$, respectively (Gowreesunker et al. 2013c).

$$\tau_{gl} = \frac{G_{\tau-gl}}{G} \quad (C1.1)$$

$$\tau_{gl-PCM} = \frac{G_{\tau-gl-PCM}}{G} \quad (C1.2)$$

$$\tau_{PCM} = \frac{\tau_{gl-PCM}}{\tau_{gl}} \quad (C1.3)$$

The transmitted radiation for the PCM-glazed unit ($G_{\tau-gl-PCM}$) was taken at the beginning of each experiment, after having applied stable irradiation to the glazing. It corresponds to the lowest transmitted irradiation level at the corresponding surrounding environmental chamber temperature, before the PCM starts to melt. In this way, a transmittance value was assigned to the temperature of the PCM, which then allowed calculating the extinction coefficients.

C2. Thermal characterisation of RT27

The thermal characterisation of RT27 was conducted by Stanislava B. Stankovic (from City University), according to the University Collaboration scheme under which this Project was based on.

Having obtained the enthalpy-temperature curves (shown in Fig. 5.3), the effective heat capacity was calculated from the derivative of the mean enthalpy curve. The liquid fraction variation was obtained by fitting a polynomial to the curvature of the mean enthalpy curve from Fig. 5.3, using the method described in Gowreesunker *et al.* (2012). Hysteresis was neglected.

These resulted in the following equations employed in the numerical validation of the study (The c_p in the fully liquid and solid states are constant) – Temperatures (T) in °C:

For $15^\circ\text{C} \leq T < 26^\circ\text{C}$;

$$c_{p\text{ eff}}(T) = 0.01202 T^4 - 0.9113 T^3 + 25.83499 T^2 - 323.96615 T + 1519.21328 \quad (\text{C1.4})$$

(kJ/kg·K) ($R^2 = 0.994$)

For $26^\circ\text{C} \leq T \leq 27.94^\circ\text{C}$;

$$c_{p\text{ eff}}(T) = -7.34132 T^2 + 376.54918 T - 4786.72094 \quad (\text{C1.5})$$

(kJ/kg·K) ($R^2=1.000$)

$$\beta = (4.39 \times 10^{-5} \cdot T^4) - (2.92 \times 10^{-3} \cdot T^3) + (7.38 \times 10^{-2} \cdot T^2) - (8.25 \times 10^{-1} \cdot T) + 3.42 \quad (\text{C1.6})$$

($R^2 = 0.991$)

The onset and end temperatures of the phase change process can be verified from Fig. C1.2(a).

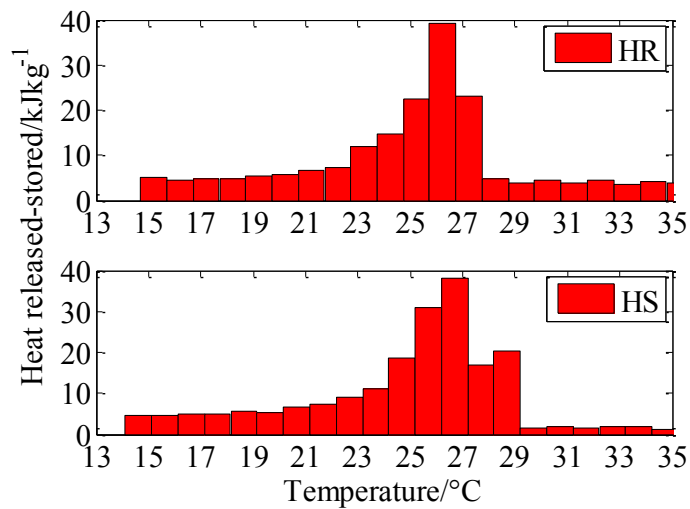


Fig. C1.2(a). Heat released-stored in given temperature intervals for RT27; HR – Heat released; HS – Heat stored. (Gowreesunker et al, 2013c)

C3. Calculation of the optical properties of RT27

(The following relations have been fully explained in the published paper from the author; Gowreesunker *et al.* (2013c) – “Experimental and numerical investigations of the optical and thermal aspects of a PCM-Glazed unit” – and all references can be found in the mentioned paper.)

This section aims at showing the general procedure followed for the development of the optical model of phase change. The experiments were carried out with irradiation intensities of 950 W/m², 550 W/m² and 260 W/m², and temperatures ranging from 13 °C to 29 °C, in order to span the entire phase change range of the PCM. Employing Eq. (C1.7), the extinction coefficients (σ_ϵ) of RT27 at different temperatures and irradiation level were calculated (where ‘s’ is the physical thickness of the PCM: 16mm for the PCM-glazed unit; or 10mm for the spectrophotometry measurements). Furthermore, it is known that the extinction coefficient is the sum of the absorption (σ_a) and scattering coefficients (σ_s), hence Eq. (C1.8).

$$\text{Log}_{10}(\tau_{pcm}) = -(\sigma_\epsilon \times s) \quad (\text{C1.7})$$

$$\sigma_\epsilon = \sigma_s + \sigma_a \quad (\text{C1.8})$$

However the issue in this formulation lies in the separation of the σ_a and σ_s terms in order to understand the thermal aspect of the radiation process. From the study by Weinlader *et al.* (2004) and as observed from this study, the PCM is non-scattering, clear and transparent in the liquid phase, and the increase in opacity as the PCM changes to solid is largely associated to the scattering process. This observation was subsequently adopted to dissect the extinction coefficient into the scattering and absorption coefficients, by assuming that the scattering process dominates during the solid phase and that the liquid phase is non-scattering.

This led to the definition of a new parameter (δ) which represents the minimum radiation absorption in the solid phase of the PCM. Thus, working from the hypothesis that the change of transmittance varies with the liquid fraction, and that scattering dominates in the solid phase whilst absorption dominates in the liquid phase, the following relations were developed.

$$\sigma_a = (\sigma_\varepsilon)[\delta\beta + (1 - \delta)] \quad (C1.9)$$

$$\sigma_s = (\sigma_\varepsilon) - \sigma_a \quad (C1.10)$$

Where:

$$\delta = \frac{\tau_{liq} - \tau_{sol}}{1 - \tau_{sol}} \quad (C1.11)$$

$$\sigma_\varepsilon = (\beta \cdot \sigma_{\varepsilon,liq}) + (1-\beta) \cdot (\sigma_{\varepsilon,sol}) \quad (C1.12)$$

It can be implied that the development of the optical relations followed a reverse engineering approach, where the relations were postulated from previous studies and hypotheses, and the verification process was then based on experimental data and numerical simulations. The experimental verification of the variation in extinction coefficient is shown in Fig. C1.2b, and the numerical validation is shown in section 5.2.

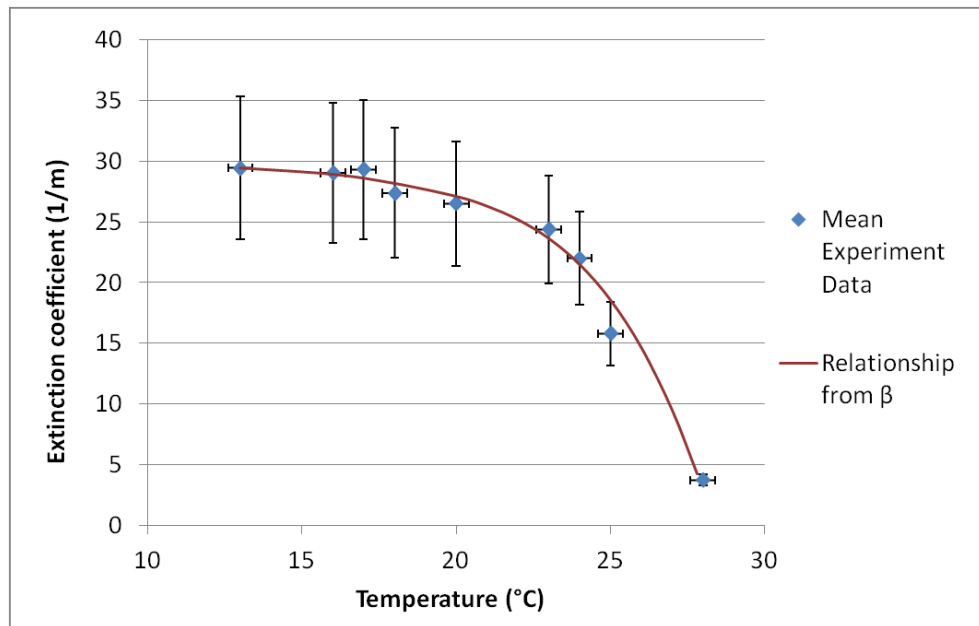


Fig. C1.2(b) Mean experimental extinction coefficients and extinction coefficients using the relationship Eq. (C1.6) and Eq. (C1.12)

C4. Error calculations

The experimental calculation for the extinction coefficient (σ_e) absolute uncertainty was determined from the general uncertainty propagation equation, in reference to Eq. (C1.7), producing Eq. (C1.13).

$$U_{\sigma_e} = \sqrt{\left(\frac{d(\log_{10}\tau)}{d\tau}\right)^2 U_{\tau}^2} \quad (\text{C1.13})$$

Where U_{σ_e} is the absolute uncertainty in the scattering coefficient, τ is the transmittance value, and U_{τ} is the absolute uncertainty in transmittance.

The error from the thickness was neglected because it could not be obtained from the glass manufacturer. The uncertainty in the transmittance U_{τ} for each irradiation level was calculated as follows, based on the uncertainties of the employed apparatus.

Table C1.1. Sensor uncertainties and sensitivities

Sensors uncertainty and sensitivity	
Sensitivity of pyranometer (η)	0.0137 mV / Wm ⁻²
Uncertainty in pyranometer	± 0.03 mV
Accuracy of data logger	0.2% + 0.01 mV
Uncertainty in Air Temperature	± 0.4 °C

The following equations were developed based on Eq. (C1.1) – Eq. (C1.3), where ‘ V ’ is the recorded voltage from the pyranometer and ‘ G ’ are the respective irradiation intensities;

$$U_{\tau_{gl}} = \left[\frac{[(0.002 * V) + 0.04]}{\eta * G_{\tau-gl}} + \frac{[(0.002 * V) + 0.04]}{\eta * G} \right] \quad (\text{C1.14})$$

$$U_{\tau_{gl-pcm}} = \left[\frac{[(0.002 * V) + 0.04]}{\eta * G_{\tau-gl-pcm}} + \frac{[(0.002 * V) + 0.04]}{\eta * G} \right] \quad (\text{C1.15})$$

$$U_{\tau_{\text{pcm}}} = \left[U_{\tau_{\text{gl}}} + U_{\tau_{\text{gl-pcm}}} \right] \quad (\text{C1.16})$$

The experimental uncertainties presented in Fig. 5.6a were obtained from Eq. (C1.15). The uncertainties in the extinction coefficient presented in Fig. C1.2b were obtained from Eq. (C1.13), where the absolute mean uncertainty in transmittance (U_{τ}) was calculated from Eq. (C1.16).

Appendix D: Numerical conditions

This appendix provides supporting material for chapter 6 of this study, relating to the numerical procedure employed for the performance evaluation of the PCM systems.

D1. HVAC sizing methodology

The sizing of the HVAC system was performed based on the mean steady state thermal loads of the airport terminal departure hall. Displacement conditioning systems are more efficient than mixed conditioning systems, because they are able to direct their cooling potential towards the conditioned space, as opposed to conditioning the entire space. According to Simmonds *et al.* (2000), 1 person occupies 4 m² in an airport terminal, and therefore based on the 48 m² floor area simulated in the 2D case, there are 12 persons at any one time in the terminal. However, the heat gains provided by these occupants vary according to Fig. 6.3. Furthermore, based on the fresh air requirement from CIBSE guide A (2006) of 15 L/s/person for a high indoor air quality, the total fresh air requirement of 0.2 kg/s for the 12 occupants. (Note that the 2D thickness of the CFD case is 1m)

Hence, for cooling purposes, the sizing is done mainly by focusing on the heat loads in the conditioned space i.e. up to a height of 2m from the floor:

1. Mean internal heat gains = 25 W/m² × 48 m² = 1200 W
2. Mean solar gains on the floor from glazing and roof for UK weather = 350 W/m² × [(9×0.5)+(62×0.01)] m² × 0.5 = 896 W
3. Ambient air ventilation heat gain = 8 K × 0.2 kg/s × 1002 J/kgK = 1603 W

Hence the mean cooling load is found to be: 3.7 kW

Conversely, for heating purposes, the displacement conditioning system behaves similar to a mixed ventilation system, due to the buoyancy effects of the low velocity inlet air at high temperature. Hence for heating purposes:

1. Mean Convective heat losses from roof and glazing = 20 K × 1 W/m²K × (9+62) m² = - 1420 W
2. Solar gains are neglected
3. Mean internal heat gains = 25 W/m² × 48 m² = 1200 W

$$4. \text{ Ambient air ventilation heat loss} = 18 \text{ K} \times 0.2 \text{ kg/s} \times 1002 \text{ J/kgK} = - 3608 \text{ W}$$

Hence the mean heating load is found to be -3.8 kW

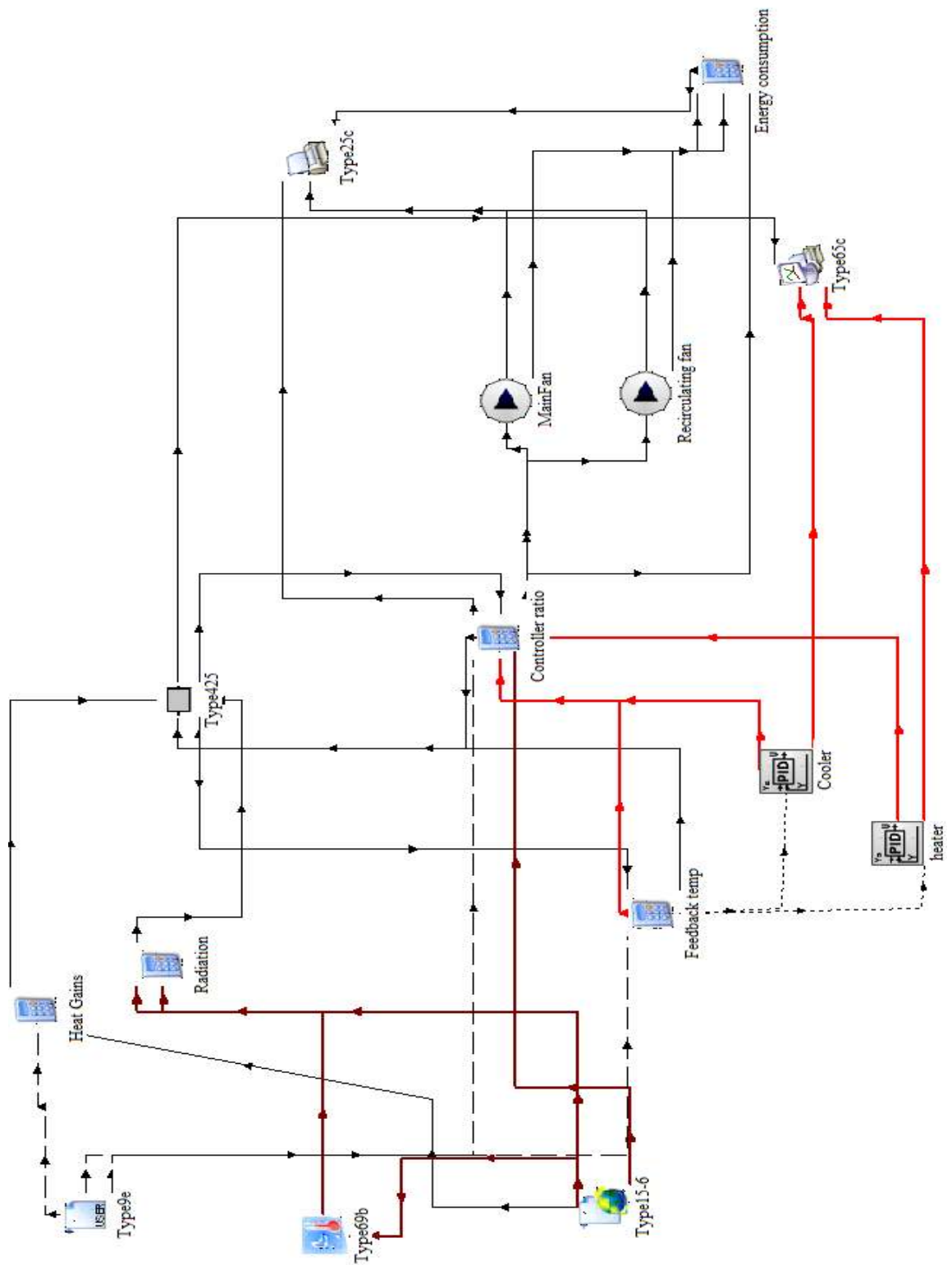
(Where: 8 K and 18 K are assumed temperature difference between the ambient and the indoor environments for cooling and heating purposes, respectively; 1002 J/kgK is the specific heat capacity of air; 0.5 is the radiation transmittance of the glazing and the radiation absorption of the floor; 0.01 is the radiation transmittance of the roof; 48, 9 and 62 m² are the floor, glazing and roof areas, respectively – refer to Table 6.1 for more information)

As a result, in order to allow the control system to have more flexibility on its influence on the indoor environment, both the heating and cooling units were sized at 4 kW. In this way, the controller could have a higher potential in controlling the indoor thermal environment, by having a higher range to adjust the supply air temperature.

Considering a load of 4kW and a temperature difference of 8K across the heating and cooling coils, the total mass flow rate across both units was found to be 0.5 kg/s. Furthermore, in displacement conditioning systems, because the diffusers are relatively close to the occupants, the air supply velocity is important in providing adequate thermal comfort. In this case, the air velocity in the conditioned zone should not generally exceed 0.25 m/s for moderate thermal environments (CIBSE B, 2006), although Fanger's equation allows a maximum of 0.4 m/s (Fanger, 1970) for a clothing factor of 1.15 and temperatures of 18-23 °C, typical of an airport terminal building (CIBSE A, 2006). Thus, as shown in the results section of the study, the mean velocities of the air in the conditioned zone are in the range of 0.15 and 0.3 m/s, abiding by the velocity comfort requirements and confirming the velocity comfort aspect of the Displacement Conditioning system.

Furthermore, as this HVAC system is a constant air volume (CAV) system, the mixing ratio of fresh and return air, in the supply air is constant. Thus: Fresh air flow rate = 0.2 kg/s; Return supply air flow rate = 0.3 kg/s; and Total air flow rate = 0.5 kg/s, with a 4 kW cooling and heating capacity.

D2. TRNSYS Screen-Shot for the normal DV HVAC system



D3. TRNSYS program file

TRNSYS - the TRAnsient SYstem Simulation program
The Solar Energy Lab at the University of Wisconsin - Madison, USA
Le Centre Scientifique et Technique du Batiment, Sophia Antipolis, France
Transsolar Energietechnik GmbH, Stuttgart, Germany
Thermal Energy System Specialists, LLC, Madison Wisconsin, USA
Release 17.00.0019

Listing file for: "D:\ACTIVEsystem\DV-freshair-floor\DV-HVAC-after-mixing.dck"

*** Notice at time : 0.000000
Generated by Unit : Not applicable or not available
Generated by Type : Not applicable or not available
Message : The TRNSYS Executable (TRNExe.exe) and main DLL (TRNDll.dll) are located in
"C:\Trnsys17\Exe"

*** Notice at time : 0.000000
Generated by Unit : Not applicable or not available
Generated by Type : 208
TRNSYS Message 75 : The Type referenced below requires descriptors instead of initial values.
Reported information : Type 208

*** Notice at time : 0.000000
Generated by Unit : Not applicable or not available
Generated by Type : 535
TRNSYS Message 75 : The Type referenced below requires descriptors instead of initial values.
Reported information : Type 535

*** Notice at time : 0.000000
Generated by Unit : Not applicable or not available
Generated by Type : 580
TRNSYS Message 76 : The following Type has been identified as allowing the unit specifications (kg/h for example) after the input specifications and initial values for the inputs. The critical parameter number, and the value of this critical parameter that indicates that the units will be supplied is also listed. This information was retrieved from the VarUnits.dat file located in the \Exe directory of your TRNSYS 16 installation.
Reported information : Type 580, Critical Parameter 11, Parameter Value 1

*** Notice at time : 0.000000
Generated by Unit : Not applicable or not available
Generated by Type : 580
TRNSYS Message 88 : The following Type has been identified as allowing FORMAT statements. This information was retrieved from the Formats.dat file located in the \Exe directory of your TRNSYS 16 installation.
Reported information : Type 580

*** Pre-Processing the TRNSYS EQUATIONs and CONSTANTs to check for fatal errors.

*** Pre-Processing of EQUATIONs and CONSTANTs completed with no fatal errors found.

*** Evaluating the EQUATIONs and CONSTANTs to determine their initial values.

*** Finished evaluating the EQUATIONs and CONSTANTs and ready to begin processing the remainder of the TRNSYS input file.

```

VERSION      17
*****
*** TRNSYS input file (deck) generated by TrnsysStudio
*** on Tuesday, February 19, 2013 at 10:27
*** from TrnsysStudio project: D:\ACTIVEsystem\DV-freshair-floor\DV-HVAC-after-mixing.tpf
***
*** If you edit this file, use the File/Import TRNSYS Input File function in
*** TrnsysStudio to update the project.
***
*** If you have problems, questions or suggestions please contact your local
*** TRNSYS distributor or mailto:software@cstb.fr
***
*****
*****
*** Units
*****
*****
*** Control cards
*****
* START, STOP and STEP

CONSTANTS  3
  START=4500
  STOP=4600
  STEP=0.1
* User defined CONSTANTS
! Start time      End time      Time step

SIMULATION      4.500000000000000E+03  4.600000000000000E+03  1.0000000000000001E-
01
! Integration      Convergence

TOLERANCES      1.000000000000000E-03  1.000000000000000E-03
! Max iterations  Max warnings  Trace limit

LIMITS  30  500  51
! TRNSYS numerical integration solver method

DFQ  1
! TRNSYS output file width, number of characters

WIDTH  80
! NOLIST statement

LIST
! MAP statement
! Solver statement      Minimum relaxation factor      Maximum relaxation factor

SOLVER  0
  1.000000000000000
  1.000000000000000
! Nan DEBUG statement

NAN_CHECK  0
! Overwrite DEBUG statement

OVERWRITE_CHECK  0
! disable time report

TIME_REPORT  0

```

! EQUATION SOLVER statement

EQUATION SOLVING METHOD 0
* Model "Type15-6" (Type 15)
*

UNIT 3 TYPE 15
*\$UNIT_NAME Type15-6
*\$MODEL .\Weather Data Reading and Processing\Standard Format\Meteonorm Files (TM2)\Type15-6.tmf
*\$POSITION 93 468
*\$LAYER Weather - Data Files #
PARAMETERS 9
! 1 File Type
! 2 Logical unit
! 3 Tilted Surface Radiation Mode
! 4 Ground reflectance - no snow
! 5 Ground reflectance - snow cover
! 6 Number of surfaces
! 7 Tracking mode
! 8 Slope of surface
! 9 Azimuth of surface
6.000000000000000E+00 3.400000000000000E+01 3.000000000000000E+00
2.000000000000000E-01 7.000000000000000E-01
1.000000000000000E+00 1.000000000000000E+00 9.000000000000000E+01
0.000000000000000E+00
*** External files
ASSIGN C:\Trmsys17\Weather\Meteonorm\Europe\GB-London-Weather-C-37790 - Copy - Copy.tmf
34
*? Which file contains the Meteonorm weather data? |1000
*-----
* Model "Type25c" (Type 25)
*

UNIT 16 TYPE 25
*\$UNIT_NAME Type25c
*\$MODEL .\Output\Printer\Unformatted\No Units\Type25c.tmf
*\$POSITION 1030 244
*\$LAYER Outputs #
PARAMETERS 10
! 1 Printing interval
! 2 Start time
! 3 Stop time
! 4 Logical unit
! 5 Units printing mode
! 6 Relative or absolute start time
! 7 Overwrite or Append
! 8 Print header
! 9 Delimiter
! 10 Print labels
1.000000000000000E-01 4.500000000000000E+03 4.600000000000000E+03
3.600000000000000E+01 0.000000000000000E+00
0.000000000000000E+00 -1.000000000000000E+00 -1.000000000000000E+00
0.000000000000000E+00 1.000000000000000E+00
INPUTS 10
! Controller ratio:AmbientinK ->Input to be printed-1
! Controller ratio:Teff ->Input to be printed-2
! Controller ratio:Actualheating ->Input to be printed-3
! Controller ratio:ActualCooling ->Input to be printed-4
! MainFan:Outlet flow rate ->Input to be printed-5


```

! Recirculating fan:Outlet flow rate ->Input to be printed-6
! Controller ratio:Tm ->Input to be printed-7
! Controller ratio:Treturnn ->Input to be printed-8
! Energy consumption:Energy ->Input to be printed-9
! Energy consumption:TotalEnergy ->Input to be printed-10
  AMBIENTINK      TEFF      ACTUALHEATING      ACTUALCOOLING
15,2
  19,2      TM      TRETURNN      ENERGY
TOTALENERGY
*** INITIAL INPUT VALUES
  ambient      effecttemp      Heating      Cooli
ng      mainfanflow
  recirculatingfanflow      Tm      Treturn      Chill
erBoilerJ      Total_energy
*** External files
  ASSIGN heterar.out 36
*? Output file for printed results |1000
*-----
* Model "Type65c" (Type 65)
*

UNIT 12 TYPE 65
*$UNIT_NAME Type65c
*$MODEL .\Output\Online Plotter\Online Plotter With File\No Units\Type65c.tmf
*$POSITION 934 618
*$LAYER Main #
  PARAMETERS 12
! 1 Nb. of left-axis variables
! 2 Nb. of right-axis variables
! 3 Left axis minimum
! 4 Left axis maximum
! 5 Right axis minimum
! 6 Right axis maximum
! 7 Number of plots per simulation
! 8 X-axis gridpoints
! 9 Shut off Online w/o removing
! 10 Logical Unit for output file
! 11 Output file units
! 12 Output file delimiter
  1.0000000000000000E+00  2.0000000000000000E+00  2.8000000000000000E+02
3.1000000000000000E+02  -1.0000000000000000E+01
  1.8000000000000000E+03  1.0000000000000000E+00  1.2000000000000000E+01
0.0000000000000000E+00  3.5000000000000000E+01
  0.0000000000000000E+00  0.0000000000000000E+00
  INPUTS 3
! Type425:Point_1 ->Left axis variable
! heater:Control signal ->Right axis variable-1
! Cooler:Control signal ->Right axis variable-2
  24,1      8,1      6,1
*** INITIAL INPUT VALUES
  Zone      heat      cool
  LABELS 3
  Temperatures
  Heat transfer rates
  Graph 1
*** External files
  ASSIGN D:\ACTIVEsystem\DV-freshair-floor\DV-HVAC-after-mixing.plt 35
*? What file should the online print to? |1000
*-----
* Model "Cooler" (Type 23)

```

```

*

UNIT 6 TYPE 23
*$UNIT_NAME Cooler
*$MODEL \Controllers\PID Controller\Type23.tmf
*$POSITION 483 607
*$LAYER Main #
PARAMETERS 2
! 1 mode
! 2 Maximum number of oscillations
1.0000000000000000E+00 3.0000000000000000E+00
INPUTS 13
! Feedback temp:Tset ->Setpoint
! Feedback temp:Feedback ->Controlled variable
! Feedback temp:cooler ->On / Off signal
! [unconnected] Minimum control signal
! [unconnected] Maximum control signal
! [unconnected] Threshold for non-zero output
! [unconnected] Gain constant
! [unconnected] Integral time
! [unconnected] Derivative time
! [unconnected] Tracking time for anti-windup
! [unconnected] Fraction of ySet for proportional effect
! [unconnected] Fraction of ySet for derivative effect
! [unconnected] High-frequency limit on derivative
TSET FEEDBACK COOLER CONST ING CONST
CONST CONST CONST CONST Y
CONST CONST CONST
*** INITIAL INPUT VALUES
0.0000000000000000E+00 0.0000000000000000E+00 0.0000000000000000E+00
0.0000000000000000E+00 1.0000000000000000E+00
0.0000000000000000E+00 -1.0000000000000001E-01 1.0000000000000001E-01
1.0000000000000001E-01 -1.0000000000000000E+00
1.0000000000000000E+00 1.0000000000000000E+00 1.0000000000000000E+01
*-----
* Model "heater" (Type 23)
*

UNIT 8 TYPE 23
*$UNIT_NAME heater
*$MODEL \Controllers\PID Controller\Type23.tmf
*$POSITION 419 692
*$LAYER Main #
PARAMETERS 2
! 1 mode
! 2 Maximum number of oscillations
1.0000000000000000E+00 3.0000000000000000E+00
INPUTS 13
! Feedback temp:Tset ->Setpoint
! Feedback temp:Feedback ->Controlled variable
! Feedback temp:heater ->On / Off signal
! [unconnected] Minimum control signal
! [unconnected] Maximum control signal
! [unconnected] Threshold for non-zero output
! [unconnected] Gain constant
! [unconnected] Integral time
! [unconnected] Derivative time
! [unconnected] Tracking time for anti-windup
! [unconnected] Fraction of ySet for proportional effect
! [unconnected] Fraction of ySet for derivative effect

```

```

! [unconnected] High-frequency limit on derivative
  TSET          FEEDBACK          HEATER          CONST  ING          CONST
  CONST         CONST            CONST            CONST   CONST         CONST  Y
  CONST         CONST            CONST
*** INITIAL INPUT VALUES
  0.0000000000000000E+00  0.0000000000000000E+00  0.0000000000000000E+00
0.0000000000000000E+00  1.0000000000000000E+00
  0.0000000000000000E+00  1.0000000000000001E-01  1.0000000000000001E-01
1.0000000000000001E-01  -1.0000000000000000E+00
  1.0000000000000000E+00  1.0000000000000000E+00  1.0000000000000000E+01
*-----
* EQUATIONS "Feedback temp"
*
EQUATIONS 9
  heater = (LT([24,1], 293))*[17,3]
  Tset = 294
  cooler = (GT([24,1], 295))*[17,3]
  intermediate = (1-(heater+cooler))*[17,3]
! Mass flow rate of air - mass flow rate of fresh air
  Massflowrate = 0.3
!mass flow rate of fresh air
  freshmass = 0.2
  Ventflow = (Massflowrate+freshmass)*[17,3]
  Feedback = [24,1]
! because outlet is 4 m^2 surface area
  MassFlux = Ventflow/4
  Lightgain = (5/0.008)*[17,3]
*$UNIT_NAME Feedback temp
*$LAYER Main
*$POSITION 359 509
*-----
* Model "Type9e" (Type 9)
*
UNIT 17 TYPE 9
*$UNIT_NAME Type9e
*$MODEL .Utility\Data Readers\Generic Data Files\Expert Mode\Free Format\Type9e.tmf
*$POSITION 90 75
*$LAYER Main #
  PARAMETERS 22
! 1 Mode
! 2 Header Lines to Skip
! 3 No. of values to read
! 4 Time interval of data
! 5 Interpolate or not-1
! 6 Multiplication factor-1
! 7 Addition factor-1
! 8 Average or instantaneous value-1
! 9 Interpolate or not-2
! 10 Multiplication factor-2
! 11 Addition factor-2
! 12 Average or instantaneous value-2
! 13 Interpolate or not-3
! 14 Multiplication factor-3
! 15 Addition factor-3
! 16 Average or instantaneous value-3
! 17 Interpolate or not-4
! 18 Multiplication factor-4
! 19 Addition factor-4

```

```

! 20 Average or instantaneous value-4
! 21 Logical unit for input file
! 22 Free format mode
  5.000000000000000E+00  0.000000000000000E+00  4.000000000000000E+00
1.000000000000000E+00 -1.000000000000000E+00
  1.000000000000000E+00  0.000000000000000E+00  1.000000000000000E+00
1.000000000000000E+00  1.000000000000000E+00
  0.000000000000000E+00  1.000000000000000E+00 -1.000000000000000E+00
1.000000000000000E+00  0.000000000000000E+00
  1.000000000000000E+00 -1.000000000000000E+00  1.000000000000000E+00
0.000000000000000E+00  1.000000000000000E+00
  3.700000000000000E+01 -1.000000000000000E+00
*** External files
  ASSIGN Trial.txt 37
*|? Input file name |1000
*-----
* EQUATIONS "Controller ratio"
*

EQUATIONS 19
!Converts ambient temperature in Kelvin
  AmbientinK = [3,1]+273.15
  QheatSet = heater*2000
!Maximum cooling capacity of auxiliary cooling coil
  QcoolSet = cooler*(-4000)
  Returnflow = Massflowrate
!Mass flow rate of fresh air
  mf = freshmass
  Ratiofresh = (mf/(mf+Returnflow))*[17,3]
  Ratioreturn = (1-Ratiofresh)*[17,3]
  ActualCooling = QcoolSet*[6,1]
  Actualheating = QheatSet*[8,1]
  Totalmassflow = mf+Returnflow
!Specific heat of air
  cpa = 1002
  Tm = (Ratiofresh*AmbientinK)+((Ratioreturn)*[24,2])
  Tsupheat = heater*((Actualheating/(Totalmassflow*cpa))+Tm)
  Tsupcool = cooler*((ActualCooling/(Totalmassflow*cpa))+Tm)
  Tsupinter = Tm*intermediate
  Treturnn = [24,2]
  Teff = ((Tsupheat+Tsupcool+Tsupinter)*[17,3])+([17,4]*[24,2])
  intermmEDIATEcf = intermediate
  Acnorrml = [17,3]
*$UNIT_NAME Controller ratio
*$LAYER Main
*$POSITION 605 392
*-----
* Model "MainFan" (Type 3)
*

UNIT 15 TYPE 3
*$UNIT_NAME MainFan
*$MODEL .\Hydronics\Fans\Variable Speed\No Humidity\Type3a.tmf
*$POSITION 815 394
*$LAYER Air Loop #
  PARAMETERS 5
! 1 Maximum flow rate
! 2 Fluid specific heat
! 3 Maximum power
! 4 Conversion coefficient

```

```

! 5 Power coefficient
  1.8000000000000000E+03  1.0000000000000000E+00  3.5999999046330000E+06
1.00000000000000001E-01  0.0000000000000000E+00
  INPUTS  3
! [unconnected] Inlet fluid temperature
! [unconnected] Inlet mass flow rate
! Controller ratio:Ratiofresh ->Control signal
  CONST          CONST          RATIOFRESH
*** INITIAL INPUT VALUES
  2.0000000000000000E+01  0.0000000000000000E+00  0.0000000000000000E+00
*-----
* Model "Recirculating fan" (Type 3)
*
  UNIT 19  TYPE 3  fan
*$UNIT_NAME Recirculating fan
*$MODEL .\Hydronics\Fans\Variable Speed\No Humidity\Type3a.tmf
*$POSITION 823 500
*$LAYER Air Loop #
  PARAMETERS 5
! 1 Maximum flow rate
! 2 Fluid specific heat
! 3 Maximum power
! 4 Conversion coefficient
! 5 Power coefficient
  1.8000000000000000E+03  1.0000000000000000E+00  3.5999999046330000E+06
1.00000000000000001E-01  0.0000000000000000E+00
  INPUTS  3
! [unconnected] Inlet fluid temperature
! [unconnected] Inlet mass flow rate
! Controller ratio:Ratioreturn ->Control signal
  CONST          CONST          RATIORETURN
*** INITIAL INPUT VALUES
  2.0000000000000000E+01  0.0000000000000000E+00  0.0000000000000000E+00
*-----
* EQUATIONS "Energy consumption"
*
  EQUATIONS 4
  Energy = Acnorrml*(ActualCooling+Actualheating)
  MainFanP = [15,3]
  AuxFanP = [19,3]
  TotalEnergy = Energy+MainFanP+AuxFanP
*$UNIT_NAME Energy consumption
*$LAYER Main
*$POSITION 1111 562
*-----
* EQUATIONS "Heat Gains"
*
  EQUATIONS 5
  Source = [17,2]*2
!to get W/m2 from kJ/hr m2
  Solargain = [3,24]*0.277777778
! glass transmittance * Glass area
  Glazeprop = 0.5*9
!Ceiling transmittance * Ceiling area
  Ceilingprop = 0.00875*62
  Floorflux = (Glazeprop+Ceilingprop)*(Solargain/48)*(1/0.1)*(0.5)
*$UNIT_NAME Heat Gains

```

```

*$LAYER Main
*$POSITION 273 40
*-----
* Model "Type69b" (Type 69)
*

UNIT 22 TYPE 69
*$UNIT_NAME Type69b
*$MODEL .\Physical Phenomena\Sky Temperature\calculate cloudiness factor\Type69b.tmf
*$POSITION 71 255
*$LAYER Main #
PARAMETERS 2
! 1 mode for cloudiness factor
! 2 height over sea level
0.0000000000000000E+00 0.0000000000000000E+00
INPUTS 4
! Type15-6:Dry bulb temperature ->Ambient temperature
! Type15-6:Dew point temperature ->Dew point temperature at ambient conditions
! Type15-6:Horizontal beam radiation ->Beam radiation on the horizontal
! Type15-6:Sky diffuse radiation on the horizontal ->Diffuse radiation on the horizontal
3,1 3,2 3,19 3,20
*** INITIAL INPUT VALUES
0.0000000000000000E+00 2.0000000000000000E+01 0.0000000000000000E+00
0.0000000000000000E+00
*-----
* EQUATIONS "Radiation"
*

EQUATIONS 8
AmbientK = [3,1]+273.15
sigma = 5.67/(10*10*10*10*10*10*10*10)
!Converting to W/m2
Solar = [3,24]* 0.277777778
RadT4 = (Solar/sigma)+(AmbientK**4)
RadT = RadT4**0.25
skysignal = LE(Solar,1)
NightskytempK = [22,1]+273.15
effectiveskyTK = ((skysignal*NightskytempK)+((1-skysignal)*RadT))
*$UNIT_NAME Radiation
*$LAYER Main
*$POSITION 313 136
*-----
* Model "CFD" (Type 425)
*

UNIT 24 TYPE 425
*$UNIT_NAME Type425
*$MODEL .\My Components\Type425.tmf
*$POSITION 550 148
*$LAYER Main #
PARAMETERS 4
! 1 Mode
! 2 No_of_inputs
! 3 No_of_outputs
! 4 Calling_mode
1.0000000000000000E+00 8.0000000000000000E+00 2.0000000000000000E+00
1.0000000000000000E+00
INPUTS 9
! [unconnected] Control_function
! Radiation:AmbientK ->Outside_air_temp

```

```

! Heat Gains:Source ->People_gain
! Radiation:effectiveskyTK ->Solar_gain
! Feedback temp:Ventflow ->Mass_flow_rate
! Controller ratio:Teff ->Vent_temp
! Feedback temp:MassFlux ->Out_mass_flux
! Heat Gains:Floorflux ->Floor_gain
! Feedback temp:Lightgain ->light
  CONST          AMBIENTK          SOURCE          EFFECTIVESKYTK
VENTFLOW
  TEFF          MASSFLUX          FLOORFLUX          LIGHTGAIN
*** INITIAL INPUT VALUES
  1.0000000000000000E+00  2.9300000000000000E+02  1.0000000000000001E-01
1.0000000000000001E-01  1.0000000000000001E-01
  2.9300000000000000E+02  1.0000000000000001E-01  1.0000000000000001E-01
6.2500000000000000E+02
  LABELS 4
  C:\Program Files\ANSYS Inc\v130\fluent\ntbin\win64\fluent.exe
  -r13.0.0 2d -i
  waza.in
  result.txt

```

*-----

END

```

TRANSIENT SIMULATION  STARTING AT TIME = 4.5000000000000000E+03
STOPPING AT TIME = 4.6000000000000000E+03
  TIMESTEP = 1 / 10
DIFFERENTIAL EQUATION ERROR TOLERANCE = 1.0000000000000002E-03
ALGEBRAIC CONVERGENCE TOLERANCE = 1.0000000000000002E-03

```

DIFFERENTIAL EQUATIONS SOLVED BY MODIFIED EULER

```

*** Notice at time      :      0.000000
  Generated by Unit     : Not applicable or not available
  Generated by Type     : Not applicable or not available
  TRNSYS Message      89 : TRNDll.dll is compiled in debug mode. External DLLs will be loaded from
the .UserLib\DebugDLLs\ directory.
  Reported information  : Not available

```

```

*** Notice at time      :      0.000000
  Generated by Unit     : Not applicable or not available
  Generated by Type     : Not applicable or not available
  Message              : The following Types were loaded from TRNDll.dll: Type15, Type23, Type65,
Type3, Type25, Type9, Type69

```

```

*** Notice at time      :      0.000000
  Generated by Unit     : Not applicable or not available
  Generated by Type     : Not applicable or not available
  Message              : "FileReader.dll" was found but did not contain any components from the input file.

```

```

*** Notice at time      :      0.000000
  Generated by Unit     : Not applicable or not available
  Generated by Type     : Not applicable or not available
  Message              : "type127.dll" was found but did not contain any components from the input file.

```

*** Notice at time : 0.000000
Generated by Unit : Not applicable or not available
Generated by Type : Not applicable or not available
Message : "Type157_demo_debug.dll" was found but did not contain any components from the input file.

*** Notice at time : 0.000000
Generated by Unit : Not applicable or not available
Generated by Type : Not applicable or not available
Message : "Type412.dll" was found but did not contain any components from the input file.

*** Notice at time : 0.000000
Generated by Unit : Not applicable or not available
Generated by Type : Not applicable or not available
Message : The following Types were loaded from "Type425.dll": Type425

*** Notice at time : 0.000000
Generated by Unit : Not applicable or not available
Generated by Type : Not applicable or not available
Message : "Type76Lib.dll" was found but did not contain any components from the input file.

*** Notice at time : 0.000000
Generated by Unit : Not applicable or not available
Generated by Type : Not applicable or not available
Message : "Type82Lib.dll" was found but did not contain any components from the input file.

*** Notice at time : 0.000000
Generated by Unit : Not applicable or not available
Generated by Type : Not applicable or not available
TRNSYS Message 199 : TRNSYS found at least one user DLL in the UserLib directory. (Note: Only DLL's including Types that are used in the simulation are loaded)
Reported information : 1 user DLL was loaded after searching in "C:\Trnsys17\UserLib\DebugDLLs"

Appendix E: Pressure drop calculations for the Airport Terminal space

This appendix provides supporting materials used in the calculation of the HVAC duct pressure drop. The specific loss coefficients used were obtained from Idelchik (1994). The different duct-sections can be referred back to Fig. 7.6 and Fig. 7.10, and all ducts are assumed to be made of galvanised steel. The calculations are for each diffuser, with an air mass flow rate of 6 kg/s.

$$\text{Static losses are obtained from (m):} \quad h_L = 4fL \frac{u^2}{2g} \quad (\text{E1.1})$$

$$\text{Specific losses (m):} \quad h_{sp} = \xi \frac{u^2}{2g} \quad (\text{E1.2})$$

$$\text{Dynamic losses (m):} \quad h_d = \frac{u^2}{2g} \quad (\text{E1.3})$$

$$\text{Power losses (W):} \quad Q_{loss} = \dot{V} \rho g h \quad (\text{E1.3})$$

Where ' f ' is the friction factor; ' L ' is the pipe length (m); ' u ' is the air velocity (m/s); ' g ' is gravity (9.81 m/s²); ' ρ ' is the density of air (1.22 kg/m³); ' ξ ' is the specific loss coefficient; ' h ' is the head loss (m); and ' \dot{V} ' is the air volumetric flow rate (m³/s).

E1. Main Supply Duct

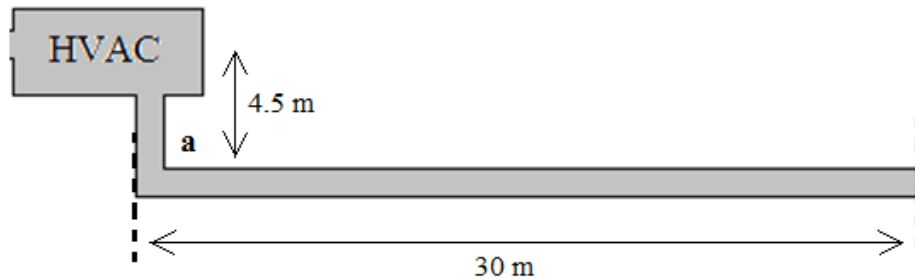


Fig. E1.1. Main Supply Duct dP

Diameter of pipe = 0.645 m ; Air-velocity = 15 m/s ; $Re = 6.17 \times 10^5$; $(k/d) = 0.00023$; $f = 0.00385$; Specific loss coefficient at ' a ' = 0.22 (for 90° bend).

$$(h_L = 9.44 \text{ m}) + (h_{sp} = 2.53 \text{ m}) + (h_d = 11.47 \text{ m}) = (h_{total} = 23.44 \text{ m})$$

$$Q_{loss} = 1346.5 \text{ W}$$

E2. Branch Supply Duct

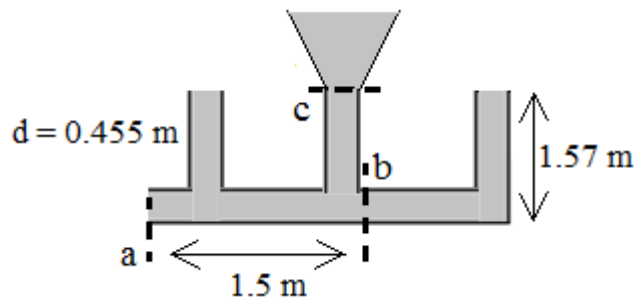


Fig. E1.2. Branch Supply Duct dP

The dominant static pressure loss was found to be for the route a-b-c.

(Same pressure drops are assumed for the by-pass routes)

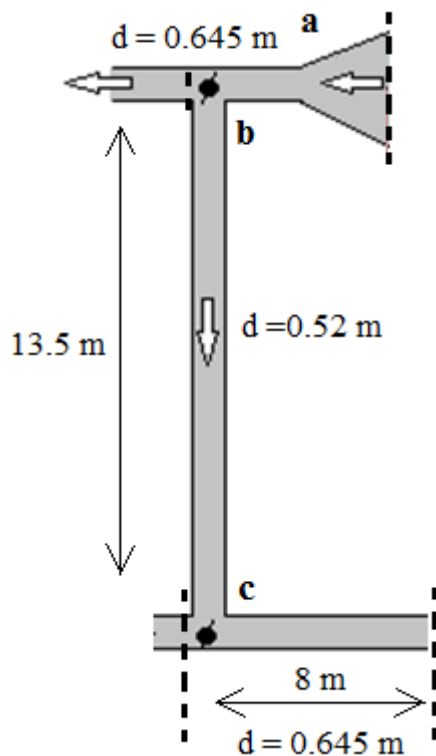
Air velocity = 10 m/s ; $(k/d) = 0.00033$; $Re = 2.9 \times 10^5$; $f = 0.0044$; $\xi_a = 0.49$; $\xi_b = 0.55$
and $\xi_c = 0.672$ (for a 71° expansion joint).

$$(h_{L, a-b} = 0.591 \text{ m}) + (h_{L, b-c} = 0.31 \text{ m}) + (h_{sp, a-c} = 12.94 \text{ m}) + (h_{sp, c} = 3.43 \text{ m}) =$$

$$(h_{total} = 17.27 \text{ m})$$

$$Q_{loss} = 992.1 \text{ W}$$

E3. Main Return Duct



Air velocity = 15 m/s ; $\xi_a = 0.04$ (for a 40° contraction) ; $\xi_b = 1.707$ (for a T-joint) ; $\xi_c = 0.22$ (for a T-joint) ; $f = 0.00385$; $g' = 0.71$;
and $L_{b\text{-exit}} = 2\text{m}$.

$$(h_{sp, a} = 0.459 \text{ m}) + (h_{sp, b} = 19.58 \text{ m}) + (h_{sp, c} = 2.525 \text{ m}) + (h_{L, b-c} = 7.3 \text{ m}) + (h_{potential, b-c} = 10.606 \text{ m}) = (h_{total} = 40.47 \text{ m})$$

$$Q_{loss} = 2333 \text{ W}$$

Fig. E1.3. Main Return Duct dP

E4. DC Diffuser Return dP

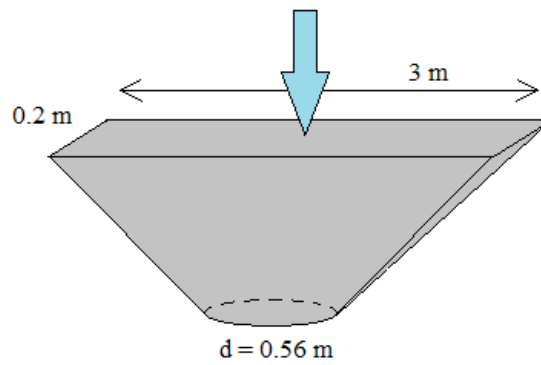


Fig. E1.4. DC Diffuser Return Path

Air velocity = 10 m/s ; $\xi = 0.08$ (for a 60° contraction) and $\xi_{\text{return branch}} = 0.4$

$h_{\text{total}} = 2.448$ m

$Q_{\text{loss}} = 138.3$ W (This path is used during night recharge of the PCM-HX system only and follows the same path as the main supply branch)

E5. Total Power Losses

Normal DC case

Total Supply Loss = 992.1 W + 1346.5 W = 2.34 kW

Total Return Loss = 2.33 kW

PCM Tiles and PCM-glazed envelope

Total Supply Loss = 2.34 kW

Total Return Loss during normal operation and winter night recharge = 2.33 kW

Total Return Loss during night ventilation (Summer/Intermediate) = 25W+31W = 56W

PCM-HX - 16mm air gap (10Pa pressure drop across plates)

Total Supply Loss = 2.34 kW + 48 W = 2.39 kW

Total Return Loss during normal operation and winter night recharge = 2.33 kW

Total Return Loss during night ventilation (Summer/Intermediate) = 138.3W +
1346.5W = 1.48 kW

PCM-HX - 8 mm air gap (45Pa pressure drop across plates)

Total Supply Loss = 2.34 kW + 216 W = 2.56 kW

Total Return Loss during normal operation and winter night recharge = 2.33 kW

Total Return Loss during night ventilation (Summer/Intermediate) = 138.3W +
1346.5W = 1.48 kW

Appendix F: Annual Energy calculation procedure

This appendix aims at describing the calculation procedure used to obtain the annual energy values presented in section 8.5.

The thermal loads are obtained using the concept of degree days, which are presented in section 7.5. Based on the definition of the distinct seasons described in Table 7.2, the seasonal Heating degree days (HDD) and Cooling Degree days (CDD) have been calculated for these periods, as shown in Table 7.3. The annual HDD and CDD are also presented in Table 7.3, and will be used to obtain the annual thermal loads. The base temperatures for the degree day calculation were obtained with reference to Figs. 8.1, whereby it was observed that heating is required for average temperature below 15°C and cooling is required for an average temperature above 18°C.

F1. Degree day (DD) procedure for each system

Having obtained the heating and cooling thermal loads results from TRNSYS in kWh/m, the thermal loads/DD are calculated for each season and for heating and cooling separately:

$$\text{Seasonal heating/DD} = \frac{\text{Seasonal Heating } \left(\frac{\text{kWh}}{\text{m}}\right)}{\text{Seasonal HDD}} \quad (\text{F1.1})$$

$$\text{Seasonal cooling/DD} = \frac{\text{Seasonal Cooling } \left(\frac{\text{kWh}}{\text{m}}\right)}{\text{Seasonal CDD}} \quad (\text{F1.2})$$

The annual thermal loads are then obtained, based on the average seasonal heating/cooling per DD, as follow:

$$\begin{aligned} \text{Annual Heating (kWh)} \\ = \frac{\sum \text{Seasonal Heating /DD}}{3} \times \text{Annual HDD} \times 300 \text{ (m)} \end{aligned} \quad (\text{F1.3})$$

$$\begin{aligned} \text{Annual Cooling (kWh)} \\ = \frac{\sum \text{Seasonal Cooling /DD}}{3} \times \text{Annual CDD} \times 300 \text{ (m)} \end{aligned} \quad (\text{F1.4})$$

Where ‘3’ is the number of seasons investigated; ‘300m’ is the overall length of the Airport Terminal space considered. The results from Eq. (F1.3) and (F1.4) are shown in Fig. 8.17.

F2. Annual Fan Powers’ calculations

The method of calculating the fan powers presented in Fig. 8.17 are explained here. The power losses of each diffuser due to pressure drops in the HVAC and the DC diffuser are individually explored in Appendix E. These same values are used here for each of the different PCM systems’ configuration investigated.

In this study, it is assumed that each DC diffuser serves a 2D thickness (or length) of 12m. Hence based on the overall length of the airport terminal space of 300m, 24 diffusers are found in this airport terminal space. The power loss for each diffuser is explained in Appendix E.

The extrapolation for the annual power demand is done based on the probabilities that the fans are used for each season. The annual fan power for each system is obtained as follows:

$$\begin{aligned} \text{Annual Fan Power (kWh)} \\ = \frac{\sum \text{Seasonal Fan Power}}{\text{Total simulation hours}} \times 8760(\text{hrs}) \times 24 \end{aligned} \quad (\text{F1.5})$$

Where: ‘8760’ is the total hours per year; and ‘24’ is the total number of diffusers in the entire airport. The results from Eq. (F1.5) are shown in Fig. 8.17.

It should be noted that the same extrapolation procedure to obtain both the annual thermal loads and annual fan powers are employed for all PCM system configurations, in order to abide by the comparative nature of the study.

Appendix G: Assumptions for costs and CO₂ emissions analysis

This appendix shows the assumptions used in the calculations of the costs and CO₂ emissions of the different PCM systems in section 8.5.3. Heating is done with gas, while chillers and fans use electricity. The energy demands are obtained from Fig. 8.17, adjusted for the respective efficiencies of the components. This analysis considers the ‘DC-only’ system as the base system, and all payback periods are calculated with reference to that base system.

$$\text{Payback [years]} = (\text{PCM Investment [£]} / (\text{Energy Savings [£/year]})$$

Assumptions for the price and CO₂ emissions factor of consumed energy:

(www.energysavingtrust.org.uk, 2013)

	Price (pence/kWh)	CO₂ emissions (kgCO₂/ kWh)
Natural Gas:	4.64	0.185
Electricity (Standard rate):	15.32	0.517
Electricity (Economy/ night rate):	9.08	0.514

Costs of PCM systems (Investments):

The prices of the PCMs are obtained from Rubitherm GmbH

(These prices are expected to be lower as the quantities ordered increase and as the PCM technology becomes more mature).

1. PCM-HX-16 configuration

- 1 diffuser contains (12 plates per row*125 rows) 1500 plates @ 13.76 [£/plate].
- 24 diffusers found in airport amounting to £495,360 of additional investment.

2. PCM-HX-8 configuration

- 1 diffuser contains (12 plates per row*190 rows) 2280 plates @ 13.76 [£/plate].
- 24 diffusers found in airport amounting to £752,947 of additional investment.

3. Ebb tiles

- Average price of paraffin blend PCMs = 10.47 [£/ m² of floor area].
- Total floor area = 14400 m²; amounting to additional investment of £150,703.

4. 'Theoretical' Energain tiles

- Average price of paraffin blend PCMs = $3.8 * 10.47$ [£/ m² of floor area].
- Total floor area = 14400 m²; amounting to additional investment of £572,670.

5. PCM Glazing

- Price of RT27 = 4.675 [£/kg].
- Total mass of RT27 in glazing and ceiling = $(62+9)*(300)*0.03$ [m³] * 820 [kg/m³] = 523,980 kg.
- Total additional costs of PCM in glazing = 523,980[kg] * 4.675 [£/kg] = £2,449,607.